Technische Universität München
TUM School of Engineering and Design

Increasing energy efficiency of neutral beam injection for DEMO: A conceptual design study

Giuseppe Starnella

Vollständiger Abdruck der von der TUM School of Engineering and Design der Technischen Universität München zur Erlangung eines

Doktors der Ingenieurwissenschaften (Dr.-Ing.)

genehmigten Dissertation.

Vorsitz:	Prof. Dr. Rafael Macián-Juan
Prüfer*innen der Dissertation:	
	1. Prof. Dr. Rudolf Neu
	2. apl. Prof. Dr.-Ing. Ursel Fantz

Die Dissertation wurde am 07.07.2022 bei der Technischen Universität München eingereicht und durch die TUM School of Engineering and Design am 18.10.2022 angenommen.

Abstract

In the pursuit of alternatives to fossil fuels, the experimental reactor ITER aims at proving the scientific and technological feasibility of fusion on a large scale. ITER will be followed by a DEMOnstration Fusion Power Plant (DEMO) with the main goals of producing electricity for the grid and demonstrating the commercial viability of fusion energy. For the latter objective, minimising the recirculating power consumed by the power plant, mainly by the external heating and current drive (H&CD) systems, is fundamental. Hence, the industrial exploitation of fusion requires a high wall-plug efficiency of the H&CD systems.

Negative-ion-based neutral beam injection (NNBI) is one of the H&CD systems considered for the European DEMO. Improving the NNBI wall-plug efficiency, which on ITER is only about 26 %, is the objective of this work. As gas neutralisation of the negative ions poses the major limitation to the ITER NBI wall-plug efficiency, the main options for its improvement on DEMO are increasing the neutralisation efficiency and/or reducing the electrical power consumed by the injector.

If a plasma is produced and sustained within the neutraliser, the collisions of the negative ions with plasma electrons and positive ions rather than with gas molecules lead to a higher neutralisation efficiency. To this end, the innovative concept of the beam-driven plasma neutraliser (BDPN) is studied in detail: an external power source is avoided as the plasma is generated by the negative ion beam that ionises the background gas while passing through the neutraliser chamber. The plasma is confined by a magnetic cusp field around the neutraliser. A zero-dimensional analytical model is built upon existing models to predict the BDPN performance on an ITER-like NBI. In order to benchmark the analytical model and to prove the BDPN feasibility, a suitable proof-of-principle experiment is identified.

On ITER, the residual ions of the neutralisation process are removed from the beam of neutral atoms and dumped at full energy. Thus, by recovering their kinetic energy and recirculating the corresponding current, one can reduce the NBI power consumption. A conceptual design of an energy recovery system (ERS) is proposed for the DEMO NNBI: the positive and negative ions at the neutraliser exit are firstly magnetically separated and subsequently decelerated and collected. A particle tracking computer code is used to evaluate the ERS efficiency. The role played by the background gas pressure along the injector is highlighted. Finally, the impact of the ERS in combination with both the gas neutraliser and the BDPN on the NBI wall-plug efficiency is estimated.

Acknowledgments

This work has been carried out within the framework of the EUROfusion Consortium, funded by the European Union via the Euratom Research and Training Programme (Grant Agreement No 101052200 — EUROfusion). Views and opinions expressed are however those of the author(s) only and do not necessarily reflect those of the European Union or the European Commission. Neither the European Union nor the European Commission can be held responsible for them.

I would like to sincerely thank my mentor, Dr. Christian Hopf, for all the support, the guidance and the valuable advice he has given me in the last four years.

Special thanks also go to Dr. P. N. Maya, who helped me to build a rate equation model for the plasma composition in the beam-driven plasma neutraliser, and to Dr. Niek den Harder for performing with the IBSimu code the numerical simulations of the particle trajectories and power loads in the energy recovery system.

Contents

Chapter 1

Introduction

The energy problem is the biggest challenge humanity has to face in this century. The world population growth, the increased urbanization and the rising access to electricity in the emerging economies lead to a huge increase in the energy demand. According to the International Energy Agency (IEA), the energy demand will rise by 1.3 % each year to 2040 [1].

Over the last century, the energy production has been based on burning fossil fuels such as coal, oil and gas which imply the emission of greenhouse gases (GHGs). Due to higher and higher GHG concentrations in the atmosphere, the global temperature is increasing: since pre-industrial times, human activity has warmed the world by about 1 °C.

At the 21st Conference of the Parties (COP21) in 2015, almost all the nations around the world adopted the Paris Agreement with the aim of limiting the global average temperature increase to 2 °C above pre-industrial levels, emphasizing the importance of striving for a maximum increase of 1.5 °C, half a degree more than the present situation. The latter, more ambitious goal was stressed by the Intergovernmental Panel on Climate Change (IPCC) Special Report on Global Warming of 1.5 °C (known as SR1.5) [2] which outlined the higher risks for natural and human systems for a global average temperature increase of 2 °C above pre-industrial levels. At the current human-induced warming rate, the 1.5 °C-threshold would be reached around 2040. Hence, urgent action is needed.

The principal GHG is CO_2. Reducing its emissions to zero means that the amount of CO_2 injected into the atmosphere is equal to the amount that is removed, a condition known as carbon neutrality.

Renewable sources such as solar, wind, hydro or biomass energy are the first choice of governments in their strategy to reduce the GHG emissions. However, the electricity production of many renewable sources is intermittent as it depends on the weather conditions. Hence, energy storage systems, e.g. batteries, are fundamental to the grid stability, but they require high investment costs. Furthermore, the electricity output is in general not sufficient to satisfy the needs of the grid. Power plants based on fossil fuels would then be needed as backup to make sure that the demand is always met.

The downsides of the renewables highlight the fact that the future energy system is rather a mix of different technologies and resources. Many countries included nuclear power in their Nationally Determined Contributions (NDCs) under the Paris Agreement [3]. Nuclear fission energy is a steady and reliable source of low-carbon base-load electricity that could support the energy production by renewables. It is, however, a very controversial zero-emission energy source due to a low public acceptance, especially after the Fukushima Daiichi accident in March 2011 which brought a few countries to phase nuclear fission power out of their energy mix [4].

Although nuclear fusion is not expected to give any significant contribution to the power generation before 2050, it is an additional valid option to consider in the long term. The efforts in pursuing its commercial realization rely on many advantages [5, 6]:

- *Fusion energy is abundant and sustainable.* The energy released is about four million times larger than that by chemical reactions such as the burning of fossil fuels and four times larger than that by fission reactions.

Furthermore, the supply of fusion fuel is plentiful. With respect to the deuterium-tritium (D–T) fusion reaction, deuterium is present in water, while tritium, although it does not exist in nature due to its half-life of about 12.3 years, can be bred from lithium which is widely available. This means that fusion is potentially accessible to everyone from everywhere in comparison to the uneven distribution of the fossil and fission fuels.

- *Zero CO_2 emissions.* Fusion does not emit GHGs as, together with energy, it produces helium, an inert and non-toxic gas.
- *No long-lived radioactive waste.* Fusion products are not radioactive. Material activation by neutrons is comparatively low.
- *Fusion is inherently safe.* There is no risk of meltdowns and major explosions. In case of accidents, the reaction stops immediately both because the conditions necessary for fusion are lost and because the quantity of fuel at any time in the reactor is sufficient only for a few seconds of power production. Hence, a chain reaction cannot develop.
- *No proliferation risk.* In a fusion reactor there are no fissile or fissionable materials that could be used to make nuclear weapons, not to mention that the fusion reaction in magnetic confinement fusion reactors is so difficult to initiate that no misuse is really feasible.

Fusion research has made outstanding progress in the last decades and the magnetic confinement concept has been identified as the most promising and fast way to achieve the commercial exploitation of fusion as energy source. In this regard, the most ambitious project is ITER, the International Thermonuclear Experimental Reactor currently under construction in southern France. The collaboration between the European Union, the United States, Japan, South Korea, India, China and Russia will result in the world's largest fusion reactor. ITER will prove the scientific and technological feasibility of fusion on a large scale, producing 500 MW of fusion power and maintaining the fusion reaction for long periods of time, from 300 s to 1 h.

ITER will not deliver electricity to the grid, but it is designed to pave the way to a DEMOnstration fusion power plant (DEMO) which, in the second half of this century, is going to produce hundreds of MW of electricity, "although in itself not fully technically or economically optimised" [7]. Finally, DEMO's features could be extrapolated to a commercial Fusion Power Plant (FPP).

Before the fusion reaction is able to sustain itself (an event called ignition), the required plasma temperature has to be reached by means of external heating. Neutral beam injection (NBI) has proved to be one of the most effective auxiliary heating systems: it has been used in most of the major fusion experiments around the world. A beam of fast neutral particles is injected into the plasma. Being neutral, the particles can penetrate the confining magnetic field. The fast neutrals are ionised by colliding with the plasma ions and electrons and are then confined inside the plasma by the magnetic field. The resulting fast ions transfer their energy to the plasma particles through collisions. Also ITER will rely on NBI heating and, although the heating mix of DEMO has not yet been decided, NBI is under consideration as auxiliary heating system in the European DEMO conceptual design [8].

Objective of the thesis

In order to facilitate the inclusion of fusion energy in the energy mix of the future, it is fundamental to make fusion an economically viable option. In particular, the difficulty in estimating the cost of something that will be available in more than 30 years calls for increasing efforts in making the fusion-based electricity cost competitive. Estimations of the cost of the electricity generated by fusion are comparable to or even lower than those for the conventional energy sources [9]. One of the major factors that severely affects the simulated economic performance of future FPPs is the recirculating power, that is the power consumed by the power plant operation. Therefore, it needs to be minimised. As the recirculating power is mostly consumed by the external heating systems, increasing their efficiency has become an important development goal already in designing DEMO, despite the fact that DEMO does not aim at being as competitive as a commercial FPP. DEMO offers the possibility of testing new technologies and improving existing systems in view of their application to a mature fusion reactor design.

In this framework, the objective of this thesis is to explore innovative concepts to increase the NBI wall-plug efficiency, defined as the ratio between the power of the neutral beam injected into the tokamak and the electrical power consumed by the system. The fast neutral beam is produced by initially extracting a negative ion beam from a plasma source and electrostatically accelerating the ions to the desired energy. Subsequently, the negative ions are neutralised in a gas cell through collisions with the gas molecules. Residual ions at the neutraliser exit are deflected onto an ion dump, while the fast neutrals are launched into the tokamak. The NBIs of ITER and DEMO extract and accelerate negative ions as the neutralisation efficiency of positive ions at the required high energies is practically zero.

The gas neutraliser is the NBI component where the highest efficiency gain is possible: the neutralisation efficiency of the ITER NBI beam of 1 MeV D^- ions is only 55 % [10]. Among the alternatives to gas neutralisation, this work focuses on plasma neutralisation which, providing a colliding target of thermal ions and electrons, promises a neutralisation efficiency higher than 80 % [11]. In particular, the concept of a beam-driven plasma neutraliser (BDPN) [12, 13] is investigated in detail: the plasma is not generated by an external power source but by the ion beam itself which ionises the background gas while passing through the chamber. The plasma is confined by a magnetic cusp field along the neutraliser walls. Building upon existing models, the underlying phenomena of plasma generation via the beam-driven mechanism are analytically described. The model results for an ITER-like NBI allow assessing whether it is worthwhile to invest in such a technology and, if so, the model is used to identify a suitable proof-of-principle experiment that would benchmark the analytical predictions and prove the feasibility of this innovative neutraliser concept.

Energy recovery [97, 99] is an additional option to increase the NBI wall-plug efficiency by reducing the electrical power consumed by the injector: the residual ions of the neutralisation process are not simply removed from the neutral beam and dumped at full energy like on ITER [14], but their kinetic energy is recovered and the corresponding current is recirculated in the system. A conceptual design of an energy recovery system (ERS) that magnetically separates the non-neutralised negative ions and the positive ions generated by the beam–gas reactions in the neutraliser and that subsequently decelerates and collects them is presented. A particle tracking computer code is used to simulate the residual ion trajectories, to assess the influence of the beam space charge and to evaluate the suppression efficiency of the secondary electrons created by the residual ions impacting with the collector walls. The role played by the background gas pressure along the injector is highlighted. In the end, the impact of the ERS in combination with both the gas neutraliser and the BDPN on the injector wall-plug efficiency is estimated.

Chapter 2

Nuclear fusion

2.1 Fusion on Earth

The energy of the stars in the universe is produced by fusion reactions. The fusion of light nuclei results in heavier nuclei whose mass is smaller than that of the initial reactants as the mass difference is converted into energy. The attempt of exploiting this energy on Earth for electricity production has been focusing on the reaction between two isotopes of hydrogen, deuterium (D) and tritium (T):

$$\mathrm{D} + \mathrm{T} \longrightarrow {}^{4}\mathrm{He} + \mathrm{n} + 17.6\ \mathrm{MeV} \tag{2.1}$$

Together with a nucleus of helium, also called α-particle, and a neutron, 17.6 MeV of energy are released as kinetic energy of the products: 14.1 MeV are carried off by the neutron and the remaining part, 3.5 MeV, by the α-particle. Deuterium is an abundant resource: it can be found in natural water with a fraction of 1 part in 6700 [15]. Tritium occurs in very small quantities in nature as it is an unstable radioactive nuclide which decays by β^- emission with a half-life of around 12.3 years. However, it is possible to use the neutron produced by the fusion reaction to breed tritium from lithium through the following reactions:

$$n + {}^{6}\mathrm{Li} \longrightarrow {}^{4}\mathrm{He} + \mathrm{T} + 4.8\ \mathrm{MeV} \tag{2.2}$$

$$n + {}^{7}\mathrm{Li} \longrightarrow {}^{4}\mathrm{He} + \mathrm{T} + n - 2.5\ \mathrm{MeV} \tag{2.3}$$

Lithium is widely available in the Earth's crust and even in the oceans, with natural abundances of 7.5 % for ^{6}Li and 92.5 % for ^{7}Li. Despite the lower abundance, ^{6}Li is going to be used to breed tritium in a fusion reactor as reaction (2.2) has a much higher cross section.

Other fusion reactions could be considered and some of them present clear advantages, like a higher energy release (D–^{3}He reaction) or neutron-free fusion (p–^{6}Li and p–^{11}B reactions, where p denotes a proton), the latter allowing the avoidance of radiation damage and material activation. However, the D–T reaction is the most conveniently achievable as its cross section is the highest and reaches the maximum at the lowest temperature, corresponding to an energy of about 100 keV. At low energies, the repulsive Coulomb force makes it impossible to bring the two positive nuclei together and achieve the fusion reaction. The fuel nuclei, therefore, have to be heated to high temperature such that their kinetic energies are high enough to overcome the electrostatic repulsion. Hence the name thermonuclear fusion.

A temperature of 100 keV is not necessary though. If a mixture of D–T nuclei is heated to a temperature of around 10–20 keV and confined for a sufficiently long time to allow particles to thermalise through many collisional processes, some of them can overcome the Coulomb barrier via quantum mechanical tunnelling and come sufficiently close to fuse. As the thermalisation results in a Maxwellian kinetic energy distribution of the reactants, the fusion reactions come mainly from the high-energy tail of the distribution.

A temperature of 10 keV is equivalent to about 100 million °C: the fuel gas mixture forms a fully ionised plasma.

2.2 Magnetic confinement

The required energy confinement time τ_{E}, defined as the ratio between the total energy in the plasma and the rate at which energy is lost, can be achieved by confining the plasma particles by means of a magnetic field: hence, the ions and electrons are restrained to move along the magnetic field lines. Closed magnetic confinement systems, in which the magnetic field lines are constrained in a specified volume, avoid the end losses of particles that would occur in an open configuration. A torus-shaped chamber has proven to be the most successful way to trap plasma particles. The toroidal magnetic field is generated by a set of ring-like coils around the torus. However, a purely toroidal magnetic field is not effective: the magnetic field in a torus is stronger on the inside, causing a vertical drift of the plasma particles that depends on their charge. Hence, ions and electrons drift in opposite directions and such charge separation produces an electric field. The direction of the resulting $\vec{E} \times \vec{B}$ drift of the whole plasma is outward, leading to a rapid loss of particles. In order to prevent the charge separation, a poloidal component of the magnetic field is needed to helically twist the magnetic field lines. On the basis of how the poloidal component of the magnetic field is generated, one can distinguish the two most common types of fusion machines: tokamaks and stellarators.

2.2.1 Tokamaks

In a tokamak, the poloidal magnetic field is produced by an electric current flowing in the plasma along the toroidal direction. Toroidal and poloidal magnetic fields together force the plasma particles to follow helical orbits. The plasma current is externally induced by transformer action: a solenoid at the centre of the tokamak acts as the primary winding, while the plasma itself is the secondary. Induction being a transient phenomenon, the plasma current can be provided only for a finite period of time. Steady-state operation, therefore, requires alternative non-inductive current drive methods. The main

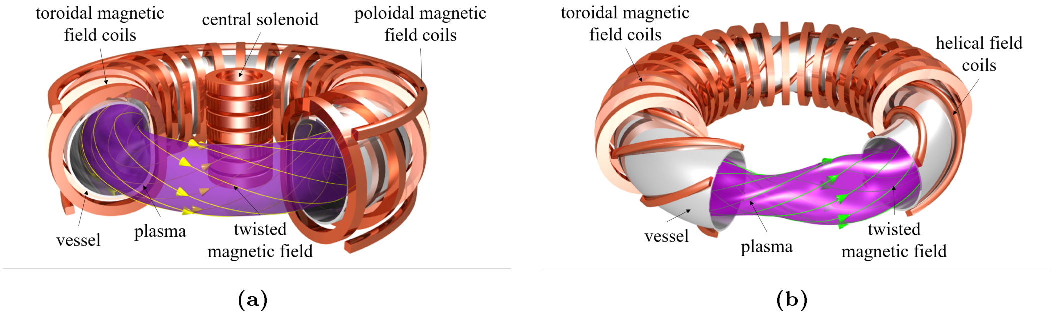

(a)

(b)

Figure 2.1: Schematic drawings of (a) a tokamak and (b) a stellarator. Pictures realised by Dr. Christian Brandt and reproduced with permission of the rights holder, Max Planck Institute for Plasma Physics.

advantage of the tokamak concept is the rotational symmetry, making a 2D description, by means of the toroidal and poloidal coordinates, exhaustive. The downsides are the pulsed operation and the loss of plasma confinement due to the instabilities generated by the plasma current. A simple schematic of a tokamak machine is shown in figure 2.1a.

2.2.2 Stellarators

In a stellarator, there is no need to drive a plasma current as the twisting of the magnetic field lines is provided by carefully designing the coils. Hence, stellarators are inherently capable of continuous operation. In the stellarators of the first generation, the toroidal magnetic field was generated by planar coils as in the case of tokamaks, while helical coils wound around the torus twisted the magnetic field lines, as schematically shown in figure 2.1b. In modern stellarators, the magnetic field is shaped by a single coil system consisting of toroidal non-planar coils with a complex geometry. This is the case of Wendelstein 7-X, the world's largest stellarator operated at IPP [16]. The coil shape of Wendelstein 7-X is the result of an optimisation of the magnetic field to reduce the energy losses of the plasma.

2.3 The gain factor Q

While the neutrons produced by the D–T fusion reaction leave the plasma with no interactions, the α-particles, being charged, are also confined by the magnetic field. This means that their kinetic energy of 3.5 MeV is transferred to the plasma through collisions, contributing to the plasma heating. If P_α is the power provided by the α-heating and P_L is the plasma energy loss rate, the external heating P_H required to reach the conditions for the thermonuclear fusion is such that [15]

$$P_\mathrm{H} + P_\alpha = P_\mathrm{L}. \tag{2.4}$$

When the α-particle heating alone counteracts the plasma losses and is able to sustain the fusion reaction by keeping the plasma hot, the external heating can be removed. This condition is called ignition.

The rate of energy loss from the plasma P_L is characterised by an energy confinement time τ_E according to the relation

$$P_\mathrm{L} = \frac{W}{\tau_\mathrm{E}}, \tag{2.5}$$

where W is the total energy in the plasma.

A conventional figure of merit in describing the ignition condition is the product of the plasma density n, the plasma temperature T and the energy confinement time τ_E, also known as triple product. In the temperature range 10–20 keV, the ignition condition reads [15]

$$nT\tau_\mathrm{E} > 5 \times 10^{21}\,\mathrm{m}^{-3}\,\mathrm{keV\,s}. \tag{2.6}$$

In order to quantify how close to ignition the plasma is, another useful parameter is the ratio Q between the power generated by the fusion reaction and the heating power that is externally supplied to the plasma:

$$Q = \frac{P_{\text{fus}}}{P_{\text{H}}}. \tag{2.7}$$

At ignition, $P_{\text{H}} = 0$, so $Q \to \infty$. The condition $Q = 1$, for which the fusion power is equal to the auxiliary power into the plasma, is called break-even. Large values of Q can be obtained without reaching ignition, but the presence of external heating lowers the overall efficiency of the machine as part of the produced power must be used to sustain the plasma.

2.4 Heating and current drive (H&CD) systems

In order to reach the required temperature of 10-20 keV and until the fusion reaction does not need to be externally sustained any more, different heating methods are used.

- **Ohmic heating** is the initial heating in a tokamak and comes from the Joule dissipation due to the ion-electron collisions of the toroidal current that is inductively driven in the plasma and mostly carried by electrons. Ohmic heating is very strong at low temperatures, but then it becomes less important as the plasma resistivity decreases with increasing temperature as $T_{\text{e}}^{-3/2}$, with T_{e} being the plasma electron temperature. Therefore, the ohmic heating is not enough to bring the tokamak plasma to ignition and additional heating is needed.

- **Neutral beam injection (NBI)**: a beam of fast neutral particles is injected into the plasma where they are ionised through collisions. Hence, the fast NBI ions are confined in the torus by the magnetic field and collide with the plasma ions and electrons, transferring their energy to the plasma particles. The need of using neutral beams comes from the fact that charged particles would be reflected back by the confining magnetic field.

- **Radiofrequency heating (RF)**: high power electromagnetic waves are launched into the plasma and absorbed at resonant frequencies, producing strong heating. A magnetised and multi-species plasma like the one of fusion reactors has different resonant frequencies which correspond to different RF heating mechanisms. The underlying principle, however, is the same: a remote high power generator transmits the electromagnetic energy to an antenna in the plasma chamber through a low-loss transmission line. According to the frequency regime, one can distinguish three main RF heating schemes:

  - **Electron cyclotron resonance heating (ECRH)**: the electromagnetic waves propagate at frequencies of the order of the electron cyclotron frequency (GHz range);
  - **Ion cyclotron resonance heating (ICRH)**: the RF heating is applied in the ion cyclotron range of frequencies (MHz range);
  - **Lower-hybrid range of frequencies (LHRF)**: it operates in the frequency range between ICRH and ECRH.

The main function of these auxiliary systems is to heat the plasma and ignite the fusion reaction. The heating should also be sufficient to favour the transition to the H-mode confinement regime [17], a high-confinement state of the plasma in which the energy confinement time increases by about a factor of two with respect to the previous low confinement regime, called L-mode.

A power deposition near the plasma centre allows for the minimum power input: NBI, ECRH and ICRH are able to provide a central plasma heating, while LHRF has limited penetration. In a tokamak, however, these systems may need to accomplish another fundamental task: to drive the toroidal current generating the poloidal magnetic field. This is a vital requirement for steady-state operation.

2.5 ITER

The feasibility of a tokamak fusion machine for the production of energy is going to be tested on a large scale for the first time by the International Tokamak Experimental Reactor (ITER), the biggest and most ambitious experiment about fusion which is being built in southern France. The ITER project is the result of a scientific collaboration between the European Union, the United States, Japan, South Korea, India, China and Russia with the aim of demonstrating the physics and technology of the fusion energy exploitation with the prospect of its commercial use through a full-developed fusion power plant (FPP). ITER, indeed, will not produce electricity. However, it will be the first fusion machine in which the α-particle heating dominates. Formally, the main mission is to produce around 500 MW of fusion power from a D–T plasma confined for 300–500 s with a gain factor Q at least equal to 10, corresponding to an external heating power of 50 MW. Hence, ITER will generate more power than that externally supplied to heat the plasma. ITER will also investigate continuous operation of a tokamak by means of non-inductive current drive for pulse durations of up to 1 h and a Q value of 5. If these two objectives are successfully achieved and the plasma confinement characteristics are favourable, a third goal is scheduled: the so-called "controlled ignition" corresponding to $Q \sim 30$ [18].

Although the ITER design is based on the knowledge and expertise gained through decades of experimental campaigns with the many smaller-scale tokamaks built and operated around the world, it represents a big extrapolation step: the linear size scale is bigger than that of the largest tokamak ever built to date by about a factor of 2 and is bigger than that of the largest superconducting tokamak currently in operation by a factor of 3–4 [18]. The principal parameters of the ITER tokamak are: the major and minor radius are 6.2 m and 2.0 m, respectively, the inductively driven plasma current is 15 MA and the nominal value of the toroidal magnetic field on the plasma axis is 5.3 T, requiring superconducting magnets to avoid the high resistive losses of normal conductors.

It is then fundamental to demonstrate the advantages in terms of safety and environment of a fusion machine in order to present nuclear fusion to the public as a convincing and reliable alternative to the carbon-based energy sources. ITER first plasma is currently planned for December 2025 [18]. The first operation scenario of ITER is going to be a non-activation phase in which hydrogen and/or helium are the main ion species [38]. The non-activation phase is important for the commissioning and validation of all tokamak systems. It will be followed by a low-activation D–D phase which provides the physics and operational basis for the D–T operation, scheduled to start in 2035 [18].

2.6 The European DEMO

The European DEMOnstration fusion power plant (DEMO) is defined by the European Roadmap to Fusion Electricity [7] as the intermediate machine between ITER and the first commercial FPP. Every ITER member country has its own strategy to reach the industrial and commercial exploitation of fusion after the realisation of ITER and, therefore, they all presented a different conceptual DEMO project [19–23]. In this work, however, reference is made only to the DEMO design study and R&D activities in Europe carried out by the EUROfusion Consortium [7, 24].

One of the central requirements of the European DEMO is the production of net electricity for the grid. DEMO will benefit from the technological and engineering knowledge gained through the construction and operation of ITER. Therefore, DEMO design is going to be carried out in parallel and modified according to the ITER results. This dependency is schematically outlined in figure 2.2. It is planned that DEMO will start operations in the second half of this century, around 20 years after ITER achieves a burning plasma with a gain factor $Q = 10$ [7].

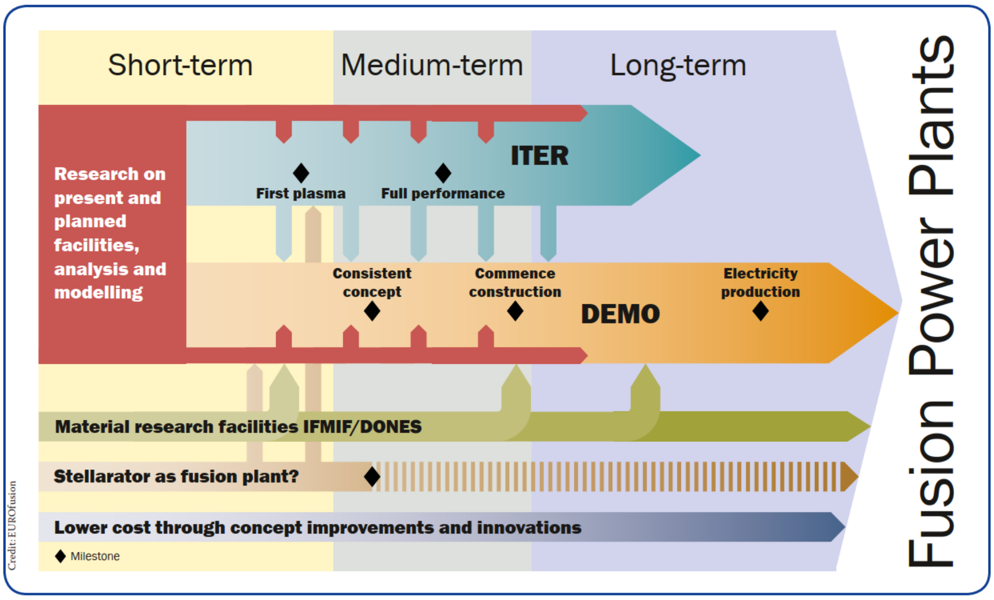

Figure 2.2: Scheme of the European Roadmap to the realisation of fusion energy, showing the main challenges and missions and their interrelations. It is well depicted how DEMO will receive inputs from ITER construction and operation and from other present and planned test facilities. Picture reprinted from [7] with permission of the rights holder, EUROfusion.

The main goals of DEMO are [7, 24]:

- an electricity power output of 300-500 MW to the grid;
- a closed fuel cycle or, in other words, tritium self-sufficiency through the breeding of tritium by neutron-lithium reactions;
- to validate materials that could withstand high neutron fluences;
- to demonstrate safety and environmental sustainability;
- to prove the feasibility of fusion relevant technologies;
- to asses the economic viability of a commercial FPP.

Relying on ITER experience, however, does not give sufficient answers to address the innovation level required in some critical areas. Hence, while at the beginning DEMO will use sufficiently well established solutions that have been tested on ITER and extrapolated to the DEMO-scale, research will continue in parallel to explore alternatives either as back-up options should criticalities arise or as economically more attractive solutions to be considered in designing an FPP. In this context, the stellarator concept is explored as long-term alternative to tokamaks for a power plant, after bringing the stellarator configuration to maturity by exploiting present devices, in particular Wendelstein 7-X [7].

Due to a lower power production and shorter pulse lengths, neutron irradiation will not be a major problem for ITER, but it will be for DEMO. Low-activation materials that are able to guarantee the required thermal and mechanical properties over long periods need to be used.

Unlike ITER, DEMO will have a complete Balance of Plant (BoP), i.e. all the systems that convert the thermal power produced by the ignited plasma into electricity to deliver to the external grid. The conventional BoP components need to be compatible with the innovative technologies and materials developed for fusion and combined into an integrated design. Engineering material data coming from fission neutron irradiation experiments are not sufficient due to very different neutron spectra and temperature conditions. In order to study and characterise materials under irradiation of neutrons with fusion-spectra, the construction of an International Fusion Materials Irradiation Facility (IFMIF) in Japan and of a smaller facility, IFMIF-DONES in Europe, is planned [25, 26].

Furthermore, also the economical aspects of the energy production are going to be taken into consideration in designing DEMO. This is not a primary objective as DEMO is not planned to be a competitive power plant. However, cost minimisation is one of the main drivers in selecting and optimising the DEMO design.

2.6.1 DEMO design strategy

Designing DEMO is a three-phase-process [7]:

- **Pre-conceptual design**: the system requirements are identified and a reference configuration, with fixed geometry and operational parameters, is assumed and referred to as *baseline*. Alternative reactor concepts are defined and compared against the baseline such that, at the end of the pre-conceptual design phase, it is possible to select either the most suitable as back-up options in case the baseline showed some critical problems or the most promising in terms of technologies that have not yet been developed but that could be available in a near future. This phase terminated in 2020.

- **Conceptual design**: the baseline and the selected configurations from the previous phase are studied and developed in detail. The aim of the conceptual design phase is to select the final DEMO design concept through a review gate in 2027.
- **Engineering design**: the chosen solutions for the final DEMO configuration are characterised from the engineering and technological point of view and prototypes are built and tested. This phase includes also the beginning of construction, around 2040.

2.6.2 DEMO options

As the conceptual design phase has just started, no official DEMO design exists and the operational requirements are not yet well defined.

At present, the focus is on two concepts [24, 27, 28], called DEMO-1 and flexi-DEMO. The baseline DEMO-1 is a pulsed fusion power plant that requires little extrapolation from the ITER experience, with a consequent minimisation of the development risks, while flexi-DEMO, even though operating in a pulsed mode too, is able to move to a steady-state regime of operation if a high confinement enhancement factor H can be achieved. The steady-state configuration demands a huge technological improvement with respect to what will be achieved by ITER, especially in providing reliable and efficient current-drive. The main design parameters of the two DEMO concepts are listed in

Table 2.1: Main design parameters of ITER [18] and of the DEMO concepts under consideration [24].

Parameter	Symbol	**ITER**	**DEMO-1**	**flexi-DEMO**	
				Pulsed	Steady-state
Major radius [m]	R_0	6.2	9.0	8.4	
Minor radius [m]	a	2.0	2.9	2.7	
Toroidal magnetic field [T]	B_T	5.3	5.9	5.8	
Plasma current [MA]	I_p	15	18	17	14
Confinement factor	H	1.0	1.1	1.1	1.5
Burn time	t_burn	300–500 s	2 h	1 h	∞
Fusion power [MW]	P_fus	500	2000	2000	
Electricity output [MW]	P_el	-	500	400	

table 2.1.

DEMO-1 is a conservative technology option and is currently favoured by the fact that it offers higher probabilities of success and a realistic schedule for a near-term production of electricity. Consequently, although also DEMO-1 requires a certain degree of advancement in order to fulfil the DEMO missions, the more ambitious innovations could be developed in parallel in the framework of a long-term R&D programme for the FPPs of the future [29]. On the other hand, it is also argued that such physics and technological improvements are not credible if not tested in the DEMO environment, advocating a small development step from DEMO to an FPP [30]. This "stepladder approach" considers DEMO a technology demonstrator, rather than a plasma physics experiment.

Chapter 3

Neutral beam injection

3.1 The NBI beamline structure

Neutral beam injection (NBI) is the heating and current drive system that is currently used and foreseen for most of the major fusion experiments around the world, including ITER.

The plasma is heated through the collisions between the plasma particles and the highly energetic ions generated by the ionisation of the fast neutrals injected into the tokamak. It is not possible to directly inject fast charged particles as these would be deflected by the confining magnetic field. Once ionised, the fast particles are confined to move around the torus and they transfer their energy to the plasma through Coulomb collisions.

Two types of neutral beam injectors exist: positive-ion-based NBI (PNBI) and negative-ion-based NBI (NNBI) which accelerate and neutralise positive and negative ion beams, respectively. The main components of an NBI beamline are similar for both positive and negative configurations and they are schematically drawn in figure 3.1: as the acceleration of particles requires them to be charged, a beam of ions is produced by an ion source and electrostatically accelerated to the desired energy. Then, the beam enters a chamber filled with gas which is called neutraliser: the neutralisation of the beam ions is achieved

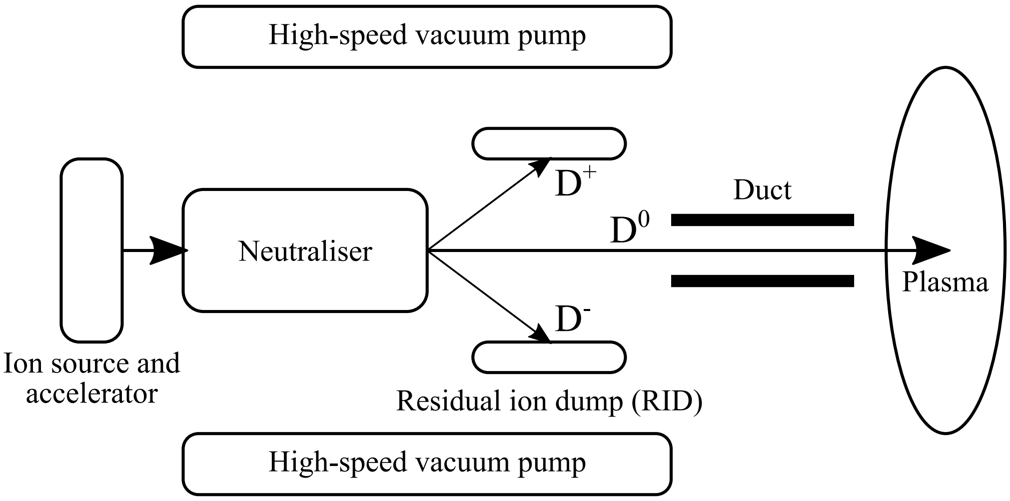

Figure 3.1: Sketch of the NBI beamline structure showing the main components for the production and transmission of a fast neutral beam up to the tokamak plasma.

through their collisions with the gas molecules. As not all the ions are neutralised, the remaining charged particles are dumped in the residual ion dump (RID) to avoid their deflection by the magnetic field against the other system components, while the fast neutrals are launched into the tokamak.

The big fusion machines under development, like ITER and DEMO, require high energy neutral beams. As the neutralisation efficiency of positive ions at high energies is vanishingly small, negative ions are the only possibility to deliver several tens of MW of power to the tokamak plasma. From here on out, therefore, only negative ions are considered.

3.1.1 Ion source

The ion source is the fundamental component of an NBI beamline. The simplest description of an ion source is that of a box filled with gas in which a dense and uniform plasma is generated. According to how the plasma is produced, one can distinguish two ion source concepts:

- **Arc sources**: the plasma is generated by the electrons emitted by hot tungsten filaments. The electrons strike an arc discharge in the filling gas between the filaments and the box walls which represent the anode.

One of the walls constitutes the first grid of the accelerator, known as plasma grid (PG). The ions are extracted through the PG apertures and subsequently accelerated. If the anode walls are covered with permanent magnets of alternating polarity to produce a cusp magnetic field, the plasma losses decrease due to the reduction of the effective anode loss area. Furthermore, the gas ionisation rate of the energetic electrons emitted by the cathode filaments increases as the electrons undergo many more collisions before being lost at the chamber walls. This configuration is called multicusp or bucket source [31].

- **Radiofrequency (RF) sources**: a coil is wound around a cylinder, called driver, placed on the back of the source chamber. RF power at about 1 MHz is applied to the coil and, hence, inductively coupled to the filling gas which becomes ionised, forming the plasma. The absence of filaments makes the design and operation of RF sources simpler as the filaments require frequent replacements and many electrical connections. RF sources are foreseen for the NBIs of ITER and future FPPs.

From the ion source the gas flows into the accelerator and then along the beamline. Due to collisions with the gas molecules, the negative ions are neutralised while being accelerated. As the neutralisation happens before the ions go through the whole accelerator, these neutrals have a lower energy than that of a neutral particle exiting the neutraliser. When the neutralisation takes place in the accelerator, it is called stripping and it represents a loss of extracted ions. Stripping produces also electrons and, if the negative ions are stripped twice, positive ions: the electrons are accelerated through the remaining part of the accelerator, causing high power loads on the component they hit, while the positive ions are accelerated backwards and deposit their power on the former acceleration grids and on the source chamber walls. Therefore, the electrons and positive ions coming from the stripping of negative ions in the accelerator represent additional losses. A low source pressure as well as very high pumping speeds in the beamline vacuum vessel are fundamental to minimise the stripping losses (the gas throughput in the ion beam source of the ITER NBI is $3.6\,\mathrm{Pa\,m^3\,s^{-1}}$ for the deuterium pulse operation) [32, 57].

3.1.2 Accelerator

After being created at the plasma grid surface, the negative ions are extracted and accelerated through a multi-aperture multi-grid system [14]. The second grid is called Extraction Grid (EG). The application of a positive potential difference between the EG and the PG allows the extraction of the negative ions and, unavoidably, of the source plasma electrons. The co-extracted electrons represent one of the major issues in the operation of negative ion sources: if they are not stopped, they would be accelerated to full energy and deposit their power on the beamline components, causing melting damage. This is avoided by embedding permanent magnets in the EG such that the co-extracted electrons are deflected and forced to impinge on the EG before they start to accelerate. Having a much larger mass, the deflection of the negative ions is very small and is compensated by means of other permanent magnets and/or beamlet steering techniques [14].

PG and EG form the so-called extraction system which is followed by the actual acceleration system. During the ITER NBI design, two different accelerator concepts were proposed, schematically shown in figure 3.2 [33, 34].

- **MAMuG** (Multi Aperture Multi Grid) accelerator: the acceleration occurs through intermediate steps. This implies many acceleration grids (AGs) with the same aperture pattern of the PG and EG and with increasing potentials. In the case of ITER, for example, with a required ion energy of 1 MeV and a PG biased at -1 MV, five acceleration stages of 200 keV are used such that the last AG results grounded. Hence the name grounded grid (GG). A potential difference of 200 kV instead of 1000 kV greatly simplifies the problem of voltage holding, reducing the

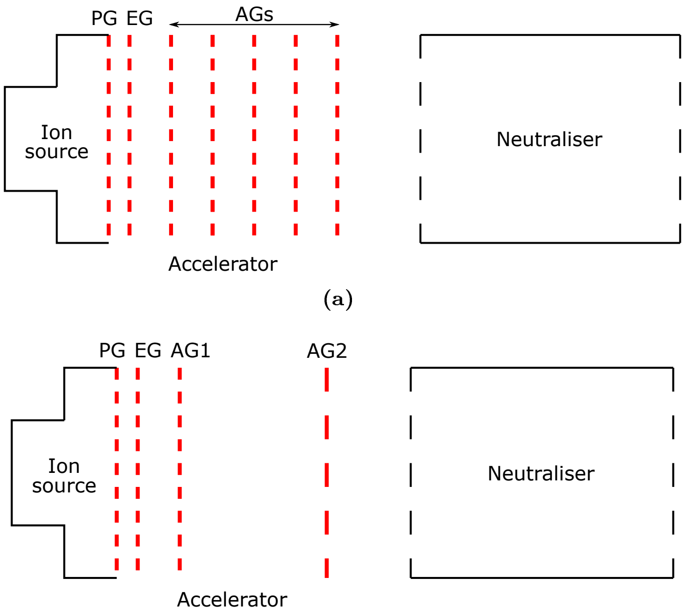

(a)

(b)

Figure 3.2: Schematic of the two electrostatic accelerators initially proposed for the ITER NBI to accelerate the negative ions to an energy of 1 MeV: (a) MAMuG concept, with five AGs corresponding to five acceleration stages of 200 keV; (b) SINGAP concept, with only two AGs as the acceleration mainly occurs in one step.

risk of high-voltage breakdowns. Furthermore, it is likely that the co-extracted electrons strike against the intermediate grids without being accelerated up to the GG to full energy.

- **SINGAP** (SINGle APerture – SINgle GAP): after a pre-acceleration stage, the main acceleration is achieved in one step, corresponding to a potential difference of 945 kV in the ITER NBI concept. The great advantage of the SINGAP accelerator is its simplicity, especially in the design of the high voltage transmission line as intermediate potentials are not needed. The stripping losses are smaller than those in the MAMuG accelerator thanks to the large gap between the two AGs that allows a better pumping access. However, the co-extracted electrons cannot be stopped and are fully accelerated, resulting in higher power loss and deposition than in MAMuG.

The MAMuG concept is a conventional and conservative design as it was successfully applied in many experimental facilities. Considering also the advantages in terms of better voltage holding and lower co-extracted electron power losses and heat loads, the MAMuG accelerator was chosen as the reference design for the ITER NBI. An exhaustive comparison between the MAMuG and SINGAP concepts, with additional pros and cons, can be found in Ref. [35].

3.1.3 Neutraliser

The beam emerging from the accelerator is made of negative ions that have the energy required to heat the tokamak plasma and drive the toroidal current generating the poloidal magnetic field. If these fast ions were directly injected into the tokamak, they would be deflected by the confining magnetic field. Therefore, they need to be neutralised. The neutralisation process is achieved by letting the beam pass through a gas cell, not by chance known as gas neutraliser. The negative ions are stripped by colliding with the gas molecules (here the stripping is called neutralisation), but the resulting neutrals could undergo a subsequent collision and be converted into positive ions (a process called re-ionisation). The competition between neutralisation and re-ionisation implies the existence of an optimum neutral fraction. The beam composition output depends on the gas target thickness, defined as the line integral of the gas density along the neutraliser length. At the optimum gas target thickness, the maximum value of the beam neutral fraction, i.e. the maximum neutralisation efficiency, is achieved.

In the case of positive ions, the neutralisation occurs through charge exchange with the gas molecules. However, the neutralisation efficiency becomes negligible for energies $> 200\,\mathrm{keV/amu}$, with amu being the atomic mass unit, as shown in figure 3.3. With negative ions, instead, the neutralisation yield remains almost constant at high energies, with a value around $55\,\%$. For this reason, ITER, DEMO and future FPPs need to rely on negative-ion-based NBIs.

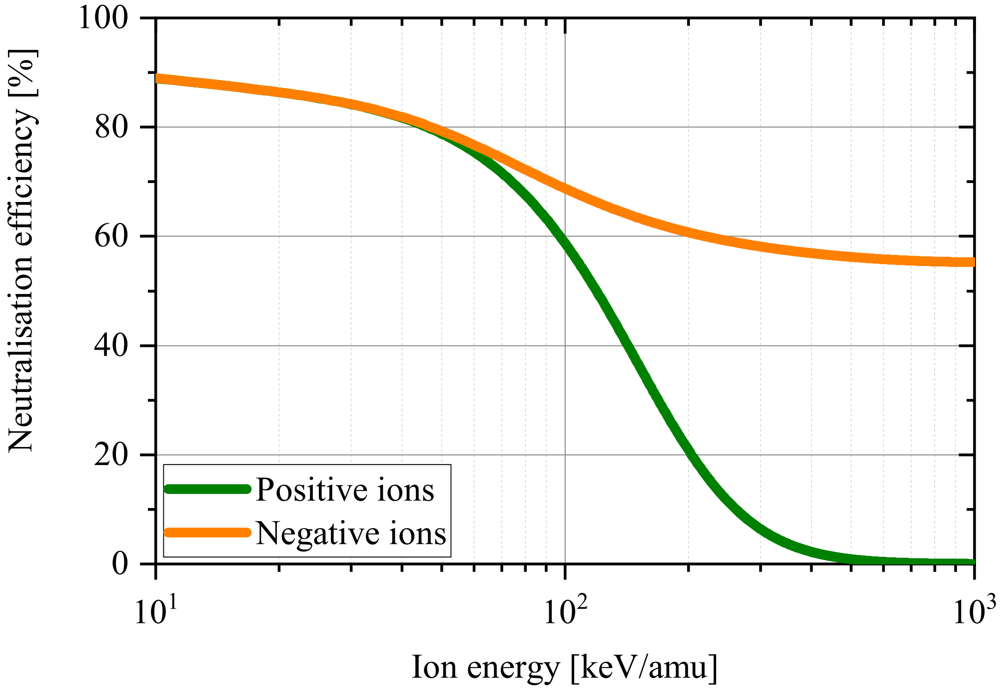

Figure 3.3: Neutralisation efficiency as function of the beam energy per atomic mass unit (amu) for both positive and negative ions.

3.1.4 Residual ion dump (RID)

Even for an optimum value of the gas target thickness, not all the negative ions entering the neutraliser are converted into neutrals. Furthermore, positive ions are produced by the processes of re-ionisation and double-stripping. The result is that the beam at the exit of neutraliser is made of fast neutral, positive and negative particles. The charged fractions, however, need to be removed from the beam as, if they were deflected by the tokamak magnetic field, they would impact against and damage the beamline structures. The function of the RID is indeed to get rid of the ions in a controlled way: through a magnetic or electric field, they are deflected towards water-cooled collector systems that are designed to withstand high power densities. The beam neutral particles are not affected by the magnetic/electric field and they can continue undisturbed towards the tokamak plasma through the drift duct [36].

3.2 ITER NBI

The main goal of ITER is a gain factor $Q = 10$ for a pulse duration of around 400 s. The auxiliary heating power envisaged for such an achievement is equal to 73 MW which will be delivered by three different systems [37]:

- 20 MW at 170 GHz from ECRH;
- 20 MW in the 40–55 MHz range from ICRH;
- 33 MW from NBI.

As far as NBI is concerned, two heating NB (HNB) lines are initially installed, each of them delivering a power of 16.7 MW [40]. A third injector could be installed at a later stage if required, for example in order to test longer pulse operations. A diagnostic NB (DNB) line is also foreseen to measure the ion temperature and the He ash content in the plasma.

The main requirements for the HNB and DNB injectors are given in table 3.1. As the initial operation scenario of ITER is going to be a non-activation phase with hydrogen and/or helium [38], ITER HNBs are expected to work both in hydrogen and deuterium.

The energy requirement of the ITER heating NBIs comes from their two main functions, i.e. plasma heating and current drive. Concerning the former function, the neutral beam can penetrate the plasma up to the desired position and deposit its power only if the energy is sufficiently high. As the ionisation cross sections decrease with increasing energy, only high energies allow obtaining the required mean-free path of the neutral particles in the plasma that, as a rule of thumb, should be of the order of the tokamak minor radius in order to achieve central plasma heating [39]. In the case of the ITER plasma, energies > 200 keV in deuterium are required.

The HNBs must also drive current: after the energetic neutrals are ionised, the fast ion velocity component parallel to the tokamak magnetic field generates a toroidal current which replaces part of the current that is driven by the

Table 3.1: Main parameters of the ITER HNB (heating) and DNB (diagnostic) injectors. The heating NBI is going to operate both in hydrogen (H) and deuterium (D) [40, 41].

Parameter	**HNB**		**DNB**
	H	D	H
Beam power [MW]	16.7/beamline		2
Beam energy [MeV]	0.87	1	0.1
Accelerated current density [A/m^2]	230	200	300
Accelerated current [A]	46	40	60
Pulse length [s]	3600		3 s ON, 20 s OFF

induced electric field. However, the slowing down of the fast ions through collisions with the plasma electrons produces a toroidal drift of the electrons resulting in an electron current in the opposite direction to the fast ion current which is, therefore, partly cancelled. Furthermore, fast ions are lost due to their interaction with the magnetic field and due to different plasma instabilities [15]. The consequence is a net driven current I_{CD} that is lower than the initial fast ion current. The current drive efficiency $\varepsilon_{\mathrm{CD}}$ is defined as [42]

$$\varepsilon_{\mathrm{CD}} = \frac{I_{\mathrm{CD}}}{P_{\mathrm{HCDcoup}}}, \tag{3.1}$$

where I_{CD} is the non-inductive driven current and P_{HCDcoup} is the external power coupled to the plasma. However, as $\varepsilon_{\mathrm{CD}}$ decreases with the tokamak major radius R_0 and the averaged plasma density $\bar{n}$, it is convenient to define the current drive figure of merit γ [42]:

$$\gamma = \frac{\bar{n}\, R_0\, I_{\mathrm{CD}}}{P_{\mathrm{HCDcoup}}} = \bar{n}\, R_0\, \varepsilon_{\mathrm{CD}} \qquad [10^{20}\,\mathrm{A\,W^{-1}\,m^{-2}}], \tag{3.2}$$

which is best suited for comparisons.

The current drive efficiency increases with increasing beam energy [43]. However, high beam energies imply the development of high voltage power supplies which is very challenging from the technological point of view. Hence, the choice of 1 MeV as reference energy of the deuterium neutrals is a compromise

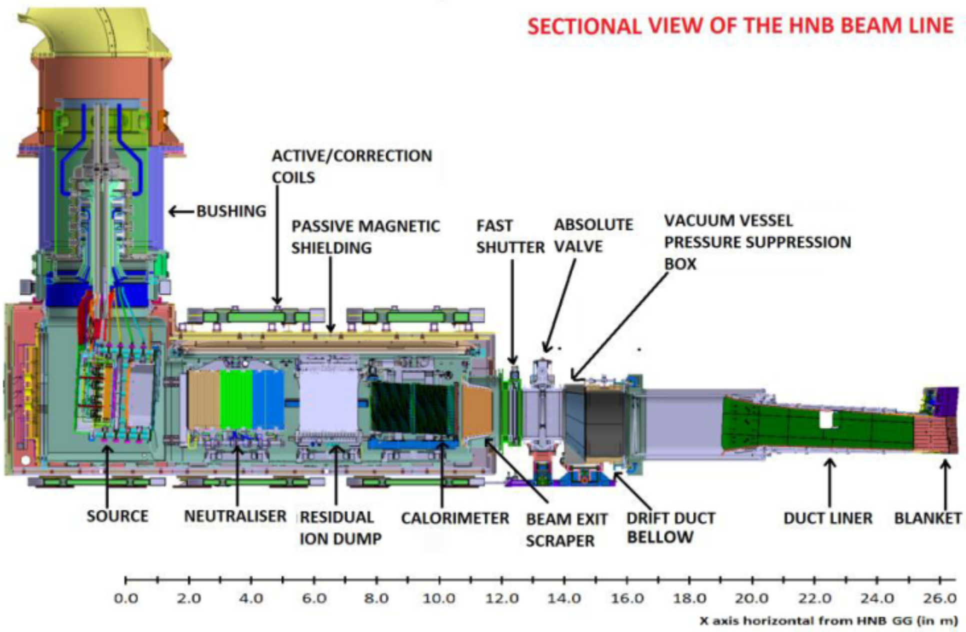

Figure 3.4: Cutaway view of the ITER HNB injector outlining the main beamline components. Picture reprinted from [40] under the terms of the Creative Commons Attribution 3.0 licence.

between the previous considerations about central heating and current drive and the need of getting the required beam power from a source of feasible size with achievable current density.

During the commissioning phase, hydrogen is going to be used to avoid material activation: the same accelerated power of 40 MW is obtained with an acceleration voltage of 870 kV and an accelerated beam current of 46 A. These parameters allow the optimisation of the beam optics, i.e. a low divergence and a good transmission of the beamlets which would otherwise hit the beamline structures, depositing high power loads and producing melting damages [39].

The main components of the ITER HNB injector are shown in the cutaway view of figure 3.4.

3.3 DEMO NBI

As an official DEMO design has not yet been chosen, the composition of the external heating mix is still an unknown.

While DEMO-1 foresees an auxiliary heating power in the range 50–100 MW [24], the operation scenarios of flexi-DEMO in continuous or quasi-continuous (pulses of the order of 1 h) mode need a higher H&CD power due to the high fraction of non-inductive plasma current that has to be externally provided. Among the H&CD systems, the NBI is the most efficient in driving current.

However, NBI could be excluded from the heating mix of DEMO [8] as, despite a high efficiency, an HNB injector is a complicated machine to construct and operate, especially if compared to the radiofrequency systems. It was decided that ECRH is the current heating baseline, while ICRH and NBI "will be developed in the frame of a risk mitigation approach" [8]. Hence, none of the H&CD systems can be ruled out at the moment.

Although the DEMO operative requirements have not yet been definitely identified, some considerations can be made on the basis of another design driver: the cost of electricity. Being the precursor of an FPP, DEMO needs to implement physics and technological solutions to increase the overall efficiency and make the produced electricity cheap. Demonstrating the commercial viability of fusion is one of the missions of DEMO. In the case of the heating and current drive systems, this translates into the minimisation of the recirculated power.

The recirculated power is the fraction of the electrical power produced by the fusion reactor that is used to operate all the sub-systems of the plant. The major part of the recirculated power is consumed by the H&CD systems [42]. A quantitative description is given by the so-called wall-plug efficiency which is defined as the ratio between the power P_{HCD} injected into the tokamak and the electrical power P_{eHCD} used to operate the system:

$$\eta_{\mathrm{wp}} = \frac{P_{\mathrm{HCD}}}{P_{\mathrm{eHCD}}}. \tag{3.3}$$

Investigating how to maximise the wall-plug efficiency for the NBI system is the goal of this work. Given the complexity of an injector beamline and the interdependence of its components, it is not straightforward to identify the

Table 3.2: Main parameters and efficiencies of the major sub-systems of the ITER HNB injector [32]. The wall-plug efficiency is derived accordingly.

	Symbol	**ITER NBI**
Species		D
Acceleration voltage [MV]	V_b	1
Accelerated current [A]	I_{acc}	40
Accelerator power loss [MW]	P_{acc}	10
Accelerator power supply efficiency	η_{PS}	0.875
Electrical power to the auxiliary systems [MW]	P_{aux}	10
Beamline transmission efficiency	η_{BT}	0.79
Neutralisation efficiency	η_{neut}	0.55
Wall-plug efficiency	η_{wp}	0.26

most convenient strategy to increase the wall-plug efficiency.

As the current DEMO baseline is a modest extrapolation from ITER, a good starting point is to analyse the wall-plug efficiency of the ITER NBI. Table 3.2 shows the main parameters and the efficiencies of the major sub-systems of the ITER HNB injector [32].

The power lost in the accelerator P_{acc} is mainly due to the stripping losses of the extracted negative ions colliding with the background gas molecules. The beam-gas collisions are responsible also for the re-ionisation losses of the neutral particles, especially in the duct, which reduce the neutral beam power injected into the reactor. The obvious solution is to decrease the gas throughput into the beamline but this would have serious consequences for the operation of the ion source and of the neutraliser, the two major gas sources along the injector: a lower gas inflow would make the production of a sufficient plasma density in the source chamber very difficult and it would make it necessary to use a much longer neutraliser to achieve the same optimum gas target thickness. The re-ionisation losses are taken into account by the beamline transmission efficiency η_{BT} which also depends on the beam optics, the injector geometry and the background gas density. The electrical power to the auxiliary systems P_{aux} is mainly used to operate the cryopumps and the RF ion source.

The NBI wall-plug efficiency is equal to the ratio between the neutral beam power injected into the tokamak P_{NBI} and the electrical power consumed by the injector P_{el}. Using the data in table 3.2,

$$P_{\mathrm{NBI}} = I_{\mathrm{acc}} V_{\mathrm{b}} \, \eta_{\mathrm{BT}} \, \eta_{\mathrm{neut}} \approx 17.4\,\mathrm{MW}. \tag{3.4}$$

In addition to the power spent to accelerate the negative ion beam, one has to consider also the power lost in the accelerator, the power supply efficiency and the power consumption of the NBI auxiliary systems in order to compute P_{el}:

$$P_{\mathrm{el}} = \frac{I_{\mathrm{acc}} V_{\mathrm{b}} + P_{\mathrm{acc}}}{\eta_{\mathrm{PS}}} + P_{\mathrm{aux}} \approx 67.1\,\mathrm{MW} \tag{3.5}$$

Therefore, the ITER NBI wall-plug efficiency is estimated as

$$\eta_{\mathrm{wp}} = \frac{P_{\mathrm{NBI}}}{P_{\mathrm{el}}} \approx 26\,\%. \tag{3.6}$$

Table 3.2 clearly shows that gas neutralisation is the main reason why the wall-plug efficiency of the ITER NBI is limited to 26 %. The neutraliser is the injector component where the biggest improvement is possible as the neutralisation efficiency of a conventional gas neutraliser for a 1 MeV D^- ion beam is only 55 %.

Over the past years, different neutralisation processes have been investigated. With the primary objective of eliminating the neutraliser gas throughput, as the D_2 injected into the neutraliser is the main gas source in the NBI beamline, alternative targets for the negative ion stripping have been proposed: carbon foils, heavy gases and metal vapours [44, 45]. In general, using heavy targets reduces the beamline gas pressure, but the corresponding neutralisation efficiencies are significantly lower. However, a lithium vapour jet neutraliser could offer a higher neutralisation efficiency with respect to a deuterium target: a neutral fraction of 62.5 % was experimentally measured in the case of a 400 keV D^- ion beam [44]. A similar efficiency is expected also for higher beam energies as it is usually the case for negative ions. A supersonic lithium vapour jet is injected across the ion beam perpendicularly to the beam path in the middle of the neutraliser. The jet would deposit and freeze onto a collection plate from which the lithium is recovered, heated to a temperature $> 180\,^{\circ}\mathrm{C}$ to melt it and injected again. A well-directed supersonic jet avoids spreading along the injector and keeps the size of the collector small [45, 46].

Photoneutralisation, in which the extra electron is removed from the negative ion by using photons, and plasma neutralisation, in which the conventional gas target is ionised and the negative ion stripping occurs through collisions with the plasma electrons and ions, could achieve very high neutralisation efficiencies. Therefore, they have received a lot of attention. More details about photoneutralisation are given in the next section, while plasma neutralisation is the topic of the next chapter.

3.3.1 Photoneutralisation

The removal of the electron from the negative ion occurs through the photodetachment process by a photon of energy $h\nu$:

$$\mathrm{D}^- + h\nu \longrightarrow \mathrm{D}^0 + \mathrm{e} \tag{3.7}$$

The photon energy must be higher than the electron affinity of the species (equal to 0.75 eV for deuterium) but lower than the ionisation potential of the atom (equal to 13.6 eV). As no other competing process is present, the neutralisation of the negative ions by photodetachment has a theoretical efficiency of 100 %. Except for a small isotope shift, the electron affinity and the photodetachment cross section are practically equal for hydrogen and deuterium, making it possible to carry out experiments in hydrogen and directly transfer the results to deuterium operation.

The cross section of reaction (3.7), however, is very small: the maximum value of $4 \times 10^{-21}\,\mathrm{m}^2$ is obtained for a photon energy between 1.4 and 1.5 eV,

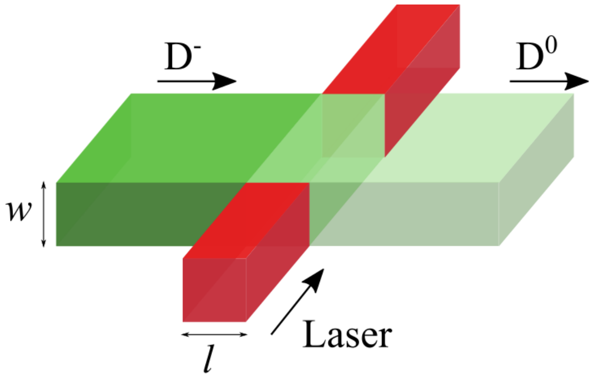

Figure 3.5: Sketch of a negative ion beam illuminated by a laser beam. Both beams have a transverse dimension w.

corresponding to a wavelength λ between 885 and 825 nm [47]. Due to the low cross section value and due to the very short time that 1 MeV D^- ions reside in the photon-illuminated region, a high photon flux is needed: assuming a beam with a 1 cm width, a photodetachment rate of 50 % requires a laser power of 3 MW for $\lambda = 1064$ nm [48, 49]. Higher efficiencies can be achieved for increasing powers.

The probability p that a negative ion is photodetached while it crosses in a finite time t the region illuminated by a spatially and temporally uniform laser beam of flux density Φ is

$$p = 1 - e^{-\sigma_{\mathrm{PD}}\,\Phi t}, \tag{3.8}$$

where σ_{PD} is the photodetachment cross section. The transit time of the ion through the interaction region is $t = l/v_{\mathrm{beam}}$ with l being the laser beam dimension along the beam path and v_{beam} the negative ion beam velocity. The situation is schematically outlined in figure 3.5. Furthermore, as the photon flux density Φ does not vary either in space or in time, Φ is computed as

$$\Phi = \frac{P}{h\nu\, lw},$$

where P is the laser power and w is the common transverse dimension of the

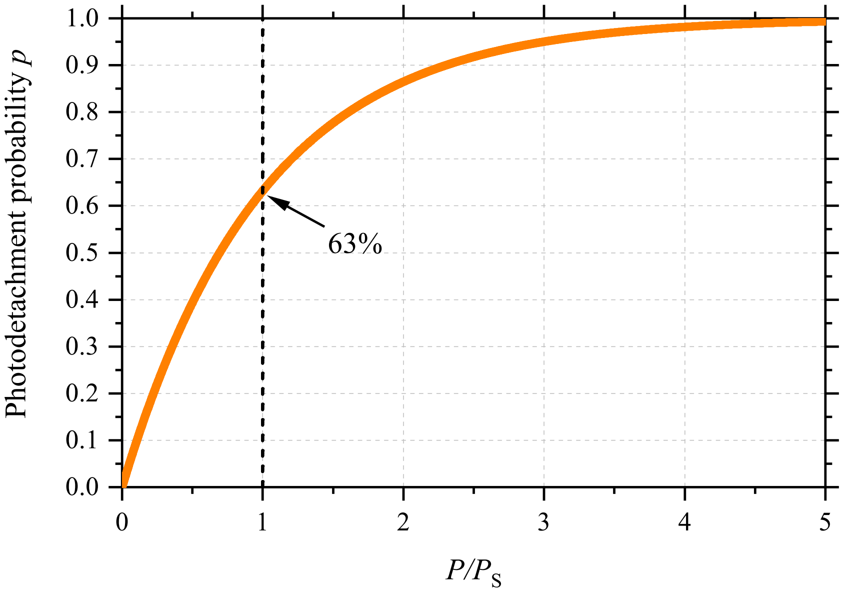

Figure 3.6: Photodetachment probability as a function of the relative laser power. P_s is the saturation laser power.

overlapping ion and laser beams. Hence, equation (3.8) becomes

$$p = 1 - \exp\left(-\frac{\sigma_\mathrm{PD}\,P}{h\nu\,w\,v_\mathrm{beam}}\right). \tag{3.9}$$

Therefore, the photodetachment probability tends asymptotically to 1 for increasing values of the laser power, as shown in figure 3.6.

The power P_S for which the population of negative ions illuminated by the laser beam is reduced by a factor of $1 - 1/e$, corresponding to a photodetachment rate of around 63 %, is called saturation laser power. From equation (3.9), one obtains

$$P_\mathrm{S} = \frac{v_\mathrm{beam}\,w}{\sigma_\mathrm{PD}}\,h\nu. \tag{3.10}$$

The linear dependence on the ion velocity explains why a 1 MeV D^- beam needs a very high photon power. Equation (3.10) also highlights the importance of working with narrow laser beams (typical widths are of the order of cm). A photodetachment rate of 95 % requires a laser power that is three times P_S.

Although the 1064 nm wavelength is higher than the value that maximises the photodetachment cross section, it is more suitable from a practical point of view thanks to the large experience in developing spectrally narrow laser beams at this wavelength, i.e. Nd:YAG lasers.

The concept of intracavity photoneutralisation [50] allows reducing the input power: as only a small fraction of the laser power is absorbed by the ions, the laser beam is reflected inside an optical cavity built around the negative ion beam which is then crossed many times by the laser beam.

In a Fabry-Pérot (FP) optical cavity [51], high amplifications of the input photon power are possible thanks to the resonant coupling between the laser beam and the high-finesse cavity for which high reflectivity mirrors at the chosen wavelength are used. The photoneutralisation of an H^- beam inside an FP cavity of medium finesse was experimentally demonstrated on a reduced scale [47]: a photodetachment rate higher than 50 % was achieved for a 1.2 keV H^- ion beam with an external 10 W laser and a cavity amplification of around 1000. The effective power inside the optical cavity is hence equal to 10 kW.

A DEMO NBI design relying on this photoneutraliser concept was proposed in [52]. In order to maximise the overlap of the narrow laser beam with the ion beam, the ion source and accelerator system is designed to produce thin beam sheets as shown in figure 3.7, with the ion beam having a large dimension in the laser beam direction. The implementation of a photoneutraliser, therefore, sets a strict requirement for the aspect ratio of the ion beam source which is very high, differently from conventional NBIs. The 3 MW photon beam of 1 cm width required to neutralise 50 % of a 1 MeV D^- ion beam could be generated by means of an FP optical cavity with a high finesse of 10000 into which a 500 W continuous-wave mono-frequency laser beam is injected. By refolding the 3 MW photon beam four times inside the cavity, the negative ion beam can be completely overlapped and crossed from side to side, achieving a neutralisation efficiency of 93 %. An energy recovery system that recovers the kinetic energy of the residual ions and converts it into electrical energy, further increasing the injector wall-plug efficiency, is also considered.

Another photoneutraliser-based DEMO NBI design [53] does not rely on FP

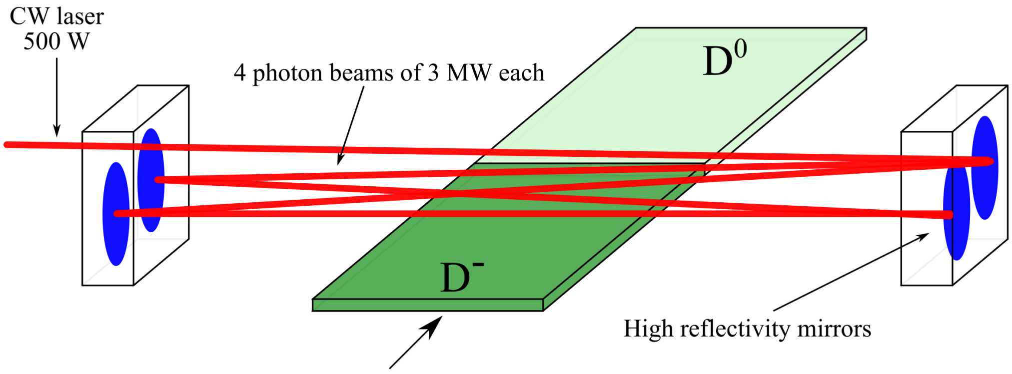

Figure 3.7: Sketch of the photoneutraliser concept suggested in [52]: an FP optical cavity is set across a single negative ion beam sheet. A 500 W continuous-wave laser is injected into the cavity to generate a 3 MW photon beam which is then refolded four times by high reflectivity mirrors. As a result, the ion beam is completely overlapped and a neutralisation of 93 % is achieved.

cavities, but on the Recirculation Injection by Nonlinear Gating (RING) concept [54]. In this case, it is the second harmonic of the multi-refolded laser beam, instead of the fundamental wavelength, to be trapped inside the optical cavity. The second harmonic generation (SHG) occurs inside the cavity via a crystal that doubles the laser frequency. Being a non-resonating optical cavity, the system is more robust against external influences and occupies less volume with respect to an FP resonator. On the other hand, higher laser powers are required, also considering that the SHG crystal is a big source of power loss in the cavity.

The big efforts in pursuing the implementation of a photoneutraliser on the HNB injector can be explained by the following advantages:

- a neutralisation efficiency $> 90\,\%$ which would determine a significant boost of the NBI wall-plug efficiency;
- no need of a gas throughput into the neutraliser chamber with a subsequent relaxation of the requirements about pumping speed and voltage holding. Therefore, the design of the ion source, pumps and high voltage systems is greatly simplified;
- as further consequence of a much lower gas injection into the beamline,

the stripping losses in the accelerator and the re-ionisation losses after neutralisation are strongly reduced;

- as the photodetachment reaction (3.7) is the only ion-charge-changing process, no positive ions are created;
- the photon beam refolding inside the optical cavity allows for a very compact photoneutraliser in the direction of the beam propagation, especially in comparison with the gas neutraliser.

Despite successful proof-of-principle experiments, photoneutralisation still presents many challenges to deal with:

- the technology needed for a full-scale system is not available, as it is the case of continuous-wave lasers able to guarantee a very high power for a single-frequency beam;
- thermal effects on the mirrors and their lifetime in the beam environment need to be thoroughly investigated;
- mitigation of mechanical vibrations;
- sophisticated schemes to tune and lock the input laser frequency for a stable resonance coupling within FP cavities are necessary;
- high power losses due to the SHG crystal in the RING concept.

The photoneutraliser is therefore not ready to be taken into consideration for the DEMO NBI design as alternative to the gas neutraliser.

3.3.2 The neutraliser as design driver

The choice of the type of neutraliser is fundamental in designing the NBI as it directly influences the geometry and requirements of all the other beamline components. The schematic of figure 3.8 gives a pictorial overview of the effects of selecting a different type of neutraliser on the NBI design.

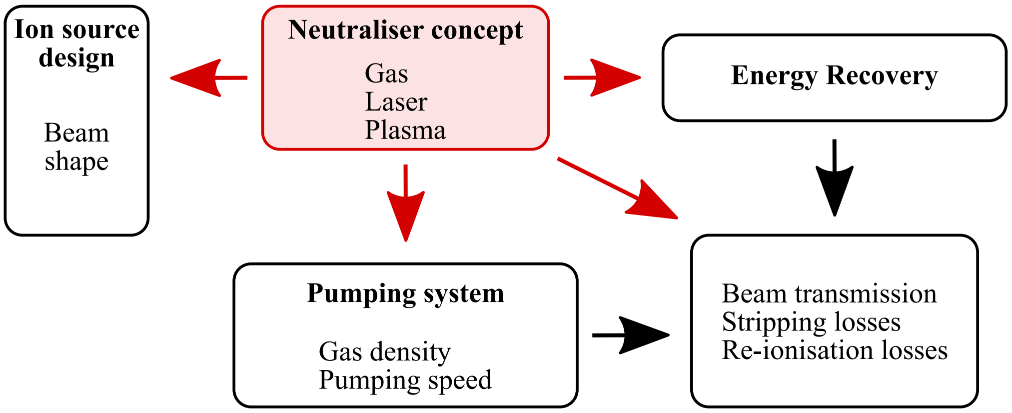

Figure 3.8: Schematic overview of the impact of the neutraliser concept on the NBI design.

The neutraliser directly influences the shape of the ion source and accelerator. The gas neutraliser is subdivided into channels in order to reduce the required gas inflow. Hence, the negative ion beam is formed of sub-beams with a rectangular cross section of high aspect ratio that fits the channel size. The aspect ratio becomes much higher in the photoneutraliser case where the beam sheets must overlap with the very narrow laser beams. The optimum aspect ratio for a plasma neutraliser, instead, is equal to one as it allows minimising the surface-area-to-volume ratio and, hence, the losses of plasma ions and electrons at the walls.

The gas density along the beamline is another fundamental design parameter that is directly determined by the neutraliser. Despite the internal subdivision into channels, the gas injected into the gas neutraliser is the main source of gas in the injector. Hence, pumping speeds of several thousands of m^3/s are needed in order to achieve high vacuum conditions. The absence of a gas throughput into the photoneutraliser and the much lower target thickness required by the plasma neutraliser strongly relax the pumping requirements. A high gas density in the beamline determines an increase of the negative ion stripping in the accelerator, before the ions are fully accelerated, and the re-ionisation losses of neutrals after the neutraliser, consequently reducing the power injected into the reactor. Furthermore, the resulting ions are deflected by the confining magnetic field and impact on the injector walls, leading to high power loads.

Another valid option to increase the NBI wall-plug efficiency is to substitute the residual ion dump (RID) with an energy recovery system (ERS) for the residual ions of the neutralisation process. Therefore, an enhancement of the wall-plug efficiency is not achieved by improving the neutralisation, but by avoiding the power loss associated to the dumping of the residual ions at full energy in the RID, as it is foreseen for the ITER NBI. An ERS could be implemented much easier on a photoneutraliser-based beamline as, differently from the cases of gas and plasma neutralisation, almost no positive ions are generated. Anyway, the energy recovery has the potential to make the gas neutraliser still an attractive option, due to the high currents of residual ions at the neutraliser exit. However, in addition to the technological challenges, an ERS could make the beamline much longer, causing higher re-ionisation and transmission losses.

These considerations underline the central role of the neutraliser in driving the NBI design [10]. Considering an alternative to the gas neutralisation in order to increase the wall-plug efficiency of the injector is not just a matter of substituting the gas cell with a different device, but implies deep modifications of many NBI sub-systems. The fact that they could have a negative impact on the total efficiency, such as additional power consumptions, makes the study of new neutralisation systems very challenging.

As the R&D about a photoneutraliser for the DEMO NBI is still at an early stage, as pointed out in section 3.3.1, this thesis focuses on plasma neutralisation in the next chapter, in particular on the simplified and promising concept of the beam-driven plasma neutraliser, and on the energy recovery of the residual ions in chapter 5.

Chapter 4

The beam-driven plasma neutraliser

In the challenge of increasing the wall-plug efficiency of high-energy HNB injectors with respect to the value of 26 % of the ITER NNBI beamline, the neutraliser plays a fundamental role: gas neutralisation currently limits the efficiency the most with a neutralisation yield of only 55 % for a 1 MeV D^- ion beam. Among the alternatives, plasma neutralisation promises high neutralisation efficiencies for negative ions at high energies. As additional advantage, the production and confinement of plasma densities of the order of $10^{18}\,\mathrm{m}^{-3}$ with ionisation degrees $> 10\,\%$ can rely on well-established technologies. Although the power required by the plasma production does not have a big impact on the wall-plug efficiency, the corresponding power source would make the injector design more complicated. An external power source could be avoided if it was the negative ion beam itself that ionises the neutral gas while passing through the chamber. The resulting plasma could then be magnetically confined inside the neutraliser through a cusp field produced by permanent magnets covering the walls. This innovative and attractive concept, first suggested by Surrey and Holmes [12], is called beam-driven plasma neutraliser (BDPN).

After outlining the gas neutralisation process and showing the advantages of having an ionised gas target, the chapter focuses on predicting the BDPN performances. In particular, the beam-driven plasma formation is described in detail by a zero-dimensional analytical model that uses the models by Surrey and Holmes [12] and Turner and Holmes [13] as starting point. However, several modifications are introduced to improve oversimplifying hypotheses and to consider processes that were neglected in the first place. The model predicts the maximum achievable ionisation degree of the background gas for a given magnetic cusp confinement and, hence, the maximum achievable neutralisation efficiency. The model outputs allow evaluating whether the BDPN is a better option than the gas neutraliser for a DEMO NBI beamline and whether it is worthwhile to invest in this technology. If that is the case, the analytical predictions will help to identify and design the most suitable proof-of-principle experiment to benchmark the analytical model and prove the concept feasibility [55].

4.1 The conventional technology of the gas neutraliser

The gas neutraliser is a gas cell at low pressure where the neutralisation of negative ions relies on the following stripping reaction:

$$\hat{\mathrm{D}}^- + \mathrm{D}_2 \longrightarrow \hat{\mathrm{D}}^0 + \mathrm{D}_2 + \mathrm{e}, \tag{4.1}$$

where the hat identifies the fast beam particles. However, the resulting fast neutral atoms $\hat{\mathrm{D}}^0$ can be destroyed by the competing reaction of re-ionisation:

$$\hat{\mathrm{D}}^0 + \mathrm{D}_2 \longrightarrow \hat{\mathrm{D}}^+ + \mathrm{D}_2 + \mathrm{e}. \tag{4.2}$$

The competition between stripping and re-ionisation is such that there exists a value of the gas target thickness for which the neutralisation of the negative ions reaches a maximum before re-ionisation prevails and makes it drop. The gas target thickness is the line integral of the background gas density n_{gas} along the neutraliser length L_{neut}:

$$nl = \int_{L_{\mathrm{neut}}} n_{\mathrm{gas}}(x)\mathrm{d}x \qquad [\mathrm{m}^{-2}].$$

Therefore, in order to reach a certain value of nl, one increases either the neutraliser length or the gas density. The former approach implies a longer beamline and the subsequent drawbacks in terms of design and costs, the latter requires higher gas inflows into the neutraliser which in turn result in a higher gas pressure in the rest of the beamline. Consequently, the stripping rates in the accelerator and the re-ionisation losses after the neutralisation increase. Hence, a compromise is needed at the NBI design stage.

In addition to reactions (4.1) and (4.2), the other charge-changing processes for the beam ions are listed in table 4.1. For every reaction, the cross section value for 1 MeV deuterium particles is given [56]. The cross section for a given collision process depends only on the relative velocity of the two colliding particles, hence on the velocity of the beam ions/neutrals if the gas molecule target is assumed at rest. Therefore, the cross section data of Ref. [56] for hydrogen are valid also for the deuterium isotope for the same particle velocity, not for the same particle energy. From this point of view, 500 keV hydrogen ions are equivalent to 1 MeV deuterium ions. Some cross section values are extrapolated from experimental data available for lower energies.

According to the cross section notation of table 4.1, the subscripts -1, 0 and 1 indicate the negative, neutral and positive beam particles, respectively. The first subscript identifies the impacting beam particle, while the second subscript identifies the fast particle generated by the reaction. Hence, the charge evolution profile of the negative ion beam as function of the gas target thickness

Table 4.1: Charge-changing reactions of the beam ions in the gas neutraliser. The corresponding cross section values are for 1 MeV deuterium particles [56]. Fast beam particles are denoted by a hat.

Reaction	Cross section	
	Notation	Value [cm^2]
$\hat{D}^- + D_2 \longrightarrow \hat{D}^0 + D_2 + e$	$\sigma_{\text{-}10}$	1.14×10^{-16}
$\hat{D}^0 + D_2 \longrightarrow \hat{D}^+ + D_2 + e$	σ_{01}	3.81×10^{-17}
$\hat{D}^- + D_2 \longrightarrow \hat{D}^+ + D_2 + 2e$	$\sigma_{\text{-}11}$	7.28×10^{-18}
$\hat{D}^0 + D_2 \longrightarrow \hat{D}^- + D_2^+$	$\sigma_{0\text{-}1}$	2.44×10^{-21}
$\hat{D}^+ + D_2 \longrightarrow \hat{D}^0 + D_2^+$	σ_{10}	1.95×10^{-20}
$\hat{D}^+ + D_2 \longrightarrow \hat{D}^- + 2D^+$	$\sigma_{1\text{-}1}$	1.20×10^{-25}

can be obtained by solving the following system of differential equations:

$$\begin{cases} \frac{\mathrm{d}F^-}{\mathrm{d}nl} = -F^-(\sigma_{\text{-}10} + \sigma_{\text{-}11}) + F^0\sigma_{0\text{-}1} + F^+\sigma_{1\text{-}1} \\ \frac{\mathrm{d}F^0}{\mathrm{d}nl} = F^-\sigma_{\text{-}10} - F^0(\sigma_{0\text{-}1} + \sigma_{01}) + F^+\sigma_{10} \\ \frac{\mathrm{d}F^+}{\mathrm{d}nl} = F^-\sigma_{\text{-}11} + F^0\sigma_{01} - F^+(\sigma_{1\text{-}1} + \sigma_{10}) \end{cases} \tag{4.3}$$

The current fractions of negative, neutral and positive beam particles with respect to the total ion beam current are indicated by F^-, F^0 and F^+, respectively, with the underlying constraint

$$F^- + F^0 + F^+ = 1.$$

The initial condition is $F^- = 1$ at the neutraliser entrance.

Figure 4.1 shows the beam charge fractions as functions of the gas target thickness for a 1 MeV D$^-$ ion beam: the neutral fraction peaks at 55 % at a gas target thickness of $1.4 \times 10^{20}\,\mathrm{m}^{-2}$. Correspondingly, the fractions of positive and negative ions are 26 % and 19 %, respectively.

A 3D CAD drawing of the ITER gas neutraliser is shown in figure 4.2.

Given the optimum gas target thickness of $1.4 \times 10^{20}\,\mathrm{m}^{-2}$, the length of 3 m was chosen as compromise to keep the gas inlet flow rate sufficiently low. To this end, other design choices were adopted [35]:

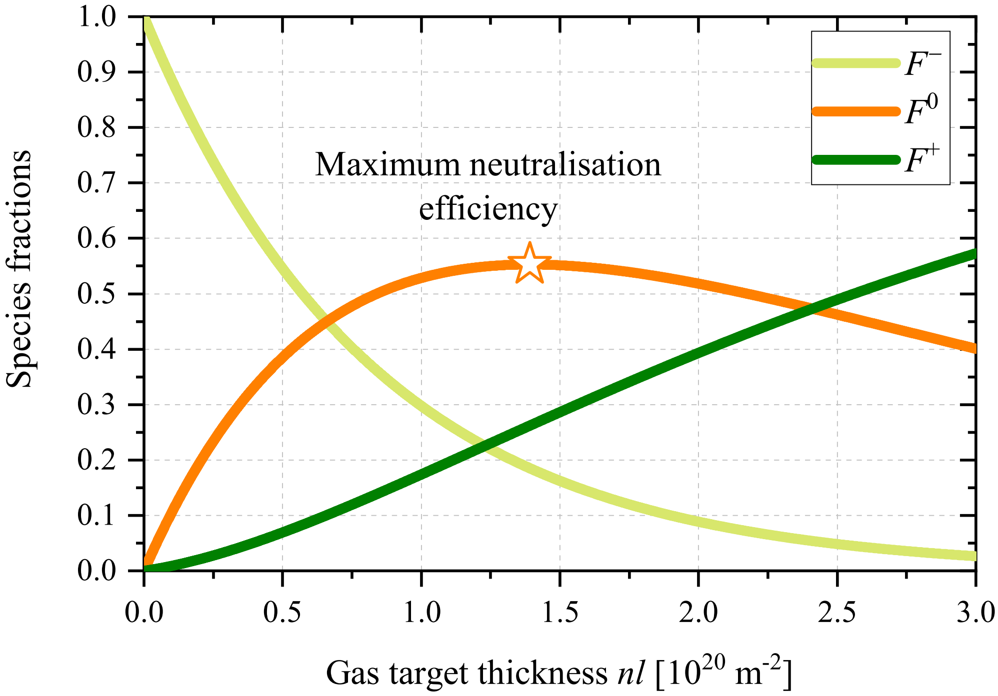

Figure 4.1: Beam charge fractions in the gas neutraliser as functions of the gas target thickness in the case of a 1 MeV D^- ion beam. F^-, F^0 and F^+ indicate the fractions of negative, neutral and positive fast beam particles, respectively. The calculation is based on the reactions and cross sections of table 4.1. The star indicates the maximum neutralisation efficiency.

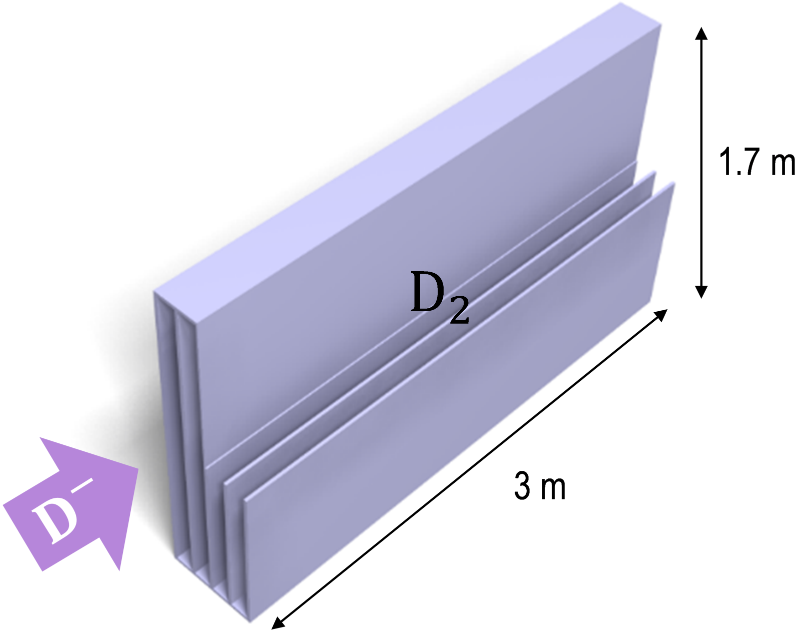

Figure 4.2: 3D CAD drawing of the ITER gas neutraliser.

- the chamber is subdivided into four channels to lower the gas conductance and, hence, the gas inflow;
- the neutraliser is decoupled from the ion beam source and the spacing between the neutraliser and the last accelerator grid, the grounded grid (GG), is big enough to allow an effective pumping (the neutraliser is mounted 1.9 m downstream of the GG and, for the same reason, the RID is 0.5 m downstream of the neutraliser exit [14]);
- the neutral gas is fed from the middle to minimise the gas throughput and to reduce the gas density at the extremities and, consequently, the gas flow from the neutraliser into the beamline;
- the injector is provided with two large cryopumps to pump the gas that is introduced into the ion source and, above all, into the neutraliser.

Each channel is 3 m long, 1.7 m high and has a tapered shape in the horizontal direction as the width varies from 105 mm at the entrance to 90 mm at the exit. Although the channel subdivision is effective in lowering the gas throughput, it increases the direct interception of the beam particles which results in power deposition on the front surfaces and on the inner walls of the neutraliser channels. The former are protected by leading edge elements, i.e. CuCrZr bars with a rounded shape. The expected power densities are $\leq 5\,\mathrm{MW\,m^{-2}}$ and the expected maximum power is 0.3 MW [14]. Both the leading edge elements and the channel wall panels are actively cooled. Precisely in order to further reduce the power density on the leading edge elements, the neutraliser channels are tapered.

The partition of the neutraliser chamber volume into four rectangular channels has a direct consequence on the beam source design: the apertures in the source and accelerator grids are organised to form four columns such that the resulting ion beam could pass through the four channels of the neutraliser and RID [39].

A low gas pressure along the NBI beamline is kept by two large cryopumps installed against the lateral walls of the injector vessel. Each cryopump is 8 m long, 2.8 m high and has a depth of 0.45 m [14]. The main goal of the cryopumps is to maintain the pressure between the accelerator and the neutraliser lower than 0.02 Pa in order to minimise the stripping losses in the accelerator. The other vacuum requirements are a deuterium gas pressure of the order of 10^{-2} Pa in the spacing between the neutraliser and the RID and a pressure in the range of 10^{-3} Pa after the RID in order to reduce the re-ionisation of the fast neutrals as far as possible. Gas baffles could also be integrated to separate the beamline vessel into different chambers and, hence, to optimise the pressure profile along the beamline. The neutraliser gas throughput is the main gas source in the injector, equal to $14.6\,\mathrm{Pa\,m^3\,s^{-1}}$ for the deuterium pulse operation of the ITER NBI [57], followed by the gas throughput in the ion beam source, equal to $3.6\,\mathrm{Pa\,m^3\,s^{-1}}$. The required pumping speed and the position of the gas baffles are determined by means of 3D Monte Carlo gas flow models which calculate the gas density distribution profile along the whole beamline [58]. An overall pumping speed for deuterium of 3600 m^3/s is estimated in [59]. More recent pressure profiles with slightly different inputs can be found in [57].

4.2 Plasma neutralisation

The idea of a plasma neutraliser was introduced by Berkner [11]: if the negative ion beam passes through a plasma, the ratio between the stripping and re-ionisation cross sections is significantly higher. The stripping of the negative ions by thermal electrons and ions occurs as

$$\hat{\mathrm{D}}^- + \mathrm{e} \longrightarrow \hat{\mathrm{D}}^0 + 2\mathrm{e} \tag{4.4}$$

$$\hat{\mathrm{D}}^- + \mathrm{D}^+ \longrightarrow \hat{\mathrm{D}}^0 + \mathrm{D}^+ + \mathrm{e}, \tag{4.5}$$

where the hat denotes the fast beam particles. In the case of a 1 MeV D^- ion beam, the cross sections of the reactions (4.4) and (4.5) are $\sigma^{\mathrm{e}}_{\text{-}10} = 8.30 \times 10^{-16}\,\mathrm{cm}^2$ and $\sigma^{\mathrm{i}}_{\text{-}10} = 8.31 \times 10^{-16}\,\mathrm{cm}^2$, respectively [11], both higher than the cross section value $\sigma^{\mathrm{g}}_{\text{-}10}$ of the gas stripping reaction (4.1). On the other hand, the corresponding re-ionisation processes

$$\hat{\mathrm{D}}^0 + \mathrm{e} \longrightarrow \hat{\mathrm{D}}^+ + 2\mathrm{e} \tag{4.6}$$

$$\hat{\mathrm{D}}^0 + \mathrm{D}^+ \longrightarrow \hat{\mathrm{D}}^+ + \mathrm{D}^+ + \mathrm{e} \tag{4.7}$$

have cross section values $\sigma^{\mathrm{e}}_{01} = 3.34 \times 10^{-17}\,\mathrm{cm}^2$ and $\sigma^{\mathrm{i}}_{01} = 3.48 \times 10^{-17}\,\mathrm{cm}^2$, respectively [11], which are almost equal to the cross section σ^{g}_{01} of the re-ionisation reaction (4.2) with a gas target. Therefore, the presence of a plasma in the neutraliser chamber would result in a higher neutralisation efficiency than for a gas neutraliser.

The neutralisation efficiency does not simply depend on the plasma density, but on its ratio with respect to the total target density, i.e. on the ionisation

Table 4.2: Charge-changing reactions of the beam ions colliding with thermal ions and electrons. The corresponding cross section values are for 1 MeV deuterium particles [11,56]. Fast beam particles are denoted by a hat.

Reaction	Cross section	
	Notation	Value [cm^2]
$\hat{\mathrm{D}}^- + \mathrm{D}^+ \longrightarrow \hat{\mathrm{D}}^0 + \mathrm{D}^+ + \mathrm{e}$	$\sigma^{\mathrm{i}}_{\text{-}10}$	8.31×10^{-16}
$\hat{\mathrm{D}}^- + \mathrm{e} \longrightarrow \hat{\mathrm{D}}^0 + 2\mathrm{e}$	$\sigma^{\mathrm{e}}_{\text{-}10}$	8.30×10^{-16}
$\hat{\mathrm{D}}^0 + \mathrm{D}^+ \longrightarrow \hat{\mathrm{D}}^+ + \mathrm{D}^+ + \mathrm{e}$	σ^{i}_{01}	3.48×10^{-17}
$\hat{\mathrm{D}}^0 + \mathrm{e} \longrightarrow \hat{\mathrm{D}}^+ + 2\mathrm{e}$	σ^{e}_{01}	3.34×10^{-17}
$\hat{\mathrm{D}}^- + \mathrm{e} \longrightarrow \hat{\mathrm{D}}^+ + 3\mathrm{e}$	$\sigma^{\mathrm{e}}_{\text{-}11}$	1.60×10^{-17}

degree:

$$\chi = \frac{n_{\mathrm{plasma}}}{n_{\mathrm{gas}} + n_{\mathrm{plasma}}}, \tag{4.8}$$

where n_{plasma} and n_{gas} are the plasma and gas densities, respectively. For a fully ionised plasma, $\chi = 1$.

Due to the re-ionisation of the fast neutrals when colliding with the background gas molecules and the plasma electrons and ions, also the neutralisation efficiency of a plasma neutraliser of given ionisation degree has a maximum for a certain value of the total target thickness. In this case, however, the target thickness is defined as

$$nl_{\mathrm{tot}} = \int_{L_{\mathrm{neut}}} (n_{\mathrm{plasma}}(x) + n_{\mathrm{gas}}(x))\,\mathrm{d}x \qquad [\mathrm{m}^{-2}],$$

where x is the spatial dimension along the beam path.

Similarly to the gas neutraliser case, the evolution of the beam charge fractions along the neutraliser length is given by

$$\begin{cases} \frac{\mathrm{d}F^-}{\mathrm{d}x} = -F^- \sum_j (\sigma^j_{\text{-}10} + \sigma^j_{\text{-}11}) n_j + F^0 \sum_j \sigma^j_{0\text{-}1} n_j + F^+ \sum_j \sigma^j_{1\text{-}1} n_j \\ \frac{\mathrm{d}F^0}{\mathrm{d}x} = F^- \sum_j \sigma^j_{\text{-}10} n_j - F^0 \sum_j (\sigma^j_{0\text{-}1} + \sigma^j_{01}) n_j + F^+ \sum_j \sigma^j_{10} n_j \\ \frac{\mathrm{d}F^+}{\mathrm{d}x} = F^- \sum_j \sigma^j_{\text{-}11} n_j + F^0 \sum_j \sigma^j_{01} n_j - F^+ \sum_j (\sigma^j_{1\text{-}1} + \sigma^j_{10}) n_j \end{cases} \tag{4.9}$$

The index j represents the particle species in the neutraliser, i.e. neutral gas

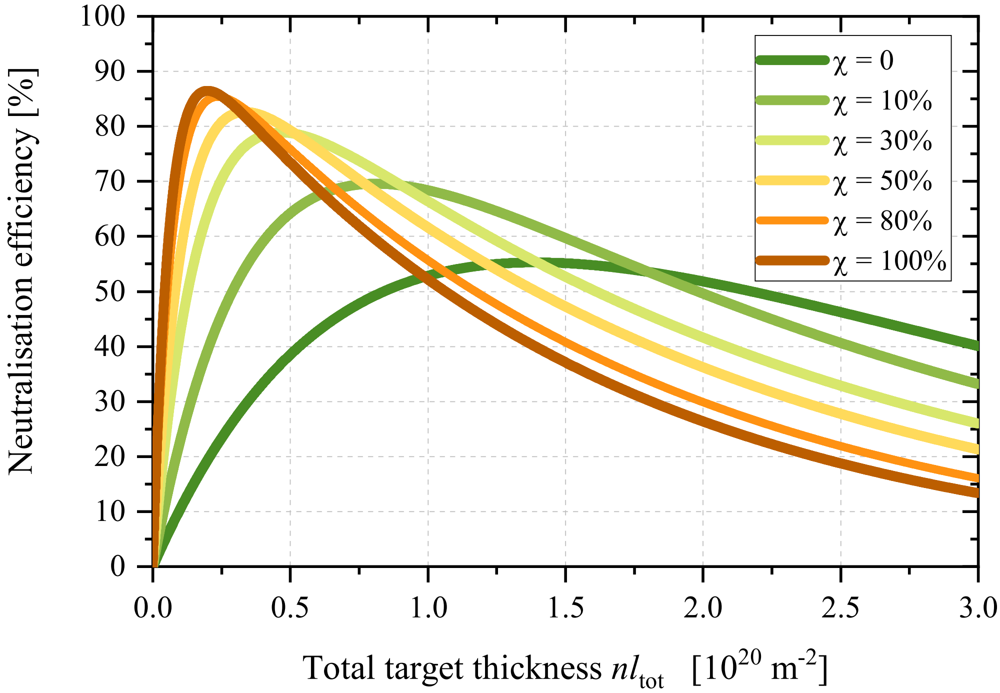

Figure 4.3: Neutralisation efficiency of a plasma neutraliser as a function of the total target thickness for different values of the ionisation degree χ in the case of a 1 MeV D$^-$ ion beam. $\chi = 0$ corresponds to the gas neutraliser case.

(gas), plasma electrons (e) and plasma ions (i). Thus, the summation term for the stripping process, for example, can be explicitly written as

$$\sum_j \sigma^j_{\text{-10}}\, n_j = \sigma^{\text{g}}_{\text{-10}}\, n_{\text{gas}} + \sigma^{\text{e}}_{\text{-10}}\, n_{\text{e}} + \sigma^{\text{i}}_{\text{-10}}\, n_{\text{i}}.$$

The considered charge-changing reactions are those listed in tables 4.1 and 4.2. The corresponding cross section values are taken from [11, 56].

In the present work, it is always assumed

$$n_{\text{e}} = n_{\text{i}} = n_{\text{plasma}}.$$

Figure 4.3 shows the calculated neutralisation efficiency of a plasma neutraliser as a function of the total target thickness for different values of the ionisation degree χ in the case of a 1 MeV D$^-$ ion beam. The curve $\chi = 0$ corresponds to the neutral fraction profile obtained with the gas neutraliser and plotted in figure 4.1, with a maximum around 55 %. One can see that the presence of a plasma enhances the neutralisation efficiency with respect to the gas neutraliser case and that the efficiency increases with the ionisation degree up to a maximum of around 86 % for a completely ionised gas target ($\chi = 1$). Simultaneously, the target thickness at which the maximum occurs decreases. For a fully ionised plasma, it is only 1/7 of that for a gas neutraliser with $\chi = 0$. If the gas conductance is the same in all the cases, this can be exploited to relax the pumping requirements or reduce the pressure in the beamline.

Hanada et al. [60] measured an increase of the neutralisation efficiency from 55 % with a gas target to 65 % with an hydrogen plasma of 10 % ionisation degree in the case of a 200 keV, 4 mA H^- ion beam. The optimum target thickness was 65 % lower than the value for gas neutralisation. These results are in good agreement with the predictions based on the cross section data for an ionisation degree of 10 %. The plasma was produced by a 40 kW DC arc discharge inside a tube lined with cusp magnets. The leakage of filament-emitted electrons through the open ends of the neutraliser chamber was prevented by applying locally a transverse magnetic field. The suppression of fast electron leakage is critical to the generation of high plasma densities and it was extensively investigated in [61]. An ionisation degree of 20 % was achieved by Dimov et al. [62] through a 300 kW arc discharge in a cylindrical vacuum chamber in which the plasma is magnetically confined. Plasma generation in a multicusp magnetic trap by ECR (electron cyclotron resonance) discharge was also proposed and demonstrated on a small scale [63].

In summary, the advantages of a plasma neutraliser compared to the gas neutraliser are:

- a higher neutralisation efficiency, possibly even exceeding 80 %;
- a lower target thickness that could translate into lower gas inflow and therefore lower losses before and after the neutraliser.

4.3 The beam-driven plasma neutraliser (BDPN)

In all the aforementioned designs and experiments of a plasma neutraliser, the plasma production needs external power sources: this does not limit the wall-plug efficiency increase as the power consumed is negligible with respect to the neutral beam power gained with increased neutralisation, but it adds complexity to the beamline. Therefore, the beam-driven plasma neutraliser (BDPN) concept is more attractive. In a BDPN, the plasma is created by the ion beam itself that ionises the background gas while passing through the chamber. Achieving a dense plasma inside the BDPN chamber relies on the confinement of the thermal ions and electrons. This confinement is provided by a magnetic cusp field which is obtained by covering the neutraliser walls with permanent magnets.

4.3.1 A proposed design for the BDPN

The key feature of the BDPN is the magnetic cusp field confining the plasma ions and electrons generated by the beam inside the gas-filled chamber. In order to show how the permanent magnets could be arranged around the neutraliser box to form a magnetic cusp field, the box dimensions and the main parameters of the magnetic confinement need to be specified. It is chosen to use the same dimensions and parameters as those assumed by Turner and Holmes [13] who based the BDPN design on the geometry of the gas neutraliser on the ITER NBI. Working on the same reference design allows a direct comparison of the analytical predictions of the BDPN performances. The corresponding 3D CAD is shown in figure 4.4a, while the reference set of parameters is listed in table 4.3. It must be underlined that such a design is not the final BDPN configuration, but it is simply used as reference in the next sections. A design optimisation represents the next step after the analytical modelling of the plasma production and confinement and is outside the scope of this work.

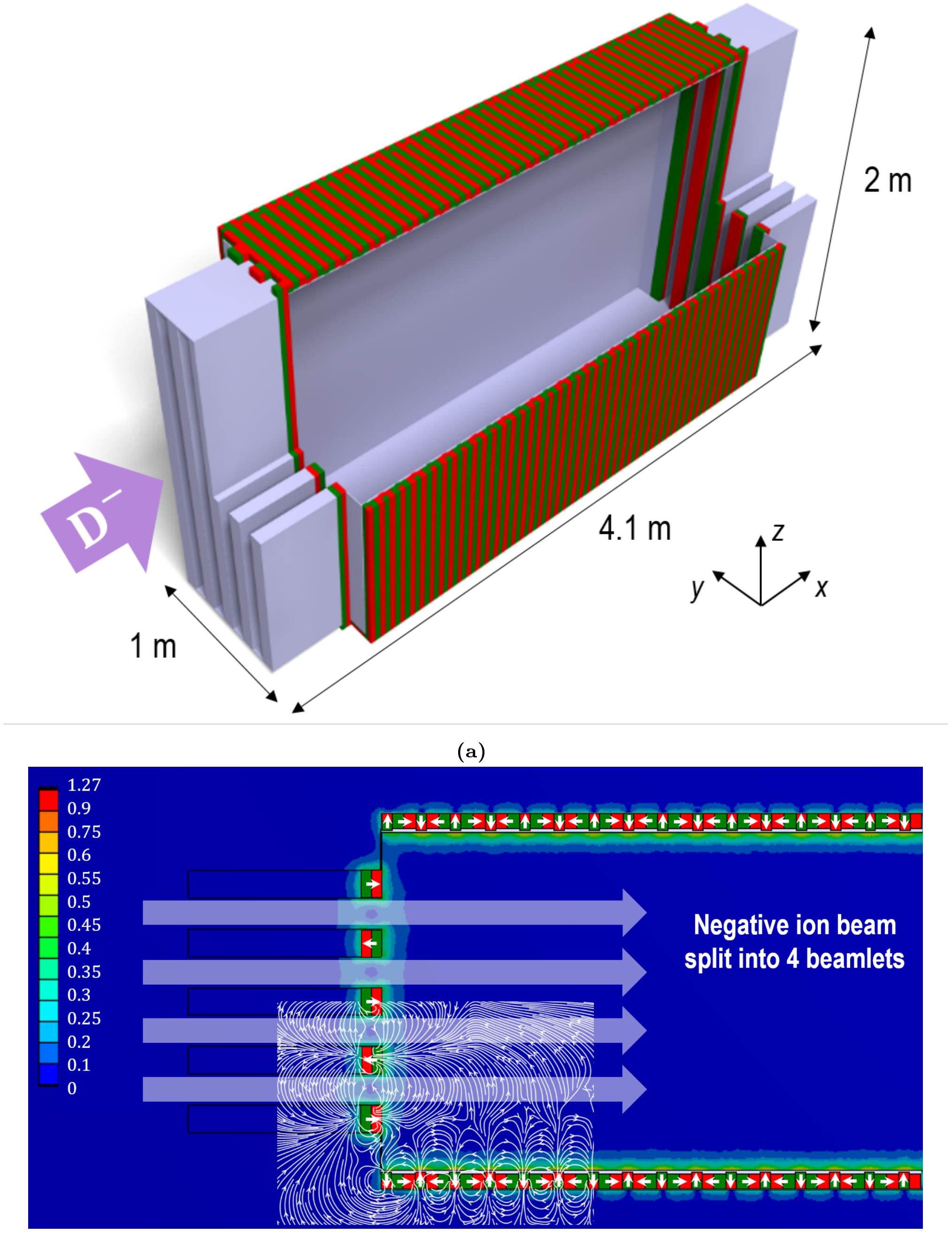

(a)

(b)

Figure 4.4: (a) Schematic 3D CAD of the BDPN for an ITER-like NBI. The poles of the permanent magnets surrounding the chamber are indicated in red and green. (b) Numerical simulation of the magnetic cusp field performed with ANSYS [64] for the longitudinal half-section of the BDPN. The box at the figure bottom shows the magnetic field lines. Pictures reprinted from [55] under the terms of the Creative Commons Attribution 3.0 licence.

Table 4.3: Dimensions and magnetic cusp field parameters for the BDPN reference design [55].

Parameter	Symbol	Value
Cusp separation	D_{cusp}	100 mm
Plasma dimensions		
	L_{plasma}	3100 mm
	H_{plasma}	1720 mm
	W_{plasma}	760 mm
Neutraliser dimensions		
	L_{neut}	3100 mm
	H_{neut}	2020 mm
	W_{neut}	1060 mm
Channel width	W_{ch}	90 mm
Channel length	L_{ch}	60 mm
Lateral magnetic cusp field	$B_{\mathrm{c,l}}$	0.8 T
End magnetic cusp field	$B_{\mathrm{c,e}}$	0.5 T

The permanent magnets, whose poles are indicated in red and green in figure 4.4, are placed on the lateral walls according to the Halbach arrangement. Magnets with a magnetisation direction perpendicular to the wall surround the neutraliser with alternating polarities to form magnetic cusps covering the walls. Interstitial magnets with a magnetisation direction parallel to the wall are used to reinforce the magnetic field on the internal side of the chamber. As a result, much higher values of the magnetic field are obtained and, as additional benefit, the magnetic field on the other side, outside the neutraliser, is decreased to lower values than those in a linear cusp configuration.

The magnetic cusps generated by the permanent magnets and surrounding the plasma occupy a certain chamber volume that is called plasma exclusion zone, as illustrated in figure 4.5. It is assumed that the cusps extend into the chamber by a distance equal to 1.5 times the cusp separation [13]. This means that the height and width of the neutraliser are obtained by adding twice this length to the corresponding plasma dimensions. The neutraliser length is assumed equal to the plasma length.

Inside the BDPN chamber, no internal walls are present as they would increase

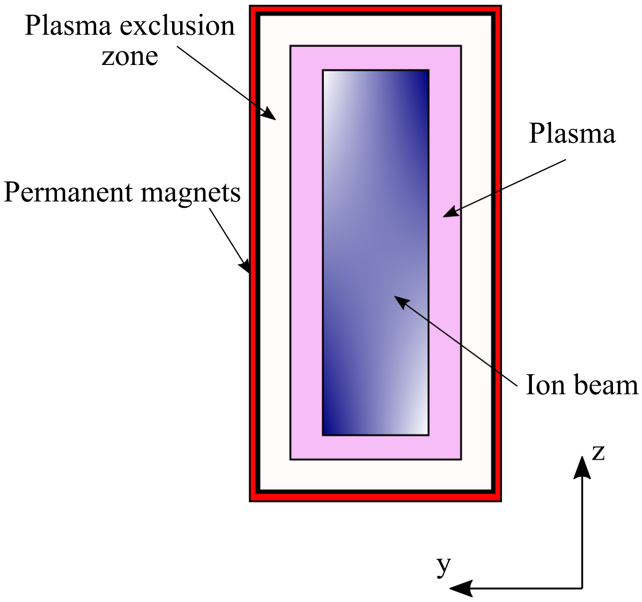

Figure 4.5: BDPN cross section in the y–z plane showing the plasma exclusion zone between the volume occupied by the plasma and the chamber walls.

the plasma loss surface and, consequently, decrease the achievable ionisation degree. Five magnet columns are placed at both extremities with alternating polarities to avoid that the plasma ions and electrons leak through the open ends of the neutraliser which let the ion beam enter and exit. The magnet columns form four channels that recall the internal subdivision of the gas neutraliser, although they do not extend into the BDPN chamber. This allows using the same ion beam shape envisaged for the ITER injector, without modifying the ion source. Hence, keeping the same ion source design as that of the ITER NBI can be considered the main driver in selecting the reference geometry of figure 4.4a as also the chamber dimensions are based on those of the ITER NBI ion beam. An additional advantage of this choice is a neutraliser cross section with an aspect ratio (height/width) that is around 2. In case of constant beam current density and constant chamber length, cross section aspect ratios as close as possible to 1 allow minimising the surface-area-to-volume ratio and, hence, the number of plasma ions and electrons that are lost at the walls. In particular, by using the analytical model that is outlined in the next sections, it has been calculated that the degree of ionisation with an aspect ratio of 2 is almost equal to the value predicted with an aspect ratio of 1.

As, unlike the gas neutraliser, the BDPN is not internally subdivided into more channels, it is suggested that the gas conductance and, therefore, the gas inflow that needs to be injected into the chamber to achieve the optimum target thickness could be reduced through elongated slits outside of the cusp-confined volume in line with the magnet columns at both ends, as depicted in figure 4.4a. Hence, they compensate for the gas conductance increase due to the absence of internal channels. The estimation of the slit length requires considerations about the beam optics and the gas density distribution along the injector. This is part of the optimisation study of the BDPN design which is not the objective of this thesis. Thus, the elongated slits will not be considered in the analytical model.

A magnetostatic simulation is performed with ANSYS [64] and shown in figure 4.4b for the longitudinal half-section of the neutraliser. The magnetic field lines are displayed only for a small portion of the system. The following magnet cross sections in the x–y plane are assumed: 30 mm × 50 mm for the cusp magnets and 70 mm × 45 mm for the interstitial magnets. Hence, the cusp separation is 10 cm. A 5 mm castellation is considered for the interstitial magnets to accommodate eventual cooling channels. It is further assumed that the copper walls of the BDPN chamber have a thickness of 5 mm from the cusp magnet surface. The magnet columns at the entrance and exit of the neutraliser, arranged in a linear cusp configuration by alternating their polarity, are 80 mm wide and 60 mm long in the x direction. Thus, 60 mm is also the length of the end channels. The magnetostatic simulation of figure 4.4b shows that using SmCo permanent magnets with a remnant induction of 1.19 T allows achieving a maximum magnetic field of ~ 0.8 T at the neutraliser internal walls and of ~ 0.5 T at the neutraliser ends. Turner and Holmes [13] suggest using NdFeB magnets which have a higher remanent induction and make higher cusp fields possible. However, neutron irradiation experiments showed that the radiation tolerance of NdFeB-type magnets is very low while SmCo-type magnets can withstand neutron fluences as high as $\sim 10^{20}\,\mathrm{neutrons/cm^2}$ without any significant loss of magnetic flux [65]. Due to the large production of neutrons on DEMO, it is expected that neutron fluxes of the order of $10^{14}\,\mathrm{neutrons\,cm^{-2}\,s^{-1}}$ or even higher will leave the tokamak through the connecting ports and stream along the NBI beamline. This was confirmed by neutron transport calculations performed via a 3D Monte Carlo code [66]. Therefore, SmCo magnets should be preferred.

4.3.2 The SHT model

A BDPN has never been built and all performance predictions so far have been obtained by modelling. The SHT model is the original attempt to capture the underlying physics of the plasma production process via the beam-driven mechanism. It is a zero-dimensional analytical model that was presented by Surrey and Holmes [12] and later refined and extended by Turner and Holmes [13]. In this work, therefore, it is referred to as SHT model after the authors' initials. The SHT model is extensively described in [12,13], so here only a brief description is given.

Plasma is formed as a result of the collisions between the fast beam particles and the neutraliser gas molecules. The beam–gas collisions create fast electrons:

- *stripped electrons*, coming from the stripping of the negative beam ions and from the re-ionisation of the fast neutral particles;
- *Rudd electrons* [67,68], generated by the ionisation of the gas molecules.

The stripped and Rudd electrons further ionise the gas and are the actual source of plasma ions and electrons. The resulting thermal particles are confined by the magnetic cusp field. By describing the confinement through an effective loss area that depends on the permanent magnet arrangement and on the hybrid Larmor radius of the plasma particles, the plasma density is computed. The collisions of the fast beam ions with the gas molecules and the plasma electrons and ions change the charge state of the beam ions. Hence, by calculating the evolution of the beam species fractions from the entrance to the exit of the neutraliser, an estimate of the neutralisation efficiency is obtained.

The SHT model, however, presents some apparent shortcomings that lead to an overestimation of the achievable plasma density. Hence, it is the starting point of a more comprehensive and detailed modelling of the BDPN which is the main objective of this chapter.

4.3.3 The revised model

With the purpose of studying some of the processes outlined in the SHT model more closely, of getting rid of oversimplifying hypotheses and of including additional reactions and phenomena that have not been taken into consideration, several modifications are introduced into the SHT model. The most important are:

- Slowing-down energy distributions are calculated for the fast electron populations instead of describing them with Maxwellian distributions. This has an impact on the secondary ionisation rates and, hence, on the achievable plasma density.

- The dissociation of the gas molecules by ion and electron impact, neglected by the SHT model, is now included. It represents an important energy loss mechanism for the plasma electrons whose temperature is therefore reduced. Furthermore, the dissociation fragments have a few eV energy that they can transfer to the gas molecules, contributing to the heating of the neutral gas. Dissociation reactions are also fundamental in the computation of the plasma species composition.

- Another process that was initially not considered is the dissociative recombination of molecular ions with plasma electrons. The effect of recombination is a strong reduction of the achievable plasma density. As its inclusion in the model requires the knowledge of the molecular ion fractions in the plasma, a plasma species composition model is implemented.

- While the SHT model assumes that the background gas is at room temperature, the increase of the gas temperature due to the reactions occurring during the plasma generation is now investigated.

A detailed description of the revised BDPN model is given in the following. Although a 1D profile along the neutraliser length is calculated for the gas density and the beam charge fractions, only the mean value in the former case and the values at the neutraliser exit in the latter case are considered. Hence, the model is zero-dimensional. Furthermore, it is highlighted that in presenting the main model equations the gas temperature is given in Kelvin, while ion and electron temperatures are expressed in energy units.

Gas density profile

With reference to the neutraliser geometry of figure 4.4 and table 4.3, the BDPN model starts with the calculation of the neutral gas density profile along the neutraliser length via a series of conductance equations. The conductance C of a tube of rectangular cross section for molecular flow conditions (the mean free path of the gas particles at low pressures is higher than the tube length) is given by the following equation:

$$C = \frac{1}{4}\sqrt{\frac{8k_{\mathrm{B}}T_{\mathrm{gas}}}{\pi M}}\frac{8a^2b^2}{3l(a+b)}, \tag{4.10}$$

where a and b are the rectangle dimensions, l is the tube length, k_{B} is the Boltzmann constant, T_{gas} is the gas temperature and M is the gas molecular

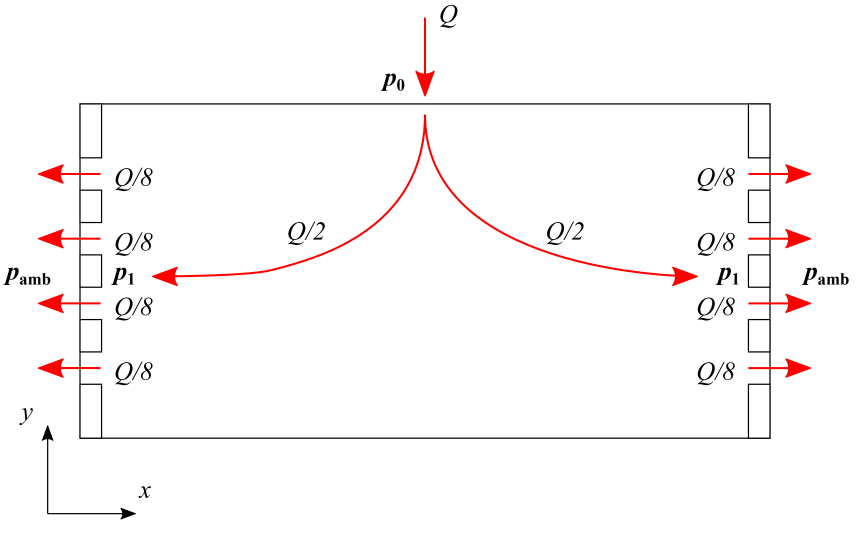

Figure 4.6: BDPN cross section in the x–y plane showing the gas path from the inlet in the centre with a flow rate Q towards the neutraliser ends. The pressures p_0, p_1 and p_{amb} are the values at the inlet, at the channel entrance and outside the chamber, respectively.

mass. T_{gas} is initially assumed equal to 300 K.

The gas inlet is in the middle of the chamber and the gas path is shown in figure 4.6. With a gas flow rate Q and an inlet pressure p_0, the gas flows from the neutraliser centre towards both extremities in the same way. Hence, a conductance C_{neut} is calculated for only half of the chamber length and is equal to 170 m^3/s. The pressure linearly drops from the value p_0 to the value p_1 at the entrance of the short channels formed by the magnet columns. Then, the flow is divided among the four channels at either end. This explains the factor 1/8 for the gas flow rate Q. The pressure linearly drops from p_1 to the vacuum vessel pressure p_{amb}, equal to 0.002 Pa. The conductance C_{ch} of a single channel is 36 m^3/s and its value takes also the cross section reduction from the main chamber to the channel into account.

The pressure profile can be calculated as

$$\begin{cases} Q/2 = C_{\mathrm{neut}}(p_0 - p_1) \\ Q/8 = C_{\mathrm{ch}}(p_1 - p_{\mathrm{amb}}) \end{cases} \tag{4.11}$$

Once the gas pressure profile along the neutraliser $p(x)$ has been computed, the gas density is obtained as

$$n_{\mathrm{gas}}(x) = \frac{p(x)}{k_{\mathrm{B}} T_{\mathrm{gas}}}. \tag{4.12}$$

The plasma density n_{plasma} is assumed constant throughout the chamber length and its initial value is zero. The density values $\bar{n}_{\mathrm{gas}}$ and n_{plasma}, with $\bar{n}_{\mathrm{gas}}$ being the mean value of the gas density, allow solving the system of differential equations (4.9) which gives the spatial evolution along the x-direction of the fractions of the beam particles D^-, D^0 and D^+.

Fast electron currents

Colliding with the background gas molecules and the plasma ions and electrons, the fast beam particles create fast electrons: stripped electrons, by negative ion stripping and re-ionisation of the neutrals, and Rudd electrons, by gas ionisation. Their currents I_{S} and I_{R} are computed as

$$\frac{\mathrm{d}I_{\mathrm{S}}}{\mathrm{d}x} = I_{\mathrm{beam}}\, F^- \sum_j (\sigma^j_{\text{-}10} + 2\sigma^j_{\text{-}11}) n_j + I_{\mathrm{beam}}\, F^0 \sum_j \sigma^j_{01} n_j \tag{4.13}$$

$$\frac{\mathrm{d}I_{\mathrm{R}}}{\mathrm{d}x} = I_{\mathrm{beam}} (F^- \sigma_{\mathrm{i\text{-}}} + F^0 \sigma_{\mathrm{i}0} + F^+ \sigma_{\mathrm{i}+}) \bar{n}_{\mathrm{gas}}, \tag{4.14}$$

with $j \in \{\mathrm{gas}, \mathrm{e}, \mathrm{i}\}$ indicating the collision target, i.e. neutral gas, plasma electrons and plasma ions, respectively. The values of the stripping and (re-)ionisation cross sections in equation (4.13) are given in table (4.1). In equation (4.14), $\sigma_{\mathrm{i\text{-}}}$, $\sigma_{\mathrm{i}0}$ and $\sigma_{\mathrm{i}+}$ are the cross sections of gas ionisation by negative, neutral and positive particles, respectively, whose values are also taken from Ref. [56]. It is assumed that $\sigma_{\mathrm{i\text{-}}} = \sigma_{\mathrm{i}+}$.

Description of the fast electrons

The neutral gas ionisation by the fast electrons produces most of the charged plasma particles. Hence, the description of their energy distributions is fundamental in predicting the resulting plasma density, especially in the case of the stripped electrons that, having a higher energy, are the main source of plasma. The stripped electrons are all created at the energy E_{stripped} given by

$$E_{\text{stripped}} = \frac{m_{\text{e}}}{m_{\text{D}}} E_{\text{beam}}$$

which is $\sim 272\,\text{eV}$ for $1\,\text{MeV}$ D^- ions. In the equation, m_{e} and m_{D} are the electron and negative deuterium ion masses, respectively.

The Rudd electrons have a birth energy distribution that was extensively investigated by Rudd et al. [67, 68], hence the name. A mean birth energy is derived as [13]

$$E_{\text{Rudd}} = 0.07\sqrt{\frac{E_{\text{beam}}}{A_{\text{D}}}},$$

where A_{D} is the atomic mass number of the negative deuterium ion.

The SHT model describes the fast electrons via Maxwellian energy distributions around a temperature U_k equal to

$$U_k = \frac{2}{3} E_k,$$

with E_k being the mean thermal energy. The index k represents the stripped (S) and Rudd electrons (R). The SHT model assumes that the mean thermal energies are equal to the birth energies, i.e. $E_{\text{S}} = E_{\text{stripped}}$ and $E_{\text{R}} = E_{\text{Rudd}}$.

This approach overestimates the energy distribution of the fast electrons because it implicitly assumes that the stripped and Rudd electrons thermalise through collisions with only electrons from their own population, neglecting the collisions with the gas molecules as well as with the thermal plasma ions and electrons. Actually, the latter collisions are dominant as, for an effective magnetic cusp confinement, the plasma density is expected to be several orders of magnitude higher than the fast electron densities. Consequently, the fast electrons slow down and thermalise with the plasma electrons whose energy distribution is given by a Maxwellian at the temperature T_{e}.

Therefore, the fast electrons would be better described by steady-state slowing-down energy distributions extending from the birth energy down to T_e. The difference in the estimated secondary ionisation rates between the two descriptions is small if the birth energy of the fast electrons is much higher than the ionisation threshold of the neutral gas. Otherwise, it can be significant: the high-energy tail of the Maxwellian distribution would still predict a finite plasma density when, actually, zero ionisation is expected. Electrons with low birth energies are generated by low energy beam ions.

The slowing-down energy distribution function $f(E,t)$ gives the number of fast electrons with energy in the interval $[E, E+\mathrm{d}E]$ at the time t. The dimensions of $f(E,t)$ are 1/eV. The time evolution of the energy distribution function is described by the following differential equation:

$$\frac{\partial f(E,t)}{\partial t} = S(E) + \frac{\partial f(E,t) R_{\mathrm{loss}}(E)}{\partial E} - \frac{f(E,t)}{\tau(E)}. \tag{4.15}$$

The first term on the right-hand side is a source term and represents the rate at which electrons with energy in the interval $[E, E+\mathrm{d}E]$ are created. The dimensions of $S(E)$ are 1/(eV s). The second term describes the electron energy reduction due to slowing-down. R_{loss} is the energy loss rate in eV/s. The electrons are lost at the walls and this is taken into account by the third term through the electron confinement time $\tau(E)$.

The electron energy loss rate R_{loss} considers two mechanisms: elastic Coulomb collisions with the plasma electrons and ions and inelastic collisions with the neutral gas molecules. On the basis of the model by Holmes [69], R_{loss} is expressed as

$$R_{\mathrm{loss}} = 2\, n_{\mathrm{plasma}}\, G E^{-\frac{1}{2}} + \bar{n}_{\mathrm{gas}}\, K_0 \exp\left(\frac{56\,\mathrm{eV}}{E}\right), \tag{4.16}$$

where, on the right-hand side, the first term describes the elastic Coulomb collisions, with the constant $G = 7.7 \times 10^{-11}\,\mathrm{eV}^{3/2}\,\mathrm{m}^3\,\mathrm{s}^{-1}$ taking the Coulomb logarithm into account, and the second term describes the inelastic collisions, with $K_0 = 2.4 \times 10^{-12}\,\mathrm{eV\,m^3\,s^{-1}}$ being an experimental constant [69].

By setting the time derivative to zero for the steady-state solution, equation (4.15) can be rewritten as

$$\frac{\mathrm{d}f(E)}{\mathrm{d}E} + a_\mathrm{f}(E)f(E) + \frac{S(E)}{R_\mathrm{loss}(E)} = 0, \tag{4.17}$$

with the coefficient $a_\mathrm{f}(E)$ equal to

$$a_\mathrm{f}(E) = \frac{1}{R_\mathrm{loss}(E)}\left(-n_\mathrm{plasma}\,GE^{-\frac{3}{2}} + \frac{56\,\mathrm{eV}\,\bar{n}_\mathrm{gas}\,K_0\exp(-56\,\mathrm{eV}/E)}{E^2} - \frac{1}{\tau(E)}\right).$$

The electron confinement time $\tau(E)$ is computed as [13]

$$\tau(E) = \frac{V_\mathrm{plasma}}{E\left(\frac{C_\mathrm{c,l}}{B_\mathrm{c,l}} + \frac{C_\mathrm{c,e}}{B_\mathrm{c,e}}\right)}, \tag{4.18}$$

where V_plasma is the plasma volume, C_c is the total cusp line length, B_c is the magnetic cusp field and the subscripts l and e refer to the lateral and end magnetic confinement, respectively.

The source term is given by the condition

$$\int_0^{+\infty} S(E)\mathrm{d}E = \frac{I}{e}, \tag{4.19}$$

where I is the fast electron current and e is the elementary charge.

Equation (4.17) requires a numerical solution. Figure 4.7 shows the steady-state slowing-down energy distribution functions calculated for the stripped and Rudd electrons in the case of an ITER-like beam of 1 MeV, 40 A D^- ions. The plotted functions $\hat{f}_k(E)$ are normalised as

$$\hat{f}_k(E) = \frac{f_k(E)}{\int_0^{+\infty} f_k(E)\mathrm{d}E} \qquad \text{with}\, k \in \{\mathrm{S}, \mathrm{R}\}.$$

The stripped electrons are all born at the energy $E_\mathrm{stripped} \approx 272\,\mathrm{eV}$, hence

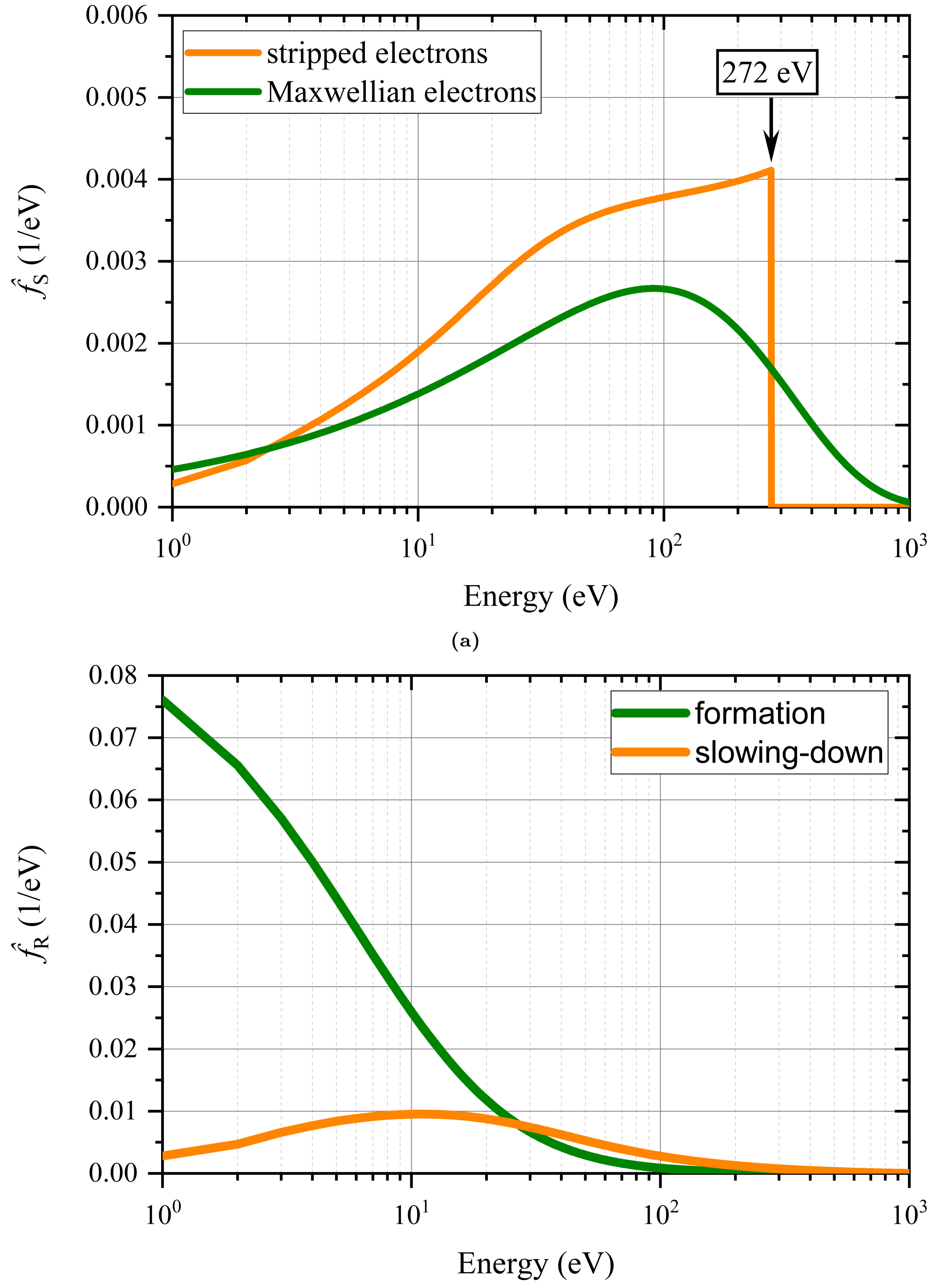

Figure 4.7: (a) Normalised slowing-down energy distribution function of the ITER-like stripped electrons (orange) compared to the Maxwellian energy distribution assumed by the SHT model (green). (b) Birth energy distribution (green) and normalised slowing-down energy distribution function (orange) of the ITER-like Rudd electrons. Pictures reprinted from [55] under the terms of the Creative Commons Attribution 3.0 licence.

the source term $S(E)$ is different from zero only at $E = E_{\text{stripped}}$. The corresponding normalised slowing-down energy distribution function $\hat{f}_{\text{S}}(E)$ is plotted in orange in figure 4.7a together with the Maxwellian energy distribution assumed by the SHT model in green. The comparison makes it clear that, if the birth energy of the stripped electrons is lower than the gas ionisation potential, the Maxwellian high-energy tail would still predict stripped-electron-induced ionisation, while the slowing-down energy distribution would compute zero ionisation.

The Rudd electrons are born with an energy distribution whose analytical expression was obtained by Rudd et al. [68]. The normalised birth energy distribution of the ITER-like Rudd electrons $\hat{f}_{\text{R,birth}}(E)$ is plotted in green in figure 4.7b. The source term $S(E)$ can be written as

$$S(E) = \frac{I_{\text{R}}}{e} f_{\text{R,birth}}.$$

The resulting normalised slowing-down energy distribution is plotted in orange in figure 4.7b. The presence of a peak is explained by the energy dependence of the loss rate due to Coulomb scattering which increases with decreasing energy as $E^{-1/2}$.

The integration of the non-normalised slowing-down energy distribution functions $f_k(E)$ allows directly computing the fast electron densities:

$$n_k = \frac{1}{V_{\text{plasma}}} \int_0^{+\infty} f_k(E) \mathrm{d}E \qquad \text{with}\, k \in \{\text{S}, \text{R}\}. \tag{4.20}$$

Therefore, three distinct electron populations are considered throughout the model: the fast stripped and Rudd electrons, whose energy distribution functions f_{S} and f_{R} have been calculated from equation (4.17), and the thermal plasma electrons, described by a Maxwellian distribution f_{P} centred around the temperature T_{e}.

Electron-ion recombination and the plasma species composition model

The background gas is further ionised by the fast stripped and Rudd electrons which produce the major part of the plasma particles. The computation of the secondary ionisation currents, together with that of the plasma electron temperature, allows estimating the plasma density in the SHT model. However, an important loss channel for low temperature plasmas ($T_\mathrm{e} < 10\,\mathrm{eV}$), like the one expected in the BDPN, was neglected: the electron-ion recombination. The impact of recombination on the ionisation degree of the BDPN plasma was firstly pointed out in [70] with the conclusion that the achievable beam-driven plasma density is about 50 % lower than the one predicted without considering recombination. This result relies on the assumption that the plasma is mainly composed of molecular ions D_2^+ and D_3^+. Indeed, the cross sections of the dissociative recombination reactions of electrons with D_2^+ and D_3^+ ions are orders of magnitude higher than that of the radiative recombination of electrons with atomic ions D^+. For the plasma density ($2.1 \times 10^{18}\,\mathrm{m}^{-3}$) and temperature values (1.1 eV) predicted by the revised BDPN model in the case of an ITER-like beam of 1 MeV, 40 A D^- ions, the following reaction frequencies are calculated: $8.4 \times 10^4\,\mathrm{s}^{-1}$ for the dissociative recombination of D_2^+ ions, $6.8 \times 10^4\,\mathrm{s}^{-1}$ for the dissociative recombination of D_3^+ ions, $0.29\,\mathrm{s}^{-1}$ for the radiative recombination of D^+ ions and $0.018\,\mathrm{s}^{-1}$ for the three-body recombination of D^+ ions. The latter frequency being very low, three-body recombination is neglected. Therefore, determining the actual impact of recombination on the BDPN plasma requires the knowledge of the composition of the plasma ion species.

To this end, a plasma composition model is included in the BDPN model by adapting and integrating an existing rate equation model [55]. The plasma composition model uses global rate equations to compute the concentrations of D, D^+, D_2^+ and D_3^+ particles in the plasma, indicated by n_1, $n_{1\mathrm{p}}$, $n_{2\mathrm{p}}$ and $n_{3\mathrm{p}}$, respectively. The reactions that produce or destroy the plasma species

Table 4.4: Main reactions considered in the plasma composition model. When not directly indicated in the table, the cross section values are taken from Janev et al. [71].

	Reaction		Cross section
1.	$D_2 + e \longrightarrow D_2^+ + 2e$	molecule ionisation	σ_{I}
2.	$D_2 + e \longrightarrow D^+ + D + 2e$	dissociative ionisation	σ_{DI} [72]
3.	$D_2 + e \longrightarrow 2D + e$	simple dissociation	σ_{D} [73]
4.	$D_2^+ + e \longrightarrow D^+ + D + e$	dissociative excitation	σ_{DE}
5.	$D_2^+ + e \longrightarrow 2D^+ + 2e$	dissociative ionisation	σ_{DI2p}
6.	$D_2^+ + e \longrightarrow 2D$	dissociative recombination	σ_{DR2p}
7.	$D^+ + D_2 \longrightarrow D_2^+ + D$	charge exchange	σ_{CX}
8.	$D_2^+ + D_2 \longrightarrow D_3^+ + D$	dissociative attachment	σ_{DA}
9.	$D + e \longrightarrow D^+ + 2e$	atom ionisation	σ_{I1}
10.	$D_3^+ + e \longrightarrow D + D_2$	dissociative recombination	$\sigma_{\mathrm{DR3p,1}}$
11.	$D_3^+ + e \longrightarrow 3D$	dissociative recombination	$\sigma_{\mathrm{DR3p,2}}$
12.	$D^+ + e \longrightarrow D$	radiative recombination	σ_{DR1p}

are listed in table 4.4. The cross section values are taken from Janev et al. [71] except for the cases of dissociative ionisation and simple dissociation whose references are given in the table.

For every process of table 4.4, a rate coefficient R_q^k is computed. The subscript q identifies the reaction and, in case the reaction involves an electron, the superscript k indicates the population to which the electron belongs. Hence, k can be equal to S, R or P to indicate the stripped, Rudd and plasma electrons, respectively.

The rate coefficient is computed as

$$R_q^k = \int_0^{+\infty} \sigma_q(E) \sqrt{\frac{2E}{m_{\mathrm{e}}}} \hat{f}_k(E)\,\mathrm{d}E, \tag{4.21}$$

where $\hat{f}_k(E)$ is the normalised energy distribution function of the electron population k.

One can then calculate the reaction frequency ν_q as

$$\nu_q = \sum_k R_q^k n_k \qquad \text{with}\, k \in \{\mathrm{S}, \mathrm{R}, \mathrm{P}\}. \tag{4.22}$$

For instance, the frequency of gas molecule ionisation by electron impact ν_I (reaction 1. in table 4.4) is equal to

$$\nu_\mathrm{I} = R_\mathrm{I}^\mathrm{S}\, n_\mathrm{S} + R_\mathrm{I}^\mathrm{R}\, n_\mathrm{R} + R_\mathrm{I}^\mathrm{P}\, n_\mathrm{P},$$

where n_S, n_R and n_P are the densities of the stripped, Rudd and plasma electrons, respectively. The densities n_S and n_R are computed via equation (4.20), while the plasma density is given by the summation of the ion species densities:

$$n_\mathrm{P} = n_\mathrm{plasma} = n_\mathrm{1p} + n_\mathrm{2p} + n_\mathrm{3p}. \tag{4.23}$$

In case of reactions 7. and 8. of table 4.4, the impacting particle is a plasma ion. The BDPN plasma being a cold plasma, the plasma electron temperature T_e is much higher than the plasma ion temperature T_i, i.e. $T_\mathrm{i} \ll T_\mathrm{e}$. In low-pressure gas discharges, indeed, the low momentum transfer between electrons and heavy particles, such as ions and gas molecules, is not compensated by a high number of collisions. On the other hand, the high momentum transfer between the plasma ions and the gas molecules allows assuming that the plasma ion temperature is almost equal to the gas temperature, i.e. $T_\mathrm{i} \approx k_\mathrm{B}\, T_\mathrm{gas}$ by expressing the plasma ion temperature in energy units.

Therefore, the frequency ν_DA of dissociative attachment of D_2^+ ions with D_2 is computed as

$$\nu_\mathrm{DA} = \sigma_\mathrm{DA}(T_\mathrm{i}) \sqrt{\frac{2T_\mathrm{i}}{m_{\mathrm{D}_2^+}}}\, n_\mathrm{2p},$$

where $m_{\mathrm{D}_2^+}$ is the mass of the D_2^+ ion.

The charge exchange (CX) process (reaction 7. in table 4.4) deserves special attention. The majority of D^+ ions in the plasma is produced through dissociative excitation of D_2^+ ions (reaction 4. in table 4.4). As the predicted D density is very low, the contribution of the atom ionisation process (reaction 9. in table 4.4) is negligible (the predicted dissociation degree for the ITER-like case is only 0.59 %). The kinetic energy distribution of the resulting D^+ ions

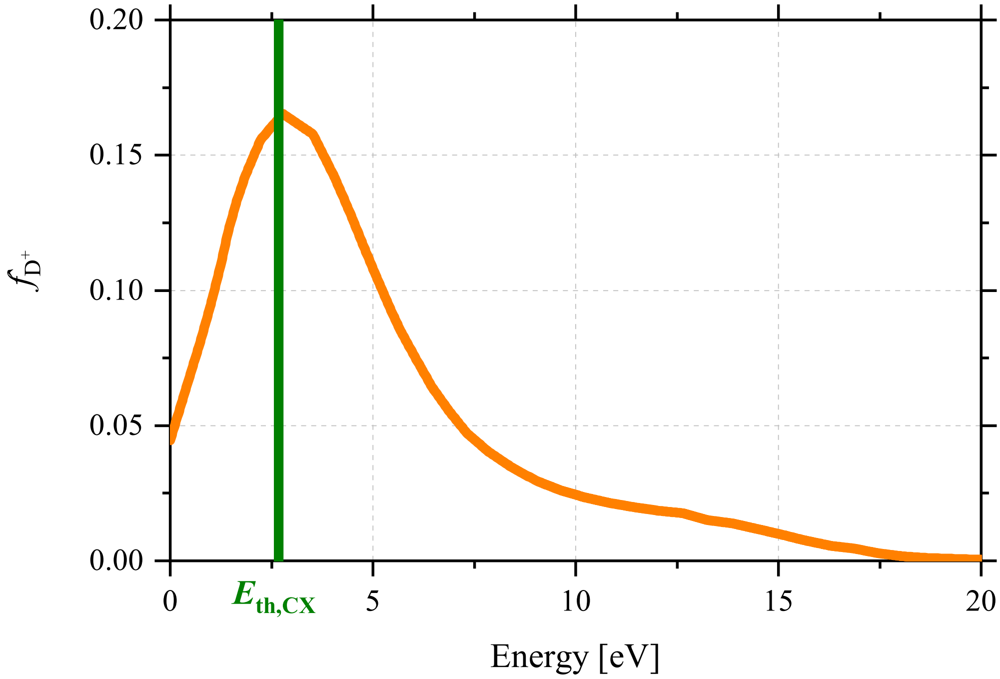

Figure 4.8: Normalised kinetic energy distribution of the D^+ ions coming from the dissociative excitation of D_2^+ ions by electron impact (reaction 4. of table 4.4). The distribution is taken from [74]. The green line indicates the threshold energy of the charge exchange process $E_{\mathrm{th,CX}}$ (reaction 7. of table 4.4).

has been experimentally measured and analytically modelled for both hydrogen and deuterium [74]: after a low-energy peak, it extends up to 20 eV, as illustrated in figure 4.8.

The CX process has a threshold energy $E_{\mathrm{th,CX}} = 2.67\,\mathrm{eV}$ for the D_2 vibrational state $\nu = 0$ [71] (higher vibrational states of the gas molecule are neglected due to the low value of the expected gas temperature, to the low gas pressure and to the low energy of the impacting particles [75]). Thus, the energy distribution of the D^+ ions plays a fundamental role as only the ions with an energy higher than $E_{\mathrm{th,CX}}$ can be destroyed by charge exchange. This is schematically shown in figure 4.8 where the red line indicates the energy threshold of the CX process. Integrating the energy distribution from zero to $E_{\mathrm{th,CX}}$ gives the fraction of D^+ ions that are not affected by CX. For the energy distribution of figure 4.8, this fraction is 0.29. Hence, 0.71 is the fraction of D^+ ions that can undergo charge exchange.

The plasma species composition model takes this distinction into account in a simple way: the D$^+$ ion density n_{1p} is split into two parts, $n_{\mathrm{1p,L}}$ and $n_{\mathrm{1p,H}}$. The former is the density of atomic ions that have been produced at an energy lower than the CX threshold energy, the latter is the density of D$^+$ ions produced at a higher energy. A global rate equation is written for each of the two populations as if they were different species. In each equation, the total source term of D$^+$ ions is multiplied by the fractions calculated by integrating the D$^+$ ion kinetic energy distribution, while the charge exchange sink term is considered only for the population with energy above the CX threshold. The rate coefficient for the CX reaction R_{CX} can then be written as

$$R_{\mathrm{CX}} = \int_{E_{\mathrm{th,CX}}}^{+\infty} \sigma_{\mathrm{CX}}(E) \sqrt{\frac{2E}{m_{\mathrm{D^+}}}}\, \hat{f}_{\mathrm{D^+,H}}\, \mathrm{d}E,$$

where $\hat{f}_{\mathrm{D^+,H}}$ is the normalised energy distribution of the D$^+$ ions with energy higher than $E_{\mathrm{th,CX}}$ and $m_{\mathrm{D^+}}$ is the deuterium atomic ion mass. Thus, the CX frequency is equal to

$$\nu_{\mathrm{CX}} = R_{\mathrm{CX}}\, n_{\mathrm{1p,H}}.$$

The total density of D$^+$ ions is obtained by summing up the densities of the two populations, i.e. $n_{\mathrm{1p}} = n_{\mathrm{1p,L}} + n_{\mathrm{1p,H}}$.

The model is very sensitive to the assumed kinetic energy distribution of the atomic ions, hence further investigation in this regard is envisaged in the near future.

The plasma species composition model is given by the following system of differential equations:

$$\begin{aligned}\frac{\mathrm{d}n_1}{\mathrm{d}t} &= (\nu_{\mathrm{DI}} + 2\nu_{\mathrm{D}})\bar{n}_{\mathrm{gas}} + \nu_{\mathrm{DA}}\bar{n}_{\mathrm{gas}} + (\nu_{\mathrm{DE}} + 2\nu_{\mathrm{DR2p}})n_{\mathrm{2p}} + \nu_{\mathrm{CX}}\bar{n}_{\mathrm{gas}} + \\ &\quad + \nu_{\mathrm{DR1p}}(n_{\mathrm{1p,L}} + n_{\mathrm{1p,H}}) + (\nu_{\mathrm{DR3p,1}} + 3\nu_{\mathrm{DR3p,2}})n_{\mathrm{3p}} - \nu_{\mathrm{I1}}n_1 - \frac{n_1 v_1}{4}\frac{S_{\mathrm{neut}}}{V_{\mathrm{neut}}}\end{aligned}$$

$$\frac{\mathrm{d}n_{\mathrm{1p,L}}}{\mathrm{d}t} = 0.29(\nu_{\mathrm{DI}}\bar{n}_{\mathrm{gas}} + (\nu_{\mathrm{DE}} + 2\nu_{\mathrm{DI2p}})n_{\mathrm{2p}} + \nu_{\mathrm{I1}}n_1) - \nu_{\mathrm{DR1p}}n_{\mathrm{1p,L}} + \\ - 0.6\sqrt{\frac{T_{\mathrm{e}}}{m_{\mathrm{1p}}}}n_{\mathrm{1p,L}}\frac{A_{\mathrm{loss}}}{V_{\mathrm{plasma}}}$$

$$\frac{\mathrm{d}n_{\mathrm{1p,H}}}{\mathrm{d}t} = 0.71(\nu_{\mathrm{DI}}\bar{n}_{\mathrm{gas}} + (\nu_{\mathrm{DE}} + 2\nu_{\mathrm{DI2p}})n_{\mathrm{2p}} + \nu_{\mathrm{I1}}n_1) - \nu_{\mathrm{DR1p}}n_{\mathrm{1p,H}} + \\ - 0.6\sqrt{\frac{T_{\mathrm{e}}}{m_{\mathrm{1p}}}}n_{\mathrm{1p,H}}\frac{A_{\mathrm{loss}}}{V_{\mathrm{plasma}}}$$

$$\frac{\mathrm{d}n_{\mathrm{2p}}}{\mathrm{d}t} = \nu_{\mathrm{I}}\bar{n}_{\mathrm{gas}} + \nu_{\mathrm{CX}}\bar{n}_{\mathrm{gas}} + \frac{I_{\mathrm{R}}}{eV_{\mathrm{plasma}}} - (\nu_{\mathrm{DE}} + \nu_{\mathrm{DI2p}} + \nu_{\mathrm{DR2p}})n_{\mathrm{2p}} + \\ - \nu_{\mathrm{DA}}\bar{n}_{\mathrm{gas}} - 0.6\sqrt{\frac{T_{\mathrm{e}}}{m_{\mathrm{2p}}}}n_{\mathrm{2p}}\frac{A_{\mathrm{loss}}}{V_{\mathrm{plasma}}}$$

$$\frac{\mathrm{d}n_{\mathrm{3p}}}{\mathrm{d}t} = \nu_{\mathrm{DA}}\bar{n}_{\mathrm{gas}} - (\nu_{\mathrm{DR3p,1}} + \nu_{\mathrm{DR3p,2}})n_{\mathrm{3p}} - 0.6\sqrt{\frac{T_{\mathrm{e}}}{m_{\mathrm{3p}}}}n_{\mathrm{3p}}\frac{A_{\mathrm{loss}}}{V_{\mathrm{plasma}}} \qquad (4.24)$$

In the equations, m_{1p}, m_{2p} and m_{3p} are the masses of the D^+, D_2^+ and D_3^+ ions, respectively. The source and sink terms in every equation are expressed through the frequencies of the reactions in table 4.4 that produce and destroy the considered plasma species, respectively. The term $I_{\mathrm{R}}/(eV_{\mathrm{plasma}})$, with I_{R} being the Rudd electron current, represents the D_2^+ ions generated through gas ionisation by the beam ions.

Wall losses

The last term in each of the equations (4.24) accounts for the wall losses. The loss rate of the D atoms escaping to the chamber walls is given as

$$\Gamma_1 = \frac{v_1}{4}\frac{S_{\mathrm{neut}}}{V_{\mathrm{neut}}},$$

where S_{neut} and V_{neut} are the surface area and volume of the neutraliser box, respectively, and v_1 is the thermal velocity of the D atoms which is equal to

$$v_1 = \sqrt{\frac{8T_{\mathrm{D}}}{\pi m_{\mathrm{D}}}} \tag{4.25}$$

with T_{D} and m_{D} being the atom temperature and mass, respectively. The D atoms coming from dissociation processes, it is assumed $T_{\mathrm{D}} = 2.3\,\mathrm{eV}$.

When dealing with the ion wall losses, the magnetic confinement has to be considered: the ions escaping to the walls are lost only if they leak through the magnetic cusps generated by the permanent magnets surrounding the chamber. Therefore, the effective loss area A_{loss} is much smaller than the neutraliser internal wall surface S_{neut}. Furthermore, the plasma being in contact with cold walls, a sheath layer is formed on the walls [76]. The ions are hence accelerated to the Bohm velocity:

$$v_{x\mathrm{p,Bohm}} = \sqrt{\frac{T_{\mathrm{e}}}{m_{x\mathrm{p}}}} \qquad \text{with}\, x \in \{1, 2, 3\}. \tag{4.26}$$

The current of ions lost at the walls can be computed as

$$I_{x\mathrm{p}} = 0.6\, v_{x\mathrm{p,Bohm}}\, e n_{x\mathrm{p}} A_{\mathrm{loss}}, \tag{4.27}$$

where the factor 0.6 takes the density reduction at the edge of the sheath into account.

The SHT model describes the effective wall loss area for the plasma electrons and ions as

$$A_{\mathrm{loss}} = 4C_{\mathrm{c}}(\rho_{\mathrm{e}}\rho_{\mathrm{i}})^{1/2}, \tag{4.28}$$

in which C_{c} is the total cusp line length and $(\rho_{\mathrm{e}}\rho_{\mathrm{i}})^{1/2}$ is the hybrid gyroradius, given by the geometric mean of the electron and ion gyroradii ρ_{e} and ρ_{i}. Although experimentally obtained in [77], it is unlikely that a rather simple relation as equation (4.28) could satisfactorily describe the plasma leakage through the magnetic cusps. However, as argued in [78], reliable expressions that are able to estimate the effective loss area in presence of magnetic cusps for different plasma parameters and different magnet arrangements are not available. Therefore, equation (4.28) continues to be used in the BDPN model, although it might underestimate the effective loss area A_{loss}. An experimental investigation is required to verify and eventually improve the plasma wall loss modelling.

The electron gyroradius is

$$\rho_{\mathrm{e}} = \frac{m_{\mathrm{e}} v_{\mathrm{e}}}{e B_{\mathrm{c}}} \qquad \text{with } v_{\mathrm{e}} = \sqrt{\frac{8 T_{\mathrm{e}}}{\pi m_{\mathrm{e}}}}, \tag{4.29}$$

where v_{e} is the mean velocity of the Maxwellian-distributed plasma electrons.

The ion gyroradius is computed as

$$\rho_{\mathrm{i}} = \frac{m_{\mathrm{i}} v_{\mathrm{i}}}{e B_{\mathrm{c}}}. \tag{4.30}$$

The plasma ions, which are accelerated to the Bohm velocity at the sheath edge, reach the wall after passing through the sheath. Hence, their energy is further increased by the potential drop ϕ across the sheath. Calling η the ratio between the sheath potential and the plasma electron temperature

$$\eta = \frac{e\phi}{T_{\mathrm{e}}},$$

the ion energy at the wall is

$$E_{\mathrm{i,wall}} = \frac{1}{2} m_{\mathrm{i}} v_{\mathrm{i}}^2 = \frac{1}{2} m_{\mathrm{i}} v_{\mathrm{i,Bohm}}^2 + T_{\mathrm{e}}\, \eta,$$

from which the plasma ion velocity v_{i} is obtained:

$$v_{\mathrm{i}} = \sqrt{\frac{T_{\mathrm{e}}}{m_{\mathrm{i}}}(1 + 2\eta)}.$$

As the relation (4.28) for the effective loss area A_{loss} does not take the different plasma ion species into account, an average ion mass m_{i} is defined as

$$m_{\mathrm{i}} = \frac{1}{n_{\mathrm{plasma}}}\Big(n_{1\mathrm{p}}m_{1\mathrm{p}} + n_{2\mathrm{p}}m_{2\mathrm{p}} + n_{3\mathrm{p}}m_{3\mathrm{p}}\Big). \tag{4.31}$$

The ratio η is calculated by demanding that the electron and ion currents to the neutraliser walls are equal. The total current of plasma ions that leak through the magnetic cusps is equal to

$$I_{\mathrm{i}} = \sum_{x=1}^{3} I_{x\mathrm{p}}, \tag{4.32}$$

where $I_{x\mathrm{p}}$ is given by equation (4.27). The current of escaping plasma electrons is expressed as

$$I_{\mathrm{e}} = \frac{1}{4}v_{\mathrm{e}}\, en_{\mathrm{plasma}}\exp(-\eta)A_{\mathrm{loss}}. \tag{4.33}$$

From the balance $I_{\mathrm{i}} = I_{\mathrm{e}}$, it results:

$$\eta = \frac{e\phi}{T_{\mathrm{e}}} = \ln\left(\frac{2.6}{n_{\mathrm{plasma}}}\sqrt{\frac{\pi m_{\mathrm{e}}}{8}}\sum_{x=1}^{3}\frac{n_{x\mathrm{p}}}{\sqrt{m_{x\mathrm{p}}}}\right)^{-1}. \tag{4.34}$$

The explicit expression of the effective wall loss area A_{loss} is obtained by substituting the gyroradius expressions (4.29) and (4.30) into equation (4.28). As the magnet arrangement on the lateral walls is different from that at the neutraliser extremities, two different effective loss areas have to be considered. The subscripts l and e are used to distinguish the respective values of the cusp line length C_{c} and of the magnetic cusp field B_{c}.

$$\begin{aligned} A_{\mathrm{loss}} &= 4C_{\mathrm{c,l}}(\rho_{\mathrm{e}}\rho_{\mathrm{i}})^{1/2} + 4C_{\mathrm{c,e}}(\rho_{\mathrm{e}}\rho_{\mathrm{i}})^{1/2} = \\ &= \left(\frac{4C_{\mathrm{c,l}}}{eB_{\mathrm{c,l}}} + \frac{4C_{\mathrm{c,e}}}{eB_{\mathrm{c,e}}}\right)(m_{\mathrm{e}}v_{\mathrm{e}}m_{\mathrm{i}}v_{\mathrm{i}})^{1/2} = \\ &= \left(\frac{4C_{\mathrm{c,l}}}{eB_{\mathrm{c,l}}} + \frac{4C_{\mathrm{c,e}}}{eB_{\mathrm{c,e}}}\right)\left(\frac{8m_{\mathrm{e}}m_{\mathrm{i}}}{\pi}T_{\mathrm{e}}^{2}(1+2\eta)\right)^{1/4}, \end{aligned} \tag{4.35}$$

with η given by equation (4.34).

The cusp line lengths $C_{\mathrm{c,l}}$ and $C_{\mathrm{c,e}}$ are computed as

$$C_{\mathrm{c,l}} = 2(H_{\mathrm{neut}} + W_{\mathrm{neut}})\left(\frac{L_{\mathrm{neut}}}{D_{\mathrm{cusp}}} + 1\right) \approx 200\,\mathrm{m} \tag{4.36}$$

$$C_{\mathrm{c,e}} = (2(n_{\mathrm{ch}} + 1) - 4)H_{\mathrm{neut}} \approx 12\,\mathrm{m}, \tag{4.37}$$

where $n_{\mathrm{ch}} = 4$ is the number of the end channels formed by the magnet columns.

The system of differential equations (4.24) is solved for the steady-state to obtain the densities of the atoms and ion species and, hence, the plasma density n_{plasma}. The plasma density is also a model input as it is needed to calculate the reaction frequencies. Thus, an iterative procedure is required to solve the plasma species composition model.

Gas molecule dissociation and the power balance

The dissociation of the gas molecules by electron impact has already been considered in the calculation of the plasma composition (reactions 2. and 3. in table 4.4). Its inclusion in the BDPN model also implies the modification of the power balance used by the SHT model to determine the plasma electron temperature T_{e}. The balance states that the power gained by the plasma electrons through collisions with the beam ions and the fast electrons is equal to the power removed by the plasma ions and electrons lost at the wall. However, an additional power consumption is now taken into account: as gas dissociation has an energy threshold, the plasma electrons spend power to dissociate the D_2 molecules. The vibrational-state-dependent threshold energy for D_2 dissociation is $E_{\mathrm{diss}} = 4.48\,\mathrm{eV}$ for the vibration state $\nu = 0$ [71].Thus, the additional power loss term reads as

$$W_{\mathrm{diss}} = V_{\mathrm{plasma}}\,\bar{n}_{\mathrm{gas}}\,n_{\mathrm{plasma}}(R^{\mathrm{P}}_{\mathrm{DI}} + R^{\mathrm{P}}_{\mathrm{D}})E_{\mathrm{diss}}, \tag{4.38}$$

where the R^{P}-terms are the Maxwellian rate coefficients (equation (4.21)) of dissociative ionisation and simple dissociation of the neutral gas molecules (reactions 2. and 3. in table 4.4).

The plasma electron power balance is modified as

$$W_{\mathrm{S}} + W_{\mathrm{R}} + W_{\mathrm{beam}} = T_{\mathrm{e}}\left(\frac{I_{\mathrm{e}}}{e} + \eta\frac{I_{\mathrm{i}}}{e}\right) + W_{\mathrm{diss}}. \tag{4.39}$$

The W-terms on the left-hand side are the energy transfers to the plasma electrons from the stripped electrons, the Rudd electrons and the beam ions, from left to right. Their expressions can be found in [13]. The term $T_{\mathrm{e}}(I_{\mathrm{e}}/e + \eta I_{\mathrm{i}}/e)$ is the power loss due to the plasma ions and electrons leaking through the magnetic cusps at the walls, with the respective currents I_{i} and I_{e} given by equations (4.32) and (4.33), respectively.

Gas dissociation was neglected by the SHT model. Adding this power loss channel for the plasma electrons translates into a reduction of the predicted plasma temperature T_{e}.

Gas heating model

The interaction of the ion beam with the background neutral gas is responsible of an increase of the gas temperature. For instance, gas temperatures up to 900 K were measured for the JET NBI neutraliser [79]. Leading to lower gas densities, gas heating is thought to be the cause of the shortfall of the neutralisation efficiency observed for the JET injectors with respect to the theoretical value [80]. Gas heating phenomena inside the gas neutraliser were modelled by Paméla [81, 82]. The predicted gas temperature for the JET neutraliser agreed well with the spectroscopic measurements in [80].

A lower gas density implies a higher gas inflow into the neutraliser to achieve the optimum target thickness and, consequently, an increased gas pressure along the beamline. This has a negative impact on the injector efficiency as higher pumping speeds are needed and/or the stripping losses in the accelerator and the re-ionisation losses after the neutraliser increase. Hence, it is important to obtain a reliable estimate of the gas temperature in the BDPN. To this end, a gas heating model based on Paméla's calculations is included in the BDPN model.

At first, an upper limit of the BDPN gas temperature T_{gas} is derived for an ITER-like beam of 1 MeV, 40 A D^- ions by balancing the total power that the ion beam loses in the neutraliser gas with the power lost by the gas molecules at the chamber walls:

$$P_{\mathrm{beam}} = S_{\mathrm{neut}} \frac{1}{4} \bar{n}_{\mathrm{gas}} \sqrt{\frac{8 k_{\mathrm{B}} T_{\mathrm{gas}}}{\pi M}} \frac{\alpha}{\gamma - 1} k_{\mathrm{B}} (T_{\mathrm{gas}} - T_{\mathrm{wall}}), \tag{4.40}$$

where P_{beam} is the ion beam power loss, S_{neut} is the neutraliser surface area, M is the gas molecular mass, $[(8 k_{\mathrm{B}} T_{\mathrm{gas}})/(\pi M)]^{1/2}$ is the gas mean velocity, α is the accommodation coefficient of the gas molecules on the walls, $\gamma = 1.4$ is the gas specific heat ratio and $T_{\mathrm{wall}} = 300\,\mathrm{K}$ is the wall temperature. It is assumed $\alpha = 0.5$ [81, 82].

The power deposited by the beam ions into the background gas P_{beam} is obtained from the ion stopping power which is the average rate at which the ions lose energy per unit length due to elastic and inelastic collisions with the gas molecules. The ion stopping power is given by the product of the stopping cross section and the mean gas density. The stopping cross section S_{SP} of a 500 keV H^+ ion in H_2 (equivalent to a 1 MeV D^+ ion in D_2) is $S_{\mathrm{SP}} \approx 4 \times 10^{-19}\,\mathrm{eV\,m}^2$ [83]. It is assumed that negative ions have the same value of stopping cross section, provided that the contribution from the stripped electrons is considered separately. It follows:

$$P_{\mathrm{beam}} = \frac{I_{\mathrm{beam}}}{e} S_{\mathrm{SP}}\, \bar{n}_{\mathrm{gas}}\, L_{\mathrm{neut}} + \frac{I_{\mathrm{S}}}{e} E_{\mathrm{stripped}} \approx 13\,\mathrm{kW}. \tag{4.41}$$

Solving equation (4.40) for this value of the deposited power gives a gas temperature upper limit of $T_{\mathrm{gas}} = 1900\,\mathrm{K}$. Balance (4.40) overestimates the gas temperature as definitely not all the power that the ion beam deposits into the neutral gas is transferred as kinetic power to the gas molecules. Additionally, the radiative energy loss of the gas molecules is neglected.

On the other hand, Paméla's model [81,82] uses more assumptions to calculate the effective energy transfer from the beam particles to the gas molecules. Hence, the model gives a more precise estimate of the gas temperature, albeit less robust than the conservative value obtained with balance (4.40).

The energy fraction that is transferred from the beam to the gas through elastic collisions is negligible: the momentum transfer cross section of a 1 MeV D^+ ion in D_2 is $1.6 \times 10^{-27}\,\mathrm{m}^2$ [84]. This value is much lower than the corresponding cross section computed for stopping

$$\hat{S}_{\mathrm{SP}} = \left(\int_0^{1\,\mathrm{MeV}} \frac{\mathrm{d}E}{S_{\mathrm{SP}}(E)} \right)^{-1} = 6.4 \times 10^{-25}\,\mathrm{m}^2.$$

Hence, gas heating occurs only indirectly.

Paméla identifies three main indirect energy transferring processes: gas molecule dissociation by beam ions, gas molecule dissociation by electron impact and reflection of the plasma ions from the neutraliser walls as energetic neutrals.

The gas heating model considers four reactions of gas dissociation by beam positive ions which are listed in table 4.5. Each reaction j with $j \in \{1,2,3,4\}$ is characterised by a cross section σ_j, whose reference is indicated in the table, and by an energy value W_j representing the kinetic energy of the corresponding dissociation products. The cross sections of the equivalent dissociation reactions where the impacting particle is a negative ion or an atom are not available. In applying Paméla's model to the ITER gas neutraliser [85], Surrey pointed out that for negative ions stripping is more likely than dissociation. A similar argument could be considered for the neutral atoms. In order to obtain a conservative estimate, it is assumed that the beam negative ions and neutrals undergo similar reactions as those listed in table 4.5 with the same

Table 4.5: Gas dissociation reactions by ion impact. Fast beam particles are denoted by a hat. For every process, the cross section symbol σ_j with the corresponding reference and the kinetic energy W_j of the dissociation products are indicated, with $j \in \{1,2,3,4\}$.

	Reaction		σ_j	W_j [eV]
1.	$\hat{\mathrm{D}}^+ + \mathrm{D}_2 \longrightarrow \hat{\mathrm{D}} + \mathrm{D} + \mathrm{D}^+$	dissociative charge exchange	σ_1 [86]	5
2.	$\hat{\mathrm{D}}^+ + \mathrm{D}_2 \longrightarrow \hat{\mathrm{D}}^+ + \mathrm{D} + \mathrm{D}^+ + \mathrm{e}$	dissociative ionisation	σ_2 [87]	5
3.	$\hat{\mathrm{D}}^+ + \mathrm{D}_2 \longrightarrow \hat{\mathrm{D}}^{(+)} + 2\mathrm{D}^+ + (2)\mathrm{e}$	double ionisation	σ_3 [56]	10
4.	$\hat{\mathrm{D}}^+ + \mathrm{D}_2 \longrightarrow \hat{\mathrm{D}}^+ + \mathrm{D}^{(*)} + \mathrm{D}$	simple dissociation	σ_4 [73]	2

cross section values σ_j and the same kinetic energies W_j of the dissociation fragments.

Reactions 2. and 3. in table 4.4 represent the gas dissociation by electrons: the kinetic energies of the dissociation fragments from dissociative ionisation (σ_{DI}) and simple dissociation (σ_{D}) are assumed equal to those for the analogous ion impact reactions, i.e. W_2 and W_4 in table 4.5, respectively.

The plasma ion temperature T_{i} being very low, one can neglect the gas dissociation by plasma ion impact. However, Paméla argues that, after being accelerated in the plasma sheath to the energy $T_{\mathrm{e}}\eta$, the plasma ions could neutralise on the walls and be reflected back as neutrals, keeping a significant fraction of the initial energy. The product of this energy fraction and the reflection probability is indicated as R_{ref}. Paméla's gas heating model assumes $R_{\mathrm{ref}} = 0.3$. Hence, the kinetic energy of the reflected neutrals is

$$W_{\mathrm{ref}} = R_{\mathrm{ref}}\, T_{\mathrm{e}}\eta. \tag{4.42}$$

In summary, both the dissociation fragments and the reflected neutrals have a few eV kinetic energy that they can partially transfer to the gas molecules through elastic collisions. It is then the secondary particles to heat the gas, hence the definition of indirect heating. The energy transfer is estimated as

$$\varepsilon_{0/+}(W) = W\xi_{0/+} = W(1 - \exp(-\sigma_{0/+}\, d_{\mathrm{m}}\, \bar{n}_{\mathrm{gas}})), \tag{4.43}$$

where the subscripts 0 and + indicate the neutral atoms and the positive ions, respectively, W is the initial kinetic energy, $\xi_{0/+}$ is the fraction of energy transferred to the gas molecules, $\sigma_{0/+}$ is the momentum transfer cross section [84] and d_m is the mean travel distance of the secondary particles. Differently from Paméla who argued that the mean path of the dissociation products up to the neutraliser walls is roughly equal to the small transverse dimension of the chamber, the following consideration is made: if a certain number of particles moves in the x direction, an equal number of particles will move in the opposite way as the dissociation fragments are born with no preferential direction. Hence, the expectation value of the travel distance along x is half the neutraliser length. As the same consideration is valid also for the y and z directions, the mean travel distance d_m is estimated as the mean of the expectation values in the three directions:

$$d_\mathrm{m} = \frac{L_\mathrm{neut} + H_\mathrm{neut} + W_\mathrm{neut}}{6}. \tag{4.44}$$

Having identified and modelled the sources of gas heating, equation (4.40) can be rewritten as

$$\sum_q P_q\, \xi_{0/+,q} = S_\mathrm{neut} \frac{1}{4} \bar{n}_\mathrm{gas} \sqrt{\frac{8 k_\mathrm{B} T_\mathrm{gas}}{\pi M}} \frac{\alpha}{\gamma - 1} k_\mathrm{B} (T_\mathrm{gas} - T_\mathrm{wall}), \tag{4.45}$$

where $P_q = (I_q/e) W_q$ with I_q being the current of dissociation fragments or energetic neutrals generated by the process q and W_q their kinetic energy. A fraction $\xi_{0/+,q}$ of this energy is transferred to the gas molecules through elastic collisions according to equation (4.43).

The explicit expression for the left-hand side of equation (4.45) depends on the considered indirect energy transferring process:

1. Molecular dissociation by beam ions.

$$P_1\, \xi_{0/+,1} = \frac{I_\mathrm{beam}}{e} \{\sigma \varepsilon\}_\mathrm{ion}\, \bar{n}_\mathrm{gas}\, L_\mathrm{neut}, \tag{4.46}$$

with

$$\{\sigma\varepsilon\}_{\rm ion} = \sigma_1(\varepsilon_0(W_1) + \varepsilon_+(W_1)) + \sigma_2(\varepsilon_0(W_2) + \varepsilon_+(W_2)) + 2\sigma_3\,\varepsilon_+(W_3) + \\ + 2\sigma_4\,\varepsilon_0(W_4),$$

where σ_j and W_j with $j \in \{1, 2, 3, 4\}$ are listed in table 4.5 and $\varepsilon_{0/+}$ is defined in equation (4.43).

2. Molecular dissociation by electron impact.

$$P_2\,\xi_{0/+,2} = \bar{n}_{\rm gas}\,V_{\rm plasma} \sum_k n_k \{R^k\varepsilon\}_{\rm e}, \tag{4.47}$$

with

$$\{R^k\varepsilon\}_{\rm e} = R^k_{\rm DI}(\varepsilon_0(W_2) + \varepsilon_+(W_2)) + 2R^k_{\rm D}\,\varepsilon_0(W_4),$$

where $R^k_{\rm DI}$ and $R^k_{\rm D}$ are the rate coefficients for dissociative ionisation and simple dissociation (reactions 2. and 3. in table 4.4), respectively, calculated according equation (4.21). The summation on k with $k \in \{\mathrm{S}, \mathrm{R}, \mathrm{P}\}$ accounts for the fact that all three of the BDPN electron populations contribute to the gas dissociation.

3. Plasma ion reflection as energetic neutrals.

$$P_3\,\xi_{0/+,3} = \frac{I_{\rm i}}{e}\varepsilon_0(W_{\rm ref}), \tag{4.48}$$

where $I_{\rm i}$ is the total current of plasma ions that escape to the wall, given by equation (4.32), and $W_{\rm ref}$ is defined in equation (4.42).

Hence, the power balance of equation (4.45) becomes

$$\frac{I_{\rm beam}}{e}\{\sigma\varepsilon\}_{\rm ion}\,\bar{n}_{\rm gas}\,L_{\rm neut} + \bar{n}_{\rm gas}\,V_{\rm plasma}\sum_k n_k\{R^k\varepsilon\}_{\rm e} + \frac{I_{\rm i}}{e}\varepsilon_0(W_{\rm ref}) = \\ = S_{\rm neut}\frac{1}{4}\bar{n}_{\rm gas}\sqrt{\frac{8k_{\rm B}T_{\rm gas}}{\pi M}}\frac{\alpha}{\gamma-1}k_{\rm B}(T_{\rm gas} - T_{\rm wall}) \tag{4.49}$$

Model solving algorithm

Due to the inclusion of many sub-models, whose inputs are often the outputs of the main code, the revised BDPN model requires many iterations to be solved. The main model results are the plasma density and temperature, n_{plasma} and T_{e}, the ionisation degree χ and the neutralisation efficiency ζ. The solving algorithm is represented by the flowchart of figure 4.9 and briefly outlined in the following:

1. The values of the gas inflow Q and gas temperature T_{gas} are initially assumed. The gas density profile n_{gas} along the neutraliser length is obtained through equations (4.11) and (4.12).

2. Starting with a plasma density $n_{\mathrm{plasma}} = 0$, the solution of the system of differential equations (4.9) gives the spatial evolution of the beam species.

3. The currents of stripped and Rudd electrons are calculated by equations (4.13) and (4.14).

4. By numerically solving equation (4.17), the slowing-down energy distributions of the fast electrons are obtained and subsequently used to compute the corresponding densities via equation (4.20).

5. After assuming a value for the plasma electron temperature T_{e}, the plasma species composition model equations (4.24) and the power balance (4.39) are solved, giving new values of n_{plasma} and T_{e}.

6. By means of an iteration cycle, the code returns to point 5. and repeats the previous steps until the plasma electron temperature has converged.

7. The power balance (4.49) of the gas heating model is solved and a new value of the gas temperature T_{gas} is obtained. Convergence is achieved with an outer iteration loop.

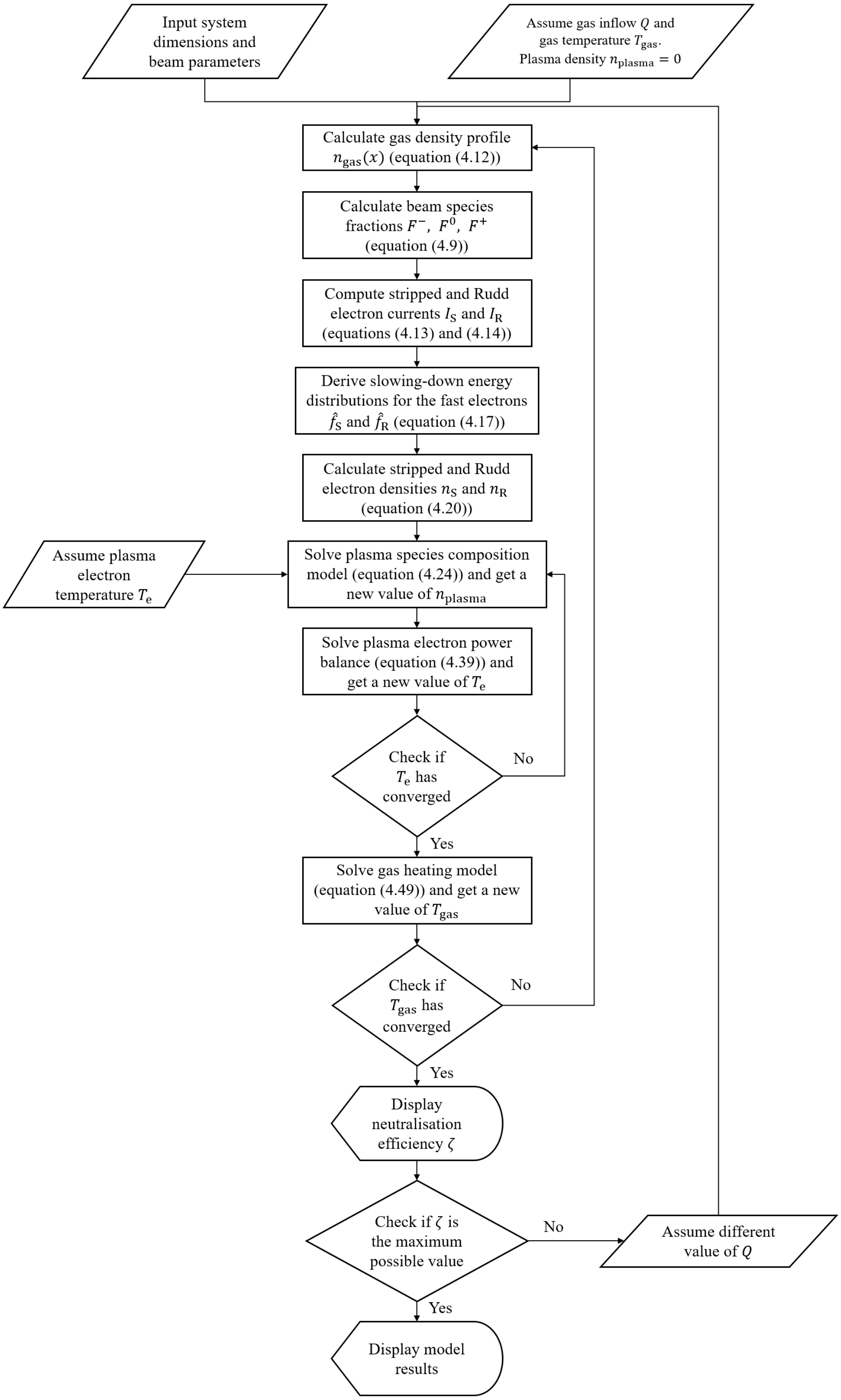

Figure 4.9: Flowchart representing the solving algorithm of the BDPN model.

8. An outer iteration cycle is finally required to optimise the gas inflow Q assumed at the beginning: the optimum value of Q is such that the corresponding gas density maximises the fraction of neutrals in the beam at the neutraliser exit, i.e. the neutralisation efficiency ζ.

4.3.4 Model predictions for the ITER-like NBI reference case

The SHT model was applied to the BDPN design outlined in section 4.3.1 [13]: the dimensions and magnet arrangement are specified in table 4.3 and an ITER-like beam of D^- ions with an energy of 1 MeV and a current of 40 A was considered. In figure 4.10, the SHT results are compared with the predictions of the revised model applied to the same reference case. This comparison is the reason why the same geometrical dimensions and input parameters as those of the SHT model have been assumed. The SHT predictions of figure 4.10, shown as orange lines, have been obtained by implementing the original SHT model. Except for small numerical differences, the results are identical to those plotted in [13].

The quantities in figure 4.10 are plotted as functions of the inlet gas flow rate Q. In order to directly compare the results of the revised model with those of the SHT model, which assumes a gas temperature of 300 K, the gas inflow rate Q obtained for the gas temperature estimated by Paméla's model is scaled to a gas temperature of 300 K using the temperature dependence of Q that is explicitly given by equations (4.10), (4.11) and (4.12). Hence, the values of Q are lower than those required to achieve the same target thickness at a higher gas temperature.

The plasma density n_{plasma} and the ionisation degree χ are drastically lower than the values predicted by the SHT model. This is mainly due to the impact of the electron-ion recombination processes. The plasma species composition model predicts that D^+ is the dominant ion species in the BDPN plasma with

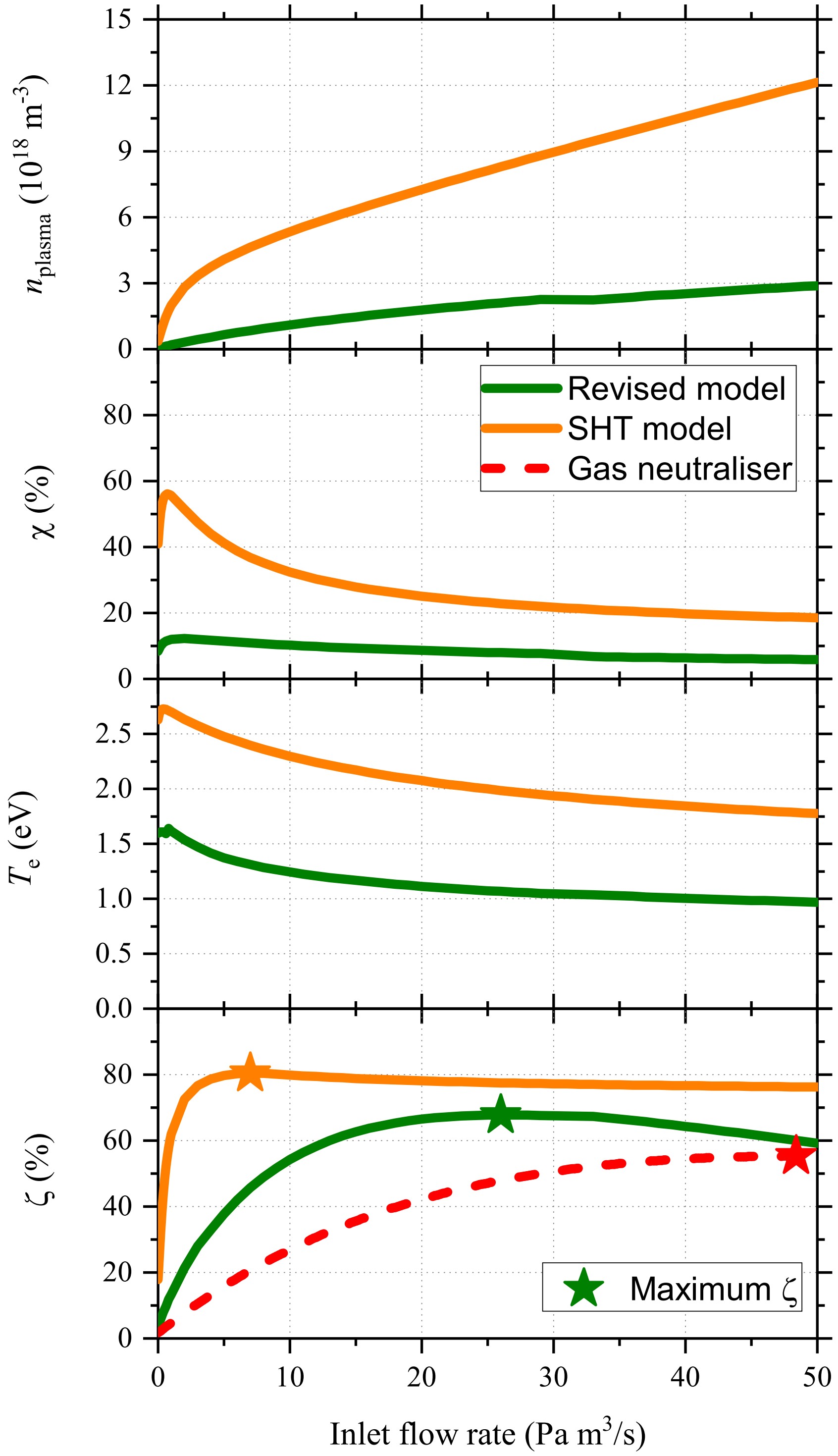

Figure 4.10: Comparison between the revised and SHT models for an ITER-like beam. The plasma density n_{plasma}, the degree of ionisation χ, the plasma electron temperature T_e and the neutralisation efficiency ζ are plotted as functions of the inlet gas flow rate Q at 300 K. The neutralisation efficiency of a gas neutraliser with the same BDPN chamber is also shown. The maximum value of ζ is indicated by a star. Picture reprinted from [55] under the terms of the Creative Commons Attribution 3.0 licence.

a fraction of 99.87 %. The D_2^+ ions are lost through dissociation into D^+ and D (reaction 4. in table 4.4) and in collisions with the gas molecules to form D_3^+ ions (reaction 8. in table 4.4). More importantly, both D_2^+ and D_3^+ are effectively destroyed by dissociative recombination (reactions 6., 10. and 11. in table 4.4). Thus, their resulting fractions are 0.08 % and 0.05 %, respectively. The effect of recombination is such that the predicted plasma density and ionisation degree are about a factor of four lower than the SHT values.

While the mean gas density increases linearly with the gas inlet flow rate, the plasma density increases less than linearly, resulting in a decreasing profile of the ionisation degree.

Including gas dissociation as an additional energy loss channel for the plasma electrons in the model causes a reduction of the plasma electron temperature T_e by about a factor of two.

It was shown in section 4.2 that the higher the ionisation degree χ, the higher the maximum neutralisation efficiency ζ. Additionally, the required target thickness and, hence, the required gas throughput become lower and lower. The dashed red line in figure 4.10 represents the case of zero ionisation degree: the maximum ζ is around 55 %. The same BDPN chamber is assumed for the considered gas neutraliser, so there are no internal channels to reduce the gas throughput as in the case of the ITER gas neutraliser. This explains why the target thickness of $1.4 \times 10^{20}\,\mathrm{m}^{-2}$ requires a gas inlet flow rate of $48\,\mathrm{Pa\,m^3\,s^{-1}}$ ($Q = 14.6\,\mathrm{Pa\,m^3\,s^{-1}}$ for the same gas target thickness for the ITER gas neutraliser [57]).

The SHT model predicting a high degree of ionisation χ, a higher maximum ζ of 80 % is obtained for a lower Q of $7\,\mathrm{Pa\,m^3\,s^{-1}}$. Due to electron–ion recombination, the revised model predicts a lower χ leading to a lower maximum ζ of 68 % for a higher gas throughput of $26\,\mathrm{Pa\,m^3\,s^{-1}}$. A geometrical optimisation of the BDPN and the inclusion of elongated slits outside the cusp-confined volume, as depicted in figure 4.4, could reduce the required gas inflow rate.

The maximum ζ of 68 % is achieved for $\chi = 8.0\,\%$. The BDPN model does

Table 4.6: Total kinetic power of the products of the energy transferring processes and the corresponding fraction that they pass on as heating power to the gas molecules via elastic collisions. The numbers refer to the BDPN plasma generated by an ITER-like beam. Table reprinted from [55] under the terms of the Creative Commons Attribution 3.0 licence.

Energy transferring process	Kinetic power [W]	Heating power [W]
Gas dissociation by		
beam ions	21	17
stripped electrons	260	210
Rudd electrons	9.8	8.0
plasma electrons	720	580
Plasma ion reflection	76	67

not take the gas depletion due to plasma formation into account. However, the value of χ is sufficiently low to neglect it.

All the outputs of the revised model are given in table 4.7 for the optimum value of Q.

The revised model gives also an estimate of the background gas temperature increase. Surrey applied Paméla's gas heating model to the ITER gas neutraliser [85] and showed that the beam-driven dissociation is the most important gas heating mechanism. The predicted gas temperature is only 100 K above wall temperature. The situation is different for the BDPN due to the confinement of high electron densities. Table 4.6 reports for each of the considered gas heating processes the total kinetic power of the dissociation products or energetic neutrals and the corresponding fraction that they transfer to the gas molecules via elastic collisions.

It turns out that, due to the high plasma density predicted by the BDPN model, gas dissociation by plasma electrons is the dominant heating mechanism. A neutral gas temperature of 520 K is estimated. A higher gas temperature demands a higher gas inlet flow rate to achieve the same target thickness. Therefore, according to the temperature dependence of Q given by equations (4.10), (4.11) and (4.12), the optimum gas inflow of 26 $\mathrm{Pa\,m^3\,s^{-1}}$ at 300 K corresponds to a value of 60 $\mathrm{Pa\,m^3\,s^{-1}}$ at 520 K. In this work, however, Q is always referred to a gas temperature of 300 K for comparison purposes.

The energy transfer from the dissociation products and reflected neutrals to the gas molecules depends on the mean travel distance of the impacting particles which is given by equation (4.44). However, the simple approach used to estimate d_{m} may underestimate the travel distance, especially for the charged dissociation fragments, and hence the energy transfer. Therefore, the gas temperature is also calculated for the limiting case $d_{\mathrm{m}} \to +\infty$, i.e. assuming that the heating powers of table 4.6 are equal to the kinetic powers of the impacting particles (see equation (4.43)). The result is a gas temperature of 560 K which is only 8 % higher than the gas temperature estimated for a mean travel distance d_{m} given by equation (4.44).

4.3.5 The BDPN proof-of-principle experiment

Although the beam-driven plasma neutraliser promises a higher neutralisation efficiency than the gas neutraliser, its feasibility has never been proved on a real NNBI beamline. The better performance has just been predicted through analytical models that need to be benchmarked. Therefore, before considering a BDPN-based DEMO NBI, a suitable proof-of-principle experiment is required to demonstrate the concept. The ideal situation is a system whose dimensions and operating parameters are as close as possible to those foreseen for the DEMO NBI. Due to the fact that the baseline DEMO-1 is a conservative reactor configuration that is very close to ITER, the DEMO injector could be approximated by an ITER-like NBI. It follows that the BDPN proof-of-principle experiment should envisage the neutralisation of a 1 MeV, 40 A D^{-} ion beam in a chamber of similar dimensions to those of the gas neutraliser, as assumed in table 4.3. This set of parameters is referred to as ITER-like BDPN. MITICA [88] would be the only test facility to be able to generate such a high-energy negative ion beam, but it has not yet come into operation and its primary objective is the test of the whole ITER NBI beamline when it does. Hence, a full-scale BDPN test on this facility is not possible in the near future.

Existing smaller-scale test facilities have to be considered, being aware that an extrapolation of the experimental results to the DEMO-scale will then be required. The fact that these smaller facilities have lower ion beam energies makes it useful to distinguish two different objectives for a possible experiment:

(i) to prove that the beam-driven mechanism can generate a plasma density and a degree of ionisation sufficient to significantly enhance the neutralisation efficiency;

(ii) to prove that a plasma of sufficient density and degree of ionisation can effectively increase the neutralisation efficiency as predicted.

Objective (i) is the core of the proof-of-principle experiment as it concerns the effectiveness of the beam-driven mechanism and of the magnetic cusp confinement in producing a sufficiently high plasma density. In this regard, the experiment should benchmark the model predictions, give confidence in their extrapolation to a DEMO-sized system and suggest improvements.

Concerning objective (ii), the starting point is a plasma of a certain density and ionisation degree. Therefore, it does not necessarily have to be produced by the ion beam, but it could as well be driven externally. Objective (ii) is not meant to be a demonstration of the neutralisation efficiency increase in presence of a plasma, also because this was already experimentally proved by Hanada et al. [60] for a 200 keV H^- ion beam (equivalent to a beam of 400 keV D^- ions). The purpose is to benchmark the enhancement of the neutralisation efficiency predicted by model for a 1 MeV deuterium ion beam or, in other words, to benchmark the cross section values of the reactions between plasma particles and 1 MeV D^- ions. The values of many of these cross sections, indeed, are not available in the literature for this energy range or for the deuterium isotope and, hence, an extrapolation is required. Furthermore, there are cases in which they are predicted from theoretical models. Although not investigated in this work, the cross section values are one of the major sources of uncertainty

in the model. Hence, the topic must be addressed in future, also through a proper experimental campaign. It is clear, however, that the use of ion beams of energy lower than 1 MeV would not give any information in the reference energy range and, therefore, would not help in reaching objective (ii).
In conclusion, objective (i) is the only driver in the design a BDPN proof-of-principle experiment with low-energy ion beams. The increase of the neutralisation efficiency with respect to an only-gas target is not of primary concern for the aforementioned reasons but, if measurable, it can be considered an added value and a valid criterion to make a choice among different experimental options.

Required diagnostics

Scanning as many BDPN model parameters as possible is fundamental for the experimental validation of the model. To this end, the main quantities to be measured are:

- plasma density through Langmuir probes;
- gas temperature via optical emission spectroscopy;
- gas flow through a flow controller and pressure gauges;
- neutralisation efficiency, if its increase is significant, by means of a residual ion dump that would deflect the residual ions in the beam after the neutralisation;
- ion species composition of the plasma via ion mass spectrometry.

Considered NBI test-bed beamlines

NBI test-bed beamlines that already exist and are at European research units who contribute (or did so in the past) to EUROfusion tasks are primarily considered to carry out a BDPN proof-of-principle experiment:

- the negative ion source test facilities BATMAN Upgrade [89], ELISE [90], SNIF [91] and NIO1 [92];
- the positive NBI system of ASDEX Upgrade (AUG) [93].

BATMAN Upgrade (BUG) is a test facility with a negative ion RF-driven source at the Max Planck Institute for Plasma Physics (IPP) Garching [89] which is 1/8 of the ITER NBI source size. Operation both in hydrogen and deuterium is possible and the beam can be accelerated up to 50 keV. BUG is used to achieve a better physics understanding of the negative ion production and extraction and to improve the RF efficiency and the beam properties.

ELISE at IPP Garching [90] has a negative ion RF-driven source that is half the size of the ITER NBI source, with almost the same width and half the height. Hence, ELISE is the intermediate step between BUG and the full-scale ITER source and its main objective is the demonstration of negative ion beam formation in large RF sources with the beam properties satisfying the ITER requirements. Beams of H^- or D^- can be formed and accelerated up to 60 keV.

SNIF was built at the Culham Centre for Fusion Energy (CCFE) to study and improve the negative ion beam production and transport [91]. The RF-driven ion source produces a negative hydrogen beam of 30 keV energy which is extracted through a single aperture. The small dimensions represent the main advantage of SNIF as they allow for small and quick modifications of the system. SNIF is the test facility suggested by Turner and Holmes for a BDPN feasibility test [13].

NIO1 is a small and flexible RF-driven ion source test facility, constructed at Consorzio RFX [92]. A 60 keV, 130 mA H^- ion beam is accelerated through a square lattice of 3×3 apertures.

ASDEX Upgrade, the medium-size tokamak operated at IPP Garching [93], has a positive HNB injector which is also taken into consideration to investigate the beam-driven plasma production by positive ions. The AUG ion source operates at 55 kV, 75 A in hydrogen.

The performance of a BDPN installed on the considered test-bed beamlines is predicted with the BDPN analytical model. The input parameters as well as the modelling results are given in table 4.7. The neutraliser cross section is based on the plasma grid (PG) dimensions. As the magnetic confinement of the neutraliser extremities requires an odd number of magnet columns, if the central columns intercept the ion beam, a certain number of PG apertures is masked to allow for the magnet bar positioning. A lower number of apertures results in a lower beam current. This explains why the current input in table 4.7 is sometimes lower than the nominal value.

The vacuum vessel pressure for the small-scale test facilities is given by the pumping speed S_{pump} installed on the beamline as

$$p_{\mathrm{amb}} = \frac{Q}{S_{\mathrm{pump}}}. \tag{4.50}$$

The model predictions for the ITER-like BDPN, already discussed in section 4.3.4, are given for the optimum gas density. This is not the case for the low-energy beamlines for which the model results are listed for the optimum gas density of the ITER-like case. This choice depends on the following considerations: firstly, if the beam energy is lower than 50 keV/amu, the neutralisation of both positive and negative ions depends on the balance between ionisation and charge exchange rather than stripping. Secondly, the ion beams are not powerful enough and produce ionisation degrees lower than 1 %. Consequently, the increase of the neutralisation efficiency ζ is negligible and ζ is almost equal to the neutralisation efficiency ζ_{gas} obtained with a target of only gas of the same thickness. This is shown in table 4.8 which for each of the considered test facilities gives the model results for the gas density that maximises the neutralisation efficiency (ζ_{max}).

As demonstrating the neutralisation efficiency increase is not the primary objective of the proof-of-principle experiment, one could think of showing the model results for the gas density that maximises the ionisation degree. Fig-

Table 4.7: Main input parameters and results of the BDPN model applied to several test facilities and to a filament-driven plasma source. The results are shown for the mean gas density that maximises the neutralisation efficiency ζ of the ITER-like case. The fractions of the D^+, D_2^+ and D_3^+ plasma ions are indicated with c_1, c_2 and c_3, respectively. The neutralisation efficiency ζ_{gas} is obtained with a target of only gas of the same thickness as that of the total target at which ζ is achieved. Table reprinted from [55] under the terms of the Creative Commons Attribution 3.0 licence.

	ITER-like	SNIF	BUG	ELISE	NIO1	AUG	Filament-driven
Inputs							
Isotope	D	H	H	H	H	H	D
I_{beam} [A]	40	0.060	2.0	20	0.063	75	-
E_{beam} [keV]	1000	30	50	60	60	55	-
L_{neut} [m]	3.1	0.50	1.0	1.0	1.0	1.0	3.1
H_{neut} [m]	2.0	0.48	0.61	1.2	0.20	0.87	2.0
W_{neut} [m]	1.1	0.40	0.43	1.1	0.20	0.59	1.1
S_{pump} [m^3/s]	-	1.0	120	700	8.0	500	-
V_{plasma} [m^3]	4.1	0.041	0.040	0.65	0.0030	0.16	4.1
Outputs							
E_{stripped} [eV]	272	16	27	33	33	30	272
I_{S} [A]	42	0.043	2.0	19	0.058	3.6	42
I_{R} [A]	17	0.012	0.86	8.7	0.027	36	-
n_{plasma} [$10^{17}\,\text{m}^{-3}$]	21	0.043	0.84	1.4	0.42	13	18
c_1 [%]	99.87	0.38	18.73	75.74	4.16	98.30	99.80
c_2 [%]	0.08	1.09	5.58	2.34	5.99	0.89	0.11
c_3 [%]	0.05	98.53	75.69	21.92	89.85	0.81	0.09
χ [%]	8.0	0.018	0.34	0.59	0.17	5.1	6.7
ζ (%)	68	56	65	63	62	26	-
ζ_{gas} (%)	48	56	64	61	61	26	-
T_{e} [eV]	1.1	0.46	1.2	1.3	0.42	1.8	1.0
$\bar{n}_{\text{gas}}$ [$10^{19}\,\text{m}^{-3}$]	2.4	2.4	2.4	2.4	2.4	2.4	2.4
A_{loss} [cm^2]	450	61	59	120	26	77	540
A_{cathode} [cm^2]	-	-	-	-	-	-	110
T_{gas} [K]	520	300	310	350	300	560	470

Table 4.8: Main results of the BDPN model applied to several test facilities. The input parameters are listed in table 4.7. In each case, the results are shown for the maximum neutralisation efficiency ζ_{max}. The fractions of the D^+, D_2^+ and D_3^+ plasma ions are indicated with c_1, c_2 and c_3, respectively. The neutralisation efficiency ζ_{gas} is obtained with a target of only gas of the same thickness as that of the total target at which ζ_{max} is achieved.

	ITER-like	SNIF	BUG	ELISE	NIO1	AUG
Outputs						
E_{stripped} [eV]	272	16	27	33	33	30
I_S [A]	42	0.086	2.5	24	0.077	48
I_R [A]	17	0.043	1.3	14	0.045	170
n_{plasma} [$10^{17}\,\text{m}^{-3}$]	21	0.12	1.1	1.8	0.58	71
c_1 [%]	99.87	0.33	17.33	76.01	3.37	99.71
c_2 [%]	0.08	0.40	4.31	1.77	4.24	0.14
c_3 [%]	0.05	99.27	78.36	22.22	92.39	0.15
χ [%]	8.0	0.012	0.27	0.46	0.14	5.4
ζ_{max} (%)	68	77	69	67	66	51
ζ_{gas} (%)	48	77	69	66	66	52
T_e [eV]	1.1	0.46	1.2	1.2	0.44	1.3
$\bar{n}_{\text{gas}}$ [$10^{19}\,\text{m}^{-3}$]	2.4	9.3	3.9	4.0	4.2	12
A_{loss} [cm^2]	450	61	58	120	26	66
T_{gas} [K]	520	300	310	350	300	780

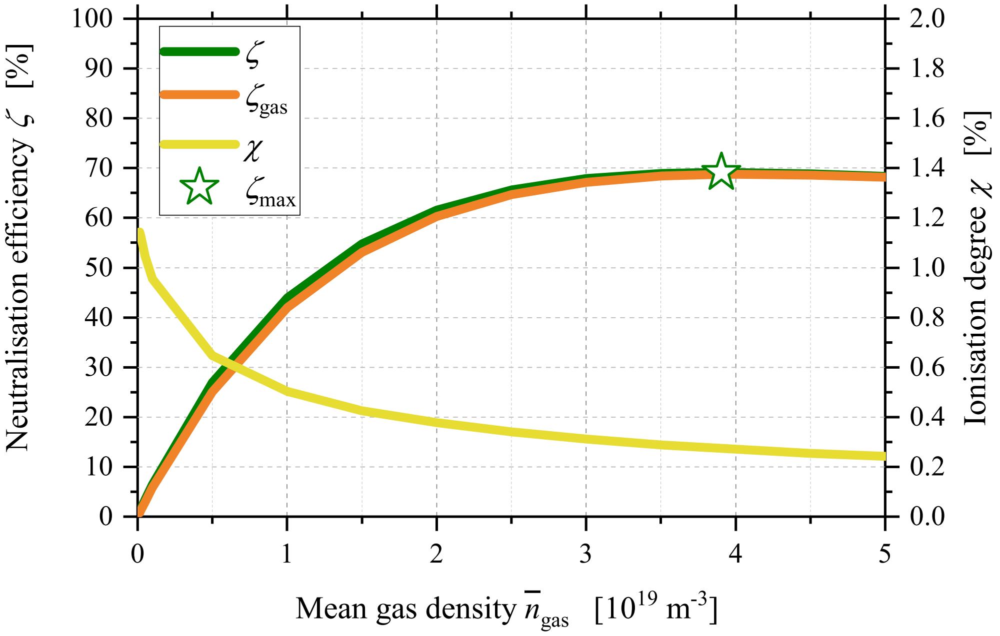

Figure 4.11: Results of the BDPN model applied to the BUG test facility, plotted as functions of the mean gas density. ζ is the neutralisation efficiency, ζ_{gas} is the neutralisation efficiency obtained with a target of only gas of the same thickness as that of the total target at which ζ is achieved, χ is the degree of ionisation (plotted on the right axis). The maximum value of ζ, called ζ_{max}, is indicated with a star.

ure 4.11 shows ζ, ζ_{gas} and the ionisation degree χ predicted by the BDPN model as functions of the mean gas density in the case of BUG. The difference between ζ and ζ_{gas} is always negligible. Lowering the gas density leads to an increase of the ionisation degree but, correspondingly, not only is ζ much lower than its maximum value ζ_{max}, but χ is still very low, around 1 %.

In summary, as a preferred operative point is not present, it has been decided to compare the model results of all test facilities in table 4.7 at the optimum gas density of the ITER-like case. These are the model predictions that will be discussed.

The case of SNIF is particularly interesting as the impact of the modifications introduced into the BDPN model is evident. The stripped electron energy of 16 eV is just above the hydrogen ionisation threshold, approximately equal to 15 eV [71]. As the slowing-down energy distribution of the stripped electrons does not extend beyond their birth energy, the induced secondary ionisation and, hence, the plasma generation, are negligible. Indeed, the predicted degree of ionisation is only 0.018 %. This would not be the case if the SHT model was applied due to the assumption of Maxwellian fast electrons and to the fact that electron–ion recombination is neglected: the SHT model predicts an ionisation degree of around 19 % for the optimum target thickness.

Having a similar beam energy, which means fast electrons of similar energy, BUG, ELISE and NIO1 show comparable results: the energy of the stripped electrons, which contribute the most to generate the plasma, is sufficiently above the gas ionisation threshold to produce a plasma density of the order of $10^{17}\,\mathrm{m}^{-3}$. However, the degree of ionisation is lower than 1 %, determining a marginal improvement of the neutralisation efficiency that would be hard to measure experimentally. The slightly better results of ELISE are due to a high beam current. Although both BUG and ELISE can operate also in deuterium, only hydrogen beams have been considered as deuterium operation would have the same issue as in SNIF, i.e. a stripped electron energy below for BUG and slightly above for ELISE the ionisation threshold of D_2 molecules.

The model results for the AUG positive ion beam highlight that the mechanism of plasma generation by positive ions is different: as no electron can be stripped from positive ions, the neutral gas ionisation is entirely due to the Rudd electrons which, therefore, play the major role in forming the plasma. The current I_S is not zero due to the electrons coming from the re-ionisation of the produced neutrals, yet it is very small. Given a high beam current of 75 A, the background gas is significantly ionised: the plasma density is of the order of $10^{18}\,\mathrm{m}^{-3}$ and the ionisation degree is 5.1 %. Nevertheless, the neutralisation efficiency does not increase with respect to the value predicted for a gas target of the same thickness: while the plasma electrons and ions increase the stripping-to-re-ionisation ratio for the negative ions, they do not enhance the conversion of positive ions into neutrals.

The main conclusion from the results of table 4.7 is that none of the considered small-scale negative ion test facilities would be able to produce an appreciable degree of ionisation of the neutral gas by the beam-driven mechanism, essentially because of the low beam power. The use of these beamlines for a proof-of-principle experiment would make it difficult not only to benchmark the analytical BPDN model but also and above all to extrapolate the results to a DEMO-scale system, even without taking the beam neutralisation into account. A positive NBI does not represent a valid alternative either, as the plasma is generated in a different way than what is expected for a negative ion beam. Therefore, underlying again that the core mission of the proof-of-principle experiment is about the plasma formation and confinement and not the neutralisation of the negative ions, a dedicated experiment is proposed where no ion beam is involved.

The filament-driven plasma source

The BDPN plasma is mostly generated by the ionisation of the background gas by the stripped electrons which, in turn, largely come from the stripping of the beam negative ions. However, as suggested by Surrey and Holmes [12], they could equivalently be produced by means of filaments, like in an arc-driven ion source. The main advantage of this solution is straightforward: the filaments can be biased to obtain electrons of the same energy as that of the stripped electrons in the ITER-like case, i.e. approximately 272 eV, allowing for a significant and very similar degree of ionisation. This implies that the Rudd electrons would be neglected, but it has previously been shown that, for plasmas driven by negative ion beams, the Rudd electrons are less important, both because produced in a lower quantity and because on average far less energetic. A second advantage is that a neutraliser chamber with the same dimensions and the same permanent magnet arrangement as those envisaged for the ITER-like BDPN can be tested, thus eliminating any need for extrapolating the results.

A drawback, however, is given by the cathode losses due to the plasma ions that are accelerated towards and lost at the filament surfaces, subsequently decreasing the achievable plasma density. Between the cathode filaments and the neutraliser plasma a double sheath is formed in which ions and electrons are accelerated in opposite directions [94]. Determining the double sheath thickness is required to estimate the effective cathode loss area for the plasma ions. A double sheath thickness t_{DS} of 1 mm is assumed [95]. The effective cathode area can then be calculated as

$$A_{\mathrm{cathode}} = N_{\mathrm{fil}}\, 2\pi (R_{\mathrm{fil}} + t_{\mathrm{DS}}) L_{\mathrm{fil}}, \tag{4.51}$$

where N_{fil}, R_{fil} and L_{fil} are the number, radius and length of the filaments, respectively. Equation (4.51) implicitly assumes that the grounded or floating filament supports do not extend into the cusp-confined region of the BDPN chamber as, otherwise, they would increase the loss surface. With filaments of length $L_{\mathrm{fil}} = 160\,\mathrm{mm}$ and radius $R_{\mathrm{fil}} = 0.75\,\mathrm{mm}$ and with the assumption of an electron emission limited by Child-Langmuir's space-charge law, the stripped electron current I_{S} for an ITER-like beam could be reproduced by means of at least 6 filaments. One can trade off filament number for increased filament length, but this choice as well as the filament placement are left to a detailed design study.

The loss of plasma ions at the cathode surface is taken into account in the BDPN model by substituting the effective loss area of equation (4.35) with a total effective loss area:

$$A_{\mathrm{loss}} = A_{\mathrm{anode}} + A_{\mathrm{cathode}}, \tag{4.52}$$

where A_{anode} is the effective anodic wall loss area of equation (4.35) and A_{cathode} is defined in equation (4.51).

The filament-driven plasma properties are predicted by the BDPN analytical model for a chamber with the same dimensions and the same arrangement of permanent magnets on the walls as those of the ITER-like BDPN. The model results are given in table 4.7 for a gas density equal to the optimum gas density of the ITER-like case. Figure 4.12 compares the model predictions for the ITER-like reference case with those for the filament-driven plasma. For all the plotted plasma parameters, the predictions are very close in the considered range of inlet gas flow rates.

Hence, the filament-driven plasma source turns out to be a valid option for a proof-of-principle experiment. This also confirms that the stripped electrons play the major role in the plasma generation. Furthermore, one can deduce that the loss of plasma ions at the cathode surface does not drastically reduce the plasma density.

The latter observation, however, is based on the assumption of a double sheath thickness of 1 mm which determines an effective cathode loss area that is around 20 % of the total loss area. In order to investigate the impact of a double sheath thicker than expected, figure 4.13 plots the plasma density as a function of the gas inflow for increasing values of the effective cathode area, with A being the cathode area calculated by assuming $t_{\mathrm{DS}} = 1\,\mathrm{mm}$. Even if

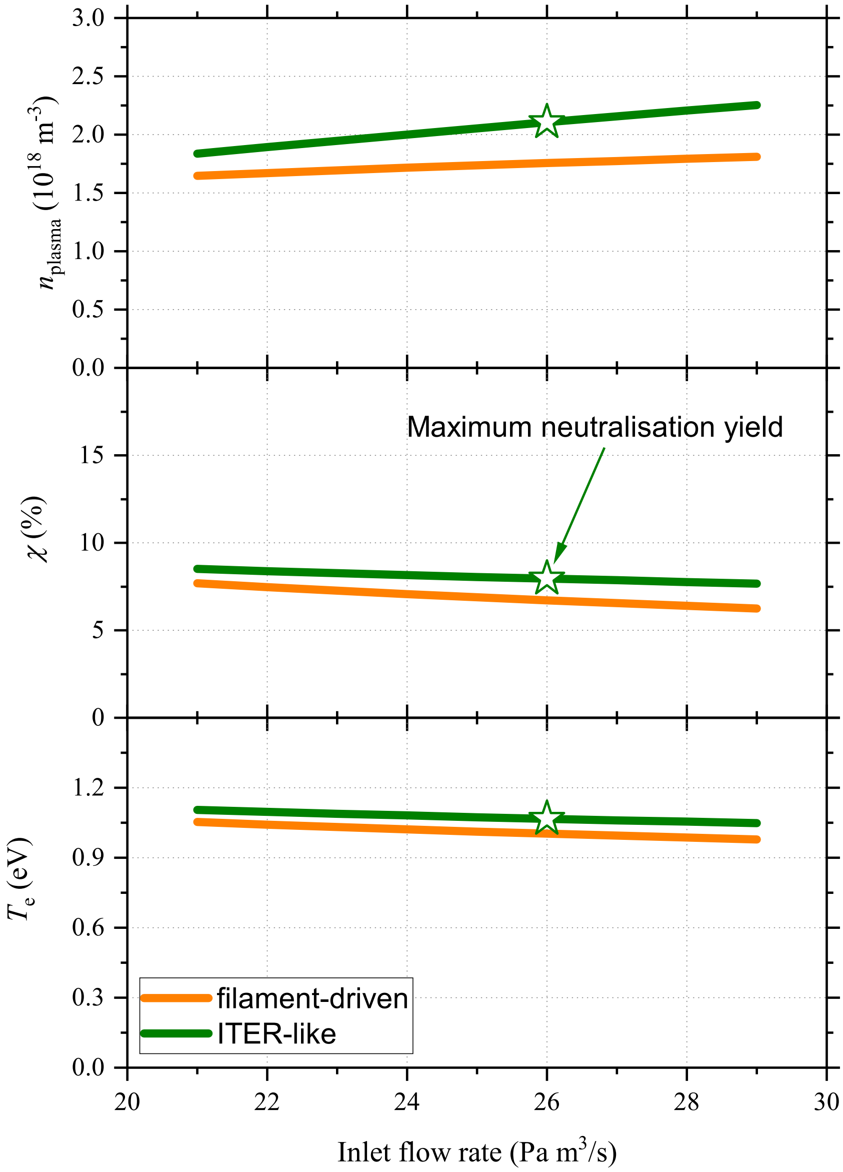

Figure 4.12: Comparison of the model predictions between the filament-driven plasma source and the ITER-like BDPN. The plasma density n_{plasma}, the degree of ionisation χ and the plasma electron temperature T_{e} are plotted as functions of the inlet gas flow rate Q at 300 K. A green star indicates the optimum gas inflow for the ITER-like BDPN. Picture reprinted from [55] under the terms of the Creative Commons Attribution 3.0 licence.

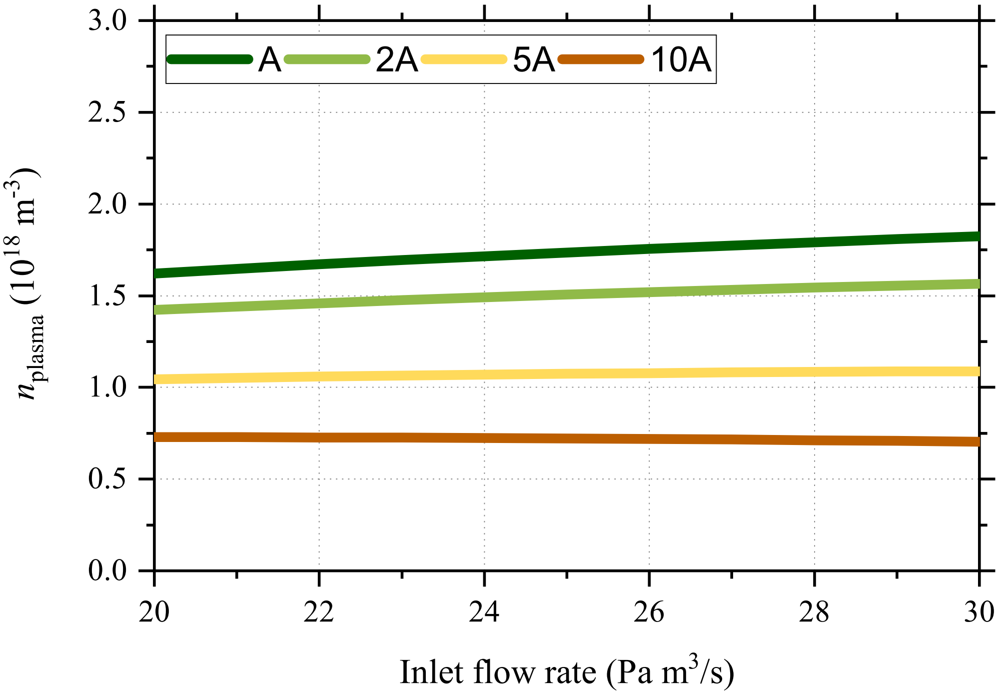

Figure 4.13: Plasma density of a filament-driven plasma source for increasing values of the effective cathode area. $A = 110\,\text{cm}^2$ is the effective cathode area for $t_{\text{DS}} = 1\,\text{mm}$. Picture reprinted from [55] under the terms of the Creative Commons Attribution 3.0 licence.

the effective cathode loss area is 10 times bigger, the plasma density reduction is given by a factor slightly higher than two. Therefore, the cathode losses, even if underestimated, do not prevent the filament-driven plasma source to be considered a good candidate for a BDPN proof-of-principle experiment.

The filament-driven concept provides also a certain degree of flexibility: one could consider downscaling the chamber in one, two or three dimensions in case of cost or space constraints. The extrapolation to the full-size system would then be required.

The system dimensions have an impact on the ion species fractions in the plasma, as highlighted by Morishita et al. [96] for negative ion sources. Therefore, the filament-driven plasma formation process is simulated for three different chambers: in addition to the full-scale ITER-like BDPN chamber, a 1-m-cube chamber and a small box with a cross section of $0.2\,\text{m} \times 0.2\,\text{m}$ and a length of $1\,\text{m}$ are also modelled. The model results are listed in table 4.9.

While in an experiment one would scan as many experimental parameters as

Table 4.9: Main input parameters and results of the BDPN model applied to filament-driven plasma sources. Three chambers with different dimensions are considered. The fractions of the D^+, D_2^+ and D_3^+ plasma ions are indicated with c_1, c_2 and c_3, respectively. Table reprinted from [55] under the terms of the Creative Commons Attribution 3.0 licence.

	Filament-driven plasma sources		
Inputs			
Arc power [kW]	12	1.7	0.070
Arc voltage [V]	272	272	272
Arc current [A]	42	6.4	0.26
N_{fil}	6	1	1
L_{neut} [m]	3.1	1.0	1.0
H_{neut} [m]	2.0	1.0	0.2
W_{neut} [m]	1.1	1.0	0.2
V_{plasma} [m^3]	4.1	0.49	0.0025
Outputs			
n_{plasma} [$10^{17}\,\text{m}^{-3}$]	18	12	0.96
c_1 [%]	99.80	99.40	21.21
c_2 [%]	0.11	0.27	7.59
c_3 [%]	0.09	0.33	71.20
χ [%]	6.7	4.7	0.39
T_{e} [eV]	1.0	1.0	0.24
$\bar{n}_{\text{gas}}$ [$10^{19}\,\text{m}^{-3}$]	2.4	2.4	2.4
$A_{\text{loss,tot}}$ [cm^2]	540	120	39
A_{cathode} [cm^2]	110	18	18
T_{gas} [K]	470	360	300

possible, for the comparison of table 4.9 it is chosen to scale the arc power with the chamber volume in order to keep the emitted electron power density constant. The arc voltage is 272 V in all cases to produce electrons with the same energy as that of the stripped electrons in the ITER-like case. Hence, the arc power is scaled by modifying the arc current. In case of a negative ion beam, the choice of keeping the electron power density constant is equivalent to keeping the energy and current density of the ion beam constant while changing the beam cross section and neutraliser length. The same mean gas density as well as the same magnetic cusp fields $B_{\text{c,l}}$ of 0.8 T and $B_{\text{c,e}}$ of 0.5 T are assumed for all three configurations.

The properties of the plasma generated in the small chamber are very different from those in the larger chambers. In particular, the plasma in the small chamber is mainly composed of D_3^+ ions.

The species composition of the filament-driven plasma in the full-scale chamber can be explained by the following considerations: the D_2^+ ions are quickly dissociated into D^+ ions (reaction 4. in table 4.4) and converted into D_3^+ ions after colliding with the gas molecules (reaction 8. in table 4.4). Both D_2^+ and D_3^+ ions are effectively destroyed by dissociative recombination (reactions 6., 10. and 11. in table 4.4). The result is that D^+ is the dominant ion species. If the chamber size slightly decreases, as in the case of the 1 m-cube chamber, the volume processes of dissociation and recombination are less effective in destroying the molecular ions, leading to higher fractions.

This argument could in principle explain the plasma species composition also in the case of the small chamber. However, there are other parameters that influence the plasma ion species fractions and that are drastically modified when downscaling the system. Due to the complexity of the BDPN model, it is not straightforward to identify these dependencies and draw definitive conclusions.

In summary, not only does the downscaling of the proof-of-principle experiment require the extrapolation of the results to the full-scale system, but it can also strongly affect the plasma species composition for very small chambers.

4.4 Summary and conclusions

A revised analytical model that predicts the performance of the beam-driven plasma neutraliser (BDPN) has been developed on the basis of the model by Surrey and Holmes [12] and Turner and Holmes [13] (SHT model). The revised model predicts the neutralisation efficiency by computing the charge state evolution of the incoming negative ion beam due to the collisions with the background gas molecules and the plasma ions and electrons along the neutraliser length. The beam–gas collisions produce fast electrons either through stripping of the negative ions (stripped electrons) or through ionisation (Rudd electrons). Secondary ionisation of the neutral gas by stripped and Rudd electrons leads to a significant plasma production. The model computes the density and the species composition of the plasma through a comprehensive set of rate equations. The plasma electron temperature is given by a power balance. The confinement of the plasma ions and electrons, which is fundamental to the beam-driven formation of the plasma, is provided by a magnetic cusp field generated by permanent magnets and is included in the model through an effective loss area for the charged species of the plasma. Using the revised model to simulate the installation of a BDPN on several test facilities allows drawing the following conclusions:

- Slowing-down energy distributions are calculated for the stripped and Rudd electrons to replace the Maxwellian energy distributions assumed in the SHT model. For ion beam energies around 30 keV/amu, the birth energy of the stripped electrons, which chiefly drive the plasma formation, is similar to or even lower than the gas ionisation potential. In this case, as the slowing-down energy distributions do not have high-energy tails like the Maxwellian, a significant reduction of the secondary ionisation and, hence, of the predicted plasma density occurs.

- Dissociation of the gas molecules by electron impact is an important energy loss channel for the plasma electrons. When applying the revised model to the ITER-like reference case, the plasma electron temperature is correspondingly decreased by about a factor of two with respect to the SHT model output.

- The plasma density reduction due to the dissociative recombination of the molecular plasma ions with the electrons is taken into account by integrating a rate equation model that computes the species composition of the plasma into the main model. For the ITER-like reference case, it is predicted that the atomic ion D^+ is the dominant ion species in the BDPN plasma as the molecular ions D_2^+ and D_3^+ are almost completely destroyed by dissociative recombination. This leads to a plasma density that is about a factor of four lower than the SHT value. Consequently, while the SHT model predicts a maximum neutralisation efficiency ζ_{max} of 80 %, ζ_{max} is estimated as around 68 % by the revised model.

- Heating of the background gas due to the interactions with the ion beam and the plasma particles is evaluated by adapting Paméla's gas heating model [81, 82]. A gas temperature increase of around 220 K is predicted for the ITER-like reference case which determines, together with the absence of internal walls, an increase of the gas conductance with respect to the ITER gas neutraliser. This means that, despite a lower optimum gas target thickness, the BDPN requires a much higher inlet gas flow rate: $60\,\mathrm{Pa\,m^3\,s^{-1}}$ versus $14.6\,\mathrm{Pa\,m^3\,s^{-1}}$ for the ITER gas neutraliser. The gas inflow can be reduced by considering elongated slits at the neutraliser extremities to reduce the gas conductance.

One of the major sources of uncertainty in the model is the description of the magnetic cusp confinement through an effective loss area for the plasma ions and electrons which is simplistically calculated as four times the product between the total cusp line length and the hybrid gyroradius of the plasma particles. It is likely that such a description would underestimate the plasma leakage through the magnetic cusps, but reliable expressions that are able to estimate the plasma losses for different plasma parameters and at any degree of magnetisation are not available. These expressions would also need to capture the 3D details of the magnetic confinement, while being simultaneously suitable for the inclusion in a model that is fundamentally zero-dimensional. The effective cusp confinement predicted by the model is such that a plasma density of $2.1\times10^{18}\,\mathrm{m^{-3}}$ is estimated with a power deposited by the ITER-like beam of only 13 kW. In comparison, NBI ion sources whose volume is much smaller than that of the BDPN require powers higher than 100 kW to achieve similar plasma densities.

Other important uncertainty sources are the cross section values and the fact that the model is sensitive to the kinetic energy distribution of the plasma atomic ions D^+. Therefore, an experiment is necessary to benchmark the analytical predictions and to validate the concept feasibility. The model, however, is used to identify the proof-of-principle experiment that is most suitable to this purpose. As a full-scale ITER- or DEMO-like BDPN test, with a 1 MeV, 40 A negative deuterium ion beam, is not possible in the near future, alternatives have to be found.

Existing NNBI test-bed beamlines, like BUG, ELISE, SNIF and NIO1, have been considered. However, due to the low beam power, with a beam ion energy in the range 30–60 keV/amu, the predicted degree of ionisation of the neutral gas by the beam-driven mechanism is always smaller than 1 %. Consequently, the increase of the neutralisation yield with respect to a target of only gas is very small and experimentally hard to quantify. Thus, using ion beams with such a low energy would make it very difficult to extrapolate the results to the DEMO-scale. In particular, it would not give any useful information about the neutralisation efficiency increase for a 1 MeV D^- ion beam, i.e. about the cross section values of the reactions between 1 MeV D^- ions and plasma ions and electrons. These values are extrapolated from experimental data available for lower energies or derived from theoretical models.

Therefore, it is suggested to drop the objective of demonstrating the enhancement of the neutralisation efficiency predicted by the model, as it requires an ion beam energy around 1 MeV, and to focus only on validating the confinement of the plasma generated via the beam-driven mechanism. To this end, a dedicated experiment is proposed in which no ion beam is involved: the stripped electrons, which are the main driver in generating the BDPN plasma, can be simulated by electrons emitted by heated and negatively biased filament, similarly to an arc-driven ion source. One can set the filament heating current and bias voltage in order to get electrons with the same current and energy as those of the ITER-like stripped electrons. The chamber dimensions and the permanent magnets layout would be as close as possible to the envisaged design for DEMO such that no result extrapolation is needed. The BDPN model is modified to account for the additional loss area for the plasma ions due to the filament surface and is applied to this system: it predicts that the plasma parameters are very close to those of the full-scale ITER-like BDPN. The filament-driven plasma source, therefore, is considered a valid option for a proof-of-principle experiment of the BDPN. It also provides a certain degree of flexibility as one can downscaling the chamber dimensions without drastically changing the plasma species composition, unless the considered chamber is very small. A cubic chamber of 1 m side length appears to be a reasonable economical compromise for an experiment. In any case, however, the extrapolation of the results to the full-scale system is then required.

In a filament-driven plasma experiment, the arc current and bias voltage as well as all changeable parameters would not be fixed at the values that have been listed in the tables of this chapter for comparison purposes, but they would be scanned over the widest range possible. This allows, for instance, producing electrons with an energy higher than 272 eV corresponding to electrons stripped from D^- ions of energy higher than 1 MeV. This is a significant advantage with respect to a hypothetical beam-driven plasma experiment.

The detailed design of the proof-of-principle experiment is outside the scope of this work. The most important aspects that the design should address are: the permanent magnet arrangement and their mounting on the chamber walls, the gas pressure distribution and the effect of the inclusion of elongated slits at both ends of the neutraliser, filament characteristics and their installation in the chamber, access of the diagnostic systems to the cusp-confined volume. In addition to providing a benchmark for the analytical predictions, the experimental data should help improving the model and give confidence in the extrapolation of the results to the DEMO-scale, if an extrapolation is required.

They should also support the optimisation design study of the DEMO BDPN as the proposed design of section 4.3.1 has been simply used as visual aid to show the arrangement of the permanent magnets and as reference for the presentation of the analytical model.

Chapter 5

Energy recovery

The aim of this chapter is a conceptual design of an energy recovery system (ERS) that could be implemented on a high-energy negative-ion-based NBI with the primary objective of increasing the wall-plug efficiency of the injector.

5.1 Working principle of energy recovery

As described in section 3.3, the NBI wall-plug efficiency is defined as

$$\eta_{\mathrm{wp}} = \frac{P_{\mathrm{NBI}}}{P_{\mathrm{el}}}, \tag{5.1}$$

where P_{NBI} is the neutral beam power injected into the tokamak and P_{el} is the electrical power used to operate the injector.

Improving the neutralisation efficiency of high-energy negative ions with respect to the value achieved by gas neutralisation, which is foreseen for the ITER NBI, leads to the increase of the neutral beam power P_{NBI} and, hence, of the wall-plug efficiency η_{wp} for future fusion reactors.

An alternative way to enhance η_{wp} is to reduce the electrical power P_{el}. This can be achieved through energy recovery (ER): the kinetic energy of the non-neutralised beam ions emerging from the neutraliser is converted back into electrical energy via electrostatic deceleration. The positive and negative re-

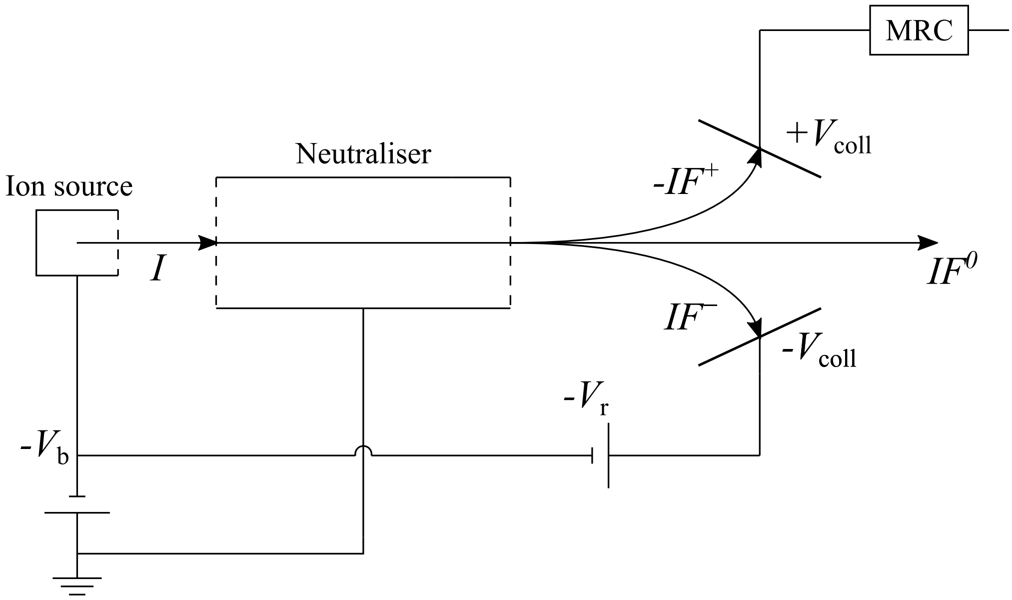

Figure 5.1: Electric schematic of the energy recovery concept. Positive currents have a negative sign.

sidual ions are first separated by an electric or magnetic field and then electrostatically decelerated in order to collect them on a lower-voltage electrode. The corresponding current is then recirculated in the system.

The ER basic principle is schematically shown in figure 5.1.

A negative ion beam of current I is extracted from the ion source at the negative potential $-V_{\mathrm{b}}$, with $V_{\mathrm{b}} > 0$. The potential difference between the grounded grid of the accelerator and the ion source accelerates the negative ions up to the energy eV_{b}. The neutralisation process inside the neutraliser, which is grounded, produces neutral, positive and negative particles with fractions F^0, F^+ and F^-, respectively. The current of neutrals IF^0 is injected into the tokamak, while the residual positive and negative ions at the neutraliser exit are deflected into different directions and decelerated to a collector. In order to ensure that all ions hit the collector, as their trajectories are not perpendicular to the equipotential surfaces of the decelerating electric field, the ions are not decelerated down to zero energy, but to a residual energy eV_{r}, with $V_{\mathrm{r}} > 0$. Hence, the collector voltage is $|V_{\mathrm{coll}}| = V_{\mathrm{b}} - V_{\mathrm{r}}$. The negative ion collector can be directly connected to the ion source potential if a bias V_{r} is provided by a small power supply. The negative ions are collected at the potential $-V_{\mathrm{coll}}$ with an efficiency g^- and circulated through the recovery power supply $-V_{\mathrm{r}}$. This leads to a direct reduction of the current I drained from the high-voltage power supply, with the reduction being equal to the negative ion current IF^-g^-. The recovery of the positive ion energy requires an additional step as the collector is biased at the positive potential $+V_{\mathrm{coll}}$ and, thus, cannot be connected to the ion source power supply. The energy of the positive ions can be converted into useful electrical power by means of modular resonant converters (MRCs) that have been developed for this purpose [97, 98]. The MRC conversion efficiency is indicated with μ. The positive ions are collected at the potential $+V_{\mathrm{coll}}$ with an efficiency g^+. In the scheme of figure 5.1, positive currents have a negative sign.

In case of no energy recovery and neglecting the power consumption of other auxiliary systems in the injector,

$$P_{\mathrm{el}} = IV_{\mathrm{b}}. \tag{5.2}$$

An energy recovery system (ERS) would reduce the electrical power as

$$\begin{aligned} P_{\mathrm{el}} = {} & \text{power effectively delivered by the high-voltage power supply} \\ & + \text{power delivered by the recovery power supply at the potential } -V_{\mathrm{r}} \\ & - \text{power output of the MRCs which is recirculated in the system.} \end{aligned} \tag{5.3}$$

Hence, using the notation of figure 5.1,

$$P_{\mathrm{el}} = IV_{\mathrm{b}}(1 - F^-g^-) + IF^-g^-V_{\mathrm{r}} - IF^+g^+(V_{\mathrm{b}} - V_{\mathrm{r}})\mu. \tag{5.4}$$

An example is made for the ITER NBI with $V_{\mathrm{b}} = 1\,\mathrm{MV}$ and $I = 40\,\mathrm{A}$. At the exit of the gas neutraliser, $F^0 = 0.55$, $F^+ = 0.26$ and $F^- = 0.19$ for the optimum gas target thickness. It is assumed $g^- = g^+ = 0.9$, $V_{\mathrm{r}} = 50\,\mathrm{kV}$ and

$\mu = 0.81$ [97–99]. The required power is reduced by around 34 % corresponding to an improvement of the NBI wall-plug efficiency of around 52 %.

The ERS would substitute the electrostatic residual ion dump (ERID) that is currently foreseen for the ITER NBI [14]. Even if their energy is not recovered, the residual ions must be removed from the neutral beam to prevent them from being deflected against the beamline components and the duct walls by the stray magnetic field from the reactor as that would result in unacceptably high local power loads. The residual ion removal on ITER is obtained electrostatically, although it is also common technology to use magnetic deflection: the ERID is formed by 4 channels, in line with those of the neutraliser, and a potential difference is applied across each channel by biasing at $-20\,\mathrm{kV}$ the second and fourth wall panels. Therefore, the ions are deflected left or right depending on their charge, while the neutrals continue undisturbed towards the tokamak. The ions are dumped at full energy onto the water-cooled wall panels. The estimated peak power load is $> 8\,\mathrm{MW\,m^{-2}}$ [14]. Although this value is acceptable from a thermo-mechanical point of view and the panels are specifically designed for this task, the high power loads on the ERID panels still remain a critical issue. Implementing an ERS on the HNB injector would have the additional advantage of strongly reducing the residual ion power that has to be dumped.

5.2 ER experimental tests

An ERS for positive-ion-based beamlines was experimentally tested [100–102]. For H, D and He beams of positive ions with energy up to 100 keV and extracted current up to 35 A, a recovery of more than 90 % of the full-energy residual ions was demonstrated. The recovery voltage V_r ranged from 5 % to 10 % of the beam acceleration potential. Specially developed electrodes were used to suppress the secondary electrons that come from the neutraliser plasma, are produced by background gas ionisation and/or are emitted by the system surfaces due to residual ion impacts. If not trapped, these electrons would be accelerated towards the collector by the same electric field that decelerates the positive ions, hence cancelling the benefits of energy recovery. A secondary electron trapping efficiency of 70 % was measured.

Unlike in the case of positive ions, the neutralisation of negative ions produces residual charged particles of both polarities. The conceptual study of an ERS for negative-ion-based NBIs, in which the residual ions are electrostatically separated, was presented by Paméla et al. [99]. Only the kinetic energy of the residual negative ions is recovered, while the positive ions are dumped at full energy. For a 1 MeV deuterium ion beam, an ERS power efficiency of about 90 % is estimated, leading to an injector cost reduction of 15 %. Two main requirements for an efficient ERS are highlighted: the suppression of the secondary electrons emitted from the recovery collector and a low gas pressure in the system to reduce beam-gas deleterious interactions, in particular the stripping of the residual negative ions that would reduce the recovered ion current and produce additional electrons. An ER experiment with a 100 keV, 1.2 A D^- ion beam was performed by Fumelli et al. [103]. The residual negative ions were decelerated down to 8 keV, i.e. 8 % of the beam acceleration potential. A power efficiency of 81 % was achieved with a very high electron trapping efficiency of 95 %. The experimentally measured power efficiency is lower than the value predicted for a 1 MeV negative ion beam because of the reactions between the background gas and the residual ions. The cross sections of these reactions at 100 keV are much higher than in the 1 MeV case.

5.3 Various proposed concepts

Even though not experimentally tested, many ERS concepts for NNBI beamlines have been proposed and numerically modelled.

For a 1.6 MeV D^- ion beam, Moir [104] calculated an ERS power efficiency of 92 %, provided that a good secondary electron suppression is ensured. Moir's paper focuses in particular on how to hold high voltages on the ion collectors: each collector uses several electrodes and the total high-voltage insulation is achieved through 100 kV insulation stages.

The ERS concept of Yoshikawa et al. [105] uses a magnetic field to separate the residual ions and auxiliary electrodes to prevent the secondary electrons emitted from the negative ion collector from being accelerated towards higher potential regions. A 96 % ER efficiency is estimated for a 500 keV negative deuterium ion beam if no power loss is assumed. With a recovery voltage V_r equal to 4 % of the beam acceleration potential, it is predicted that 100 % of the ions are collected. Both Moir and Yoshikawa et al. assume that the energy of both residual negative and positive ions is recovered, but neither of them specifies how to practically do it with positive ions.

As the positive ion collector cannot be directly connected to the ion source power supply, Hopman [106] suggested to operate the gas neutraliser at a lower-than-optimum gas target thickness to increase the residual D^- fraction (see figure 4.1). The resulting decrease of the neutral beam power could be compensated by increasing the ion source area.

In the ERS design study of Araki et al. [107], also the positive ions are decelerated but only to reduce the heat flux on the beam dump. The charge separation occurs via the stray magnetic field from the tokamak reactor. The downside of this choice is that the recovery efficiency, like the stray magnetic field, varies with time depending on the reactor operational parameters. In order to re-use the recovered positive ion power, Matsuoka et al. [108] suggested to separate the negative and positive residual ions with a varying magnetic field to directly collect an AC electric power that can be either sent to the commercial electric grid or recirculated in the system through a step-down transformer and a low-voltage inverter. The beamline wall-plug efficiency would improve from 45 % to 70 %. However, this design requires pulsed operation of the ion source as the ion beam needs to be chopped when the magnetic field polarity is changed.

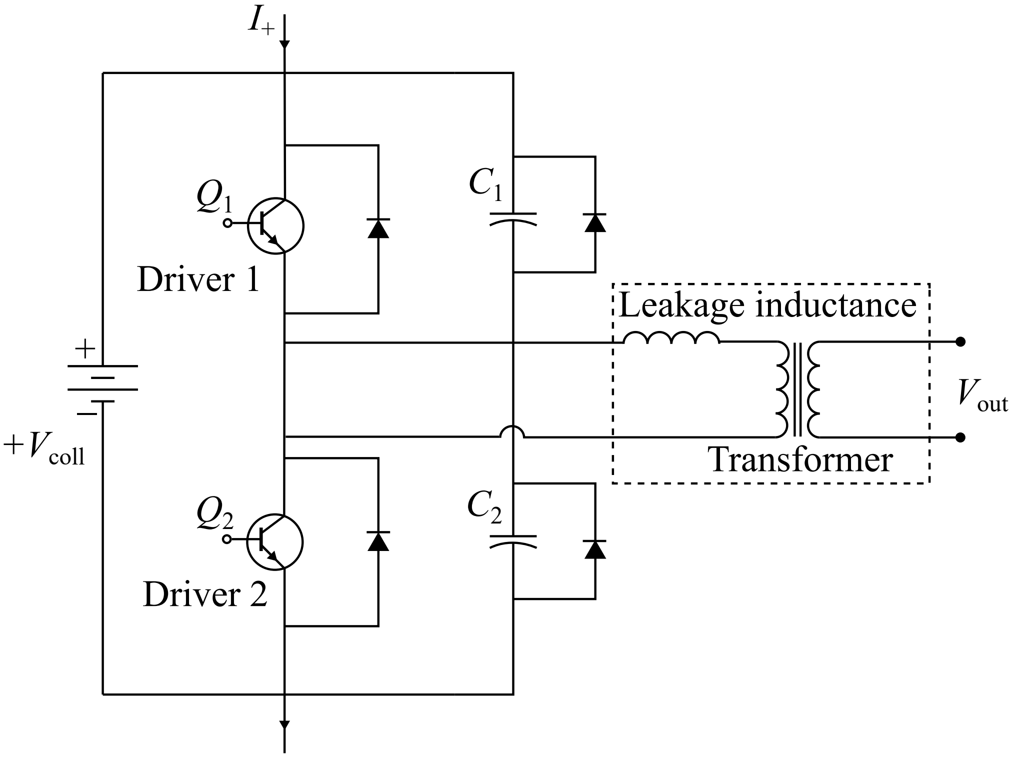

Figure 5.2: Schematic of a resonant converter module. $+V_{\text{coll}}$ is the positive ion collector voltage and I_+ is the current of the recovered residual positive ions.

Modular resonant converters (MRCs), also called energy conversion modules (ECMs), were proposed by McAdams et al. [97] to practically convert the recovered positive ion power into electrical power. The positive ion collector voltage $+V_{\text{coll}}$ is achieved by connecting several converter modules in series. A schematic of a resonant converter module is shown in figure 5.2. Every module is based on a capacitive half-bridge inverter and a high-voltage transformer [109]. The two capacitors of the half-bridge inverter and the transformer inductance form a resonant tank that converts the recovered positive ion DC input into a sinusoidal current. This AC output feeds the transformer that provides voltage scaling. The module outputs can be connected in parallel to obtain a low-voltage, high current that is fed back to the grid. A 3 kV MRC, composed of three 1 kV-modules connected in series, was built and tested [98]. A conversion efficiency of 81 % was measured. This value being almost equal to the efficiency of one module, one can expect the same conversion efficiency with any number of stacked modules. Although higher values can be obtained by improving and optimising the MRC design, a conversion efficiency μ of 81 % is assumed in this work.

As highlighted by Simonin et al. [52], energy recovery becomes particularly simple with photoneutralisation as almost only non-neutralised negative ions are present at the neutraliser exit. Therefore, the need of modifying the beamline to include the high-voltage electrode that decelerates the residual positive ions and the resulting additional complexities in the NBI design are avoided.

The ERS design of Variale et al. [110] does not require to separate the residual ions at the neutraliser exit. The beam of neutral, negative and positive particles enters a collector chamber where the negative ions are decelerated down to almost zero energy. This causes an increase of the corresponding charge density. Consequently, the space charge force felt by the negative ions increases and pushes them towards the chamber walls. Furthermore, as the negative ion beam becomes slower, it spends more time in the chamber, allowing it to expand and ultimately blow up such that the negative ions are collected on the chamber walls. On the other hand, the positive ions are accelerated and come out the other end of the chamber with an energy that is almost twice their initial energy. A second collector chamber, which is suitably biased, decelerates the positive ion beam until it blows up and the ions are collected on the walls. As the neutral beam particles travel undisturbed throughout the two chambers, a beam of only neutrals exits the double-stage collector towards the reactor. After presenting an axisymmetric system for the small negative ion source test facility NIO1 in Ref. [110], an ERS of rectangular geometry, suitable for the ITER NBI beam, was proposed in Ref. [111]. Although ion trajectory simulations predict that the space charge effect leads to the collection of almost all ions, the space charge compensation has not been investigated: the secondary particles with a polarity opposite to that of the decelerating ions, mostly produced by the ionisation collisions between the beam ions and the background gas molecules, reduce the repelling force due to space charge. For sufficiently high gas pressures, the beam blow-up is then prevented. Hence, in order to avoid the space charge compensation, high pumping speeds are required. It is not clear, however, how the collector chambers could be effectively pumped. Other aspects of this concept that need to be further studied are the suppression of the secondary electrons emitted by the chamber surfaces onto which the ions impact and the high-voltage holding on the two collectors, the latter being particularly challenging also because of the large system dimensions.

5.4 Conceptual design of an ERS for the DEMO NBI

All the issues that have been highlighted by the aforementioned investigations on energy recovery are considered and suitable solutions are proposed in designing an ERS for the DEMO NBI. As the baseline DEMO-1 is a modest extrapolation from ITER, the DEMO NBI is again approximated by considering the ITER injector. Particular emphasis is placed on how to modify the NBI beamline to accommodate the ERS components. The main features of the proposed ERS concept are presented by identifying three main steps in the recovery of the residual ion energy: charge separation, deceleration and ion collection.

5.4.1 Charge separation

At the neutraliser exit, the residual negative and positive ions are separated into different directions before decelerating and collecting them on dedicated circuits. Two possibilities are considered: electrostatic or magnetostatic separation.

Figure 5.3 shows the schematic of the electrostatic charge separation. The residual ions are deflected by two parallel electrodes of length L_{def} separated

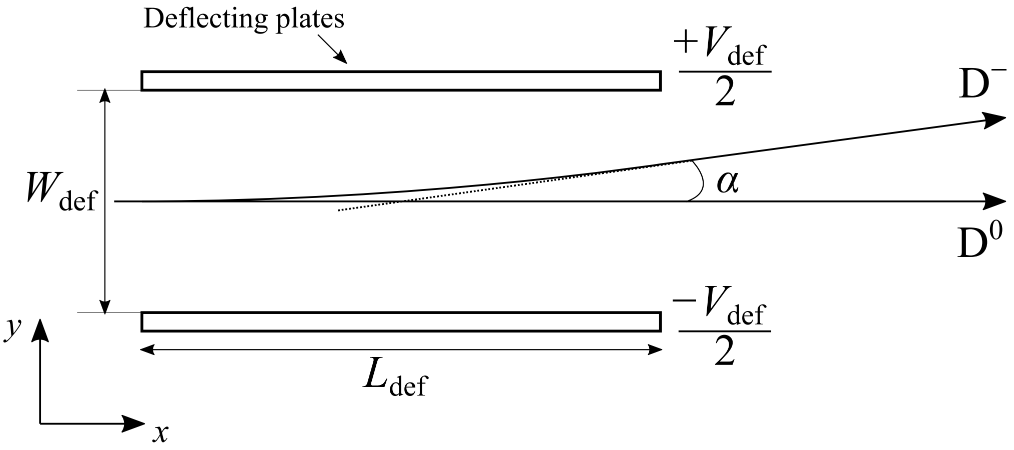

Figure 5.3: Schematic of the electrostatic charge separation. Positive ions are symmetrically deflected.

by a distance W_def across which a potential difference V_def is applied. A uniform electrostatic field of intensity $V_\text{def}/W_\text{def}$ is produced in the y-direction. If an ion of either polarity travels in the x-direction with an energy E_beam, equivalent to a velocity $v_\text{beam} = (2E_\text{beam}/m_\text{ion})^{1/2}$, with m_ion being the ion mass, the deflection angle α at the exit of the electrodes is such that

$$\tan\alpha = \frac{eV_\text{def}\,L_\text{def}}{2W_\text{def}\,E_\text{beam}}. \tag{5.5}$$

For an ion energy of 1 MeV, already small deflections require high electric fields. For example, in order to get $\alpha = 30°$ with reasonable dimensions of the deflection system, e.g. $L_\text{def}/W_\text{def} \approx 3$, a potential difference of around 0.4 MV is needed. As the electric field accelerates the ions in the y-direction, the higher the electric field, the higher the power consumption. Considering the same example as before, the estimated power consumption for a deflection of 30° is around 6 MW. Furthermore, high potentials applied to the large surfaces of the deflecting electrodes would make it more difficult to assure the voltage holding capability of the vacuum.

Therefore, the magnetostatic separation of the residual ions is preferred. The corresponding schematic is shown in figure 5.4: a uniform magnetic field B_m

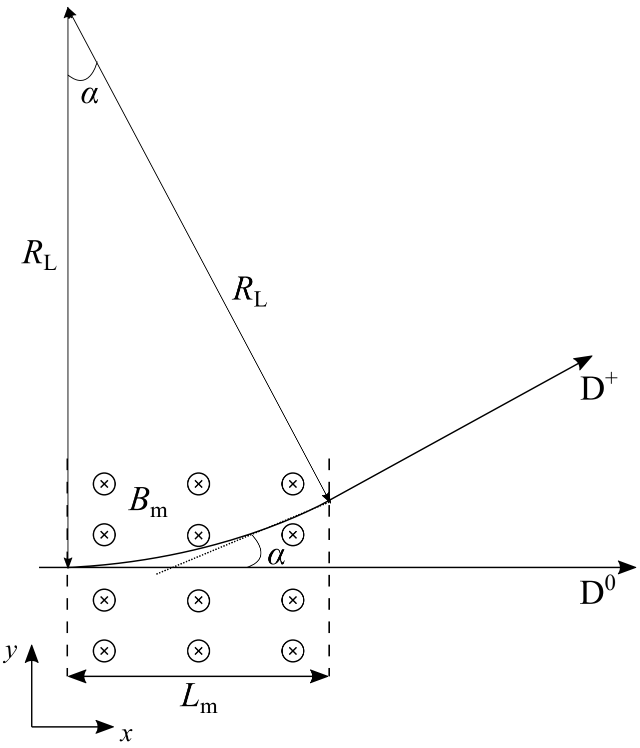

Figure 5.4: Schematic of the magnetostatic charge separation. Negative ions are symmetrically deflected.

is applied in a region of length L_m. The deflection angle α is then given as

$$\sin\alpha = \frac{L_\mathrm{m}}{R_\mathrm{L}}, \tag{5.6}$$

where R_L is the ion Larmor radius

$$R_\mathrm{L} = \frac{m_\mathrm{ion} v_\mathrm{beam}}{e B_\mathrm{m}}.$$

In this case, the same deflection $\alpha = 30°$ is obtained with a small magnetic field of around 0.1 T over a region of length $L_\mathrm{m} = 1\,\mathrm{m}$.

The most commonly used method to generate a uniform magnetic field is a Helmholtz coil system in which two identical coils carrying the same current in the same direction are placed symmetrically around the same axis at a certain distance h. Both coils have the same number of turns. The separation distance h is a function of the coil dimensions such that the second spatial derivative of the magnetic field component along the axis is zero at the centre of the system: for circular coils of radius R_{h}, $h = R_{\mathrm{h}}$, while for square coils of side L_{h}, $h = 0.5445L_{\mathrm{h}}$ [112]. The result is a highly uniform magnetic field, although only in a small volume around the centre. For example, circular Helmholtz coils provide an axial field uniformity of the order of 1 % in a cube of about $0.25R_{\mathrm{h}}$ side around the coil system centre [113]. Using three, four or five coils allows setting higher-order derivatives to zero and, hence, achieving much larger volumes of uniform field [114, 115]. A highly uniform magnetic field prevents the deformation of the residual ion beams and, consequently, the increase of the collector dimensions. However, the downside of systems using more than two coils is that the additional coils would partially block beam access to the homogenous field volume.

In the case of the ITER NBI, the negative ion beam emerging from the plasma grid has a rectangular cross section of width 0.58 m and height 1.5 m [14]. Hence, only square/rectangular coils are considered. However, due to the big dimensions of the ion beam, a region of highly uniform magnetic field over the beam cross section would require unfeasible dimensions of the Helmholtz coils. It follows that a reasonable compromise between beam deformation, due to a low degree of uniformity of the magnetic field, and coil size has to be made.

Magnetic coils are already present in the design of the ITER NBI: the Magnetic Field Reduction System (MFRS) has the purpose of minimising the stray magnetic field from the ITER tokamak in the injector [116, 117]. The MFRS comprises a Passive Magnetic Shield (PMS), made of thick magnetic steel plates surrounding the vessel, and Active Correction and Compensation Coils (ACCC), a set of coils that cover the beam path and produce a vertical magnetic field in the direction opposite to the tokamak stray field. Both the PMS and the ACCC are shown in figure 5.5.

Coils 1, 2 and 3 are placed below the injector, coils 4, 5 and 6 are placed above the injector. Coils 3 and 6 cover the ion source and accelerator, coils 2 and 5 the neutraliser, coils 1 and 4 roughly the area occupied by the RID

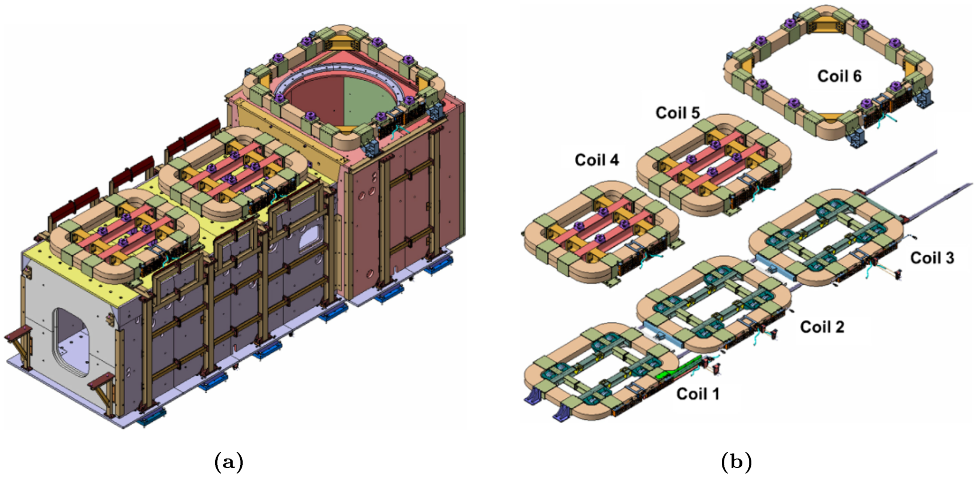

Figure 5.5: (a) Complete Magnetic Field Reduction System (MFRS) of the ITER NBI. (b) Active Correction and Compensation Coils (ACCC) of the ITER NBI. Pictures reprinted from [116] with permission of the rights holder, Elsevier.

and the calorimeter. They avoid that the charged fractions of the beam are deflected by the stray magnetic field and strike against the beamline components, causing an increase of the beam transmission losses and local high power loads. The magnetic field to be compensated goes from around 35 mT in the RID to around 12 mT in the ion source [117]. Only two types of coils will be manufactured: the common design coil (CDC) and coil 6 [116]. The CDC dimensions are 3.43 m × 4.33 m and its cross section is 196 mm high and 500 mm wide. Coils 1, 2 and 3 are simply a CDC, while coils 4 and 5 are two CDCs electrically connected in series.

In designing an ERS for the DEMO NBI with the magnetostatic separation of the residual ion charges, one could take advantage of the fact that an MFRS similar to that envisaged for the ITER NBI needs to be provided also for the DEMO injector. Therefore, the coils of the ACCC system, in particular coils 1 and 4 of the ITER ACCC, could be used not only to compensate the stray magnetic field from the tokamak, but also to separate the residual ions at the neutraliser exit. Thus, for simplification purposes, two square coils of side $L_\mathrm{h} = 3.5\,\mathrm{m}$ separated by a distance h almost equal to the height of the beamline vessel [14] are considered. As starting point, it is also assumed that

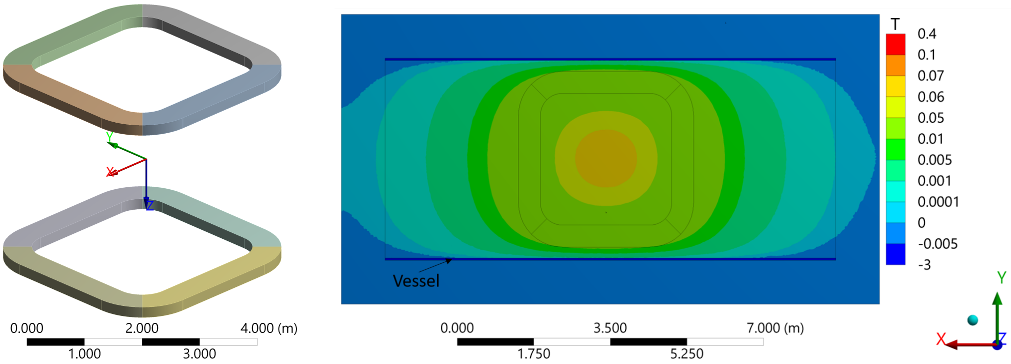

(a) **(b)**

Figure 5.6: (a) 3D model of two square CDCs of side $L_\mathrm{h} = 3.5\,\mathrm{m}$ separated by a distance $h = 3.5\,\mathrm{m}$. The coil current is $NI = 191\,\mathrm{kA\,turns}$. (b) Colour map of the vertical component $\vec{B}_\mathrm{z}$ of the magnetic field for the system cross section in the x–y plane at $z = 0$. The beamline vessel is also shown.

the coils are inside the vessel such that the produced magnetic field is not attenuated by the vessel structure. Hence, $h = 3.5\,\mathrm{m}$ is assumed.

The magnetic field generated by the two coils is calculated with a magnetostatic simulation based on the finite element method and performed with ANSYS [64]. The 3D model is shown in figure 5.6a. Each coil carries a current NI with N being the number of turns. It is assumed that NI is equal to the nominal current in the coil 4 of the ITER ACCC (figure 5.5b), i.e. $NI = 191\,\mathrm{kA\,turns}$ [116]. Although it is not shown, a stainless steel vessel encloses the coils. The vessel has dimensions similar to those of the ITER beamline vessel [14], i.e. 10.3 m long, 4.6 m wide and 4.2 m high. The beam moves in the positive x-direction. Figure 5.6b is a cross section of the computational domain in the x–y plane at the centre of the system, i.e. for $z = 0$, with a colour map of the magnetic field component along the z-axis. The calculated magnetic field in the centre of the coil system is around 65 mT.

More importantly, figure 5.6b highlights a drawback of magnetic separation: the stray magnetic field of the deflecting coils. As the coils would be placed immediately at the exit of the neutraliser in order to minimise the beamline length, the magnetic field in the neutraliser would be very high, leading to unwanted deflections of the beam ions against the neutraliser walls and to a corresponding decrease of the transmission efficiency. For example, the maximum vertical field $\vec{B}_{\mathrm{z}}$ allowed in the ITER gas neutraliser is [117]

$$|\vec{B}_{\mathrm{z}}| < 27\,\mathrm{mT} \qquad \text{or} \qquad \int B_{\mathrm{z}}\,\mathrm{d}l < 1.8 \times 10^{-4}\,\mathrm{T\,m}, \tag{5.7}$$

where the integral is calculated along the neutraliser length. Therefore, the fringe magnetic field produced by the deflecting coils must be shielded. A soft iron yoke is a common method of magnetic shielding. Furthermore, it provides a return path to the magnetic flux, leading to an increase of the generated field or, equivalently, to a decrease of the required coil currents for the same field. However, a massive yoke around the coils would either block the ions or, if placed in the transverse direction, would not suppress the fringe field in the neutraliser. This latter effect can already be seen in figure 5.6b where the vessel stainless steel accommodates most of the magnetic field lines, greatly reducing the fringe magnetic field only in the y-direction.

Hence, a different solution is proposed: a thick shield made of soft steel at the neutraliser exit. The shield is modelled in figure 5.7a. As for the PMS plates of the ITER NBI, a thickness of 150 mm is assumed. An aperture is provided to let the ion beam pass through. Special care must be taken in designing the aperture as the accumulation of the fringe magnetic field lines in the shield could modify the ion trajectories. Assuming an ion beam cross section of width 0.58 m and height 1.5 m, ion trajectory simulations with different aperture dimensions led to the selection of an aperture of width 0.92 m and height 2.0 m for which no noticeable ion deflection occurs. Furthermore, the shield can also serve as baffle dividing the NBI beamline vessel into different pumping chambers [59]. This reduces the gas flow from the source and neutraliser region to the downstream parts of the beamline, consequently reducing the re-ionisation losses due to the collisions of the beam neutrals with the gas molecules.

Figure 5.7b shows the colour map of the magnetic field vertical component for

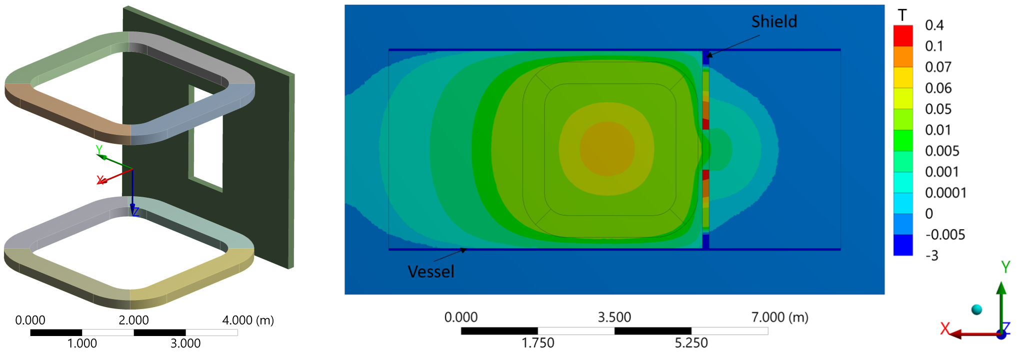

(a) (b)

Figure 5.7: (a) 3D model of two square CDCs of side $L_\mathrm{h} = 3.5\,\mathrm{m}$ separated by a distance $h = 3.5\,\mathrm{m}$. The coil current is $NI = 191\,\mathrm{kA\,turns}$. A soft steel shield of thickness 150 mm is used to suppress the fringe magnetic field in the neutraliser region. The aperture in the shield is 0.92 m wide and 2.0 m high. (b) Colour map of the vertical component $\vec{B}_\mathrm{z}$ of the magnetic field for the system cross section in the x–y plane at $z = 0$. The beamline vessel is also shown.

the cross section of the computational domain in the x–y plane passing through the origin of the reference system. The same contour bands as figure 5.6b are used. One can see that the passive shield is highly effective in reducing the fringe field in the neutraliser region. In particular, the integral of the vertical component of the magnetic fringe field over a neutraliser length of 3 m satisfies the condition (5.7) if the neutraliser is placed around 0.55 m away from the passive shield.

The computation of the magnetic field generated by the coil system allows calculating the residual ion trajectories and evaluating the beam deflection and deformation. As first approach, the trajectories are computed analytically. The trajectory of a residual ion of charge $q = \pm e$ and velocity $\vec{v}_\mathrm{ion}$ is obtained by solving the equation of motion due to the Lorentz force in the absence of electric fields:

$$\frac{\mathrm{d}^2\vec{r}}{\mathrm{d}t^2} = \frac{q}{m_\mathrm{ion}}\,\vec{v}_\mathrm{ion} \times \vec{B}_\mathrm{tot}, \tag{5.8}$$

where $\vec{r}$ is the ion position vector.

It is assumed that the beam of residual negative ions emerging from the neutraliser has the same cross section as that at the plasma grid, i.e. a rectangle of width 0.58 m and height 1.5 m. The same assumption is made for the residual

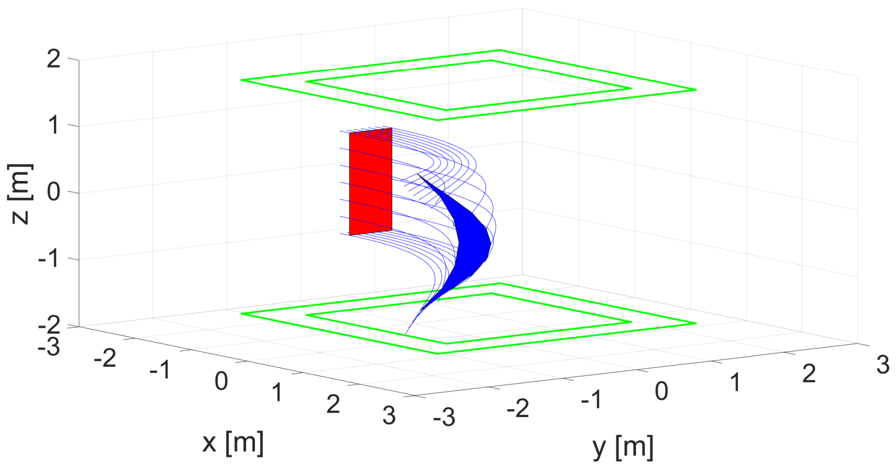

Figure 5.8: Schematic of the magnetic deflection of the residual negative ion beam. The beam at the neutraliser exit (in red) has a rectangular cross section of width 0.58 m and height 1.5 m. The trajectories of several ions at the beam boundary are calculated by using the magnetic field values given by ANSYS and shown as blue lines. The resulting beam cross section at the collector is plotted in blue.

positive ions. The initial ion velocity is $\vec{v}_{\mathrm{ion}} = v_{\mathrm{beam}}\hat{\imath}$ with $\hat{\imath}$ being the unit vector in the x-direction which is the neutral beam direction. The situation is schematically depicted in figure 5.8 where the red rectangle represents the cross section of the residual ion beam at the neutraliser exit. In order to roughly asses how the beam shape is affected by the magnetic field and to estimate the collector size, a certain number of ions at the beam contour are simulated. The magnetic field values are obtained with ANSYS and used to numerically solve equation (5.8). The resulting trajectories are shown in figure 5.8. Due to the low uniformity of the vertical magnetic field, the ions at the top and bottom parts of the beam are deflected more, leading to a half-moon-shape of the beam at the collector. Furthermore, the magnetic deflection focusses the beam, i.e. compresses the beam cross section in the y-direction. The deformed beam can be enclosed by a rectangle of width 0.8 m and height 2.0 m. These dimensions are then used for the collector sizing.

The low uniformity of the separating magnetic field also implies that it is not possible to define a single ion deflection angle α as done in equation (5.6). For every trajectory j calculated in figure 5.8, one can calculate a corresponding

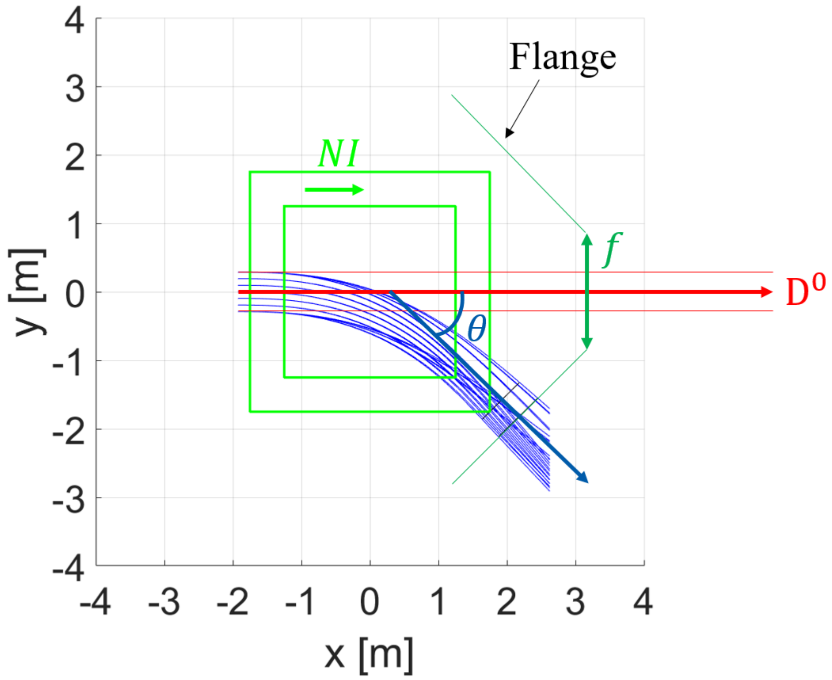

Figure 5.9: Schematic of the magnetic deflection of the residual negative ion beam in the x-y plane. NI is the coil current, θ is the mean deflection angle, f is the distance between the two collector flanges.

deflection angle α_j. By averaging these values, a mean deflection angle θ is defined, as outlined in figure 5.9. Ultimately, for fixed coil dimensions and separation distance, θ depends on the coil current NI generating the magnetic field. Therefore, only one parameter needs to be specified.

5.4.2 Ion deceleration and voltage holding

After being separated by the magnetostatic field generated by the two-coil system, the residual ions are electrostatically decelerated to almost zero energy. The design of the decelerating system presents the same degree of complexity and most of the same issues as those of the accelerator. This is an advantage as one can in principle adopt the same design solutions that have been found for the ion acceleration. One of the most critical issues is the voltage holding. When a high potential difference is applied between two electrodes, an electrical breakdown occurs if a current starts flowing through the insulation and causes a short circuit between the electrodes. The minimum voltage that causes a breakdown in the insulating medium is called breakdown voltage V_{bd}. The high-voltage breakdown is a stochastic phenomenon: every time a potential difference is applied, the same electrode gap will break down at different voltages. Thus, the V_{bd} value accounts for a certain statistical variability [118].

The most common insulating materials are gases. Breakdowns in gases are due to the gas ionisation: ions and electrons are produced and accelerated towards the electrodes. If the applied voltage is sufficiently large, more and more charged particles are produced in an avalanche process that leads to high currents in the gas.

The breakdown probability primarily depends on the electric field strength, i.e. the rate at which the voltage changes per unit length. In other words, it is most likely that high-voltage breakdowns occur where the electric field is the highest. Therefore, critical factors are the electrode spacing, the gas pressure, temperature and species, the electrode material, geometry and surface finish, the presence of magnetic fields, contaminants and radiation, history of the electrodes [119].

In general, the breakdown voltage of gases is a function of the product of the gas pressure p and the distance d between the electrodes:

$$V_{\mathrm{bd}} = f(pd). \tag{5.9}$$

Equation (5.9) is known as Paschen's law and has been experimentally determined for many gases [119].

Accordingly, vacuum should be the perfect insulator as breakdowns via the process of collisional ionisation cannot occur as there are practically no gas particles between the electrodes. Thus, the V_{bd} values are very high. However, due to the presence of metallic electrodes, a sufficiently high voltage causes a breakdown even in vacuum. Although the electrode surface plays a critical role, the breakdown mechanism in vacuum is still not completely clear and many explanations have been proposed [119].

The clump theory has been successfully applied to describe many experimental observations, especially in the cases with gap lengths of several centimetres [120–124]. According to the clump mechanism, loosely bound particles, called clumps, are present on the surfaces of the electrodes. When a high voltage is applied between the electrodes, the clumps get charged, detach from the surfaces by electrostatic repulsion and are accelerated across the gap. The impact of the clumps against the opposite electrode releases a gas cloud from the electrode surface. Then, a discharge can take place, leading to a breakdown. The clump mechanism was first suggested by Cranberg [120] who assumed that a breakdown occurs if the clump energy per unit area is higher than a constant value C' that depends on the geometry and characteristics of the electrodes. The clump energy per unit area is given by the product of the voltage across the gap and the charge density on the clump. The latter being proportional to the electric field E at the electrode of origin, the breakdown criterion reads as

$$V_{\mathrm{bd}}\, E = C'. \tag{5.10}$$

In case of parallel plane electrodes separated by a distance d, $E = V/d$. Hence, equation (5.10) becomes

$$V_{\mathrm{bd}} = (C'd)^{1/2}. \tag{5.11}$$

Equation (5.10) can be generalised as

$$V_{\mathrm{bd}} = C d^{\alpha}, \tag{5.12}$$

where $\alpha \in [0.2, 1.2]$ depends on the gap length and on the electrode geometry and material. Both parameters α and C need to be experimentally determined. Concerning the ITER NBI ion source and accelerator, there are two positions where the voltage hold-off capability of the vacuum must be guaranteed:

- Between the accelerator grids. The MAMuG accelerator concept minimises the risk of breakdown by splitting the voltage difference of 1 MV into five steps of 200 kV each, as outlined in section 3.1.2. This solution offers a better voltage holding than the SINGAP accelerator concept in which the ions are accelerated in one step through a potential difference of 945 kV [34]. As the calculated gas pressure in the accelerator is several 10^{-2} Pa [57], the gaps between the MAMuG grids are designed to simultaneously fulfil both the breakdown criteria of the clump theory (equation (5.12)) and of Paschen's law (equation (5.9)) [35]. A minimum gap length of 85 mm between two grids separated by a potential difference of 200 kV is foreseen [14].

- Between the beam source, which is biased at -1 MV, and the surrounding beam source vessel, which is at the ground potential. In this gap, a gas pressure between 10^{-5} Pa (without gas injection) and 0.05 Pa is expected. A necessary value of around 1 m for the gap length is obtained from extrapolation of past experiments [125]. The voltage holding capability of this system was evaluated by a probabilistic model based on the Cranberg-Slivkov theory for clump-induced breakdowns [126]. Both the model results and recent experimental tests pointed out the difficulty in sustaining a potential difference of 1 MV in a single gap due to the occurrence of breakdowns. Therefore, one or more intermediate electrostatic shields between the source and the vacuum vessel have been proposed to improve the voltage holding [126–128].

In designing the residual ion decelerator, one could follow a MAMuG-type approach and split the potential difference into more steps. The main advantages would be stable voltage holding and small gaps between the electrodes, resulting in a compact system. However, a SINGAP-type decelerator would be much simpler, especially because intermediate potentials would not be required. At the exit of the neutraliser, one cannot discern the single beamlets any more. Additionally, the residual ion trajectories are affected by the separating magnetostatic field. Thus, the decelerator electrodes cannot be multi-aperture grids like in the accelerator, but they are simple frames. A SINGAP-type deceleration is therefore considered.

In line with the electric diagram of figure 5.1, the decelerator consists of a grounded frame followed by the residual ion collector biased at a potential $\pm V_{\mathrm{coll}}$. Single-gap systems require large gap spacings: the potential difference of 1 MV between the ITER ion source and the grounded vacuum vessel is designed to be held over a distance of around 1 m that might not even be sufficient. However, it was also experimentally demonstrated that 940 kV could be held over a gap of 350 mm under a D_2 pressure of 0.03–0.07 Pa [129, 130]. Higher voltages were not attempted in order to avoid damaging the power supply. The difference between the gap lengths is firstly explained by the different pressure ranges as it is known that adding small quantities of gas to the vacuum improves the voltage holding [122, 123, 129]. The explanation of this pressure effect is not clear. It was suggested that it might be due to the sputtering action of the ions formed through gas ionisation which blunt the micro-protrusions that are present on the electrode surfaces [131]. This process, however, cannot explain the reversibility of the pressure effect when going back to low gas pressures. Hence, the pressure effect was alternatively attributed to the increase of the work function of the metallic emitters following the gas adsorption on the surfaces [131]. In any case, although a small increase of the background gas pressure allows achieving higher breakdown voltages, a large increase of the gas pressure would bring the system closer to the Paschen breakdown. Secondly, the lower gap length in the experiments of Svensson et al. [129] is due to the completely different shapes and sizes of the electrodes with respect to the ion-source–vacuum-vessel system: the test facility is a scaled version of the ITER SINGAP accelerator [33] and, therefore, the high voltages are applied on rectangular planar grids. As the geometry of the decelerator frames resembles the geometry of this experimental setup, it is assumed that the results on voltage holding can be transferred to the

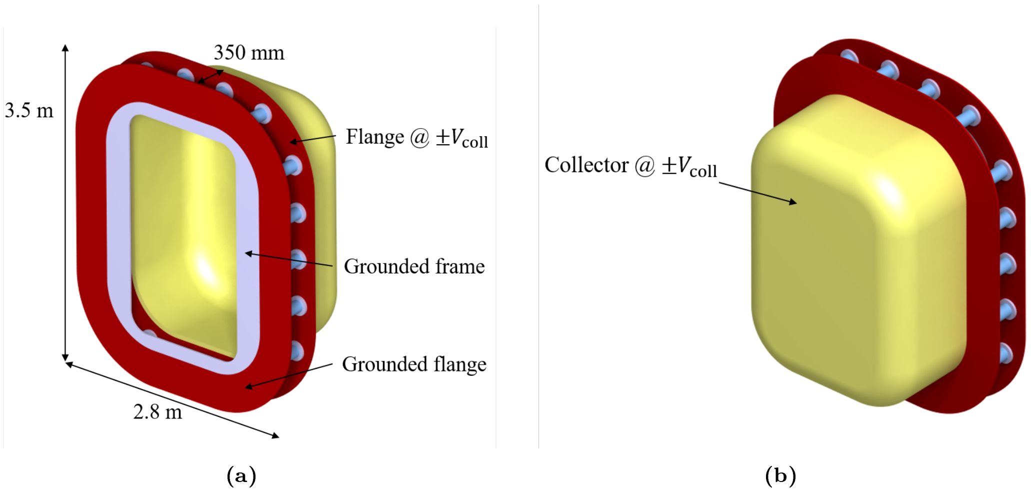

Figure 5.10: 3D CAD of the decelerator.

decelerator design.

The electrode shape plays an important role in the design of high-voltage systems: breakdowns are likely to be initiated in regions where localised enhancements of the electric field occur. Therefore, sharp corners and edges are removed and large radius curvatures are used for all the system surfaces.

Figure 5.10 shows a 3D CAD of the decelerator. A grounded frame is supported by a mounting flange of height 3.5 m and width 2.8 m. The flange size and shape are similar to those of the accelerator flanges. A second mounting flange sustains a 1 m deep cup that collects the residual ions. Both this flange and the collector are biased at $\pm V_{\mathrm{coll}}$. The gap between the flanges is 0.35 m long. The two flanges are connected through cylindrical ceramic post-insulators, similarly to the grid supporting system in the accelerator design [14,132]. The junction between the ceramic, the flange metal and the vacuum could cause a localised enhancement of the electric field and thus induce a breakdown that propagates along the post-insulator surface. This phenomenon is called triple junction effect and it is due to the lower electrical permittivity of the vacuum with respect to the ceramic permittivity [118]. The triple points are hence covered by electrostatic shields that enclose both extremities of the post-insulators. The grounded flange can be directly supported from above and below in the beamline vessel, thus holding the entire structure.

In the design of the ERS, the positions where the vacuum voltage holding is critical are:

- Between the grounded and biased flanges of the decelerator. A potential difference of around 1 MV is applied. As previously highlighted, the decelerator design recalls that of the SINGAP acceleration scheme. Thus, the results of the voltage holding experiments for the SINGAP accelerator are used [123,129]. Between the decelerator electrodes, a pressure of several 10^{-2} Pa is expected (around 0.02 Pa at the neutraliser exit [57]). Although it is slightly lower than the experimentally determined pressure range of 0.03–0.07 Pa, in which stable voltage holding was achieved, a decelerating gap length of 350 mm is assumed.

  The experimental results can be generalised according to the clump theory by applying equation (5.12). As the breakdown voltage $V_{\rm bd}$ is 940 kV and the gap spacing d is 350 mm, assuming an exponent $\alpha = 0.5$, one gets $C = 50\,\mathrm{kV/mm^{0.5}}$. Hence, equation (5.12) becomes

  $$V_{\rm bd} = 50\,\frac{\mathrm{kV}}{\mathrm{mm}^{0.5}}\,d^{0.5}. \tag{5.13}$$

- Between the two decelerators. The negative and positive residual ion collectors being biased at $-V_{\rm coll}$ and $+V_{\rm coll}$, respectively, a potential difference of $2V_{\rm coll}$, almost equal to 2 MV, exists between the two deceleration systems. The ideal solution would be using intermediate electrostatic shields that prevent the biased surfaces from directly facing each other. However, this would strongly complicate the injector design. As preliminary approach, the clump theory is used to estimate the distance between the decelerators that minimises the occurrence of breakdowns. In particular, it is assumed that equation (5.13) is valid also for this gap. For example, assuming $V_{\rm coll} = 1$ MV and, hence, $V_{\rm bd} = 2$ MV, one

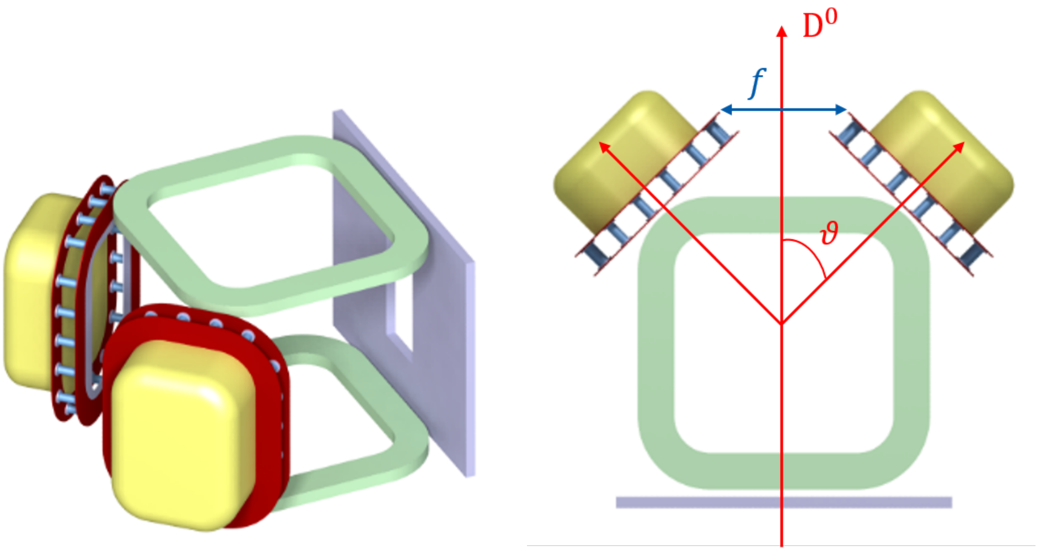

(a) (b)

Figure 5.11: (a) ERS 3D CAD showing the coil system, the magnetic shield and the decelerators for the residual positive and negative ions. (b) Top view of the ERS 3D CAD highlighting the angle θ between the decelerators and the neutral beam direction and the distance f between the two biased flanges.

obtains from equation 5.13 a minimum gap spacing d of around 1.6 m.

- Between the decelerators biased at $\pm V_{\text{coll}}$ and the grounded beamline vessel. The situation is very similar to the voltage holding issue between the ion beam source, biased at -1 MV, and the grounded beam source vessel. Therefore, the same design solutions, as high gap distances or intermediate electrostatic shields, can be adopted.

The two decelerators are placed right at the coil exit, as shown in figure 5.11, forming an angle θ with respect to the neutral beam direction. θ corresponds to the mean deflection angle of the residual ions (see figure 5.9).

As discussed in the previous section, fixing θ sets the coil current NI. Additionally, it determines the beam deformation at the coil exit and, hence, the collector dimensions. The condition that fixes θ is given by the vacuum insulation capability to sustain a potential difference of around 2 MV between the two decelerators, i.e. it depends on the distance f between the two decelerators, shown in figures 5.9 and 5.11b. The clump theory predicts a minimum distance $f_{\mathrm{min}} = 1.6\,\mathrm{m}$. The angle θ is then assessed through the following procedure:

1. a tentative value of the coil current NI is set and used to compute the magnetic field distribution with ANSYS;
2. the magnetic field values allow calculating the trajectories of the residual ions at the beam contour and defining a mean deflection angle θ (the system is symmetric with respect to the neutral beam direction at the coil centre);
3. the distance f between the biased flanges of the two decelerators is estimated;
4. the coil current NI is varied and the previous steps repeated until the minimum angle θ satisfies the condition $f > f_{\mathrm{min}}$.

The minimisation of θ is important to keep the transverse dimension of the beamline vessel as small as possible. The algorithm led to the following results: $\theta = 45°$, $NI = 136\,\mathrm{kA\,turns}$, $f = 1.7\,\mathrm{m}$ and a collection cup of width 1.4 m and height 2.4 m. The geometries in figures 5.8, 5.9, 5.10 and 5.11 have all been built using these parameters.

5.4.3 Ion collection

The last step of energy recovery is the collection of the residual ions that have been previously separated according to their charge and decelerated to almost zero energy. To this end, a collection cup of width 1.4 m, height 2.4 m and depth 1 m is considered. The collector bias voltage $|V_{\mathrm{coll}}|$ cannot be equal to $V_{\mathrm{b}} = 1\,\mathrm{MV}$, i.e. the residual ions are not decelerated to zero energy. This is due to the fact that the ion trajectories are not perpendicular to the equipotential surfaces of the decelerating electric field. As the transverse ion velocity is not reduced by the electric field, in case of full deceleration the ions do not hit the collector surface but are reflected back. The non-orthogonality between the ion trajectories and the electric field equipotential surfaces depends on several factors: the geometry of the electrodes, the divergence of the ion beam, the influence of the separating magnetic field and the beam space charge.

Space charge

Because of the Coulomb repulsion, there exists a potential difference between the axis and the boundary of the ion beam. Hence, the ions experience a defocusing outward electric force that makes the beam spread radially [133, 134]. Assuming a steady-state uniform ion beam with a constant current density J propagating with an axial velocity v_{beam}, the beam charge density ρ_{b} is

$$\rho_{\mathrm{b}} = \frac{J}{v_{\mathrm{beam}}}. \tag{5.14}$$

The space charge effect increases with decreasing ion velocities. Therefore, the deceleration of the residual ions to almost zero energy may eventually lead to the blow-up of the beam. The ERS design of Variale et al. [110, 111] is based on the space-charge-induced beam blow-up of the residual ions that, subsequently, are collected on the walls of the surrounding collectors. For the ERS concept proposed in this thesis, however, the beam blow-up is an unwanted phenomenon and its occurrence before the beams enter the collectors must be avoided.

The secondary particles produced by the ionisation collisions between the residual ions and the background gas molecules mitigate the repulsive space charge force. In the case of the residual negative ions, while the secondary electrons created by gas ionisation are repelled, the secondary positive ions remain trapped in the potential well of the beam, thus reducing the electric field due to the space charge. Such an effect is known as space charge compensation or neutralisation. In the case of the residual positive ions, the secondary positive ions coming from the ionisation collisions are ejected, while the secondary electrons remain inside the beam. However, due to a lower mass, the electrons oscillate very fast across the transverse beam dimensions, leading to a lower compensation of the space charge with respect to the case of a negative ion beam [135].

Space charge compensation of positive and negative ion beams used for neutral beam injection has been extensively investigated both analytically [136–141] and via numerical simulations [133,134,142,143]. In the case of the ITER NBI (both heating and diagnostic injectors), Surrey [139] showed that the ion beam in the drift region between the accelerator and the neutraliser is fully space charge compensated. Inside the neutraliser, where the gas density is much higher, over-compensation is achieved, i.e. the positive ion density at the beam axis becomes higher than the beam ion density, resulting in a significant focusing force on the beam. However, given the difficulty in reliably estimating the degree of space charge compensation, it is generally assumed in designing NBI systems that the space charge forces are completely compensated [141]. This is even more the case for negative ion beams, for which over-compensation is often predicted [139,142,143], for high energy ion beams [140] and for background gas pressures of the order of 10^{-2} Pa [139,140].

Hence, if an ERS is implemented on an ITER-like beamline, one can assume that the residual ion beams in the drift region between the neutraliser exit and the decelerator entrance are fully space charge compensated. Such an assumption, however, cannot be made for the decelerators because not only does the residual ion velocity decrease but, at the same time, the compensating secondary charges trapped inside the beams are accelerated. Therefore, according to equation (5.14), while the charge density of the decelerating ion beams increases, the charge density of the accelerating secondary charges decreases. This could result in the loss of space charge compensation and, subsequently, in the increase of the effective beam divergence. Ultimately, the beam blow-up could occur. The effect of space charge on the residual ion deceleration and collection is investigated by using a particle tracking code.

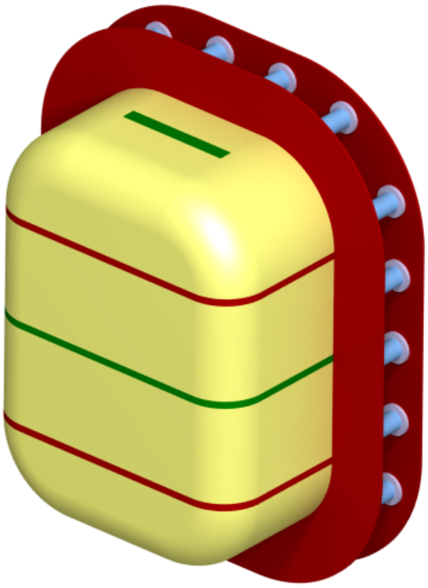

Figure 5.12: Permanent magnet arrangement on the walls of the residual negative ion collector. The magnet poles are indicated in red and green.

Secondary electron emission induced by ion impact

An important aspect to consider when collecting the residual negative ions is the emission of secondary electrons from the collector surfaces onto which the ions impact. The secondary electrons emitted in the negative ion collector, which is negatively biased with respect to the grounded frame, experience a positive potential difference. In other words, the same electric field that decelerates the residual negative ions will accelerate the secondary electrons into the opposite direction. This would cancel the benefits of energy recovery and drastically reduce the ERS efficiency. Therefore, a secondary electron suppression system has been foreseen in all the ERS designs presented at the beginning of this chapter. In almost all cases, the acceleration of the secondary electrons is prevented by an electric field, e.g. with dedicated electrodes or biased windows in front of the collector itself, with a negative potential with respect to the collector.

In the present design, however, the electrostatic trapping of the secondary electrons is not ideal due to the high ratio between the size of an eventual biased window and the deceleration gap. Furthermore, additional electrodes would complicate the decelerator design. A different strategy is therefore followed. Firstly, geometrical capture is exploited to some degree by executing the collector electrodes as cups with a certain depth, limiting the solid angle through which secondary charges can escape. A depth of 1 m has been selected in order to limit the system dimensions. Secondly, a magnetic cusp field is generated on the collector walls by permanent magnets, as depicted in figure 5.12. In this way, the secondary electrons are deflected and forced to hit the walls close to their origin. Some simple magnet configurations have been investigated and their trapping efficiency has been estimated by a particle tracking computer code. Among the options studied, the configuration of figure 5.12 allows achieving a high trapping efficiency with a simple arrangement of the permanent magnets.

Creation of additional secondary charges

In addition to the secondary electrons that are emitted from the collector surfaces onto which the residual negative ions impact and that are accelerated towards the grounded frame if not stopped, additional secondary charges are created in the collectors and eventually accelerated following the reactions between the residual ions and the background gas. The main processes are:

- gas ionisation by the residual D^- and D^+ ions;
- stripping and double stripping of the residual D^- ions;
- charge exchange of the residual D^+ ions with the gas molecules.

Secondary charges are also created via sputtering of the collector surfaces due to the bombardment of the residual ions [144].

In summary, the collection of the residual ions presents several aspects to investigate:

- estimating the minimum voltage V_r that allows collecting as many residual ions as possible with a very few electrostatic reflections;
- assessing the space charge impact on the ion trajectories in the deceleration phase;
- estimating the suppression efficiency of the secondary electrons emitted by the residual negative ions impinging on the collector surfaces;
- evaluating the power losses due to the acceleration of the secondary charges generated in the collectors by the reactions between the residual ions and the background gas and by sputtering.

They will be studied in more detail with the help of a particle trajectory simulation code.

5.4.4 Summary of the ERS design

The design choices of the previous sections led to the ERS design of figure 5.13. A brief summary is given in the following:

- The residual negative and positive ions at the neutraliser exit are separated into different directions by a magnetostatic field generated by a Helmholtz-like coil system. The coils have a square shape of 3.5 m side and are separated by a distance of 3.5 m. The coil current is 136 kA turns. The mean deflection angle of the residual ions with respect to the neutral beam direction is 45°.
- The ACCC design is used as reference for the separating coils. The coils could have the double function of minimising the stray magnetic field from the tokamak and of separating the residual ions. Only the latter function is considered in this work to define the coil parameters.
- As the fringe magnetic field of the coils may lead to unwanted ion deflections in the neutraliser, it is suppressed by a soft steel shield of 150 mm

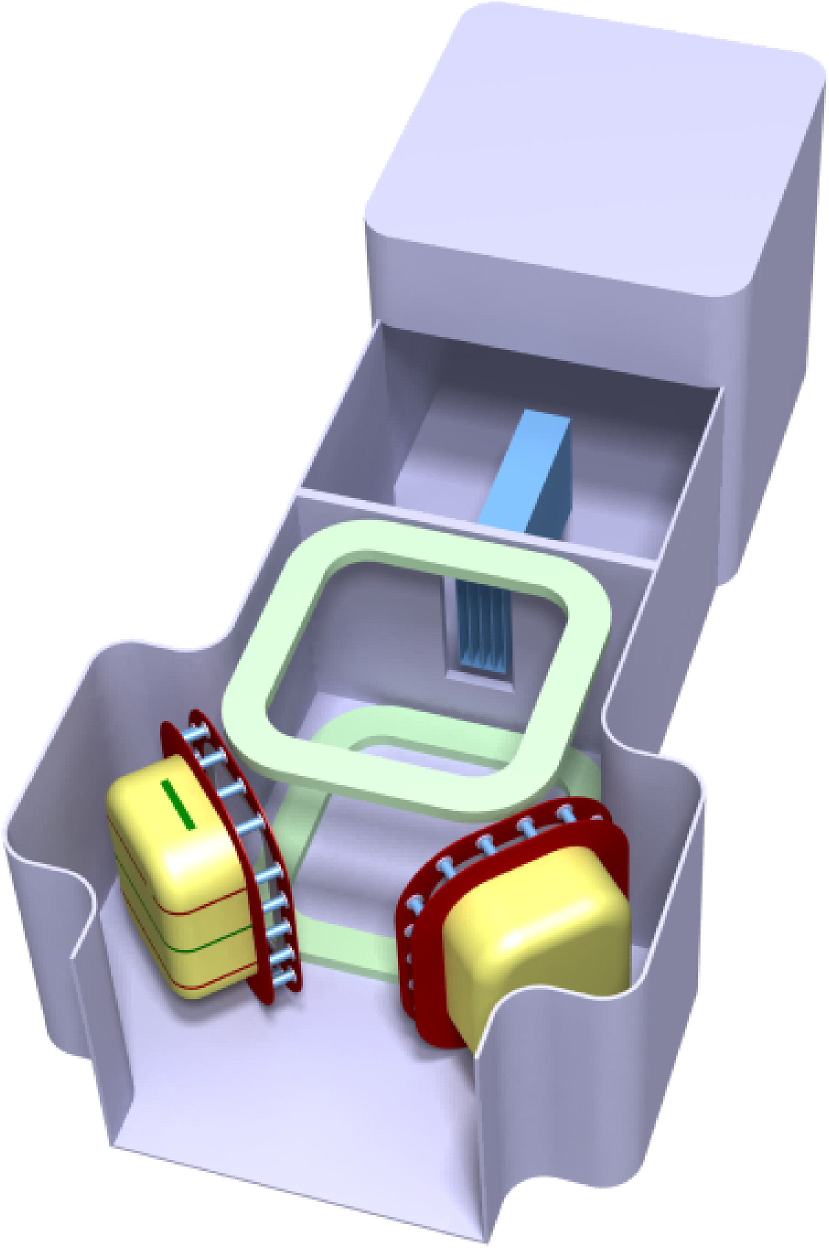

Figure 5.13: 3D CAD of the proposed ERS for an ITER-like beamline.

thickness placed between the coils and the neutraliser. An aperture 0.92 m wide and 2.0 m high lets the beam pass through. The shield can also be used as gas baffle to reduce the gas pressure in the downstream part of the beamline.

- The deceleration of the residual ions occurs in the decelerators whose structure consists of two mounting flanges with a height of 3.5 m and a width of 2.8 m. The closest flange to the coils is grounded, the other flange is biased at $\pm V_{\mathrm{coll}}$. The reference electric schematic is shown in figure 5.1. The flanges are connected through cylindrical ceramic post-insulators. The biased flange sustains the collector cup. The cup has a width of 1.4 m, a height of 2.4 m and a depth of 1 m. The whole decelerator structure is sustained by a supporting system between the vessel and the top and bottom parts of the grounded flange (the supporting system is not shown in figure 5.13).

- The residual ions undergo a one-step deceleration, thus making the voltage holding a critical issue. For the same reason, care must be taken in placing the decelerators far apart from each other. On the basis of the breakdown description by the clump theory and of experimental results, the minimum distances that guarantee the vacuum insulation capability to sustain high potential differences between the biased surfaces in the ERS are estimated. In particular, a gap of 350 mm between the decelerator flanges and a distance of 1.7 m between the two decelerators are adopted. The voltage holding condition is fulfilled by keeping the mean deflection angle and, thus, the transverse dimension of the vessel as small as possible.

- Peak values of the electric field that may lead to unwanted breakdowns and, hence, spoil the vacuum insulation are avoided by using large radius curvatures for all the corners and edges in the system.

- The secondary electrons emitted by the residual negative ions impinging on the collector surfaces are suppressed by magnetostatic deflection. To this end, the walls of the negative ion collector cup are covered with permanent magnets generating a cusp magnetic field.

- The beamline vessel has similar dimensions as those of the ITER beamline vessel [14]: it is 10.3 m long, 4.6 m wide and 4.2 m high. Instead of considering a bigger vessel to accommodate the decelerators, the width is increased only at the level of the decelerators. A longer vessel is however needed, e.g. to place the calorimeter. Additionally, the space for the pumps and the distance to assure the voltage holding between the biased decelerators and the grounded vessel have not been considered. The detailed injector design is outside the scope of this work.

5.5 Particle tracking simulations

Numerical simulations of the residual ion trajectories are performed to estimate the efficiency of the ERS design presented in the previous sections [145].

Ion Beam Simulator (IBSimu) [146, 147] is a 3D ray-tracing code in which the particle equation of motion due to the Lorentz force is solved using mesh-based maps for the electric and magnetic fields.

The ERS geometry of figure 5.13 is imported into the code. The magnetic field generated by the deflecting coils and the magnetic cusp field due to the permanent magnets on the negative ion collector walls are calculated with ANSYS Workbench [64]. The electric field distribution inside the vessel, in particular between the decelerator flanges, is obtained with ANSYS Mechanical APDL [148] after assuming a bias voltage $|V_{\text{coll}}|$. The magnetic and electric field values are imported into IBSimu and adapted to the code meshing through interpolation.

The starting point is a beam of deuterium particles with a rectangular cross section of 0.58 m width and 1.5 m height at the neutraliser exit. The beam ions have an energy of 1 MeV and a current of 40 A. The beam species composition is the one at the exit of the ITER gas neutraliser calculated for the optimum gas target thickness (see section 4.1), i.e. 26 % of D^+, 19 % of D^- and 55 % of D^0. The species distribution across the beam cross section is uniform. The beam divergence is 7 mrad (as for the ion beam of the ITER NNBI [14]). Furthermore, it is assumed that the space charge of the residual ion beams coming from the magnetostatic separation is completely compensated. As outlined in section 5.4.3, this hypothesis is reasonable in the drift region between the neutraliser exit and the decelerator entrance, but it could not be valid in the decelerators. Therefore, it will be later relaxed.

IBSimu simulations are also used to investigate the emission of secondary electrons from the negative ion collector walls and the power loads on the collectors due to the impacting residual ions.

Three cases are investigated:

- Case 1: $|V_{\mathrm{coll}}| = 950\,\mathrm{kV}$ without permanent magnets on the negative ion collector walls;
- Case 2: $|V_{\mathrm{coll}}| = 950\,\mathrm{kV}$ with permanent magnets on the negative ion collector walls;
- Case 3: $|V_{\mathrm{coll}}| = 975\,\mathrm{kV}$ with permanent magnets on the negative ion collector walls.

In Cases 1 and 2, a recovery voltage V_{r} of 50 kV is provided, corresponding to 5 % of the beam acceleration potential V_{b}, while V_{r} is 25 kV in Case 3, i.e. 2.5 % of V_{b}. Hence, the residual energy of the decelerated ions is 50 keV in Cases 1 and 2 and 25 keV in Case 3. The purpose of Case 1 is to assess the influence of the fringe magnetic field of the deflecting coils on the secondary electron trajectories. If they were deflected against the lateral walls of the collector, the use of permanent magnets would not be necessary.

Table 5.1: Inputs and outputs of the particle tracking simulations performed by IBSimu for an ITER-like beam in the ERS for three different cases.

	Case 1	Case 2	Case 3
Residual ion energy [keV]	50	50	25
Permanent magnets	No	Yes	Yes
Negative ion collection efficiency g^- [%]	99.68	99.69	97.76
Positive ion collection efficiency g^+ [%]	99.40	99.40	96.71
Current of emitted secondary electrons I_{SE} [A]	8.562	8.617	7.532
Secondary electron trapping efficiency g_{SE} [%]	89.48	98.64	97.80

5.5.1 Ion collection

The main outputs of the tracking simulations are the collection efficiencies of the residual positive (g^+) and negative ions (g^-). Not all residual ions reach the collector surfaces because of electrostatic reflections. These are due to the non-orthogonality between the ion trajectories and the equipotential surfaces of the decelerating electric field.

An example of ion trajectories simulated with IBSimu is shown in figure 5.14 for Case 2. The trajectories of the residual positive ions are plotted in red, those of the residual negative ions in blue, while the colour orange represents the neutral atoms that, being unaffected by the coil magnetic field, continue straight towards the tokamak. Already from a graphical point of view, one can see that the residual ions are successfully separated and collected.

The ion collection efficiencies for all the considered cases are listed in table 5.1. The numbers in the table confirm that practically all residual ions are collected for a residual ion energy of 50 keV. If the ion velocity is further decreased, more ions are lost due to electrostatic reflections. However, the collection efficiency for an ion residual energy of 25 keV is still very high and close to 100 %.

5.5.2 Trapping of secondary electrons

In order to simulate the emission of secondary electrons following the impact of the residual negative ions onto the collector surfaces, the following assumptions

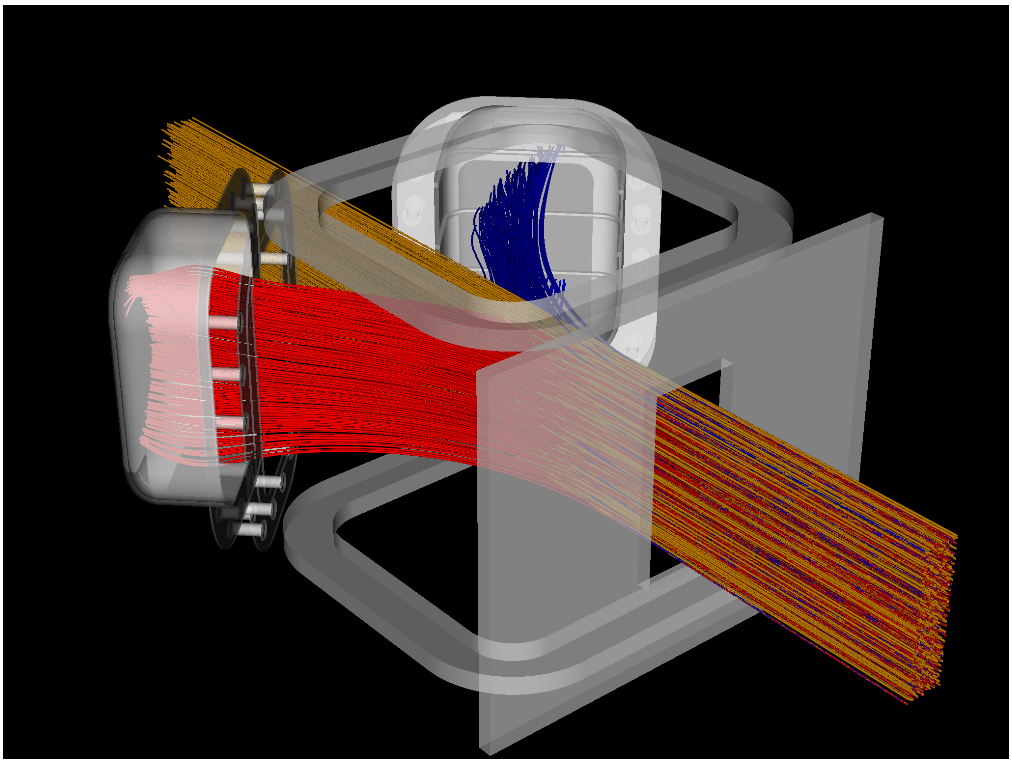

(a)

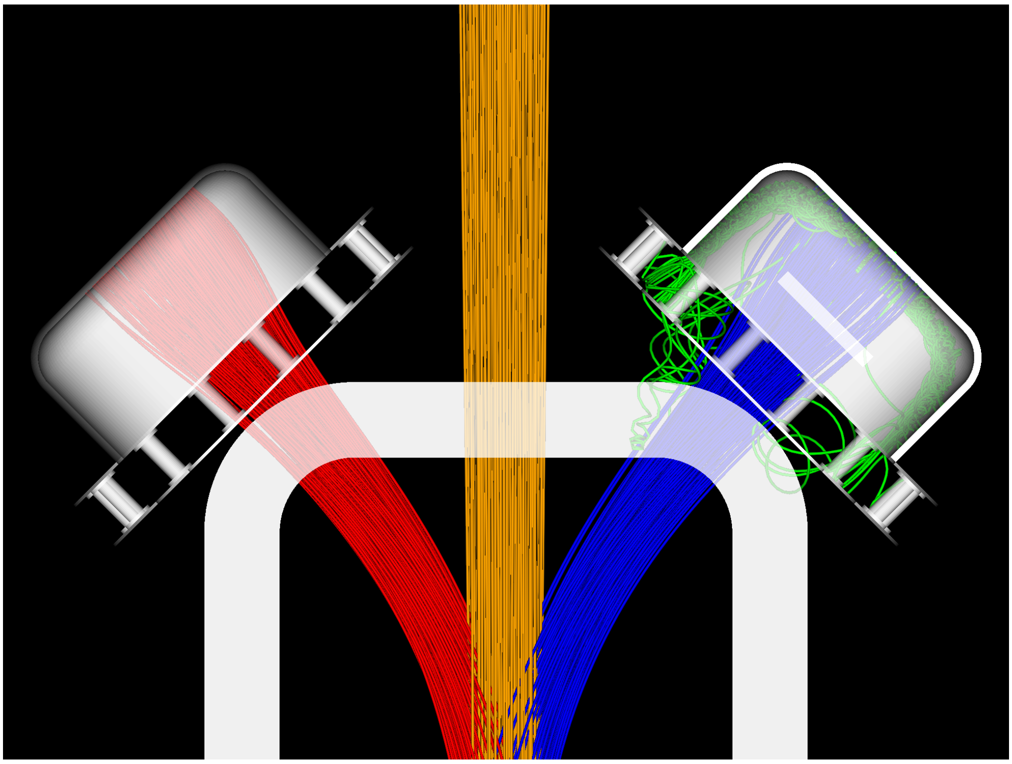

(b)

Figure 5.14: Particle simulations performed by IBSimu for an ITER-like beam in the ERS in Case 2. Particles are identified by different colours: negative ions, blue; positive ions, red; neutrals, orange; secondary electrons emitted by the negative ion collector surfaces, green. (a) Lateral view. (b) Top view.

are made:

- The secondary electron yield (SEY) as a function of the energy and impacting angle of the negative deuterium ions is taken from Fubiani et al [149].
- The angular dependence of the emitted electrons is described by a cosine distribution.
- The secondary electron energy spectrum has a bell-like shape in the range 0–50 eV. Therefore, as suggested by Fubiani et al., it is assumed that the secondary electrons are emitted at a fixed energy, equal to 10 eV, as this energy is negligible with respect to the energy that the electrons gain if accelerated by the decelerator electric field.

The trajectories of the secondary electrons emitted by the negative ion collector in Case 2 are plotted in green in the top view of figure 5.14 and for different views of the collector in figure 5.15.

Almost all secondary electrons remain inside the collector mainly because either

- they are deflected by the magnetic cusp field against the collector surfaces as soon as they are emitted or
- they are trapped in a magnetic mirror as they gyrate back and forth around the magnetic field lines generated by the permanent magnets.

Some of them, however, manage to escape. A secondary electron trapping efficiency g_{SE}, i.e. the fraction of emitted secondary electrons that remain inside the cup and are not accelerated through the decelerator electrodes, is calculated and shown in table 5.1 for all the considered cases.

It is interesting to observe that the fringe magnetic field of the coil system is very effective in deflecting the emitted electrons onto the lateral walls of the cup. Indeed, the trapping efficiency without permanent magnets on the

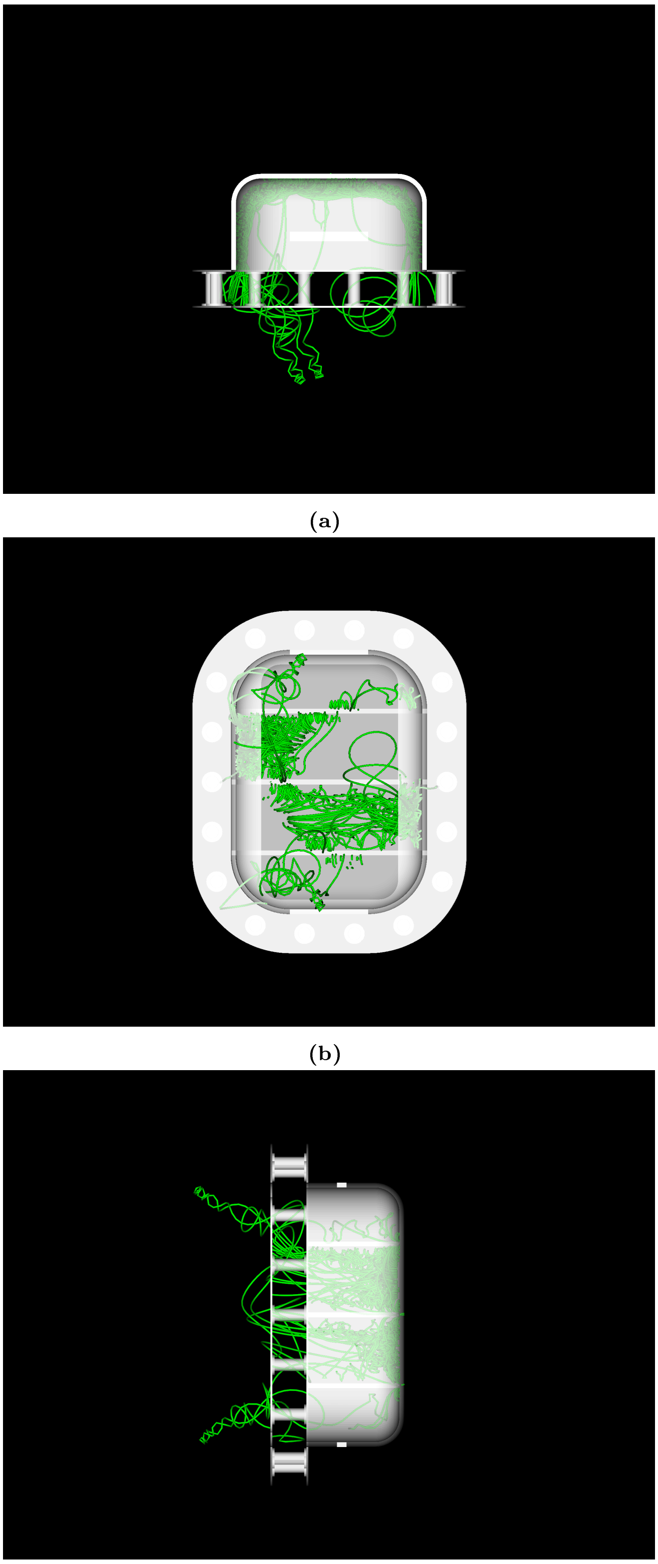

(a)

(b)

(c)

Figure 5.15: Trajectories of the secondary electrons emitted by the negative ion collector in Case 2 computed by IBSimu and shown for different views of the collector. (a) Top view. (b) Frontal view. (c) Lateral view.

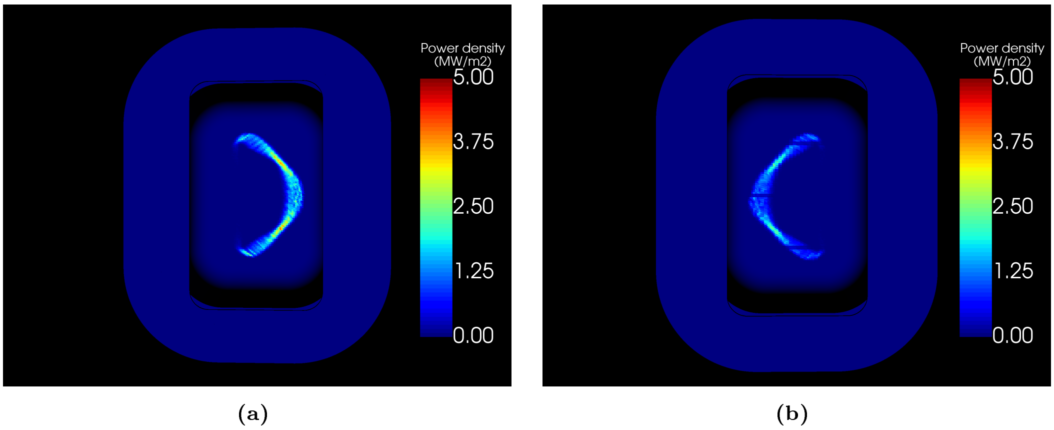

(a) (b)

Figure 5.16: Power density on the collector back plate due to the impact of the residual ions in Case 2. (a) Positive ion collector. (b) Negative ion collector.

collector walls is around 90 %. Nonetheless, it can be increased to almost 100 % by means of the magnetic cusp field.

5.5.3 Power deposition on the collectors

The power loads on the collector back plates due to the impact of the residual ions are shown in figure 5.16 for Case 2. The maximum power load on the positive ion collector is lower than $5\,\mathrm{MW\,m^{-2}}$ (figure 5.16a), while it is lower than $3\,\mathrm{MW\,m^{-2}}$ on the negative ion collector (figure 5.16b) due to a lower fraction of negative ions. Hence, the power deposited by the ions on the collector back plates does not pose any critical issue. In Case 3, where the ions hit the collector surface with a lower velocity, the power densities are even lower than those in Case 2.

5.5.4 Effect of space charge

The results shown so far have been obtained by IBSimu for residual ion beams that are fully space charge compensated all along their way up to the collector back plates. This, however, could not be the case in the decelerators as, while the residual ions decelerate (subsequently increasing the beam charge density), the compensating secondary charges, which are generated by gas ionisation and

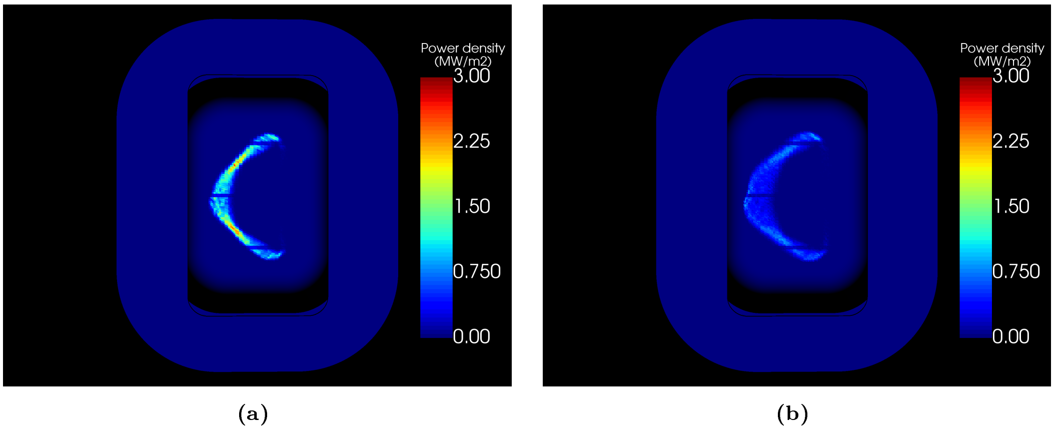

(a) (b)

Figure 5.17: Power density on the collector back plate due to the impact of the residual negative ions in Case 2. The space charge of the residual negative ion beam is (a) fully compensated and (b) uncompensated.

Table 5.2: Residual ion collection efficiencies computed by IBSimu in Cases 2 and 3 with a full and without space charge compensation.

	Case 2		Case 3	
Residual ion energy [keV]	50		25	
Space charge compensation [%]	100	0	100	0
Negative ion collection efficiency g^- [%]	99.69	99.38	97.76	0.04
Positive ion collection efficiency g^+ [%]	99.40	97.98	96.71	0.00

trapped inside the beams, accelerate. Therefore, the impact of space charge on the ion trajectories is investigated by considering the worst-case scenario, i.e. the residual ion beams in the decelerators are uncompensated.

Figure 5.17 shows the power density on the collector back plate due to the impact of the residual negative ions in Case 2 for the cases of complete compensation, on the left, and no compensation, on the right. Figure 5.17a is the same as figure 5.16b but with a different colour map for the power density. One can see that, for a recovery voltage V_r of 50 kV, the space charge does increase the beam divergence, yet almost all ions are still collected. The ion collection efficiencies with full and without compensation are listed in table 5.2. They are close to 100 % even in the pessimistic scenario of uncompensated beams.

On the other hand, if a recovery voltage V_r of 25 kV is assumed, the space charge forces on the beam become so strong that the beam blows up. Indeed, the ion collection efficiency computed by IBSimu for Case 3 without space charge compensation are practically zero.

5.6 Efficiency calculations

After presenting the ERS design and performing particle tracking simulations to determine the main system parameters, an ERS efficiency can now be defined and the impact of the ERS on the NBI wall-plug efficiency evaluated.

5.6.1 ERS efficiency

Considering a beam of current I_{acc} accelerated through a potential difference V_{b}, the power associated with the residual ions at the neutraliser exit is

$$P_{\mathrm{res}} = I_{\mathrm{acc}} V_{\mathrm{b}} (F^{-} + F^{+}), \tag{5.15}$$

with F^{-} and F^{+} being the fractions of the residual negative and positive ions, respectively.

With reference to the electric schematic of figure 5.1, using an ERS reduces the power wasted in residual ions as

$$P_{\mathrm{res,ERS}} = P_{\mathrm{res}} - P_{\mathrm{rec}}, \tag{5.16}$$

with

$$P_{\mathrm{rec}} = I_{\mathrm{acc}}\, F^{-} g^{-} (V_{\mathrm{b}} - V_{\mathrm{r}}) + I_{\mathrm{acc}}\, F^{+} g^{+} (V_{\mathrm{b}} - V_{\mathrm{r}}) \mu - I_{\mathrm{SE}} (1 - g_{\mathrm{SE}})(V_{\mathrm{b}} - V_{\mathrm{r}}). \tag{5.17}$$

The first and second terms on the right-hand side of equation (5.17) account for the recovery of the residual negative and positive ion energy, respectively. The term $I_{\mathrm{SE}}(1 - g_{\mathrm{SE}})(V_{\mathrm{b}} - V_{\mathrm{r}})$ is the power loss due to the acceleration of the secondary electrons that are emitted by the negative ion collector following the impact of the residual ions and that are not suppressed by the magnetic cusp field.

The ERS efficiency can then be defined as

$$\eta_{\mathrm{ERS}} = \frac{P_{\mathrm{rec}}}{P_{\mathrm{res}}}. \tag{5.18}$$

In the following, an ITER-like negative deuterium ion beam with a current I_{acc} of 40 A and an energy eV_{b} of 1 MeV is assumed.

At the exit of the gas neutraliser in case of optimum gas target thickness, the species fractions are: $F^{-} = 0.19$, $F^{+} = 0.26$ and $F^{0} = 0.55$. By using the efficiencies of table 5.1 and assuming an MRC conversion efficiency μ of 0.81, one obtains $\eta_{\mathrm{ERS}} = 84\,\%$ for $V_{\mathrm{r}} = 50\,\mathrm{kV}$ and $\eta_{\mathrm{ERS}} = 83\,\%$ for $V_{\mathrm{r}} = 25\,\mathrm{kV}$. The ERS efficiency is almost identical in the two cases as the higher degree of energy recovery achieved by decelerating the ions to a lower energy is counterbalanced by a lower collection efficiency due to the electrostatic reflections of the ions. As this latter effect increases for decreasing velocities, there is no benefit in decelerating the ions to an energy lower than 50 keV. Additionally, space charge expansion becomes critical for lower recovery voltages if the residual ion beams are not fully compensated. Therefore, only the residual energy of 50 keV is considered in the following.

An ERS could also be used in combination with a beam-driven plasma neutraliser. In this case, according to the predictions of the analytical model presented in the previous chapter, the species fractions at the exit of the ITER-like BDPN for an optimum target thickness are: $F^{-} = 0.13$, $F^{+} = 0.19$ and $F^{0} = 0.68$. The data of table 5.1 for Case 2, which are obtained with IBSimu for different yet similar fractions of residual ions, are used. Hence, one obtains $\eta_{\mathrm{ERS}} = 83\,\%$.

The recovery of the residual positive ion energy presents more complications compared to the case of negative ions. Not only is a positive high-voltage power supply needed, which in turn requires dedicated high-voltage transmission line and bushing to enter the vacuum vessel, but the recovered positive ion power must also be converted into useful electrical power by means of modular resonant converters whose efficiency, tested on a small scale, is only around 80 % [98]. Therefore, one could recover only the residual negative ion energy and dump the residual positive ions at full energy. In this case, the ERS efficiency would be only 39 % with a gas neutraliser and 38 % with a BDPN. The results are summarised in table 5.3.

5.6.2 Impact of ER on the NBI wall-plug efficiency

Using the nomenclature of table 3.2, the NBI wall-plug efficiency is estimated as

$$\eta_{\mathrm{wp}} = \frac{P_{\mathrm{NBI}}}{P_{\mathrm{el}}} = \frac{I_{\mathrm{acc}} V_{\mathrm{b}}\, \eta_{\mathrm{BT}}\, \eta_{\mathrm{neut}}}{\dfrac{I_{\mathrm{acc}} V_{\mathrm{b}} + P_{\mathrm{acc}}}{\eta_{\mathrm{PS}}} + P_{\mathrm{aux}}}, \tag{5.19}$$

where the numerator P_{NBI} is the neutral beam power delivered to the tokamak, the denominator P_{el} is the electrical power consumed by the injector, η_{BT} is the beamline transmission efficiency, η_{neut} is the neutralisation efficiency, P_{acc} is the power lost in the accelerator due to stripping of the negative ions, η_{PS} is the ion source power supply efficiency and P_{aux} is the power consumption of the auxiliary systems. The electrical power P_{aux} is mostly consumed by the cryopumps, the RF ion source, the ACC coils and the water cooling systems.

As an ITER-like injector is considered, the same values of the parameters in equation (5.19) as those in table 3.2 are assumed. Therefore, with a gas neutraliser, for which the maximum neutralisation efficiency is $\eta_{\mathrm{neut}} = 0.55$, the wall-plug efficiency is $\eta_{\mathrm{wp}} = 26\,\%$. With a BDPN, for which the maximum neutralisation efficiency predicted by the analytical model of chapter 4 is $\eta_{\mathrm{neut}} = 0.68$, $\eta_{\mathrm{wp}} = 32\,\%$.

Providing the injector with an ERS could reduce the power invested in the acceleration of the residual ions. In modifying the electrical power consumed by the injector P_{el}, also the efficiency of the additional power supplies is taken into account. In particular, it is assumed that the power supply providing the recovery potential $-V_{\mathrm{r}}$ and the power supply applying the potential $+V_{\mathrm{coll}}$ to the positive residual ion collector have the same efficiency η_{PS} as that of the ion source power supply, i.e. $\eta_{\mathrm{PS}} = 0.875\,\%$.

The power P_{el} is then given by the summation of the following terms:

+ the power effectively delivered by the ion source power supply as, the negative residual ion collector being directly connected to the ion source potential, the current drained from the high-voltage power supply is reduced by the residual negative ion current $I_{\mathrm{acc}}\,F^{-}g^{-}$

$$\frac{I_{\mathrm{acc}}V_{\mathrm{b}}(1 - F^{-}g^{-}) + P_{\mathrm{acc}}}{\eta_{\mathrm{PS}}}$$

+ the power P_{aux} consumed by the auxiliary systems

+ the power delivered by the recovery power supply at the potential $-V_{\mathrm{r}}$

$$\frac{I_{\mathrm{acc}}\,F^{-}g^{-}V_{\mathrm{r}}}{\eta_{\mathrm{PS}}}$$

− the power output of the MRCs which is recirculated in the system

$$I_{\mathrm{acc}}\,F^{+}g^{+}(V_{\mathrm{b}} - V_{\mathrm{r}})\mu\,\eta_{\mathrm{PS}}$$

+ the power loss due to the acceleration of the secondary electrons generated by the residual ions impacting on the negative ion collector

$$\frac{I_{\mathrm{SE}}(1 - g_{\mathrm{SE}})(V_{\mathrm{b}} - V_{\mathrm{r}})}{\eta_{\mathrm{PS}}}.$$

Hence, P_{el} is calculated as

$$\begin{aligned} P_{\mathrm{el}} = \frac{I_{\mathrm{acc}}V_{\mathrm{b}}(1 - F^{-}g^{-}) + P_{\mathrm{acc}}}{\eta_{\mathrm{PS}}} + P_{\mathrm{aux}} + \frac{I_{\mathrm{acc}}\,F^{-}g^{-}V_{\mathrm{r}}}{\eta_{\mathrm{PS}}} + \\ - I_{\mathrm{acc}}\,F^{+}g^{+}(V_{\mathrm{b}} - V_{\mathrm{r}})\mu\,\eta_{\mathrm{PS}} + \frac{I_{\mathrm{SE}}(1 - g_{\mathrm{SE}})(V_{\mathrm{b}} - V_{\mathrm{r}})}{\eta_{\mathrm{PS}}}. \end{aligned} \tag{5.20}$$

Table 5.3: ERS efficiency and wall-plug efficiency calculated for an NNBI that foresees either a gas neutraliser or a BDPN. Three cases are considered: no energy recovery, only the energy of the residual negative ions D^- is recovered, the energy of both residual positive D^+ and negative ions D^- is recovered. The recovery voltage is $V_r = 50\,\text{kV}$. The efficiencies are calculated for the optimum target thickness in the neutraliser.

Efficiency	ER	Gas neutraliser + ERS	BDPN + ERS
η_{ERS}	D^-	39 %	38 %
	D^- and D^+	84 %	83 %
η_{wp}	None	26 %	32 %
	D^-	29 %	34 %
	D^- and D^+	33 %	37 %

For an ITER-like gas-neutraliser-based NNBI and a recovery voltage V_r of 50 kV, $\eta_{\text{wp}} = 33\,\%$ if the energy of the residual ions of both polarities is recovered and $\eta_{\text{wp}} = 29\,\%$ if only the energy of the residual negative ions is recovered.

For the combination BDPN+ERS, the NBI wall-plug efficiency is $\eta_{\text{wp}} = 37\,\%$ if the energy of both residual D^- and D^+ ions is recovered and $\eta_{\text{wp}} = 34\,\%$ if only the energy of the residual D^- ions is recovered. The results are summarised in table 5.3.

The efficiencies of table 5.3 are calculated for the beam species fractions that one obtains at the neutraliser exit for an optimum target thickness in the case of a beam of D^- ions with an energy of 1 MeV. Figure 5.18 shows the wall-plug efficiency as a function of the target thickness in the case of the gas neutraliser. The upper part of the figure shows the evolution of the beam species fractions, while in the lower part the corresponding values of wall-plug efficiency are plotted for the cases in which the energy of both the residual negative and positive ions is recovered (red line) and only the negative ion energy is recovered (green line). A bias voltage $V_r = 50\,\text{kV}$ is assumed. In evaluating equation (5.20), the term $I_{\text{SE}}(1 - g_{\text{SE}})(V_b - V_r)/\eta_{\text{PS}}$ is neglected as the value of the current of secondary electrons emitted by the collector surface, although roughly proportional to the fraction of residual negative ions, needs

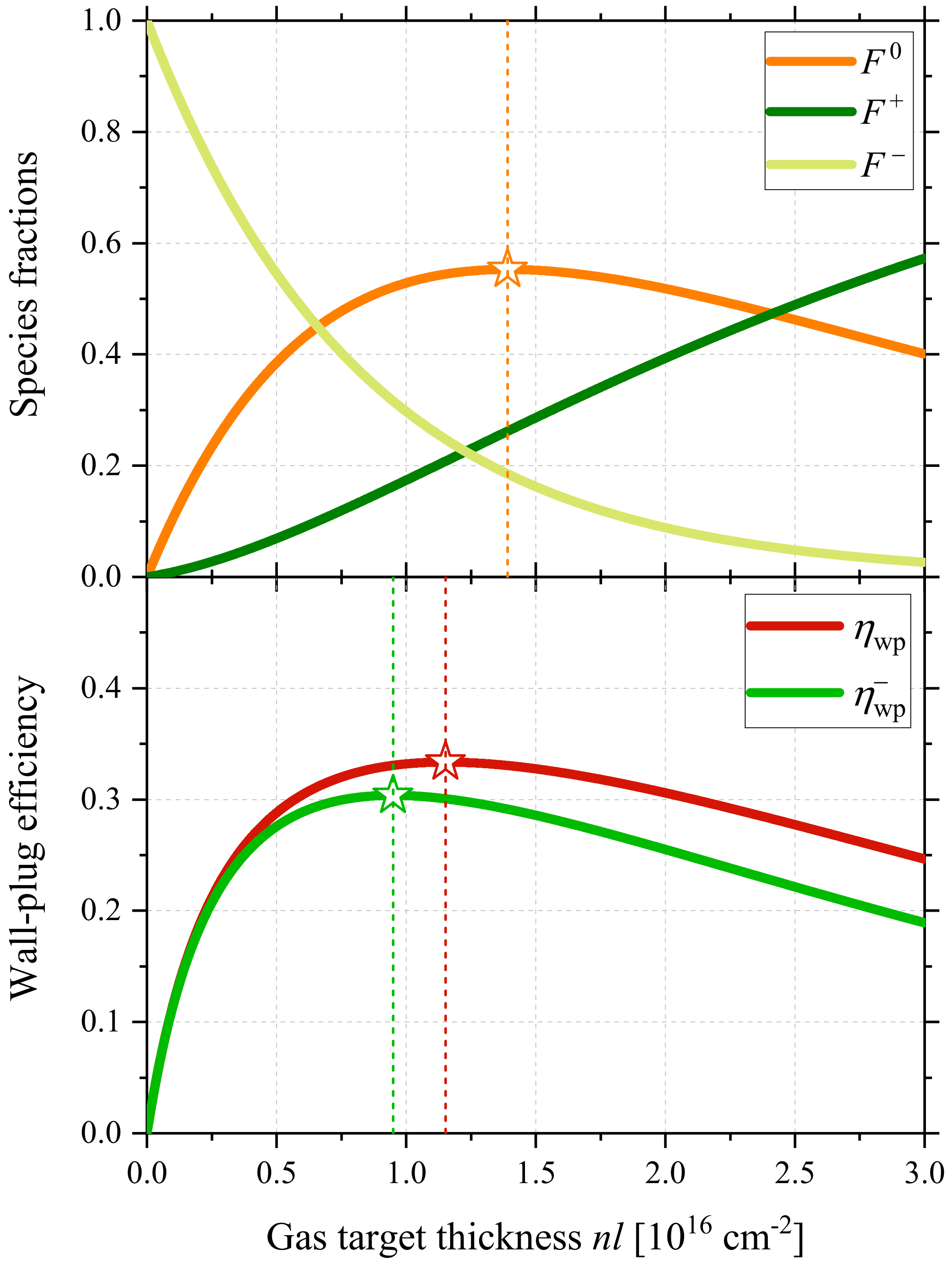

Figure 5.18: Beam charge fractions with a gas neutraliser and NBI wall-plug efficiency as functions of the gas target thickness for a 1 MeV D^- ion beam. F^0, F^+ and F^- indicate the fractions of neutral, positive and negative beam particles, respectively. η_{wp} and η^-_{wp} are the injector wall-plug efficiency if the energy of both residual positive and negative ions or only the energy of the residual negative ions is recovered, respectively. A recovery voltage $V_r = 50\,kV$ is assumed. The stars identify the maximum values.

to be estimated by particle tracking simulations as done with IBSimu for the optimum ion fraction. However, as one can expect secondary electron trapping efficiencies close to 100 %, the loss term can be neglected: for the optimum gas target thickness, it is only 0.13 MW with respect to a power of 57 MW invested in the ion acceleration. The ion collection efficiencies are the same as those listed in table 5.1 for Case 2.

One can observe that the maximum wall-plug efficiency is obtained for a gas target thickness that is close to the value for which the maximum neutralisation efficiency is achieved. The maximum value of η_{wp} is 33 %. If only the residual D^- ion energy is recovered, the wall-plug efficiency η^-_{wp} is higher for gas thicknesses lower than the optimum one due to a higher fraction of residual negative ions. However, η^-_{wp} slightly increases from a value of 29 % for the optimum gas target thickness to a maximum value of 30 %. Therefore, it is not advantageous in terms of injector power efficiency to operate in the left region of the graph as suggested by Hopman [106]. This would imply that the neutral fraction at the neutraliser exit is lower than 55 %, leading to a lower neutral beam power injected into the tokamak. As the current density from negative ion sources is limited, a lower power injection could be compensated by increasing the net extraction area, e.g. with a higher grid transparency or a bigger source and/or by increasing the acceleration voltage. These solutions, however, require drastic modifications and, most likely, an increase of the ancillary power [97].

5.6.3 The influence of the background gas pressure

Equation (5.20) neglects the power losses due to the reactions between the residual ions and the background gas. Evaluating these losses requires the knowledge of the gas pressure distribution along the system and the detailed velocity profile of the residual ions. A rough estimate is given by using simplifying hypotheses:

- A constant background gas pressure equal to that expected at the exit of the ITER gas neutraliser [57], i.e. 0.02 Pa, is assumed. This pressure corresponds to a gas density $n_{\mathrm{gas}} = 4.8 \times 10^{18}\,\mathrm{m}^{-3}$ for a gas temperature of 300 K.

- The residual ion energy profile is approximated by splitting the ERS into two regions: the residual ions travel a distance L_{sep} from the neutraliser exit to the decelerator entrance with an energy equal to eV_{b} and then a distance L_{coll} from the decelerator grounded frame up to the collector back plate with a constant energy equal to eV_{r}. A deceleration region is therefore neglected and it is assumed that the ion energy decreases from eV_{b} to eV_{r} as soon as the residual ions enter the decelerator. On the basis of the dimensions of the ERS of figure 5.13, the path lengths of the residual ions are approximated as $L_{\mathrm{sep}} = 4\,\mathrm{m}$ and $L_{\mathrm{coll}} = 1.4\,\mathrm{m}$.

The main reactions with the background gas molecules are:

- Residual negative ions.

  Stripping ($\sigma_{\text{-}10}$): $\hat{\mathrm{D}}^- + \mathrm{D}_2 \longrightarrow \hat{\mathrm{D}}^0 + \mathrm{D}_2 + \mathrm{e}$

  Double stripping ($\sigma_{\text{-}11}$): $\hat{\mathrm{D}}^- + \mathrm{D}_2 \longrightarrow \hat{\mathrm{D}}^+ + \mathrm{D}_2 + 2\mathrm{e}$

- Residual positive ions.

  Charge exchange (σ_{10}): $\hat{\mathrm{D}}^+ + \mathrm{D}_2 \longrightarrow \hat{\mathrm{D}}^0 + \mathrm{D}_2^+$

- Beam neutral atoms.

  Re-ionisation (σ_{01}): $\hat{\mathrm{D}}^0 + \mathrm{D}_2 \longrightarrow \hat{\mathrm{D}}^+ + \mathrm{D}_2 + \mathrm{e}$

Fast beam particles are denoted by a hat. The values of the cross sections σ are taken from Ref. [56].

The residual ion fractions at the neutraliser exit are F^- and F^+. After being deflected by the separating magnetic field, the residual ions reach the decelerator entrance with fractions F^-_{coll} and F^+_{coll}. On the other hand, the beam neutrals travel undisturbed towards the reactor and their fraction decreases from F^0 at the neutraliser exit to F^{*0} at the end of the ERS. The reduced beam species fractions are computed as:

$$F^-_{\mathrm{coll}} = F^-(1 - (\sigma^{\mathrm{b}}_{\text{-}10} + \sigma^{\mathrm{b}}_{\text{-}11})n_{\mathrm{gas}}\, L_{\mathrm{sep}}) \tag{5.21}$$

$$F^+_{\mathrm{coll}} = F^+(1 - \sigma^{\mathrm{b}}_{10}\, n_{\mathrm{gas}}\, L_{\mathrm{sep}}) \tag{5.22}$$

$$F^{*0} = F^0(1 - \sigma^{\mathrm{b}}_{01}\, n_{\mathrm{gas}}\, L_{\mathrm{ERS}}), \tag{5.23}$$

where L_{ERS} is the distance that the beam neutrals travel from the neutraliser exit to the end of the ERS. L_{ERS} is approximately 4.5 m. The superscript b indicates that the cross sections are evaluated at the energy eV_{b}.

Inside the decelerators, one has to consider not only the reduction of the residual ion fractions, but also the power loss due to the back-acceleration of the secondary charges created by the reactions between the residual ions and the background gas and by sputtering of the collector surfaces by the incident ions, as outlined in section 5.4.3. The secondary electrons generated in the negative ion collector and the positive ions generated in the positive ion collector are accelerated backwards to the energy $e(V_{\mathrm{b}} - V_{\mathrm{r}})$.

The residual ion fractions decrease from F^-_{coll} and F^+_{coll} at the decelerator entrance to F^{*-} and F^{*+} at the collector back plates. Hence, by using equations (5.21) and (5.22), one can write

$$\begin{aligned} F^{*-} &= F^-_{\mathrm{coll}}(1 - (\sigma^{\mathrm{r}}_{\text{-}10} + \sigma^{\mathrm{r}}_{\text{-}11})n_{\mathrm{gas}}\, L_{\mathrm{coll}}) = \\ &= F^-(1 - (\sigma^{\mathrm{b}}_{\text{-}10} + \sigma^{\mathrm{b}}_{\text{-}11})n_{\mathrm{gas}}\, L_{\mathrm{sep}})(1 - (\sigma^{\mathrm{r}}_{\text{-}10} + \sigma^{\mathrm{r}}_{\text{-}11})n_{\mathrm{gas}}\, L_{\mathrm{coll}}) \end{aligned} \tag{5.24}$$

$$\begin{aligned} F^{*+} &= F^+_{\mathrm{coll}}(1 - \sigma^{\mathrm{r}}_{10}\, n_{\mathrm{gas}}\, L_{\mathrm{coll}}) = \\ &= F^+(1 - \sigma^{\mathrm{b}}_{10}\, n_{\mathrm{gas}}\, L_{\mathrm{sep}})(1 - \sigma^{\mathrm{r}}_{10}\, n_{\mathrm{gas}}\, L_{\mathrm{coll}}), \end{aligned} \tag{5.25}$$

The superscript r indicates that the cross sections are evaluated at the energy eV_{r}. The above equations highlight that the bigger the ERS dimensions, the higher the losses of beam ions for the same background gas density. Therefore, limiting the ERS dimensions has been one of the drivers in designing the ERS concept proposed in this chapter.

It is assumed that all the secondary charges generated in the decelerators are back-accelerated, hence neglecting the effect of the fringe magnetic field generated by the separating coils which could deflect the secondary particles against the collector walls as it does with the secondary electrons emitted by the surface of the negative ion collector. In view of the assumption that the residual ions are fully decelerated as soon as they enter the decelerators, if the collisions with the background gas destroy the impacting residual ions, the power gain associated with the deceleration from the energy eV_b to the energy eV_r must be explicitly taken into account. Denoting the fast beam particles by a hat, the main processes that create secondary charges in the decelerators are:

- Gas ionisation by residual D^- and D^+ ions ($\sigma_{\text{i-}/+}$):

  $\hat{\mathrm{D}}^{-/+} + \mathrm{D}_2 \longrightarrow \hat{\mathrm{D}}^{-/+} + \mathrm{D}_2^+ + \mathrm{e}$.

  The power associated with the back-acceleration of the secondary electrons in the negative ion collector and of the secondary positive ions in the positive ion collector must be counted as additional invested power.

- Stripping of residual D^- ions ($\sigma_{\text{-}10}$): $\hat{\mathrm{D}}^- + \mathrm{D}_2 \longrightarrow \hat{\mathrm{D}}^0 + \mathrm{D}_2 + \mathrm{e}$.

  The loss of D^- ions due to stripping is described by equation (5.24). The residual negative ion is simply considered lost, but its deceleration compensates for the back-acceleration of the secondary electron.

- Double stripping of D^- ions ($\sigma_{\text{-}11}$): $\hat{\mathrm{D}}^- + \mathrm{D}_2 \longrightarrow \hat{\mathrm{D}}^+ + \mathrm{D}_2 + 2\mathrm{e}$.

  The loss of D^- ions due to double stripping is described by equation (5.24). The residual negative ion is simply considered lost, but its deceleration compensates for the back-acceleration of one of the two secondary electrons. The power associated with the back-acceleration of the second electron must be counted as additional invested power. If double stripping occurs outside the decelerator, i.e. before the residual ion is fully decelerated, the resulting positive ion could be accelerated in the collector. However, it is likely that the positive ion is deflected by the fringe magnetic field and does not enter the decelerator. The corresponding power loss is therefore neglected.

- Charge exchange of D^+ ions (σ_{10}): $\hat{\mathrm{D}}^+ + \mathrm{D}_2 \longrightarrow \hat{\mathrm{D}}^0 + \mathrm{D}_2^+$.

  The loss of D^+ ions due to charge exchange is described by equation (5.25). The residual positive ion is simply considered lost, but its deceleration compensates for the back-acceleration of the secondary positive ion.

- Sputtering.

  Assuming that the collectors are made of copper, the sputtering yield for deuterium ions with an energy of around 50 keV, i.e. the average number of particles removed from the collector copper surfaces per incident ion, is of the order of 10^{-2} [144]. Hence, considering that only a small portion of these particles are emitted as ions and that copper has one of the highest sputtering yields, the contribution of sputtering in creating secondary charges is negligible.

Therefore, the total power loss P_{sec} due to the back-acceleration of the secondary charges created by the residual ions in the decelerators is calculated as

$$P_{\mathrm{sec}} = \frac{I_{\mathrm{acc}}(F^{-}_{\mathrm{coll}}(\sigma^{\mathrm{r}}_{\text{i-}} + \sigma^{\mathrm{r}}_{\text{-11}}) + F^{+}_{\mathrm{coll}}\sigma^{\mathrm{r}}_{\mathrm{i+}})n_{\mathrm{gas}}\, L_{\mathrm{coll}}(V_{\mathrm{b}} - V_{\mathrm{r}})}{\eta_{\mathrm{PS}}}. \tag{5.26}$$

Finally, one can include the power losses due to the reactions between the residual ions and the background gas by modifying equation (5.20) as

$$\begin{aligned} P_{\mathrm{el}} = {} & \frac{I_{\mathrm{acc}}V_{\mathrm{b}}(1 - F^{*-}g^{-}) + P_{\mathrm{acc}}}{\eta_{\mathrm{PS}}} + P_{\mathrm{aux}} + \frac{I_{\mathrm{acc}}\,F^{*-}g^{-}V_{\mathrm{r}}}{\eta_{\mathrm{PS}}} + \\ & - I_{\mathrm{acc}}\,F^{*+}g^{+}(V_{\mathrm{b}} - V_{\mathrm{r}})\mu\,\eta_{\mathrm{PS}} + \frac{I_{\mathrm{SE}}(1 - g_{\mathrm{SE}})(V_{\mathrm{b}} - V_{\mathrm{r}})}{\eta_{\mathrm{PS}}} + P_{\mathrm{sec}}, \end{aligned} \tag{5.27}$$

while the numerator of the wall-plug efficiency in equation (5.19) becomes

$$P_{\mathrm{NBI}} = I_{\mathrm{acc}} V_{\mathrm{b}}\, \eta_{\mathrm{BT}}\, F^{*0}\, \eta_{\mathrm{reion}}. \tag{5.28}$$

The reduced beam species fractions F^{*0}, F^{*-}, F^{*+} and the power loss P_{sec} due to the acceleration of the secondary charges for a background gas pressure of 0.02 Pa are listed in table 5.4 for an ERS combined with both a gas neutraliser and a BDPN. The beam species fractions at the neutraliser exit are obtained for the optimum target thickness in the neutralisers. The resulting wall-plug efficiency is computed and listed in the same table. A recovery voltage $V_{\mathrm{r}} =$ 50 kV is assumed. The power loss $I_{\mathrm{SE}}(1 - g_{\mathrm{SE}})(V_{\mathrm{b}} - V_{\mathrm{r}})/\eta_{\mathrm{PS}}$ is neglected as the value obtained for a fraction F^{-} of residual negative ions impacting onto the collector surface equal to 0.19 is only 0.13 MW. Furthermore, the reduced fraction F^{*-} is much lower than F^{-}. The ion collection efficiencies are the same as those listed in table 5.1 for Case 2.

The reference case in table 5.4 is the case in which the ion–gas collisions are neglected, as firstly assumed at the beginning of this section. The comparison with the reference case highlights that the interactions of the beam ions with the background gas at a pressure of 0.02 Pa strongly reduce the fractions of residual ions that reach the collector back plate. Additionally, the neutral beam power at the ERS exit is lower and the power loss due to the acceleration of the secondary charges is of several MW. This results in a reduction of the wall-plug efficiency which is even lower than the value predicted for an injector that does not use energy recovery.

The role played by the background gas pressure p_{gas} is investigated in figure 5.19 where the wall-plug efficiency is plotted as a function of p_{gas} for both the combinations gas neutraliser-ERS and BDPN-ERS. In both cases, the wall-plug efficiency is higher than the reference value for p_{gas} around 0.01 Pa if the energy of both residual D^{-} and D^{+} ions is recovered, while a pressure of several 10^{-3} Pa is required if the energy of only the residual D^{-} ions is recovered.

Table 5.4: Wall-plug efficiency of an NNBI with either a gas neutraliser or a BDPN for different background gas pressures. The efficiency is calculated for the optimum target thickness in the neutraliser. The beam species fractions after the collisions with the background gas and the power terms in equation (5.27) are also shown. In the reference case, the beam–gas collisions are neglected.

		ER	Gas neutraliser + ERS		
			Reference	0.001 Pa	0.02 Pa
F^{*-}			0.19	0.18	0.059
F^{*+}			0.26	0.26	0.17
F^{*0}			0.55	0.55	0.50
$(I_{\mathrm{acc}}V_{\mathrm{b}} + P_{\mathrm{acc}})/\eta_{\mathrm{PS}}$	[MW]		57	57	57
$I_{\mathrm{acc}}\,F^{*-}g^{-}(V_{\mathrm{b}} - V_{\mathrm{r}})/\eta_{\mathrm{PS}}$	[MW]		8.2	7.9	2.6
$I_{\mathrm{acc}}\,F^{*+}g^{+}(V_{\mathrm{b}} - V_{\mathrm{r}})\mu\,\eta_{\mathrm{PS}}$	[MW]		6.9	6.8	4.5
$I_{\mathrm{SE}}(1 - g_{\mathrm{SE}})(V_{\mathrm{b}} - V_{\mathrm{r}})/\eta_{\mathrm{PS}}$	[MW]		0.13	-	-
P_{aux}	[MW]		10	10	10
P_{sec}	[MW]		-	0.11	1.9
η_{wp}	[%]	None	26	26	26
		D^-	29	29	24
		D^- and D^+	33	32	25

		ER	BDPN + ERS		
			Reference	0.001 Pa	0.02 Pa
F^{*-}			0.13	0.12	0.041
F^{*+}			0.19	0.19	0.12
F^{*0}			0.68	0.68	0.62
$(I_{\mathrm{acc}}V_{\mathrm{b}} + P_{\mathrm{acc}})/\eta_{\mathrm{PS}}$	[MW]		57	57	57
$I_{\mathrm{acc}}\,F^{*-}g^{-}(V_{\mathrm{b}} - V_{\mathrm{r}})/\eta_{\mathrm{PS}}$	[MW]		5.6	5.4	1.8
$I_{\mathrm{acc}}\,F^{*+}g^{+}(V_{\mathrm{b}} - V_{\mathrm{r}})\mu\,\eta_{\mathrm{PS}}$	[MW]		5.1	5.0	3.3
$I_{\mathrm{SE}}(1 - g_{\mathrm{SE}})(V_{\mathrm{b}} - V_{\mathrm{r}})/\eta_{\mathrm{PS}}$	[MW]		0.13	-	-
P_{aux}	[MW]		10	10	10
P_{sec}	[MW]		-	0.076	1.4
η_{wp}	[%]	None	32	32	32
		D^-	34	34	29
		D^- and D^+	37	37	31

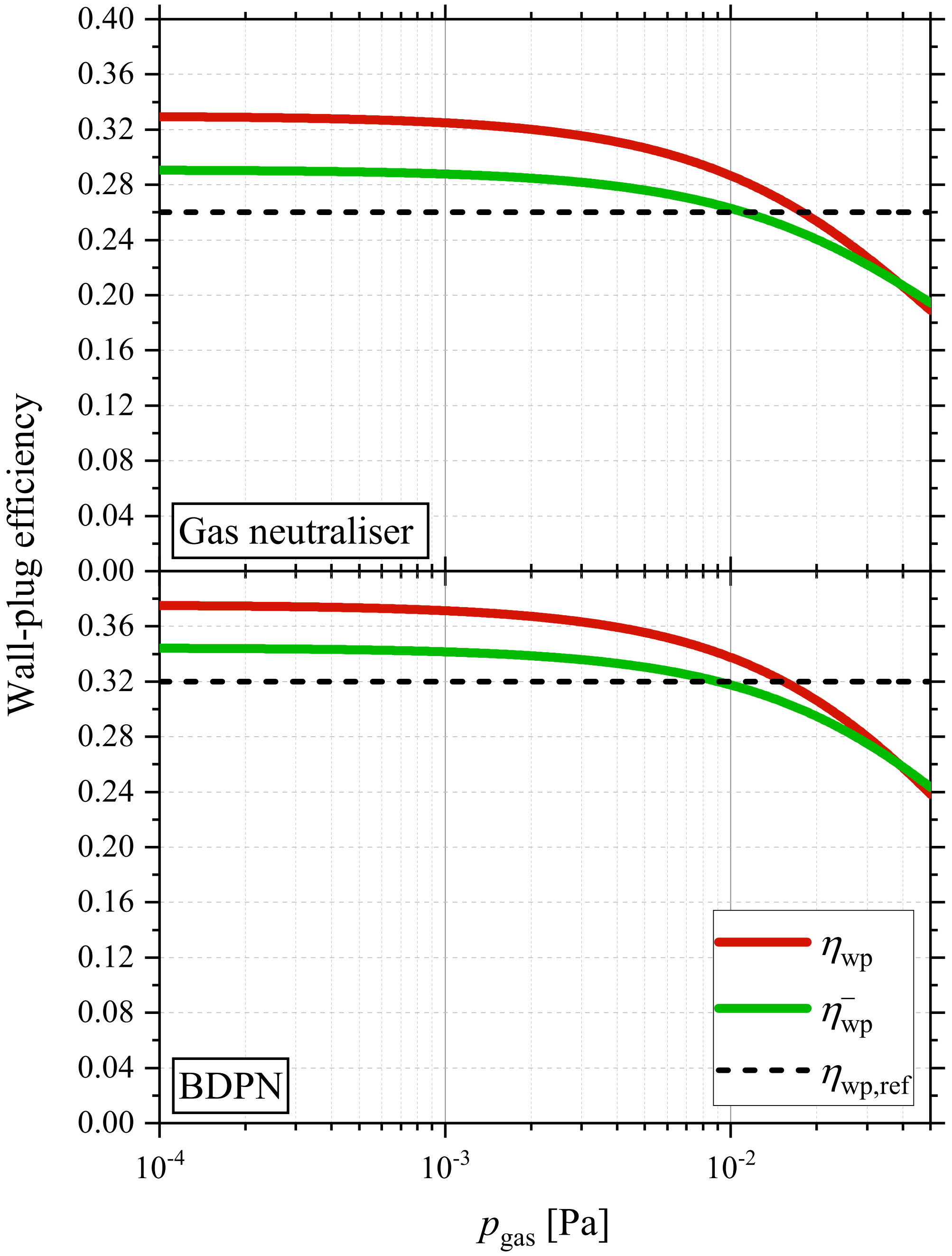

Figure 5.19: NBI wall-plug efficiency η_{wp} as a function of the background gas pressure p_{gas} for the ERS combined with both the gas neutraliser and the BDPN. η^-_{wp} is the injector wall-plug efficiency if only the energy of the residual negative ions is recovered. The values $\eta_{\mathrm{wp,ref}}$ neglect the beam–gas collisions.

In general, a background gas pressure of the order of 10^{-3} Pa allows minimising the deleterious effects of the reactions between the beam ions and the gas molecules. The power losses and the wall-plug efficiency for a gas pressure of 10^{-3} Pa are listed in table 5.4. One can see that the efficiency values are very close to those of the reference case.

Such a low value of gas pressure in the ERS region would be possible for two main reasons: the magnetic shield at the neutraliser exit reduces the gas flow coming from the upstream part of the injector and the open structure of the energy recovery system allows a better pumping access compared to the ERID on the ITER NBI. It is however a demanding situation for the pumps: in the case of the gas neutraliser, if the gas inlet is in the middle of the chamber, half of the optimum gas throughput $Q = 14.6\,\mathrm{Pa\,m^3\,s^{-1}}$ will flow into the ERS region. Assuming that this is the only gas source, a background gas pressure of 10^{-3} Pa downstream of the neutraliser would require a pumping speed of $7300\,\mathrm{m^3/s}$. Such a simple estimate is already more than twice the pumping speed foreseen for the ITER NNBI which is $3600\,\mathrm{m^3/s}$ for deuterium [59]. Additionally, one has to consider that a lower background gas density would impose distances between the electrodes higher than those assumed in the proposed ERS conceptual design in order to guarantee stable voltage holding. Higher distances lead to a longer and wider beamline resulting in an increase of the power losses despite a lower background gas density. Therefore, a compromise needs to be found.

5.7 Summary and conclusions

The conceptual design of an energy recovery system (ERS) for the DEMO NBI has been proposed with the aim of increasing the injector wall-plug efficiency. The DEMO NBI is approximated by considering the ITER injector. Energy recovery consists in decelerating to almost zero energy the residual ions of the neutralisation process after separating them depending on their charge.

- The collected current of residual negative ions can be directly recirculated in the system by connecting the negative ion collector, biased at $-V_{\mathrm{coll}}$, to the ion source potential $-V_{\mathrm{b}}$ by providing a bias $-V_{\mathrm{r}}$ such that $V_{\mathrm{coll}} = V_{\mathrm{b}} - V_{\mathrm{r}}$. This leads to a reduction of the current drained from the high-voltage power supply at $-V_{\mathrm{b}}$.

- The positive ion collector is biased at $+V_{\mathrm{coll}}$. Hence, it cannot be connected to the ion source power supply. The recovered positive ion power can be converted into electrical power and hence recirculated by using modular resonant converters (MRCs) whose efficiency, tested on a small scale, is however just above $80\,\%$.

The ERS design choices have been explained in detail and here briefly summarised by identifying the three main steps of energy recovery:

- **Charge separation**: the residual negative and positive ions are separated at the neutraliser exit into different directions by a magnetostatic field generated by a Helmholtz-like coils which are based on the ACCC design. Hence, they could also be used to minimise the stray magnetic field from the tokamak. In order to avoid unwanted deflections of the beam ions in the neutraliser, the fringe magnetic field of the coils is reduced by a soft steel shield placed between the coils and the neutraliser. An aperture in the shield lets the beam pass through. The shield acts also as gas baffle, reducing the gas pressure in the downstream part of the beamline.

- **Ion deceleration**: the residual ions undergo a one-step deceleration between a grounded frame and a collector biased at $\pm V_{\mathrm{coll}}$. Thus, the ions are decelerated down to the energy eV_{r}. A complete deceleration is not possible because of the electrostatic reflections due to the non-orthogonality between the ion trajectories and the equipotential surfaces of the decelerating electric field. The grounded frame and the biased collector are supported by mounting flanges connected through ceramic post-insulator. The whole decelerator structure is sustained by a supporting system mounted on the grounded flange. Considerations about voltage holding allow sizing the system: using the clump theory to describe the breakdown probability and on the basis of experimental results, the distances between the decelerator flanges and between the two decelerators required to sustain high potential differences in vacuum are determined. Peak values of the electric field that may cause unwanted breakdowns are avoided by using large radius curvatures for all the edges of the system.

- **Ion collection**: the most important issue in collecting the decelerated residual ions is the emission of secondary electrons induced by ion impact on the collector surfaces. In the negative ion collector, these electrons experience a positive potential difference and are hence accelerated towards the grounded frame, cancelling the benefits of energy recovery. In order to suppress them before being accelerated, permanent magnets are placed on the collector walls. The resulting magnetic cusp field suppresses the secondary electrons close to their origin. Additional secondary charges are created by the interactions between the residual ions and the background gas in the collectors, while the contribution of the collector surface sputtering in creating secondary charges is negligible for the residual energy of the ions in the collectors.

The proposed ERS design has been tested in combination with the gas neutraliser using the particle tracking code IBSimu. The trajectories of the residual ions from the neutraliser exit to the collector back plates with and without space charge compensation, the emission of secondary electrons from the negative ion collector and the powers loads on the collectors due to the impacting residual ions have been investigated. The numerical simulations show that both the ion collection efficiencies and the secondary electron suppression efficiency are close to 100 % for two values of the recovery voltage V_r, i.e. 25 kV and 50 kV. When the hypothesis of full space charge compensation of the residual ion beams in the collectors is removed, the ion collection efficiencies at $V_\mathrm{r} = 50\,\mathrm{kV}$ slightly decrease as the space charge force increases the effective divergence of the beams and, hence, the occurrence of electrostatic deflections. The beam charge density increasing for lower ion velocities, at $V_\mathrm{r} = 25\,\mathrm{kV}$ the space charge force is so strong that the residual ion beams blow up before reaching the collector walls. The power loads on the collector back plates do not pose any critical issue.

The ERS efficiency is defined as the fraction of residual ion power that is recovered. As first approximation, the collisions between residual ions and background gas are neglected. In the case of a gas neutraliser, the ERS efficiency is 84 % for $V_\mathrm{r} = 50\,\mathrm{kV}$ and 83 % for $V_\mathrm{r} = 25\,\mathrm{kV}$. Hence, decelerating the ions to an energy of 25 keV does not improve the ERS efficiency because of a lower ion collection due to the electrostatic reflections of the ions.

Therefore, a voltage of 50 kV, corresponding to 5 % of the beam acceleration potential V_b, is assumed as the minimum recovery voltage that allows collecting almost all residual ions even in the case of uncompensated beams. For an ERS in combination with the BDPN, the ERS efficiency is 83 %.

The wall-plug efficiency of an ITER-like injector is 26 % with a gas neutraliser and 32 % with a BDPN. Implementing an ERS increases the wall-plug efficiency to 33 % and 37 %, respectively. The recovery of the residual positive ion energy is more challenging compared to the case of negative ions: a positive high-voltage power supply is needed, together with dedicated transmission line and bushing to enter the NBI vacuum vessel, and the recovered positive ion power must be converted into useful electrical power by using MRCs whose efficiency is only around 80 %. Hence, one could decide to recover only the residual negative ion energy and to dump the residual positive ions at full energy. In this case, the wall-plug efficiency is 29 % with a gas neutraliser and 34 % with a BDPN.

One of the main findings is the significant impact of the background gas pressure along the injector: including the collisions between the residual ions and the background gas causes a strong reduction of the wall-plug efficiency. These collisions have three main deleterious effects:

- reduction of the residual ions that reach the collectors, mainly because of stripping and double stripping for the negative ions and of charge exchange for the positive ions;
- reduction of the beam neutrals that exit the ERS because of re-ionisation;
- acceleration of the secondary charges created by the residual ions colliding with the background gas molecules in the collectors.

For a gas pressure of 0.02 Pa, which is the pressure expected at the exit of the ITER gas neutraliser, the wall-plug efficiency is reduced to 25 % for an ERS after the gas neutraliser and to 31 % for an ERS after the BDPN. In other words, the wall-plug efficiency is even lower than that of an NBI without energy recovery.

The values of wall-plug efficiency are similar to those obtained by neglecting the interactions with the background gas for a gas pressure of around 10^{-3} Pa. A lower value of the background gas pressure in the ERS region would be possible due to the presence of the magnetic shield and to the ERS open structure that allows a good pumping access. However, in that case, there would be some aspects that need to be further investigated:

- A lower gas pressure implies higher distances between the electrodes in the ERS than those assumed in the proposed design in order to assure stable voltage holding. This means that the beamline becomes longer and wider leading to an increase of the power losses despite a lower gas pressure. A reasonable compromise between gas pressure and injector size has to be made.

- A lower gas pressure makes it difficult to achieve full space charge compensation of the residual ion beams in the decelerators as less compensating secondary charges are produced by ionisation. This would reduce the ion collection efficiencies and, hence, the injector wall-plug efficiency.

Such an analysis requires the detailed profile of the background gas pressure along the beamline and of the residual ion energy in the decelerators. Additionally, voltage holding experiments are needed to confirm that high voltages can be sustained at different gas pressures.

Chapter 6

Conclusions and outlook

In order to demonstrate the commercial viability of fusion, the heating and current drive systems of the European DEMO will have a higher energy efficiency than that of the ITER systems. This thesis has focused on how to increase the wall-plug efficiency of the negative-ion-based neutral beam injection (NNBI). Two concepts have been proposed and investigated with reference to an ITER-like NNBI as the current DEMO baseline design, DEMO-1, is a modest extrapolation from ITER.

In chapter 4, the beam-driven plasma neutraliser (BDPN) has been presented as alternative to the gas neutraliser foreseen for the ITER NNBI. An analytical model has been developed to predict the BDPN performance.

For an ITER-like beam of D^- ions with an energy of $1\,\mathrm{MeV}$ and a current of $40\,\mathrm{A}$, the model applied to the BDPN design assumed in this thesis predicts a plasma density of $2.1 \times 10^{18}\,\mathrm{m}^{-3}$ with D^+ being the dominant ion species, an ionisation degree of $8.0\,\%$ and a plasma electron temperature of $1.1\,\mathrm{eV}$. The resulting neutralisation efficiency is $68\,\%$. Furthermore, a neutral gas temperature of $520\,\mathrm{K}$ is estimated which, together with the absence of internal channels, leads to a gas inlet flow rate of $60\,\mathrm{Pa\,m^3\,s^{-1}}$ (in comparison, the optimum gas inflow rate for the gas neutraliser is $14.6\,\mathrm{Pa\,m^3\,s^{-1}}$ [57]).

As an ITER-like ion beam that would benchmark these analytical predictions is not available in the near future, it is suggested to drop the objective of demonstrating the neutralisation efficiency improvement, which requires an ion beam energy around 1 MeV, and to focus only on validating the confinement of the plasma generated through the beam-driven mechanism. To this end, the filament-driven plasma experiment, in which no ion beam is involved and the electrons emitted by heated filaments are used to simulate the electrons that are mainly responsible for the plasma generation, i.e. the stripped electrons, has been identified as the most suitable proof-of-principle experiment. The main advantages are:

- electrons with the same current and energy as the ITER-like stripped electrons can be generated;
- a full-scale test is possible such that no result extrapolation to the DEMO scale is necessary;
- many parameters, like the filament heating current and bias voltage, can be scanned over a wide range making it possible, for instance, to simulate negative ion beams with an energy higher than 1 MeV.

While the wall-plug efficiency of the ITER NNBI is only 26 %, the use of a BDPN would increase it to 32 %. This enhancement justifies the efforts in pursuing the BDPN technology. A detailed design of the proof-of-principle experiment and the optimisation of the DEMO BDPN design are envisaged as next steps in the near future.

In chapter 5, the conceptual design of an energy recovery system (ERS) for an ITER-like NNBI has been proposed and its performance has been simulated by using a particle tracking code. One can conclude that:

- a voltage of 50 kV, corresponding to 5 % of the beam acceleration potential, is the minimum recovery voltage for the residual ion deceleration as a lower voltage would imply a lower ion collection efficiency due to electrostatic reflections, especially if the beams of residual ions are not fully space charge compensated;

- the suppression efficiency of the secondary electrons emitted from the collector surfaces following the ion impact by means of the magnetic cusp field generated by permanent magnets on the walls of the negative ion collector is close to 100 %;
- the background gas pressure along the NNBI strongly influences the impact of the ERS on the wall-plug efficiency due to the collisions between the residual ions and the gas molecules and to the acceleration of the resulting secondary charges.

For the gas pressure expected on the ITER NNBI, which is around 0.02 Pa at the neutraliser exit [59], an ERS would be counterproductive as the resulting wall-plug efficiency with either the gas neutraliser or the BDPN is lower than the value achieved without energy recovery.

Energy recovery becomes advantageous if the background gas pressure is reduced down to around 10^{-3} Pa. In this case, the wall-plug efficiency is increased to 32 % by implementing the ERS with the gas neutraliser and to 37 % for the combination BDPN+ERS. Such a low value of gas pressure in the ERS region would be very demanding for the pumps: for example, in the case of the gas neutraliser, it has been estimated that the required pumping speed is $7300\,\mathrm{m^3\,s^{-1}}$ which is more than twice the pumping speed foreseen for the ITER NNBI. However, the open structure of the ERS outlined in this thesis allows a better pumping access with respect to ITER. Hence, the reduction of the background gas density along the injector is not a reason to stop considering energy recovery as a valid method to increase the NNBI wall-plug efficiency. It is however necessary as next step to investigate the consequences of a lower gas pressure on the ERS design, especially in terms of voltage holding and space charge compensation of the ion beams.

Bibliography

[1] IEA, “World Energy Outlook 2019”, tech. rep., IEA, Paris, 2019. Available: `https://www.iea.org/reports/world-energy-outlook-2019`.

[2] IPCC, “Global Warming of 1.5°C. An IPCC Special Report on the impacts of global warming of 1.5°C above pre-industrial levels and related global greenhouse gas emission pathways, in the context of strengthening the global response to the threat of climate change, sustainable development, and efforts to eradicate poverty”, tech. rep., IPCC, 2018. In Press. Available: `https://www.ipcc.ch/sr15/`.

[3] K. Gi, F. Sano, K. Akimoto, R. Hiwatari, and K. Tobita, “Potential contribution of fusion power generation to low-carbon development under the Paris Agreement and associated uncertainties”, *Energy Strategy Reviews*, vol. 27, p. 100432, Jan. 2020. `https://doi.org/10.1016/j.esr.2019.100432`.

[4] IEA, “Technology Roadmap - Nuclear Energy 2015”, tech. rep., IEA, Paris, 2015. Available: `https://www.iea.org/reports/technology-roadmap-nuclear-energy-2015`.

[5] “Advantages of fusion”. `https://www.iter.org/sci/Fusion`. Accessed on: Apr. 1, 2022.

[6] M. Kikuchi, K. Lackner, and M. Q. Tran, eds., *Fusion Physics.* Vienna: International Atomic Energy Agency, 2012.

[7] EUROfusion, "European Research Roadmap to the Realisation of Fusion Energy", tech. rep., EUROfusion, 2018. Available: `https://www.euro-fusion.org/eurofusion/roadmap/`.

[8] M. Q. Tran, P. Agostinetti, G. Aiello, K. Avramidis, B. Baiocchi, M. Barbisan, V. Bobkov, S. Briefi, A. Bruschi, R. Chavan, I. Chelis, C. Day, R. Delogu, B. Ell, F. Fanale, A. Fassina, U. Fantz, H. Faugel, L. Figini, D. Fiorucci, R. Friedl, T. Franke, G. Gantenbein, S. Garavaglia, G. Granucci, S. Hanke, J.-P. Hogge, C. Hopf, A. Kostic, S. Illy, Z. Ioannidis, J. Jelonnek, J. Jin, G. Latsas, F. Louche, V. Maquet, R. Maggiora, A. Messiaen, D. Milanesio, A. Mimo, A. Moro, R. Ochoukov, J. Ongena, I. G. Pagonakis, D. Peponis, A. Pimazzoni, R. Ragona, N. Rispoli, T. Ruess, T. Rzesnicki, T. Scherer, P. Spaeh, G. Starnella, D. Strauss, M. Thumm, W. Tierens, I. Tigelis, C. Tsironis, M. Usoltceva, D. Van Eester, F. Veronese, P. Vincenzi, F. Wagner, C. Wu, F. Zeus, and W. Zhang, "Status and future development of Heating and Current Drive for the EU DEMO", *Fusion Engineering and Design*, vol. 180, p. 113159, July 2022. `https://doi.org/10.1016/j.fusengdes.2022.113159`.

[9] D. Maisonnier, D. Campbell, I. Cook, L. Di Pace, L. Giancarli, J. Hayward, A. Li Puma, M. Medrano, P. Norajitra, M. Roccella, P. Sardain, M. Q. Tran, and D. Ward, "Power plant conceptual studies in Europe", *Nuclear Fusion*, vol. 47, pp. 1524–1532, Oct. 2007. `https://doi.org/10.1088/0029-5515/47/11/014`.

[10] C. Hopf, G. Starnella, N. den Harder, B. Heinemann, and U. Fantz, "A conceptual system design study for an NBI beamline for the European DEMO", *Fusion Engineering and Design*, vol. 146, pp. 705–708, Sept. 2019. `https://doi.org/10.1016/j.fusengdes.2019.01.060`.

[11] K. H. Berkner, R. V. Pyle, S. E. Savas, and K. R. Stalder, "Plasma neutralizers for H^- or D^- beams", in *Second international symposium on*

the production and neutralization of negative hydrogen ions and beams, (Upton, NY, USA), Oct. 1980. `https://www.osti.gov/biblio/6790798`.

[12] E. Surrey and A. Holmes, "The beam driven plasma neutralizer", in *AIP Conference Proceedings*, vol. 1515, p. 532, Feb. 2013. `https://doi.org/10.1063/1.4792825`.

[13] I. Turner and A. J. T. Holmes, "Model for a beam driven plasma neutraliser based on ITER beam geometry", *Fusion Engineering and Design*, vol. 149, p. 111327, Dec. 2019. `https://doi.org/10.1016/j.fusengdes.2019.111327`.

[14] R. S. Hemsworth, D. Boilson, P. Blatchford, M. Dalla Palma, G. Chitarin, H. P. L. de Esch, F. Geli, M. Dremel, J. Graceffa, D. Marcuzzi, G. Serianni, D. Shah, M. Singh, M. Urbani, and P. Zaccaria, "Overview of the design of the ITER heating neutral beam injectors", *New Journal of Physics*, vol. 19, p. 025005, Feb. 2017. `https://doi.org/10.1088/1367-2630/19/2/025005`.

[15] J. Wesson, *Tokamaks.* New York: Oxford University Press, third ed., 2004.

[16] C. Beidler, G. Grieger, F. Herrnegger, E. Harmeyer, J. Kisslinger, W. Lotz, H. Maassberg, P. Merkel, J. Nührenberg, F. Rau, J. Sapper, F. Sardei, R. Scardovelli, A. Schlüter, and H. Wobig, "Physics and Engineering Design for Wendelstein VII-X", *Fusion Technology*, vol. 17, pp. 148–168, Jan. 1990. `https://doi.org/10.13182/FST90-A29178`.

[17] F. Wagner, G. Becker, K. Behringer, D. Campbell, A. Eberhagen, W. Engelhardt, G. Fussmann, O. Gehre, J. Gernhardt, G. v. Gierke, G. Haas, M. Huang, F. Karger, M. Keilhacker, O. Klüber, M. Kornherr, K. Lackner, G. Lisitano, G. G. Lister, H. M. Mayer, D. Meisel, E. R.

Müller, H. Murmann, H. Niedermeyer, W. Poschenrieder, H. Rapp, H. Röhr, F. Schneider, G. Siller, E. Speth, A. Stäbler, K. H. Steuer, G. Venus, O. Vollmer, and Z. Yü, “Regime of Improved Confinement and High Beta in Neutral-Beam-Heated Divertor Discharges of the ASDEX Tokamak”, *Physical Review Letters*, vol. 49, pp. 1408–1412, Nov. 1982. `https://doi.org/10.1103/PhysRevLett.49.1408`.

[18] D. J. Campbell, T. Akiyama, R. Barnsley, M. Bassan, L. R. Baylor, L. Bertalot, F. Escourbiac, L. M. Giancarli, P. Gitton, J. Guirao, M. Kocan, V. Krasilnikov, U. Kruezi, M. Lehnen, S. Maruyama, Y. Ma, M. Merola, N. Mitchell, C. S. Pitcher, A. R. Raffray, R. Reichle, P. Shigin, A. Sirinelli, V. Udintsev, J. G. van der Laan, G. Vayakis, A. Wallander, M. Walsh, and C. Watts, “Innovations in Technology and Science R&D for ITER”, *Journal of Fusion Energy*, vol. 38, pp. 11–71, Jan. 2019. `https://doi.org/10.1007/s10894-018-0187-9`.

[19] Y. Wan, J. Li, Y. Liu, X. Wang, V. Chan, C. Chen, X. Duan, P. Fu, X. Gao, K. Feng, S. Liu, Y. Song, P. Weng, B. Wan, F. Wan, H. Wang, S. Wu, M. Ye, Q. Yang, G. Zheng, G. Zhuang, Q. Li, and CFETR team, “Overview of the present progress and activities on the CFETR”, *Nuclear Fusion*, vol. 57, p. 102009, June 2017. `https://doi.org/10.1088/1741-4326/aa686a`.

[20] R. Srinivasan and the Indian DEMO Team, “Design and analysis of SST-2 fusion reactor”, *Fusion Engineering and Design*, vol. 112, pp. 240–243, Nov. 2016. `https://doi.org/10.1016/j.fusengdes.2015.12.044`.

[21] K. Kim, K. Im, H. C. Kim, S. Oh, J. S. Park, S. Kwon, Y. S. Lee, J. H. Yeom, C. Lee, G.-S. Lee, G. Neilson, C. Kessel, T. Brown, P. Titus, D. Mikkelsen, and Y. Zhai, “Design concept of K-DEMO for near-term implementation”, *Nuclear Fusion*, vol. 55, p. 053027, Apr. 2015. `https://doi.org/10.1088/0029-5515/55/5/053027`.

[22] B. V. Kuteev, Y. S. Shpanskiy, and DEMO-FNS Team, "Status of DEMO-FNS development", *Nuclear Fusion*, vol. 57, p. 076039, June 2017. `https://doi.org/10.1088/1741-4326/aa6dcb`.

[23] C. E. Kessel, J. P. Blanchard, A. Davis, L. El-Guebaly, L. M. Garrison, N. M. Ghoniem, P. W. Humrickhouse, Y. Huang, Y. Katoh, A. Khodak, E. P. Marriott, S. Malang, N. B. Morley, G. H. Neilson, J. Rapp, M. E. Rensink, T. D. Rognlien, A. F. Rowcliffe, S. Smolentsev, L. L. Snead, M. S. Tillack, P. Titus, L. M. Waganer, G. M. Wallace, S. J. Wukitch, A. Ying, K. Young, and Y. Zhai, "Overview of the fusion nuclear science facility, a credible break-in step on the path to fusion energy", *Fusion Engineering and Design*, vol. 135, pp. 236–270, Oct. 2018. `https://doi.org/10.1016/j.fusengdes.2017.05.081`.

[24] G. Federici, C. Bachmann, L. Barucca, C. Baylard, W. Biel, L. V. Boccaccini, C. Bustreo, S. Ciattaglia, F. Cismondi, V. Corato, C. Day, E. Diegele, T. Franke, E. Gaio, C. Gliss, T. Haertl, A. Ibarra, J. Holden, G. Keech, R. Kembleton, A. Loving, F. Maviglia, J. Morris, B. Meszaros, I. Moscato, G. Pintsuk, M. Siccinio, N. Taylor, M. Q. Tran, C. Vorpahl, H. Walden, and J. H. You, "Overview of the DEMO staged design approach in Europe", *Nuclear Fusion*, vol. 59, p. 066013, Apr. 2019. `https://doi.org/10.1088/1741-4326/ab1178`.

[25] S. M. González de Vicente, J.-L. Boutard, S. J. Zinkle, and H. Tanigawa, "Materials testing facilities and programmes for fission and ion implantation damage", *Nuclear Fusion*, vol. 57, p. 092011, June 2017. `https://doi.org/10.1088/1741-4326/aa6a67`.

[26] D. Stork, R. Heidinger, T. Muroga, S. J. Zinkle, A. Moeslang, M. Porton, J.-L. Boutard, S. Gonzalez, and A. Ibarra, "Towards a programme of testing and qualification for structural and plasma-facing materials in

‘fusion neutron’ environments”, *Nuclear Fusion*, vol. 57, p. 092013, June 2017. `https://doi.org/10.1088/1741-4326/aa60af`.

[27] R. Wenninger, R. Kembleton, C. Bachmann, W. Biel, T. Bolzonella, S. Ciattaglia, F. Cismondi, M. Coleman, A. J. H. Donné, T. Eich, E. Fable, G. Federici, T. Franke, H. Lux, F. Maviglia, B. Meszaros, T. Pütterich, S. Saarelma, A. Snickers, F. Villone, P. Vincenzi, D. Wolff, and H. Zohm, “The physics and technology basis entering European system code studies for DEMO”, *Nuclear Fusion*, vol. 57, p. 016011, Oct. 2016. `https://doi.org/10.1088/0029-5515/57/1/016011`.

[28] G. Federici, W. Biel, M. R. Gilbert, R. Kemp, N. Taylor, and R. Wenninger, “European DEMO design strategy and consequences for materials”, *Nuclear Fusion*, vol. 57, p. 092002, June 2017. `https://doi.org/10.1088/1741-4326/57/9/092002`.

[29] R. Kemp, R. Wenninger, G. Federici, H. Reimerdes, R. Ambrosino, R. Brown, and M. Coleman, “Exploring a broad spectrum of design options for DEMO”, *Fusion Engineering and Design*, vol. 136, pp. 970–974, Nov. 2018. `https://doi.org/10.1016/j.fusengdes.2018.04.049`.

[30] H. Zohm, F. Träuble, W. Biel, E. Fable, R. Kemp, H. Lux, M. Siccinio, and R. Wenninger, “A stepladder approach to a tokamak fusion power plant”, *Nuclear Fusion*, vol. 57, p. 086002, June 2017. `https://doi.org/10.1088/1741-4326/aa739e`.

[31] R. S. Hemsworth and T. Inoue, “Positive and negative ion sources for magnetic fusion”, *IEEE Transactions on Plasma Science*, vol. 33, pp. 1799–1813, Dec. 2005. `https://doi.org/10.1109/TPS.2005.860090`.

[32] R. S. Hemsworth and D. Boilson, “Considerations for the development of neutral beam injection for fusion reactors or DEMO”, in *AIP Conference*

Proceedings, vol. 1869, p. 060001, 2017. `https://doi.org/10.1063/1.4995788`.

[33] H. P. L. de Esch, R. S. Hemsworth, and P. Massmann, "Updated physics design ITER-SINGAP accelerator", *Fusion Engineering and Design*, vol. 73, pp. 329–341, Oct. 2005. `https://doi.org/10.1016/j.fusengdes.2005.07.003`.

[34] G. Fubiani, R. S. Hemsworth, H. P. L. de Esch, and L. Svensson, "Analysis of the two accelerator concepts foreseen for the neutral beam injector of the International Thermonuclear Experimental Reactor", *Physical Review Special Topics - Accelerators and Beams*, vol. 12, p. 050102, May 2009. `https://doi.org/10.1103/PhysRevSTAB.12.050102`.

[35] IAEA, "ITER Design Description Document 5.3, N53 DDD 29 01-07-03 R0.1", tech. rep., IAEA, Vienna, 2003.

[36] M. Urbani, R. Hemsworth, B. Schunke, J. Graceffa, E. Delmas, L. Svensson, D. Boilson, A. Krylov, A. Panasenkov, G. Agarici, R. Stafford Allen, C. Jones, M. Kalsey, A. Muir, J. Milnes, F. Geli, and P. Sherlock, "The ITER neutral beam front end components integration", *Fusion Engineering and Design*, vol. 88, pp. 2110–2114, Oct. 2013. `https://doi.org/10.1016/j.fusengdes.2013.02.131`.

[37] M. J. Singh, "Status of Heating and Current Drive Systems Planned for ITER", *IEEE Transactions on Plasma Science*, vol. 44, pp. 1514–1524, Sept. 2016. `https://doi.org/10.1109/TPS.2016.2577709`.

[38] S. H. Kim, F. M. Poli, F. Koechl, E. Militello-Asp, A. R. Polevoi, R. Budny, T. A. Casper, A. Loarte, T. C. Luce, Y.-S. Na, M. Romanelli, M. Schneider, J. A. Snipes, P. C. de Vries, and The ITPA Topical Group on Integrated Operation Scenarios, "Development of ITER non-

activation phase operation scenarios", *Nuclear Fusion*, vol. 57, p. 086021, June 2017. `https://doi.org/10.1088/1741-4326/aa763e`.

[39] R. Hemsworth, H. Decamps, J. Graceffa, B. Schunke, M. Tanaka, M. Dremel, A. Tanga, H. P. L. De Esch, F. Geli, J. Milnes, T. Inoue, D. Marcuzzi, P. Sonato, and P. Zaccaria, "Status of the ITER heating neutral beam system", *Nuclear Fusion*, vol. 49, p. 045006, Mar. 2009. `https://doi.org/10.1088/0029-5515/49/4/045006`.

[40] M. J. Singh, D. Boilson, A. R. Polevoi, T. Oikawa, and R. Mitteau, "Heating neutral beams for ITER: negative ion sources to tune fusion plasmas", *New Journal of Physics*, vol. 19, p. 055004, May 2017. `https://doi.org/10.1088/1367-2630/aa639d`.

[41] M. J. Singh and H. P. L. De Esch, "Physics design of a 100 keV acceleration grid system for the diagnostic neutral beam for international tokamak experimental reactor", *Review of Scientific Instruments*, vol. 81, p. 013305, Jan. 2010. `https://doi.org/10.1063/1.3271535`.

[42] J. Pamela, A. Bécoulet, D. Borba, J.-L. Boutard, L. Horton, and D. Maisonnier, "Efficiency and availability driven R&D issues for DEMO", *Fusion Engineering and Design*, vol. 84, pp. 194–204, June 2009. `https://doi.org/10.1016/j.fusengdes.2009.02.028`.

[43] T. Oikawa, K. Ushigusa, C. B. Forest, M. Nemoto, O. Naito, Y. Kusama, Y. Kamada, K. Tobita, S. Suzuki, T. Fujita, H. Shirai, T. Fukuda, M. Kuriyama, T. Itoh, Y. Okumura, K. Watanabe, L. Grisham, and JT-60 Team, "Heating and non-inductive current drive by negative ion based NBI in JT-60U", *Nuclear Fusion*, vol. 40, pp. 435–443, Mar. 2000. `https://doi.org/10.1088/0029-5515/40/3Y/301`.

[44] C. J. Anderson, R. J. Girnius, A. M. Howald, and L. W. Anderson, "Production of fast H^0 atoms by stripping H^- ions in gas and vapor

targets", *Physical Review A*, vol. 22, pp. 822–834, Sept. 1980. `https://doi.org/10.1103/PhysRevA.22.822`.

[45] L. R. Grisham, "Lithium jet neutralizer to improve negative hydrogen neutral beam systems", *Physics of Plasmas*, vol. 14, p. 102509, Oct. 2007. `https://doi.org/10.1063/1.2792331`.

[46] F. Duré, A. Lifschitz, J. Bretagne, G. Maynard, A. Simonin, and T. Minea, "Modeling of the lithium based neutralizer for ITER neutral beam injector", *Chemical Physics*, vol. 398, pp. 17–26, Apr. 2012. `https://doi.org/10.1016/j.chemphys.2011.10.005`.

[47] D. Bresteau, C. Blondel, and C. Drag, "Saturation of the photoneutralization of a H^- beam in continuous operation", *Review of Scientific Instruments*, vol. 88, p. 113103, Nov. 2017. `https://doi.org/10.1063/1.4995390`.

[48] A. Simonin, J. Achard, K. Achkasov, S. Bechu, C. Baudouin, O. Baulaigue, C. Blondel, J. P. Boeuf, D. Bresteau, G. Cartry, W. Chaibi, C. Drag, H. P. L. de Esch, D. Fiorucci, G. Fubiani, I. Furno, R. Futtersack, P. Garibaldi, A. Gicquel, C. Grand, P. Guittienne, G. Hagelaar, A. Howling, R. Jacquier, M. J. Kirkpatrick, D. Lemoine, B. Lepetit, T. Minea, E. Odic, A. Revel, B. A. Soliman, and P. Teste, "R&D around a photoneutralizer-based NBI system (Siphore) in view of a DEMO Tokamak steady state fusion reactor", *Nuclear Fusion*, vol. 55, p. 123020, Nov. 2015. `https://doi.org/10.1088/0029-5515/55/12/123020`.

[49] A. Simonin, R. Agnello, S. Bechu, J. M. Bernard, C. Blondel, J. P. Boeuf, D. Bresteau, G. Cartry, W. Chaibi, C. Drag, B. P. Duval, H. P. L. de Esch, G. Fubiani, I. Furno, C. Grand, P. Guittienne, A. Howling, R. Jacquier, C. Marini, and I. Morgal, "Negative ion source development for a photoneutralization based neutral beam system for future fusion

reactors", *New Journal of Physics*, vol. 18, p. 125005, Dec. 2016. `https://doi.org/10.1088/1367-2630/18/12/125005`.

[50] J. H. Fink, "Photodetachment technology", in *AIP Conference Proceedings*, vol. 111, p. 547, 1984. `https://doi.org/10.1063/1.34383`.

[51] W. Chaibi, C. Blondel, L. Cabaret, C. Delsart, C. Drag, and A. Simonin, "Photo-neutralization of Negative Ion Beam for Future Fusion Reactor", in *AIP Conference Proceedings*, vol. 1097, p. 385, 2009. `https://doi.org/10.1063/1.3112535`.

[52] A. Simonin, C. Blondel, W. Chaibi, C. Dechelle, C. Drag, and E. Villedieu, "Towards a maintainable and high efficiency neutral beam system for future fusion reactors", *Nuclear Fusion*, vol. 61, p. 046003, Mar. 2021. `https://doi.org/10.1088/1741-4326/abdac2`.

[53] P. Sonato, P. Agostinetti, T. Bolzonella, F. Cismondi, U. Fantz, A. Fassina, T. Franke, I. Furno, C. Hopf, I. Jenkins, E. Sartori, M. Q. Tran, J. Varje, P. Vincenzi, and L. Zanotto, "Conceptual design of the DEMO neutral beam injectors: main developments and R&D achievements", *Nuclear Fusion*, vol. 57, p. 056026, Mar. 2017. `https://doi.org/10.1088/1741-4326/aa6186`.

[54] A. Fassina, F. Pretato, M. Barbisan, L. Giudicotti, and R. Pasqualotto, "A feasibility study of a NBI photoneutralizer based on nonlinear gating laser recirculation", *Review of Scientific Instruments*, vol. 87, p. 02B318, Feb. 2016. `https://doi.org/10.1063/1.4935897`.

[55] G. Starnella, C. Hopf, and P. N. Maya, "On suitable experiments for demonstrating the feasibility of the beam-driven plasma neutraliser for neutral beam injectors for fusion reactors", *Nuclear Fusion*, vol. 62, p. 066038, Apr. 2022. `https://doi.org/10.1088/1741-4326/ac5f18`.

[56] C. F. Barnett, “Atomic data for fusion. Volume 1: Collisions of H, H_2, He and Li atoms and ions with atoms and molecules”, tech. rep., Oak Ridge National Laboratory, July 1990.

[57] M. J. Singh, D. Boilson, R. S. Hemsworth, F. Geli, J. Graceffa, M. Urbani, E. Dlougach, A. Krylov, B. Schunke, and J. Chareyre, “Powerloads on the front end components and the duct of the heating and diagnostic neutral beam lines at ITER”, in *AIP Conference Proceedings*, vol. 1655, p. 050011, 2015. `https://doi.org/10.1063/1.4916468`.

[58] A. Krylov and R. S. Hemsworth, “Gas flow and related beam losses in the ITER neutral beam injector”, *Fusion Engineering and Design*, vol. 81, pp. 2239–2248, Sept. 2006. `https://doi.org/10.1016/j.fusengdes.2006.03.006`.

[59] M. Dremel, C. Day, R. Hemsworth, R. Pearce, and C. Mayaux, “Cryopump design for the ITER heating neutral beam injector”, *Nuclear Fusion*, vol. 49, p. 075035, July 2009. `https://doi.org/10.1088/0029-5515/49/7/075035`.

[60] M. Hanada, M. Kashiwagi, T. Inoue, K. Watanabe, and T. Imai, “Experimental comparison between plasma and gas neutralization of high-energy negative ion beams”, *Review of Scientific Instruments*, vol. 75, pp. 1813–1815, May 2004. `https://doi.org/10.1063/1.1699462`.

[61] M. Kashiwagi, M. Hanada, T. Yamana, T. Inoue, T. Imai, M. Taniguchi, and K. Watanabe, “Suppression of fast electron leakage from large openings in a plasma neutralizer for N-NB systems”, *Fusion Engineering and Design*, vol. 81, pp. 2863–2869, Nov. 2006. `https://doi.org/10.1016/j.fusengdes.2006.07.067`.

[62] G. I. Dimov, I. S. Emelev, and A. A. Ivanov, “A plasma target for neutralization of the negative ion beam”, in *AIP Conference Proceedings*, vol. 1771, p. 070015, 2016. `https://doi.org/10.1063/1.4964239`.

[63] V. A. Zhil'tsov, E. Y. Klimenko, P. M. Kosarev, V. M. Kulygin, V. V. Platonov, N. N. Semashko, A. A. Skovoroda, V. P. Ukhov, and A. A. Mehed'kin, “The development of a negative ion beam plasma neutralizer for ITER NBI”, *Nuclear Fusion*, vol. 40, pp. 509–513, Mar. 2000. `https://doi.org/10.1088/0029-5515/40/3Y/310`.

[64] “ANSYS Workbench, 2019 R3, ANSYS, Inc”.

[65] C. H. Chen, J. Talnagi, J. Liu, P. Vora, A. Higgins, and S. Liu, “The effect of neutron irradiation on Nd-Fe-B and Sm_2Co_{17}-based high-temperature magnets”, *IEEE Transactions on Magnetics*, vol. 41, pp. 3832–3834, Oct. 2005. `https://doi.org/10.1109/TMAG.2005.854985`.

[66] D. L. Hernandez and A. Valentine, “Final Report EFDA-A-2P7B36”, tech. rep., EUROfusion, 2020.

[67] M. E. Rudd, “Energy and angular distributions of secondary electrons from 5-100-keV-proton collisions with hydrogen and nitrogen molecules”, *Physical Review A*, vol. 20, pp. 787–796, Sept. 1979. `https://doi.org/10.1103/PhysRevA.20.787`.

[68] M. E. Rudd, Y.-K. Kim, D. H. Madison, and T. J. Gay, “Electron production in proton collisions with atoms and molecules: energy distributions”, *Reviews of Modern Physics*, vol. 64, pp. 441–490, Apr. 1992. `https://doi.org/10.1103/RevModPhys.64.441`.

[69] A. J. T. Holmes, “A one-dimensional model of a negative ion source”, *Plasma Sources Science and Technology*, vol. 5, pp. 453–473, Aug. 1996. `https://doi.org/10.1088/0963-0252/5/3/014`.

[70] A. Pimazzoni, E. Sartori, and G. Serianni, "On the role of dissociative recombination on the effectiveness of a plasma neutralizer in DEMO fusion plant", *Fusion Engineering and Design*, vol. 171, p. 112693, Oct. 2021. `https://doi.org/10.1016/j.fusengdes.2021.112693`.

[71] R. K. Janev, D. Reiter, and U. Samm, "Collision processes in low-temperature hydrogen plasmas (Jül–4105)", tech. rep., Forschungszentrum Jülich GmbH, Germany, 2003. `https://juser.fz-juelich.de/record/38224/files/Juel_4105_Reiter.pdf`. Accessed on: Apr. 1, 2022.

[72] J.-S. Yoon, M.-Y. Song, J.-M. Han, S. H. Hwang, W.-S. Chang, B. Lee, and Y. Itikawa, "Cross Sections for Electron Collisions with Hydrogen Molecules", *Journal of Physical and Chemical Reference Data*, vol. 37, pp. 913–931, June 2008. `https://doi.org/10.1063/1.2838023`.

[73] L. H. Scarlett, J. K. Tapley, D. V. Fursa, M. C. Zammit, J. S. Savage, and I. Bray, "Electron-impact dissociation of molecular hydrogen into neutral fragments", *The European Physical Journal D*, vol. 72, Feb. 2018. `https://doi.org/10.1140/epjd/e2017-80649-8`.

[74] M. O. Abdellahi El Ghazaly, J. Jureta, X. Urbain, and P. Defrance, "Total cross sections and kinetic energy release for the electron impact dissociation of H_2^+ and D_2^+", *Journal of Physics B: Atomic, Molecular and Optical Physics*, vol. 37, pp. 2467–2483, May 2004. `https://doi.org/10.1088/0953-4075/37/12/003`.

[75] F. Gaboriau and J. P. Boeuf, "Chemical kinetics of low pressure high density hydrogen plasmas: application to negative ion sources for ITER", *Plasma Sources Science and Technology*, vol. 23, p. 065032, Oct. 2014. `https://doi.org/10.1088/0963-0252/23/6/065032`.

[76] F. F. Chen, *Introduction to Plasma Physics and Controlled Fusion*. Springer, Cham, third ed., 2016.

[77] N. Hershkowitz, K. N. Leung, and T. Romesser, “Plasma Leakage Through a Low-β Line Cusp”, *Physical Review Letters*, vol. 35, pp. 277–280, Aug. 1975. `https://doi.org/10.1103/PhysRevLett.35.277`.

[78] Y. Jiang, G. Fubiani, L. Garrigues, and J. P. Boeuf, “Magnetic cusp confinement in low-β plasmas revisited”, *Physics of Plasmas*, vol. 27, p. 113506, Nov. 2020. `https://doi.org/10.1063/5.0014058`.

[79] E. Surrey and B. Crowley, “Spectroscopic measurement of gas temperature in the neutralizer of the JET neutral beam injection system”, *Plasma Physics and Controlled Fusion*, vol. 45, pp. 1209–1226, June 2003. `https://doi.org/10.1088/0741-3335/45/7/312`.

[80] B. Crowley, S. J. Cox, E. Surrey, I. Jenkins, D. Keeling, T. T. C. Jones, and A. R. Ellingboe, “Neutralisation of intense ion beams at JET”, in *20th IEEE/NPSS Symposium on Fusion Engineering*, pp. 232–235, IEEE, 2003. `https://doi.org/10.1109/FUSION.2003.1426628`.

[81] J. Paméla, “Gas heating effects in the neutralisers of neutral beam injection lines, EUR-CEA-FC 1279”, tech. rep., Association Euratom-CEA, France, 1985.

[82] J. Paméla, “Gas heating effects in the neutralizers of neutral beam injection lines”, *Review of Scientific Instruments*, vol. 57, pp. 1066–1068, June 1986. `https://doi.org/10.1063/1.1139192`.

[83] C. F. Barnett, J. A. Ray, E. Ricci, M. I. Wilker, E. W. McDaniel, E. W. Thomas, and H. B. Gilbody, “Atomic data for controlled fusion research”, tech. rep., Oak Ridge National Lab., TN (USA), Feb. 1977.

[84] T. Tabata and T. Shirai, “Analytic cross sections for collisions of H^+, H_2^+, H_3^+, H, H_2, and H^- with hydrogen molecules”, *Atomic Data and Nuclear*

Data Tables, vol. 76, pp. 1–25, Sept. 2000. `https://doi.org/10.1006/adnd.2000.0835`.

[85] E. Surrey, “Gas heating in the neutralizer of the ITER neutral beam injection systems”, *Nuclear Fusion*, vol. 46, pp. S360–S368, May 2006. `https://doi.org/10.1088/0029-5515/46/6/S18`.

[86] H. S. W. Massey, E. H. S. Burhop, and H. B. Gilbody, *Electronic and Ionic Impact Phenomena Vol 4: Recombination and Fast Collisions of Heavy Particles.* Oxford: Clarendon Press, second ed., 1974.

[87] M. B. Shah and H. B. Gilbody, “Ionisation of H_2 by fast protons and multiply charged ions of He, Li, C, N and O”, *Journal of Physics B: Atomic and Molecular Physics*, vol. 15, pp. 3441–3453, Oct. 1982. `https://doi.org/10.1088/0022-3700/15/19/013`.

[88] V. Toigo, R. Piovan, S. Dal Bello, E. Gaio, A. Luchetta, R. Pasqualotto, P. Zaccaria, M. Bigi, G. Chitarin, D. Marcuzzi, N. Pomaro, G. Serianni, P. Agostinetti, M. Agostini, V. Antoni, D. Aprile, C. Baltador, M. Barbisan, M. Battistella, M. Boldrin, M. Brombin, M. Dalla Palma, A. De Lorenzi, R. Delogu, M. De Muri, F. Fellin, A. Ferro, A. Fiorentin, G. Gambetta, F. Gnesotto, L. Grando, P. Jain, A. Maistrello, G. Manduchi, N. Marconato, M. Moresco, E. Ocello, M. Pavei, S. Peruzzo, N. Pilan, A. Pimazzoni, M. Recchia, A. Rizzolo, G. Rostagni, E. Sartori, M. Siragusa, P. Sonato, A. Sottocornola, E. Spada, S. Spagnolo, M. Spolaore, C. Taliercio, M. Valente, P. Veltri, A. Zamengo, B. Zaniol, L. Zanotto, M. Zaupa, D. Boilson, J. Graceffa, L. Svensson, B. Schunke, H. Decamps, M. Urbani, M. Kushwah, J. Chareyre, M. Singh, T. Bonicelli, G. Agarici, A. Garbuglia, A. Masiello, F. Paolucci, M. Simon, L. Bailly-Maitre, E. Bragulat, G. Gomez, D. Gutierrez, G. Mico, J.-F. Moreno, V. Pilard, M. Kashiwagi, M. Hanada, H. Tobari, K. Watanabe, T. Maejima, A. Kojima, N. Umeda, H. Yamanaka, A. Chakraborty,

U. Baruah, C. Rotti, H. Patel, M. V. Nagaraju, N. P. Singh, A. Patel, H. Dhola, B. Raval, U. Fantz, B. Heinemann, W. Kraus, S. Hanke, V. Hauer, S. Ochoa, P. Blatchford, B. Chuilon, Y. Xue, H. P. L. De Esch, R. Hemsworth, G. Croci, G. Gorini, M. Rebai, A. Muraro, M. Tardocchi, M. Cavenago, M. D'Arienzo, S. Sandri, and A. Tonti, "The PRIMA Test Facility: SPIDER and MITICA test-beds for ITER neutral beam injectors", *New Journal of Physics*, vol. 19, p. 085004, Aug. 2017. `https://doi.org/10.1088/1367-2630/aa78e8`.

[89] B. Heinemann, M. Fröschle, H.-D. Falter, U. Fantz, P. Franzen, W. Kraus, R. Nocentini, R. Riedl, and B. Ruf, "Upgrade of the BATMAN test facility for H^- source development", in *AIP Conference Proceedings*, vol. 1655, p. 060003, 2015. `https://doi.org/10.1063/1.4916472`.

[90] B. Heinemann, H.-D. Falter, U. Fantz, P. Franzen, M. Froeschle, W. Kraus, C. Martens, R. Nocentini, R. Riedl, E. Speth, and A. Staebler, "The negative ion source test facility ELISE", *Fusion Engineering and Design*, vol. 86, pp. 768–771, Oct. 2011. `https://doi.org/10.1016/j.fusengdes.2010.11.031`.

[91] J. Zacks, R. McAdams, J. Booth, K. Flinders, A. J. T. Holmes, M. Simmonds, B. Stevens, P. Stevenson, E. Surrey, S. Warder, A. Whitehead, and D. Young, "Preliminary results from the Small Negative Ion Facility (SNIF) at CCFE", in *AIP Conference Proceedings*, vol. 1515, p. 569, 2013. `https://doi.org/10.1063/1.4792829`.

[92] M. Cavenago, T. Kulevoy, S. Petrenko, V. Antoni, M. Bigi, E. Gazza, M. Recchia, G. Serianni, and P. Veltri, "Design of a versatile multi-aperture negative ion source", *Review of Scientific Instruments*, vol. 81, p. 02A713, Feb. 2010. `https://doi.org/10.1063/1.3271247`.

[93] A. Stäbler, J.-H. Feist, E. Speth, J. L. Dunne, S. Goetz, B. Heinemann, A. Krauss, R.-C. Kunze, H. Lohnert, J. Sielanko, W. Szyszko,

O. Vollmer, and K. Wittenbecher, “Design of the neutral beam injection system for ASDEX-Upgrade”, in *Fusion Technology 1988*, pp. 620–624, Elsevier, 1989. `https://doi.org/10.1016/B978-0-444-87369-9.50096-2`.

[94] I. Langmuir, “The Interaction of Electron and Positive Ion Space Charges in Cathode Sheaths”, *Physical Review*, vol. 33, pp. 954–989, June 1929. `https://doi.org/10.1103/PhysRev.33.954`.

[95] Y. Chen, C. Hu, and Y. Xie, “Analysis of Effects of the Arc Voltage on Arc Discharges in a Cathode Ion Source of Neutral Beam Injector”, *Plasma Science and Technology*, vol. 18, pp. 453–456, Apr. 2016. `https://doi.org/10.1088/1009-0630/18/4/21`.

[96] T. Morishita, T. Inoue, T. Iga, K. Watanabe, and T. Imai, “High proton ratio plasma production in a small negative ion source”, *Review of Scientific Instruments*, vol. 75, pp. 1764–1766, May 2004. `https://doi.org/10.1063/1.1695623`.

[97] R. McAdams, A. J. T. Holmes, M. Porton, A. Benn, E. Surrey, and T. T. C. Jones, “Advanced energy recovery concepts for negative ion beamlines in fusion power plants”, in *AIP Conference Proceedings*, vol. 1515, p. 559, 2013. `https://doi.org/10.1063/1.4792828`.

[98] J. Zacks and S. Wray, “Installation and Testing of an Energy Conversion system on SNIF (HCD-3.2.1-T027)”, tech. rep., EUROfusion, 2019.

[99] J. Pamela and S. Laffite, “Conceptual study of a purely electrostatic energy recovery system for negative-ion-based neutral beam injectors”, *Nuclear Instruments and Methods in Physics Research Section A: Accelerators, Spectrometers, Detectors and Associated Equipment*, vol. 295, pp. 453–460, Nov. 1990. `https://doi.org/10.1016/0168-9002(90)90726-M`.

[100] M. Fumelli, F. Jequier, and J. Pamela, “Experimental results of energy recovery on a neutral beam injector”, *Plasma Physics and Controlled Fusion*, vol. 31, pp. 495–508, Apr. 1989. `https://doi.org/10.1088/0741-3335/31/4/001`.

[101] M. Fumelli, “Cadarache Laboratory Studies of a Neutral Beam Injector with Energy Recovery”, *Fusion Technology*, vol. 17, pp. 571–576, July 1990. `https://doi.org/10.13182/FST90-A29193`.

[102] J. Paméla, M. Araki, M. Fumelli, F. Jequier, S. Laffite, Y. Ohara, M. Seki, K. Watanabe, and K. Yokoyama, “Energy recovery experiments with a powerful neutral beam injector equipped with a high atomic ion yield plasma generator”, *Nuclear Instruments and Methods in Physics Research Section A: Accelerators, Spectrometers, Detectors and Associated Equipment*, vol. 294, pp. 299–312, Sept. 1990. `https://doi.org/10.1016/0168-9002(90)91847-5`.

[103] M. Fumelli, F. Jequier, J. Paméla, M. Hanada, Y. Okumura, and K. Watanabe, “Energy recovery experiments with a powerful 100 keV D^- based neutral beam injector”, in *AIP Conference Proceedings*, vol. 287, p. 909, 1992. `https://doi.org/10.1063/1.44803`.

[104] R. W. Moir, “Direct Energy Conversion Beam Dump for a 1.6-MeV Neutral Beam for the International Thermonuclear Experimental Reactor”, *Fusion Technology*, vol. 25, pp. 129–136, Mar. 1994. `https://doi.org/10.13182/FST94-A30262`.

[105] K. Yoshikawa, Y. Nimura, Y. Yamamoto, and H. Watanabe, “Direct Energy Recovery from Unneutralized Ion Beams in a Negative-Ion-Beam-Based Neutral Beam Injection System”, *Fusion Technology*, vol. 17, pp. 527–539, July 1990. `https://doi.org/10.13182/FST90-A29189`.

[106] H. J. Hopman, "Energy recovery for negative ion based neutral beam lines", *Nuclear Fusion*, vol. 29, pp. 685–689, Apr. 1989. `https://doi.org/10.1088/0029-5515/29/4/013`.

[107] M. Araki, Y. Ohara, and Y. Okumura, "Design Study of a Beam Energy Recovery System for a Negative-Ion-Based Neutral Beam Injector", *Fusion Technology*, vol. 17, pp. 555–565, July 1990. `https://doi.org/10.13182/FST90-A29191`.

[108] M. Matsuoka, M. Araki, and M. Mizuno, "Beam Direct Converter with Varying Magnetic Field", *Fusion Technology*, vol. 26, pp. 1296–1303, Dec. 1994. `https://doi.org/10.13182/FST94-A30314`.

[109] M. Wolf and A. Pokryvailo, "High Voltage Resonant Modular Capacitor Charger Systems With Energy Dosage", in *2005 IEEE Pulsed Power Conference*, IEEE, June 2005. `https://doi.org/10.1109/PPC.2005.300477`.

[110] V. Variale, M. Cavenago, P. Agostinetti, P. Sonato, and L. Zanotto, "Ion collector design for an energy recovery test proposal with the negative ion source NIO1", *Review of Scientific Instruments*, vol. 87, p. 02B305, Feb. 2016. `https://doi.org/10.1063/1.4932383`.

[111] V. Variale, V. Valentino, M. Cavenago, C. Baltador, E. Sartori, and G. Serianni, "Beam energy recovery for fusion and collector design for tests on compact sources", *Review of Scientific Instruments*, vol. 91, p. 013516, Jan. 2020. `https://doi.org/10.1063/1.5128668`.

[112] A. F. Restrepo, E. Franco, H. Cadavid, and C. R. Pinedo, "A comparative study of the magnetic field homogeneity for circular, square and equilateral triangular helmholtz coils", in *2017 International Conference on Electrical, Electronics, Communication, Computer, and Optimization*

Techniques (ICEECCOT), IEEE, Dec. 2017. `https://doi.org/10.1109/ICEECCOT.2017.8284514`.

[113] R. Grisenti and A. Zecca, “Design data for a triple square coil system”, *Review of Scientific Instruments*, vol. 52, pp. 1097–1099, July 1981. `https://doi.org/10.1063/1.1136715`.

[114] R. Merritt, C. Purcell, and G. Stroink, “Uniform magnetic field produced by three, four, and five square coils”, *Review of Scientific Instruments*, vol. 54, pp. 879–882, July 1983. `https://doi.org/10.1063/1.1137480`.

[115] J. L. Kirschvink, “Uniform magnetic fields and double-wrapped coil systems: Improved techniques for the design of bioelectromagnetic experiments”, *Bioelectromagnetics*, vol. 13, no. 5, pp. 401–411, 1992. `https://doi.org/10.1002/bem.2250130507`.

[116] J. Alonso, G. Barrera, S. Cabrera, E. Rincón, L. Ríos, A. Soleto, A. El-Ouazzani, J. Graceffa, D. Shah, M. Urbani, and G. Agarici, “Some aspects of the design of the ITER NBI Active Correction and Compensation Coils”, *Fusion Engineering and Design*, vol. 96-97, pp. 392–395, Oct. 2015. `https://doi.org/10.1016/j.fusengdes.2015.04.011`.

[117] L. Ríos, B. Ahedo, J. Alonso, G. Barrera, S. Cabrera, E. Rincón, F. Ramos, A. El-Ouazzani, J. Graceffa, M. Urbani, D. Shah, and G. Agarici, “Assembly and gap management strategy for the ITER NBI vessel passive magnetic shield”, *Fusion Engineering and Design*, vol. 96-97, pp. 573–576, Oct. 2015. `https://doi.org/10.1016/j.fusengdes.2015.02.055`.

[118] D. C. Faircloth, “Technological Aspects: High Voltage”, tech. rep., CERN, 2014. `http://dx.doi.org/10.5170/CERN-2013-007.381`.

[119] M. S. Naidu and V. Kamaraju, *High Voltage Engineering.* McGraw-Hill, second ed., 1996.

[120] L. Cranberg, "The Initiation of Electrical Breakdown in Vacuum", *Journal of Applied Physics*, vol. 23, pp. 518–522, May 1952. `https://doi.org/10.1063/1.1702243`.

[121] K. Watanabe, M. Mizuno, Y. Ohara, M. Tanaka, K. Kobayashi, E. Takahashi, and T. Uede, "dc voltage holding experiments of vacuum gap for high-energy ion sources", *Journal of Applied Physics*, vol. 72, pp. 3949–3956, Nov. 1992. `https://doi.org/10.1063/1.352247`.

[122] P. Spolaore, G. Bisoffi, F. Cervellera, R. Pengo, and F. Scarpa, "The large gap case for HV insulation in vacuum", *IEEE Transactions on Dielectrics and Electrical Insulation*, vol. 4, no. 4, pp. 389–393, 1997. `https://doi.org/10.1109/94.625353`.

[123] P. Massmann, D. Boilson, H. P. L. de Esch, R. S. Hemsworth, and L. Svensson, "Voltage holding and dark currents in the Cadarache 1 MV ion beam facility", in *20th International Symposium on Discharges and Electrical Insulation in Vacuum*, IEEE, 2002. `https://doi.org/10.1109/ISDEIV.2002.1027372`.

[124] A. Kojima, M. Hanada, A. Hilmi, T. Inoue, K. Watanabe, M. Taniguchi, M. Kashiwagi, N. Umeda, H. Tobari, S. Kobayashi, Y. Yamano, and L. R. Grisham, "Vacuum insulation of the high energy negative ion source for fusion application", *Review of Scientific Instruments*, vol. 83, p. 02B117, Feb. 2012. `https://doi.org/10.1063/1.3672471`.

[125] M. Tanaka, R. S. Hemsworth, M. Kuriyama, L. Svensson, D. Boilson, T. Inoue, H. Tobari, M. Kashiwagi, M. Taniguchi, N. Umeda, and K. Watanabe, "1-MV Vacuum Insulation for the ITER Neutral Beam In-

jectors", *IEEE Transactions on Plasma Science*, vol. 39, pp. 1379–1385, June 2011. `https://doi.org/10.1109/TPS.2011.2138720`.

[126] T. Patton, N. Pilan, P. Bettini, G. Chitarin, A. De Lorenzi, D. Marcuzzi, E. Sartori, M. Siragusa, and L. Trevisan, "MITICA intermediate electrostatic shield: Concept design, development, and first experimental tests identification", in *AIP Conference Proceedings*, vol. 2052, p. 030002, 2018. `https://doi.org/10.1063/1.5083730`.

[127] A. Kojima, H. Tobari, N. Umeda, M. Kashiwagi, M. Ichikawa, J. Hiratsuka, N. Shibata, Y. Yamashita, M. Dairaku, H. Yamanaka, K. Watanabe, Y. Yamano, and L. R. Grisham, "Demonstration of 1 MV insulation for the vacuum insulated beam source in the ITER neutral beam system", *Nuclear Fusion*, vol. 59, p. 086042, July 2019. `https://doi.org/10.1088/1741-4326/ab1ab0`.

[128] D. Aprile, T. Patton, N. Pilan, and G. Chitarin, "Design of a System for Performing High-Voltage Holding Test Campaigns on a Mockup of MITICA Negative Ion Source", *IEEE Transactions on Plasma Science*, vol. 48, pp. 1555–1559, June 2020. `https://doi.org/10.1109/TPS.2020.2966911`.

[129] L. Svensson, D. Boilson, H. P. L. de Esch, R. S. Hemsworth, and A. Krylov, "Experimental results from the Cadarache 1 MV test bed with SINGAP accelerators", *Nuclear Fusion*, vol. 46, pp. S369–S378, May 2006. `https://doi.org/10.1088/0029-5515/46/6/S19`.

[130] H. P. L. de Esch, M. Kashiwagi, M. Taniguchi, T. Inoue, G. Serianni, P. Agostinetti, G. Chitarin, N. Marconato, E. Sartori, P. Sonato, P. Veltri, N. Pilan, D. Aprile, N. Fonnesu, V. Antoni, M. J. Singh, R. S. Hemsworth, and M. Cavenago, "Physics design of the HNB accelerator for ITER", *Nuclear Fusion*, vol. 55, p. 096001, Aug. 2015. `https://doi.org/10.1088/0029-5515/55/9/096001`.

[131] R. Latham, ed., *High Voltage Vacuum Insulation - Basic Concepts and Technological Practice.* Academic Press, first ed., 1995.

[132] N. Pilan, D. Marcuzzi, A. Rizzolo, L. Grando, G. Gambetta, S. Dalla Rosa, V. Kraemer, T. Quirmbach, G. Chitarin, R. Gobbo, G. Pesavento, A. De Lorenzi, L. Lotto, R. Rizzieri, M. Fincato, L. Romanato, L. Trevisan, V. Cervaro, and L. Franchin, "Electrical and structural R&D activities on high voltage dc solid insulator in vacuum", *Fusion Engineering and Design*, vol. 96-97, pp. 563–567, Oct. 2015. `https://doi.org/10.1016/j.fusengdes.2015.05.057`.

[133] N. Chauvin, "Space-Charge Effect", tech. rep., CERN, 2013. `http://dx.doi.org/10.5170/CERN-2013-007.63`.

[134] T. Kalvas, "Beam Extraction and Transport", tech. rep., CERN, 2013. `http://dx.doi.org/10.5170/CERN-2013-007`.

[135] M. Reiser, *Theory and Design of Charged Particle Beams.* Wiley-VCH, second ed., Mar. 2008.

[136] M. D. Gabovich, "Ion-beam plasma and the propagation of intense compensated ion beams", *Soviet Physics Uspekhi*, vol. 20, pp. 134–148, Feb. 1977.

[137] I. A. Soloshenko, "Transportation of intensive ion beams (invited)", *Review of Scientific Instruments*, vol. 69, p. 1088, 1998. `https://doi.org/10.1063/1.1148748`.

[138] A. J. T. Holmes, "Theoretical and experimental study of space charge in intense ion beams", *Physical Review A*, vol. 19, pp. 389–407, Jan. 1979. `https://doi.org/10.1103/PhysRevA.19.389`.

[139] E. Surrey, "Space Charge Neutralization in the ITER Negative Ion Beams", in *AIP Conference Proceedings*, vol. 925, p. 278, 2007. `https://doi.org/10.1063/1.2773666`.

[140] E. Surrey and M. Porton, “Space Charge Neutralization of DEMO Relevant Negative Ion Beams at Low Gas Density”, in *AIP Conference Proceedings*, vol. 1390, p. 482, 2011. `https://doi.org/10.1063/1.3637420`.

[141] A. J. T. Holmes and R. McAdams, “Space charge compensation of positive ion beams used in magnetic fusion applications”, *Nuclear Fusion*, vol. 62, p. 066017, Apr. 2022. `https://doi.org/10.1088/1741-4326/ac544c`.

[142] P. Veltri, M. Cavenago, and G. Serianni, “Study of space charge compensation phenomena in charged particle beams”, *Review of Scientific Instruments*, vol. 83, p. 02B709, Feb. 2012. `https://doi.org/10.1063/1.3670342`.

[143] E. Sartori, T. J. Maceina, P. Veltri, M. Cavenago, and G. Serianni, “Simulation of space charge compensation in a multibeamlet negative ion beam”, *Review of Scientific Instruments*, vol. 87, p. 02B917, Feb. 2016. `https://doi.org/10.1063/1.4933252`.

[144] R. Behrisch and W. Eckstein, eds., *Sputtering by Particle Bombardment*. Springer, Berlin, Heidelberg, first ed., 2007.

[145] N. den Harder, G. Orozco, I. Zammuto, C. Hopf, and the ASDEX Upgrade Team, “Modeling neutral beam transport in fusion experiments: Studying the effects of reionisation and deflection”, *Fusion Engineering and Design*, vol. 146, pp. 518–521, Sept. 2019. `https://doi.org/10.1016/j.fusengdes.2019.01.011`.

[146] T. Kalvas, O. Tarvainen, T. Ropponen, O. Steczkiewicz, J. Ärje, and H. Clark, “IBSIMU: A three-dimensional simulation software for charged particle optics”, *Review of Scientific Instruments*, vol. 81, p. 02B703, Feb. 2010. `https://doi.org/10.1063/1.3258608`.

[147] "Ion Beam Simulator". `http://ibsimu.sourceforge.net/`. Accessed on: Apr. 1, 2022.

[148] "ANSYS Mechanical APDL, 2019 R3, ANSYS, Inc".

[149] G. Fubiani, H. P. L. de Esch, A. Simonin, and R. S. Hemsworth, "Modeling of secondary emission processes in the negative ion based electrostatic accelerator of the International Thermonuclear Experimental Reactor", *Physical Review Special Topics - Accelerators and Beams*, vol. 11, p. 014202, Jan. 2008. `https://doi.org/10.1103/PhysRevSTAB.11.014202`.